UNIVERSITE D'AIX-MARSEILLE

ECOLE DOCTORALE DE PHYSIQUE ET SCIENCES DE LA MATIERE

Laboratoire de Physique des Interactions Ioniques et Moléculaires

Thèse présentée pour obtenir le grade universitaire de docteur

Discipline : Matière Condensée et Nanosciences

Daniel BEATO MEDINA

Characterization of 2D architectures on metallic substrates by electron spectroscopy and microscopy

Soutenue le 28/10/2016 devant le jury:

Carmelo PIRRI	IS2M, Mulhouse	Rapporteur
Alberto VERDINI	IOM CNR, Laboratorio TASC, Trieste	Rapporteur
Bruno GRANDIDIER	IEMN, Lille	Examinateur
Guy LE LAY	PIIM AMU, Marseille	Examinateur
Thierry ANGOT	PIIM AMU, Marseille	Directeur de thèse
Eric SALOMON	PIIM AMU, Marseille	Codirecteur de thèse

Agradecimientos

Agradezco en primer lugar a los miembros del jurado, Bruno Grandidier, Guy Le Lay, Carmelo Pirri y Alberto Verdini, que hayan aceptado aportar sus capacidades y su tiempo para evaluar mi trabajo y mejorar su calidad. Espero transmitirles mi interés por lo recogido en la tesis y que la lectura les sea provechosa.

Es mi deseo reservar un pequeño hueco en esta tesis para aquellas personas que consciente o inconscientemente han tenido una repercusión positiva en la realización de este trabajo. En agradecimiento, no puedo por menos que dedicaros el fruto de mi esfuerzo:

A Eric, quien desde el primer momento acogió con interés la idea de recibirme como doctorando y bajo cuya tutela he podido no sólo aprovechar sus aptitudes académicas y científicas, sino también disfrutar de su calidad humana y cercanía. Espero que esta empresa te haya resultado tan grata como a mí.

A Thierry por dirigir oficialmente mi aprendizaje. Pocas cualidades son más apropiadas para la formación que la experiencia, la sinceridad, la escucha y el sentido del humor, y él ha sabido ser la combinación de dichos rasgos convirtiendo el grupo "Plasma-Superficie" en un núcleo de ambiente familiar.

Al resto del equipo "Plasma-Superficie", por los incontables momentos de convivencia y cómo habéis contribuido a que esta experiencia académica tenga muchas más facetas.

A los miembros del taller de mecánica, por haber puesto sus habilidades al servicio del progreso de mi tesis.

A todos los que forman el laboratorio P.I.I.M. por haber contribuido a redondear más si cabe toda mi esfera académico-laboral. En especial quiero reconocer la labor del equipo de administración por su inestimable ayuda con trámites y papeleos.

A mis compañeros de despacho: Othmen, el silencioso y sonriente compañero, "decano" del despacho. Kostya, el contrapunto torbellino que imbuía de cordialidad nuestra atmósfera. 杨鑫, quien ha compartido estos tres años conmigo y ha propiciado un ambiente de trabajo atento y minucioso, no exento de destellos de calidez. Florin, alegría, espíritu amistoso y aires gamberros, ha mantenido a raya la posibilidad de un despacho demasiado gris. Roba, la última incorporación, un dechado de atenciones y buenas intenciones.

Y al otro lado de los Pirineos, a mis amigos. Afortunadamente sois numerosos y no sé si alguno tendrá conciencia de cómo sus acciones se propagan hasta dejar una huella en este trabajo. En cualquier caso este es un buen lugar para expresaros mi gratitud por todo lo que hacéis por mí y por mantenerme en vuestras vidas.

A mi familia, a toda ella en su más amplia extensión, por apoyarme, sostenerme y demostrarme que ciertos lazos son irrompibles. Sin vuestro cariño en la distancia estos tres años habrían sido mucho peores. Mención especial a mi padre, guardián irredento de mi felicidad, sobre cuya espalda reposa no sólo el éxito de este doctorado, sino la práctica totalidad de lo que lo ha precedido.

Finalmente pero primera en mi corazón a mi madre. Siempre quisiste tener un hijo "doctor", pero desgraciadamente no llegaste a leer estas palabras. Todo este trabajo está sobre todo dedicado a ti. Tuya más que de nadie es la impronta que dejan mis acciones, y espero que esta tesis, como todos los demás actos, sean dignos homenajes de ti.

Index

Summary

Nanosciences and surface science are key elements in the conception of a diversity of innovative materials designed to better cope with the needs of current technology. Within this context, we have resolved to characterise the properties of different two-dimensional structures grown on silver substrates with the help of several complementary techniques of surface analysis.

Firstly, we have studied auto-assembled 2D films of cobalt phthalocyanine on Ag(100) substrates. In situations with coverages close to the monolayer, two phases were observed: the (5x5) and the (7x7). The electron energy loss spectroscopy has allowed us to support the existence of two inequivalent charge transfer mechanisms between the substrate and the molecules. On one hand, the (5x5) reconstruction displays a transfer that involves the silver atoms and only the cobalt atoms of the molecules. On the other hand, the phenomenon rather occurs between the substrate and lowest unoccupied molecular orbital in the case of the (7x7) phase. A fine analysis of the adsorption geometry of the molecules on the surface performed by means of photoelectron diffraction along with the comparison to simulations in the framework of multiple scattering approximation have made it possible to identify the presence of sites of adsorption particular to each phase as the underlying cause for the distinct charge transfer mechanisms.

Secondly, we have synthesised both monolayer and multilayer silicene by evaporating silicon atoms on Ag(111) substrates. Silicene is a two-dimensional material akin to graphene but made of one or a few layers of silicon atoms. However, many physical properties of this allotrope are still unexplained. For this reason, we have decided to delve into the characteristics of multilayer silicene as it's less well-known than its monolayer counterpart. With this aim, the system has been subjected to experiments of photoemission spectroscopy and diffraction. In this manner, several hypotheses on the very nature of this material have been tested. In particular, we have observed that both the silver substrate and the silicene on top display at least two different characters (bulk and interface) manifested through the splitting of the analysed core levels. Furthermore, the ratio of intensities as a function of the angle of observation have hinted at a puzzling stratification of the system.

On another matter also related to silicene, we have studied its functionalization by adsorption of F_4TCNQ molecules and atomic hydrogen. We attest that hydrogenation is a convenient way of protecting monolayer silicene from damaging chemical reactions such as oxidation. Unfortunately, the multilayer variant undergoes a more drastic change as a non-reversible etching takes place on its surface instead. Regarding the F_4TCNQ exposure, these molecules were successfully used in the past to dope supported graphene, but an analogue experiment didn't alter significantly the electronic properties of our multilayer silicene near the Fermi level. We suspect that the unexpected stratification deduced from the photoemission spectra, which seems to include a silver layer on top of multilayer silicene, could be at the origin of this divergent behaviour (compared to its carbon cousin). In effect, a silver layer on top could be able to provide enough electrons to saturate the acceptor molecules without modifying the electron bands, thus rendering the doping fruitless.

Résumé

La physique des surfaces et nanosciences est une discipline qui permet la conception d'une diversité de matériaux innovants pour mieux répondre aux besoins de la technologie actuelle. Dans ce contexte, nous nous sommes intéressés à caractériser les propriétés de différentes structures 2D élaborées sur des substrats d'argent en combinant différentes techniques d'analyses de surface.

D'une part nous avons étudié des films 2D auto-assemblés à base de phtalocyanine de cobalt adsorbées sur Ag(100). Au régime de la monocouche, deux phases ont été essentiellement observées : la (5×5) et la (7×7). La spectroscopie de pertes d'énergie nous a permis de mettre en évidence deux mécanismes de transfert de charge métal/molécule différents. Un entre le substrat et les atomes de cobalt de la molécule dans le cas de la (5×5). L'autre, pour la phase (7×7), entre le substrat et l'orbitale moléculaire la plus basse inoccupée de la molécule. Une analyse fine de la géométrie d'adsorption des molécules sur la surface d'Ag(100) par diffraction de photoélectrons, et une comparaison avec des simulations réalisées dans le cadre de diffusion multiple, nous ont permis d'établir l'existence de différents sites d'adsorption, dépendant de la phase, et comme étant à l'origine de ces différences de mécanismes de transfert de charges.

D'autre part, nous avons synthétisé, par évaporation d'atomes de silicium sur de l'Ag(111), du silicene en monocouche et multicouche. Le silicène est un matériau bidimensionnel analogue du graphène constitué d'une ou plusieurs couches d'atomes de silicium. Néanmoins, de nombreuses questions restent ouvertes quant aux propriétés physiques du silicene. Ainsi nous avons entrepris des mesures dans le but de comprendre les propriétés structurales du silicene en multicouche. Pour cela nous avons engagé des mesures par spectroscopie de photoémission et diffraction de photoélectrons, et comparé nos données avec des simulations réalisées dans le cadre la diffusion multiple. Plusieurs hypothèses concernant la nature de ce matériau ont pu être testées. En particulier nous avons observé que l'argent et le silicene présentent au moins deux caractères différents (interface et *bulk*) qui se manifestent par le dédoublement des niveaux de cœur analysés. Néanmoins, les rapports d'intensité des diverses composantes en fonction de l'angle d'observation ont signalé une stratification qui n'est pas évidente à interpréter.

Par ailleurs nous avons étudié la fonctionnalisation du silicene par hydrogénation et adsorption de molécules de F_4TCNQ. Nous avons constaté que l'hydrogénation est une bonne manière de protéger la monocouche, par exemple de l'oxydation, mais beaucoup plus destructive vis à vis du silicène multicouche, qu'elle détériore par attaque chimique. Par ailleurs, nous avons déposé des couches de molécules F_4TCNQ, molécules utilisées avec succès pour le dopage du graphène, sur silicène multicouche dans le but d'en modifier ses propriétés électroniques. Nous n'avons malheureusement pas été en mesure d'observer une modification notable de la structure électronique près du niveau de Fermi. Ceci potentiellement en raison de la couche d'argent formée en surface, lequel disposerait de suffisamment d'électrons pour empêcher l'effet du dopage escompté.

Introduction

The present thesis belongs to the field of physics of surfaces and interfaces and revolves around the characterisation of two-dimensional architectures on metallic substrates by means of electron spectroscopy and microscopy. The general objective is the comprehension at a very fundamental level of the mechanisms involved in the formation, the reactivity and the electronics of several interfaces.

Given the nature of the experiments, they have been performed in the *Nautilus* laboratory of the Plasma-Surface team under ultra-high vacuum conditions or in synchrotron beamlines of similar characteristics[1,2].

This work has its roots in a zone of convergence of surface physics and materials at the nanometric scale. Starting from the industrial revolution, many processes have decreased in size as the technology evolved. One paradigmatic example is the electronic components inside the computers. Processing power has been growing steadily following the Moore's law[3] while transistors of the chips have increased in number as they shrunk in size. In the most optimistic perspectives of organic electronics, the transistors can still be reduced nearly to the molecular scale[4], but in any case it is undeniable that the current trend pushes towards the miniaturisation of technological devices.

In this context, the discovery of graphene[5] supposed a groundbreaking finding awarded with the Nobel Prize for its fascinating theoretical and experimental properties. It paved the way for the conception and study of other two-dimensional allotropes, such as silicene[6], the silicon-based cousin of graphene. Silicene constitutes one of the central elements of this thesis, and some of its intriguing characteristics will be studied in the following pages.

With regard to the experimental techniques, they have been diverse and offered different approaches and information about the systems in question. The reciprocal space and thus the periodic structure has been explored with Low Energy Electron Diffraction (LEED). It reveals the Fourier transform of the lattice on surface and gives a preliminary judgement on its level of order and defects. More precise and local structural information has been garnered with the Scanning Tunnelling Microscope (STM). The output consists in height maps of electronic density, which is strongly correlated with the position of the atoms in the analysed situations. The vibrational excitations of the systems have been probed with the High Resolution Electron Energy Loss Spectrometry (HREELS) technique, which is highly sensitive to the quantity of adsorbates on surface and to their chemical nature. Upon thoughtful study, it can even reveal distortions in molecules and small chemical shifts due to charge transfers. Finally, photoemission spectroscopy has been crucial to determine the growth and stratification of some samples. Its diffractive counterpart has also offered detailed descriptions through very precise parameters of interfaces of organic molecules on metallic substrates.

The corpus of the thesis begins with succinct introductions to the elements involved in the studies, that is to say, both the experimental techniques and the chemical species that have been part of some of the systems.

After this preliminary section, the first chapter is devoted to the interfaces produced when the organic molecule cobalt phthalocyanine is evaporated on Ag(100) substrates. Phthalocyanines are a group of molecules with many possible applications and known to form highly ordered 2D superlattices over long ranges. They and their derivatives constitute around a quarter of the artificial organic pigments used to this day[7]. In addition, they have been investigated to a lesser extent as catalysts for reduction-oxidation reactions, donor molecules for devices like FET transistors[8] and lately they have been considered as memory elements in quantum computing[9].

In any case, the study reported in the chapter comes from a more fundamental level. The assembly of the interface will be analysed in great detail. The subsequent discussion will delve into the geometrical configuration of the surface and how this affects the electronic properties of the system, exposing some key aspects of the association of organic molecules with metallic substrates.

The second chapter revolves around the formation of silicene. Its gradual growth on Ag(111) surfaces will be examined by means of spectroscopic data acquired at the *ANTARES* beamline of the *SOLEIL* synchrotron. The information will be useful to establish a discussion on the nature of silicene with respect to its thickness. This topic has been actively debated lately as a result of coetaneous evidences supporting confronted hypotheses[10,11]. X-ray photoelectron diffraction simulations will again be compared to experimental patterns to underpin the affirmations about the stratification of the material.

Finally, the last chapter will focus on the functionalization of silicene with hydrogen or deuterium and the strong electron acceptor F_4TCNQ. The lightest element has been proposed as a convenient way to tune the magnetic and electronic properties of silicene[12,13,14]. It has even been proposed as an agent capable of producing the freestanding variant by detaching it from the substrate[15]. In any case, the effect of the exposure to hydrogen will be thoroughly reported form the structural and spectroscopic points of view. This will constitute one of the first experimental approaches to the reactivity of silicene and will add arguments to refine its comparison with ordinary silicon. Finally, the doping with F_4TCNQ of silicene will close the thesis in a further attempt to exploit its predicted ambipolar properties by mitigating its intrinsic n-doping.

As a whole, this work is conceived as a panorama on diverse physical properties of 2D architectures on metals combining pieces of information offered by complementary experimental techniques. In the end, a convincing global picture of the studied systems will be assembled, and the multidisciplinary approach undertaken will demonstrate its persuasive advantages.

References:

1. http://www.synchrotron-soleil.fr/Recherche/LignesLumiere/ANTARES
2. https://www.elettra.trieste.it/it/lightsources/elettra/elettra-beamlines/aloisa/aloisa.html
3. Moore, G. E., Electronics, Volume 38, Number 8 (1965)
4. Kubatkin, S. et al., Nature 425 (6959): 698–701 (2003)
5. Geim A. K. and Novoselov K. S., Nature Materials 6, 183 - 191 (2007)
6. Vogt, P. et al., Phys. Rev. Let. 108, 155501 (2012)
7. Gerd Löbbert "Phthalocyanines" Ullmann's Encyclopedia of Industrial Chemistry, Wiley-VCH, Weinheim (2002)
8. Chaidogiannos, G. et al., Applied Physics A 96 (3): 763 (2009).
9. *New material for quantum computing discovered out of the blue*. phys.org. October 27, 2013
10. De Padova, P. et al., 2D Materials 1, 021003 (2014)
11. Chun-Liang, L. et al., J. Phys. Chem. C, 120 (12), 6689–6693 (2016)
12. Huang B. et al., Phys. Rev. X 4, 021029 (2014)
13. Osborn T. H. et al., Chem. Phys. Let. 511, 101–105 (2011)
14. Wang, X. Q. et al., Phys. Chem. Chem. Phys., 14, 3031–3036 (2012)
15. Tsetseris L. and Kaltsas D., Phys.Chem.Chem.Phys., 16, 5183 (2014)

Chapter I:
The experimental and numerical techniques

Low energy electron diffraction

1. Theoretical basis

Low energy electron diffraction (LEED) is an experimental technique which relies on subjecting a surface to a beam of electrons with energies in the range between 5 and 200 eV. Such electrons, with a penetration depth of a few angstrom by virtue of their energy, undergo interactions with the surface and are scattered principally along some favoured directions closely linked to the surface geometrical structure.

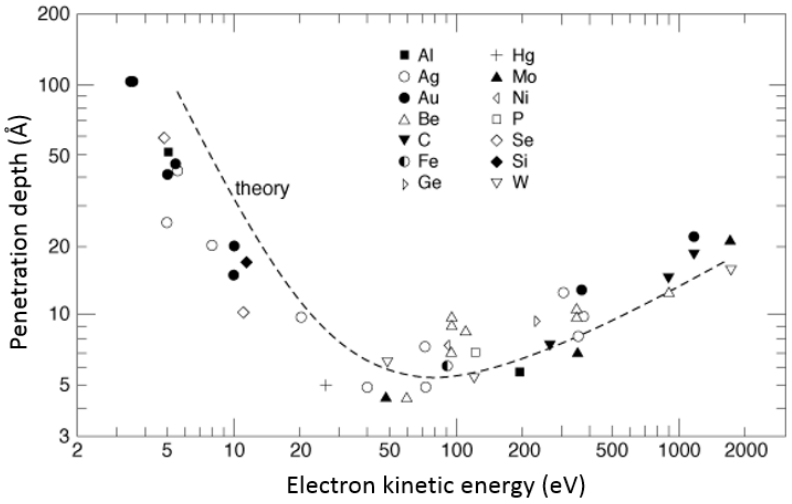

Figure 1: Penetration depth of the electrons as a function of their energy in different materials[1]

As a result of the periodicity of an ideal surface, it's possible to determine the position of every atom or molecule from the positions of the atoms and molecules in the unit cell (r_1, r_2… r_n) and a basis with as many vectors as the dimension of space, 2 in the particular case of a surface ($\vec{a}$ and $\vec{b}$).

Likewise, in situations in which the magnitudes have a periodic behaviour, it's usually convenient to apply the Fourier transform. This operation performed over the two-dimensional lattice that represents the surface returns the corresponding lattice in the reciprocal space, which can also be generated by means of the reciprocal unit cell (r_1*, r_2*… r_n*) and a reciprocal basis ($\vec{a}$* y $\vec{b}$*).

The intensity of the diffracted beam along a particular direction is proportional to the norm of the structure factor F_g, whose value is given by:

$$F_g = \sum_i f_i \, e^{-2\pi i(\overrightarrow{\Delta k}\cdot\vec{r}_i)}$$

In this expression, f_i and r_i stand for the atomic form factor and the position of the ith atom respectively, while $\overrightarrow{\Delta k}$ is the vector that results from the subtraction of the ingoing wavevector from the outgoing wavevector of the electrons.

By introducing the Fourier series of the atomic form factor in the previous expression, it becomes:

$$F_g = \sum_i \sum_{\vec{g}} f_{\vec{g},i} e^{-2\pi i(\overrightarrow{\Delta k} - \vec{g})\cdot \vec{r}_i}$$

Here, $f_{g,i}$ represents the coefficients of the Fourier series of f_i and $\vec{g}$ runs over all the nodes of the reciprocal space.

In view of this equation, it's clear that a scattering event with a variation of the wavevector identical to a vector of the reciprocal lattice $\vec{g}$, will lead to a null argument in the exponential. This will result in turn in a non-vanishing contribution to the structure factor, and thus a beam with a high intensity will be observed. This is the so-called Laue condition:

$$\overrightarrow{\Delta k} = \vec{g}(x, y, z) = x\vec{a}^* + y\vec{b}^* + z\vec{c}^*$$

Given that the attenuation in the direction perpendicular to the surface implies the negligibility of the transfer of momentum in the normal direction[2], the reasoning can be restricted to the subspace parallel to the surface.

$$\overrightarrow{\Delta k_{||}} = \overrightarrow{g_{||}}$$

Since the study is also limited to the elastic scattering, the conservation of energy has to be imposed, that is to say the conservation of the module of the wavevector:

$$|\vec{k}_i| = |\vec{k}_f|$$

A graphical tool that is enlightening for the comprehension of these two conditions is the Ewald's sphere, shown in the figure below:

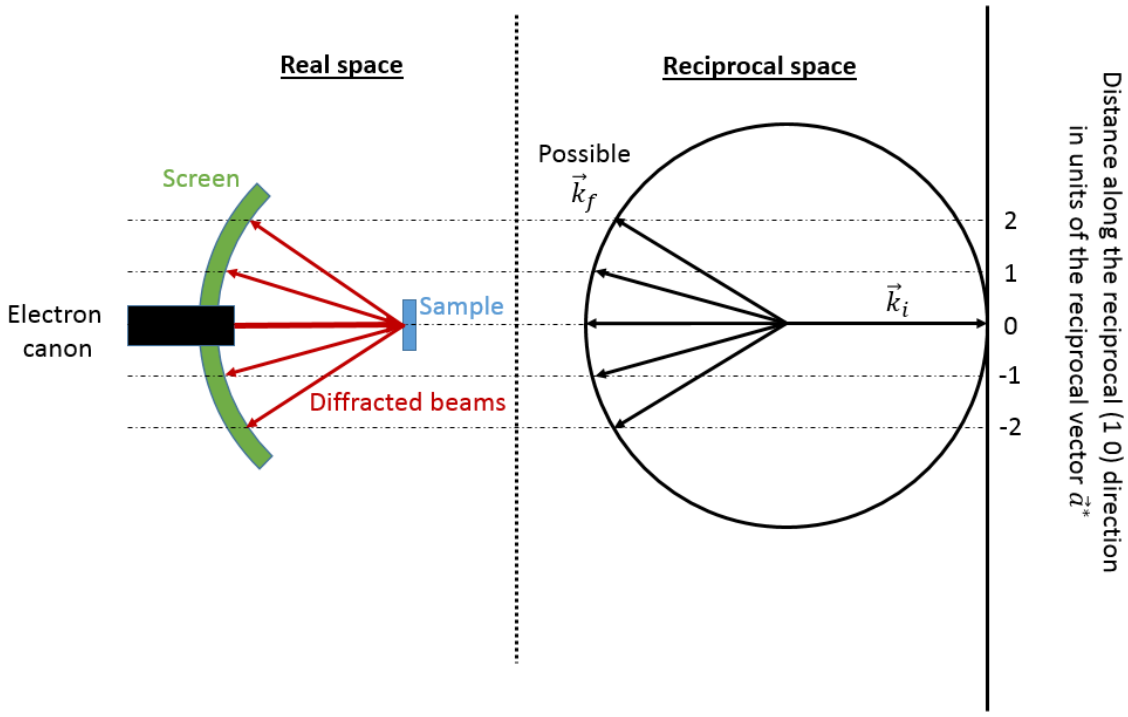

Figure 2: Diagram of the LEED device (left) along with Ewald's sphere (right)

On the right side, the scattering in the reciprocal space can be seen. The elastic scattering implies that the incident and diffracted wavevectors have to have the same length, so their tips have to lie on the surface of a sphere if they have a common origin.

Furthermore, according to Laue condition, the wavevector variation has to be equal to one of the vectors of the reciprocal space.

Consequently, the directions of diffraction will be given by the intersections of the sphere with the straight lines parallel to the incidence that pass through the points which meet the Laue criteria. Those intersections will indicate the directions of diffraction.

Alternatively, the condition of constructive interference (i.e. the difference of path Δs covered by the electrons scattered from adjacent atoms has to be equal to an integral multiple of their corresponding wavelength λ_e) makes it easier to grasp the connection between the geometry of the device, the angle of emission θ, the wavelength of the electrons and the distance between nodes of the surface d.

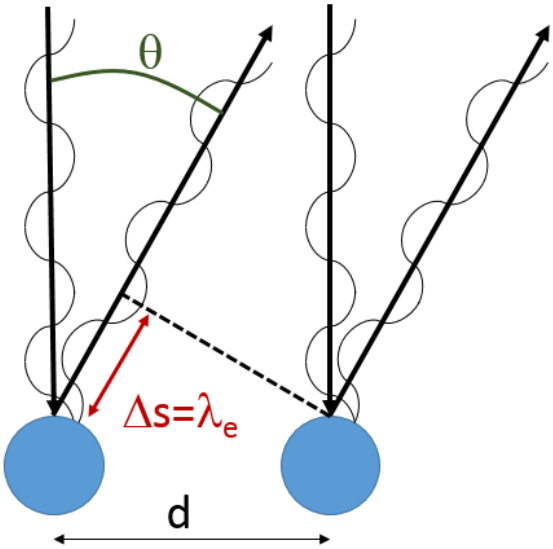

Figure 3: Situation of first order constructive interference

Under these conditions, the following expression is immediate:

$$\frac{\lambda_e}{d} = \sin\theta$$

Moreover, the angle of the first order of diffraction is linked as well to the distance from the centre r at which the first diffracted beam will be visible, allowing the introduction of this magnitude and the radius of the screen R in the equation:

$$\frac{\lambda_e}{d} = \frac{r}{R}$$

2. Experimental device

The LEED device that has been used throughout this thesis is a *Omicron SPECTALEED*. It mainly consists of:

1) One electron gun with a cathode set to a voltage *V* which allows the emission of a collimated beam of low energy electrons.
2) Two grids (numbers 1 and 4) set to the same potential as the sample.
3) Two additional grids (numbers 2 and 3) to deflect the electrons that have taken part in inelastic processes.
4) A fluorescent screen set to a voltage of 5 or 6kV.

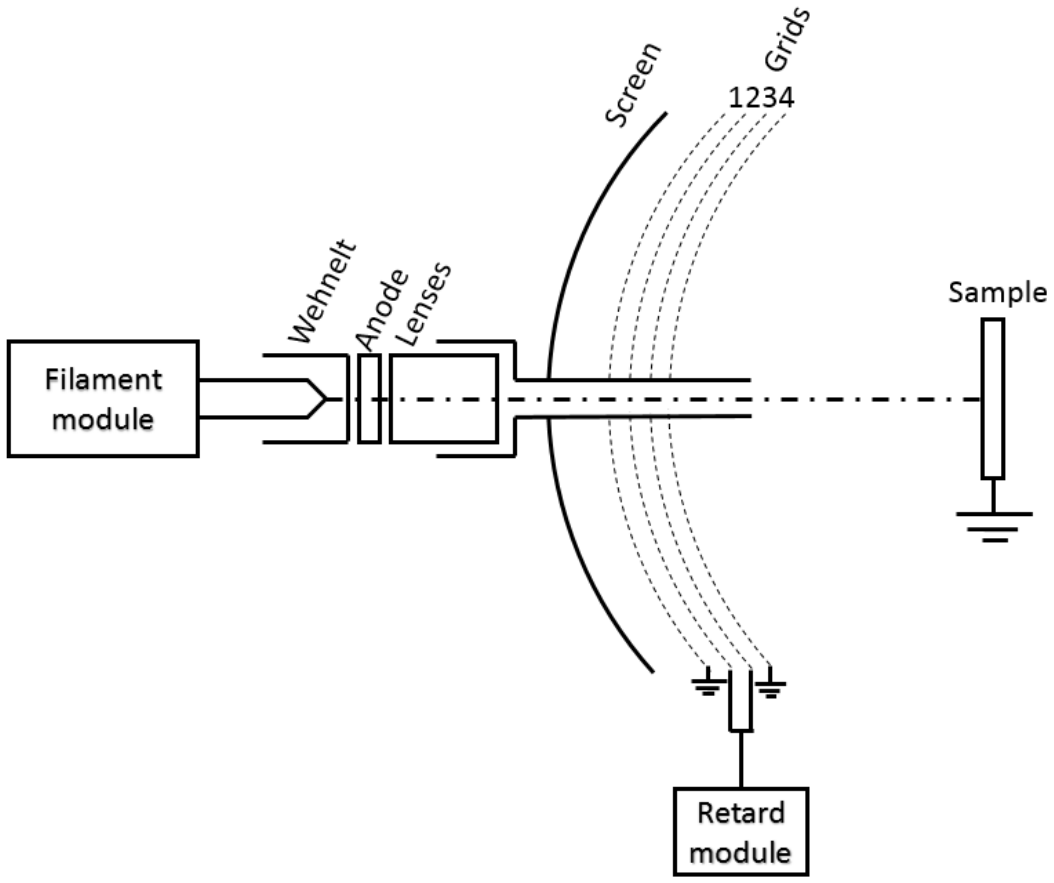

Figure 4: Diagram of the LEED device

The electron gun contains a filament that is heated by means of the Joule effect produced by an electric current. Additionally the filament is set to a negative potential with respect to the sample driving the emitted electrons towards the latter with energies in the range between 1 and 1000 eV. However, for the reported experiments, the energies were seldom selected in the interval beyond 100eV.

After the interaction with the target, the grids #1 and #4 have the purpose of attracting the electrons elastically scattered, whereas the grids #2 and #3 prevent the impact on the screen of most of the electrons that undergo inelastic processes.

Finally, the voltage of the screen accelerates the selected electrons towards it and the impacts trigger the fluorescence phenomenon, hence making luminous spots appear and revealing the diffraction pattern.

3. Analysis of LEED patterns

The luminous signal emitted by the screen is recorded by means of a CCD camera, whose mains characteristics are the high quantum efficiency, the adjustable integration of the signal and the linear dependence of the output with the luminous flux on the detector.

The following image portrays as example the pattern of the (5×5) reconstruction of cobalt phthalocyanine on a substrate of Ag(100).

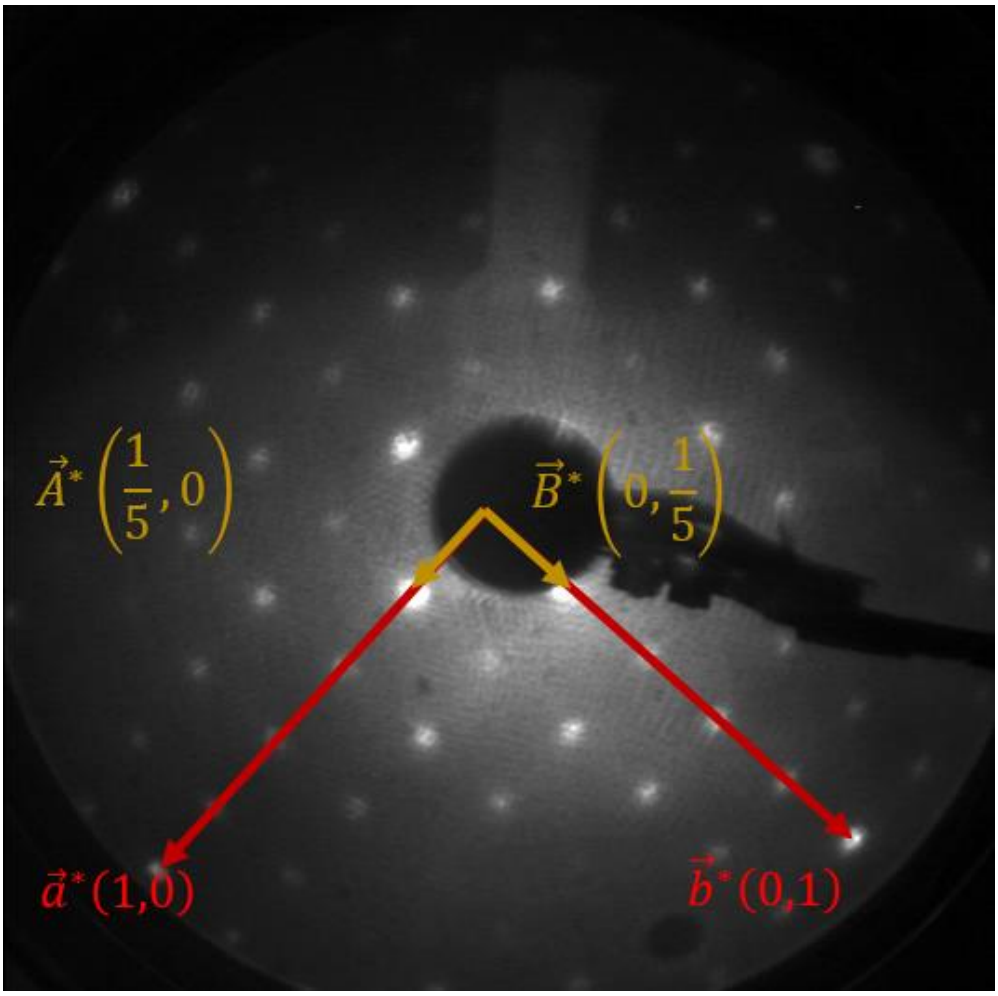

Figure 5: LEED pattern of CoPc(5×5) on Ag(100)

LEED pattern images provide information about both the geometry and the quality of the surface.

Indeed, the definition and the sharpness of the diffraction spots are related to the quality of surface. Accordingly, the existence of large domains and the scarcity of defects will redound to the formation of fine, intense, well-defined spots. However, if the surface displays a significant disorder, the spots will be fainter, more disperse and the background will become more intense, thereby decreasing the signal to noise ratio.

Regarding the geometry, on the figure 5 the vector bases in the reciprocal space appear superimposed (the red ones correspond to the Ag(100) and the golden ones to the CoPc arrangement).

The reciprocal lattice is the Fourier transform of the lattice in the real space. Consequently, since the diffraction pattern is a direct representation of the reciprocal lattice, it would be theoretically possible to obtain the structure in the real space by applying the inverse Fourier transform.[2]

Nevertheless, this process isn't as easy as it might seem due the limited amount of diffraction spots included in an image, the noise, the presence of the electron canon in the field of view etc.

On the contrary, the analysis from the definition of the basis of reciprocal vectors is feasible, specifically:

$$\vec{a}^* = 2\pi \frac{\vec{b} \times \vec{u}_z}{\left|\vec{a} \times \vec{b}\right|} \; ; \; b^* = 2\pi \frac{\vec{u}_z \times \vec{a}}{\left|\vec{a} \times \vec{b}\right|}$$

Bearing that in mind, given that the vectors of the reciprocal space are known from the LEED pattern, it's possible to obtain their respective real counterparts by applying the following expressions:

$$\vec{a} = 2\pi \frac{\vec{b}^* \times \vec{u}_z^*}{\left|\vec{a}^* \times \vec{b}^*\right|} ; \; \vec{b} = 2\pi \frac{\vec{u}_z^* \times \vec{a}^*}{\left|\vec{a}^* \times \vec{b}^*\right|}$$

These transformations involve rotations of 90º and rescalings, so the applications that account for the transfers from one basis to the other one can be written under the form of matrices.

Finally, some other linear relationships can be used to pass from the basis of the substrate to the one of the surface reconstruction and to follow the inverse path, in both the real and the reciprocal spaces:

$$\vec{V}_i = \sum_j G_{ij} \cdot \vec{v}_j \; ; \vec{V}_i^* = \sum_j G_{ij}^* \cdot \vec{v}_j^*$$

Furthermore, the equation below involving the change of basis matrices holds:

$$G_{ij} = \left[\left(G_{ij}^*\right)^{-1}\right]^T$$

References:

1. Seah M. P. and Dench W. A., Surf. Interface Anal. 1, 2 (1979)
2. Kittel C., *Introduction to Solid State Physics*, 7th Ed., Wiley, (1996)
3. Davisson C. and Germer L. H., Phys. Rev. 31, 155 (1928).
4. Warren B. E., *X-ray diffraction* Addison-Wesley, Reading MA/Dover, Mineola NY (1969/1990)
5. Pendry J. J., *Low Energy Electron Diffraction*, Academic press, (1974)

Scanning tunnelling microscopy

1. Theoretical basis

In a lecture in 1959, Richard Feynman claimed that in order to make atomic-level manipulations, it's necessary to be able to see what is going on. The scanning tunnelling microscope (STM), whose patent was registered in 1982, was the first answer to that need, and has so far been a fundamental tool for the development of nanotechnology. It's needless to say that its creators, G. Binnig and H. Rohrer[1], were awarded the Nobel Prize in 1986 because of their groundbreaking contribution of the studies of matter at the nanometric level.

One of the most convenient characteristics of the STM technique lies in the direct production of images that are quite similar to topographic maps of the surface. Yet, the reach of the atomic level through this experimental tool made it necessary to improve the comprehension of additional details at this microscopic scale.

The STM itself includes a conductive tip with the size of one atom (ideally) at the end that gets close enough to a conductive surface to establish a tunnelling current. The data are registered as the tip is accurately displaced over the sample in tiny steps with the help of piezoelectric translators. The most common and easiest framework to address this question is the analogy with the rectangular potential barrier. In this context, it's straightforward to show that the current obeys the following dependency:

$$I \propto e^{-2\kappa d}$$

where I is the current, d stands for the width of the potential barrier and κ represents the decay constant within the barrier:

$$\kappa = \hbar^{-1}\sqrt{2m\phi}$$

This parameter is related to the mass of the electron m and the effective local work function ϕ. In typical cases, κ has values around 1 $Å^{-1}$ and thus, the current drops by an order of magnitude when the separation between the tip and the surface varies only 1 Å. Consequently, if the current were to be maintained at a value with an uncertainty of 2%, this would only induce variations in the distance of 0.01 Å, which is an exceptional sensitivity to the corrugation of the surface.

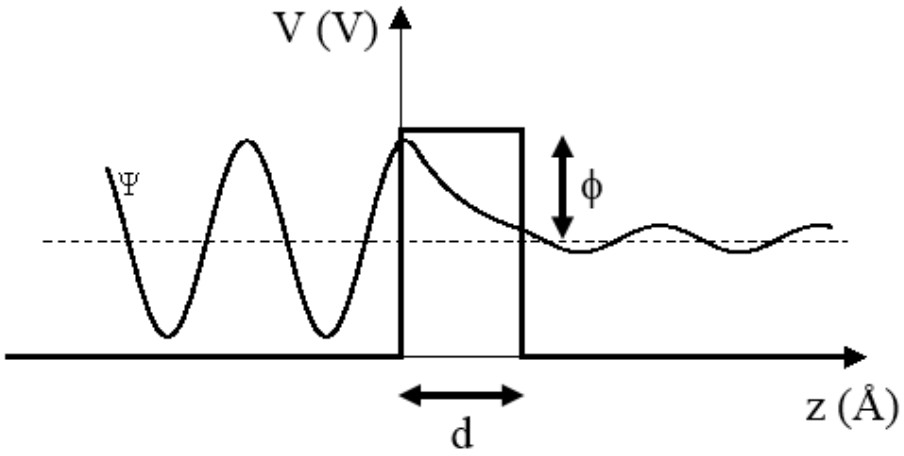

Figure 1: Schematic view of the tunnelling through a rectangular barrier[4]

Nevertheless, the simple interpretation of STM images as topographic maps of the surfaces loses validity as subatomic structure appears. Indeed, as the process involves electronic states at the Fermi level, it seems reasonable that the spatial structure of the states of both the surface and the tip play a role in the outcome of the data acquisition.

With the intention of improving the description of the process, and considering first-order perturbation theory and low temperatures, the current can be written as[2]:

$$I = \frac{2\pi e}{\hbar} \sum_{\mu,\nu} f(E_\mu)[1 - f(E_\nu + eV)]\left|M_{\mu\nu}\right|^2 \delta(E_\mu - E_\nu)$$

In this expression, *f(E)* is the Fermi distribution, E_μ the energy of the state μ, and each index runs over all the states of the surface and the tip respectively. Finally, $M_{\mu\nu}$ is the tunnelling matrix element, which was shown by Bardeen[3] to be:

$$M_{\mu\nu} = \frac{\hbar^2}{2m} \int dS\left(\Psi_\mu^* \nabla \Psi_\nu - \Psi_\nu^* \nabla \Psi_\mu\right)$$

where Ψ_ν is the wave function of the corresponding state and the integral is to be calculated over any plane in the barrier region.

The microscope admits two basic operation modes:

The first one is the so-called constant current mode, which consists in bringing the tip close enough to the surface with an electric potential difference between a few millivolts and a few volts so that a tunnelling current becomes measurable. This current is kept constant by a feedback loop by modifying the height *z* over the surface of the tip. The data obtained in that fashion are the height variations as a function of the position on the surface.

The second one is the constant height mode. This mode implies keeping the height of the tip and the voltage constant during the scan while keeping track of the sudden changes in the current.

Each mode has its own advantages and drawbacks. To keep it simple, the constant current mode is the appropriate choice for uneven surfaces as it prevents the tip from scraping the surface. On the other hand, the constant height mode is much faster as it doesn't involve the operation of the *z* translator. This does not only boost the speed of the data acquisition, but it also reduces the impact of the thermal drift and the piezoelectric creep.

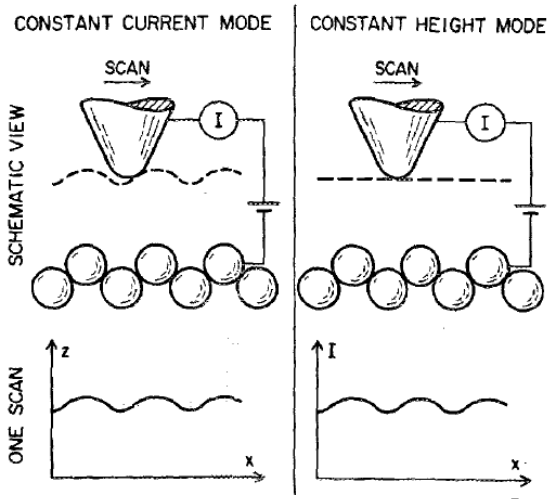

Figure 2: Typical operation modes of STM[7]

In the context of this thesis, the STM was always used in constant current mode to preserve the state of the tip. Furthermore, a linear electronic correction for the thermal and mechanical drift was kept enabled in order to improve the quality of the images.

As it has already been noted, the tunnelling process involves the electronic states of the surface and the ones of the tip. If possible, it would be interesting to make the tip's contribution irrelevant so as to gather directly information from the surface without the need for a deconvolution of the effect of the tip.

Tersoff[4] proposed that the tip itself could be ignored in the case of having a tip whose states were arbitrarily localised. If these requirement is fulfilled with a sufficiently low voltage, the current depends only on the surface local density of states at the tip position. So bearing that in mind, the images previously considered as topographic maps of the sample, become a contour of constant Fermi-level local density of states. This simplification doesn't even need "punctual" tips as long as the tip wave functions resemble an s-orbital whose centre would be the "position" of the tip. In practice, the easiest way to achieve this is to prepare a single-atom tip.

Regarding the resolution, the final image $I(x)$ is usually considered as the convolution of an ideal image $I_0(x)$ and the instrumental resolution function $F(x)$:

$$I(x,y) = \iint F(x',y')I_0(x-x',y-y')dx'dy'$$

A perfect characterization of $F(x,y)$ would allow (under the condition of a negligible noise) the deconvolution to obtain the original image $I(x,y)$.

2. Experimental device[5]

The following images show a schematic view of the main parts of the STM that was used during this thesis.

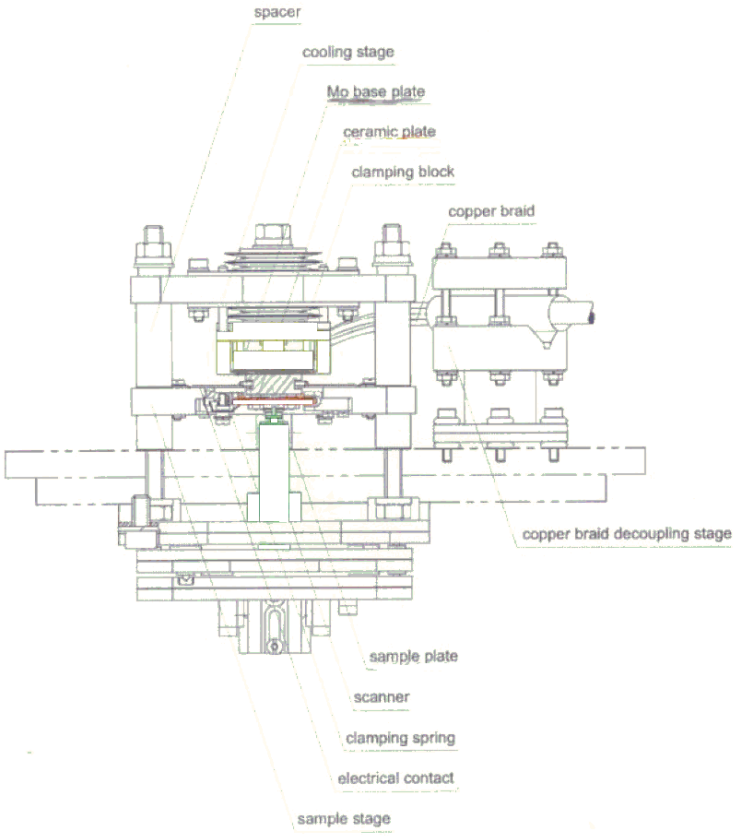

Figure 3: Detail of the STM platform

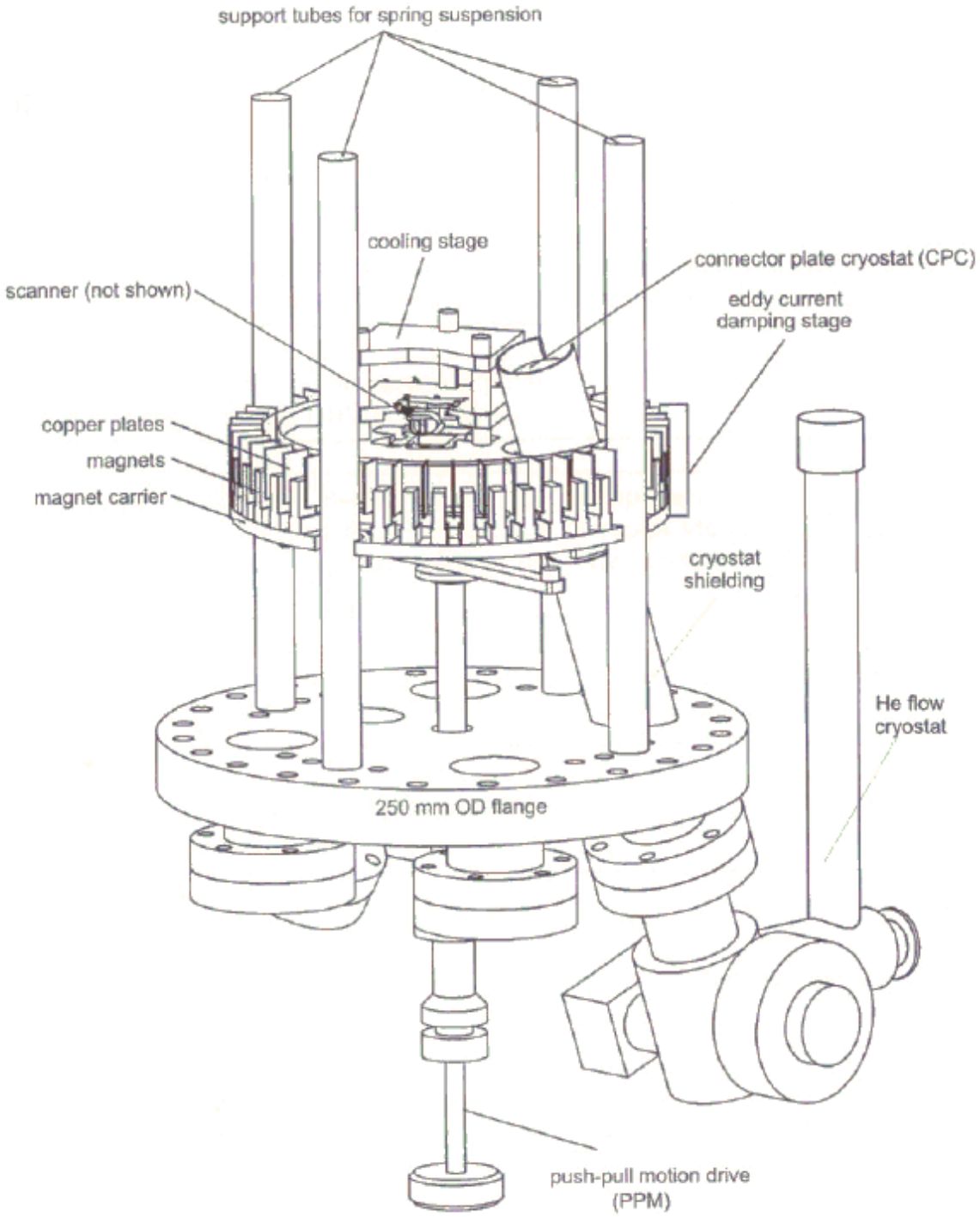

Figure 4: Side view of the STM's frame

It's a Variable Temperature STM developed by *OMICRON*. In spite of having cooling and heating facilities, it was always used at room temperature. It combines a high resolution, an easy sample and tip handling and a reliable vibration isolation.

The vibration decoupling is essential for attaining high resolution scans. Indeed, the base plate is suspended by four soft springs which are protected by surrounding columns. The resonance frequency of the suspension system is 2 Hz.

Vibrations of the suspension system are intercepted using a nearly non-periodic eddy current dumping mechanism. That's the reason why the base plate is surrounded by a ring of copper plates which come down between permanent magnets.

All the suspension system is blocked during the displacements of the sample to avoid any deterioration.

One fundamental element of this technique is the tip itself. As it has already been stated, its characteristics have an important effect on the resolution and the aspect of the images, for example a double tip will produce one image composed of two superimposed. Therefore, the preparation of the tip, which fundamentally consists of two stages, appears as a fundamental preliminary of the STM measurements[6].

The first stage is the electrochemical attack of a tungsten filament by sodium hydroxide (NaOH). This procedure makes it possible to obtain tips with sizes in the range of a few nanometers. In particular, the tungsten filament (whose diameter has a value of 0.38mm) is submerged into a NaOH solution with a concentration of 2 mol/L. Afterwards, an alternating voltage of around 12 volts is set between the filament and an additional electrode. This triggers a chemical reaction that progressively "dissolves" the filament up to limit imposed by the meniscus (the meniscus itself shapes the tip). The aforementioned reaction is:

$$W(s) + 2OH^{-}(aq) + 2H_2O(l) \rightarrow WO_4^{2-}(aq) + 3H_2(g)$$

The last step is the heating of the tip under ultra-high vacuum conditions by electron bombardment (the usual parameters were a current of 6.7 A, a voltage of 0.5 kV and a duration of 10 s). The objective of such a procedure is the removal of both the sodium hydroxide remnants and the tungsten oxide, as well as the casting of the tip into a better, more regular shape. The reason behind the short bombardments is the possibility of the tip becoming rounded at too high temperatures.

3. Analysis of STM data

The result of the STM scans is a set of images provided by the software *SCALA PRO 5.0,* which also serves as an interface for operating the device. Those images have already been treated beforehand by the program itself but require further processing. One example of such images is shown below:

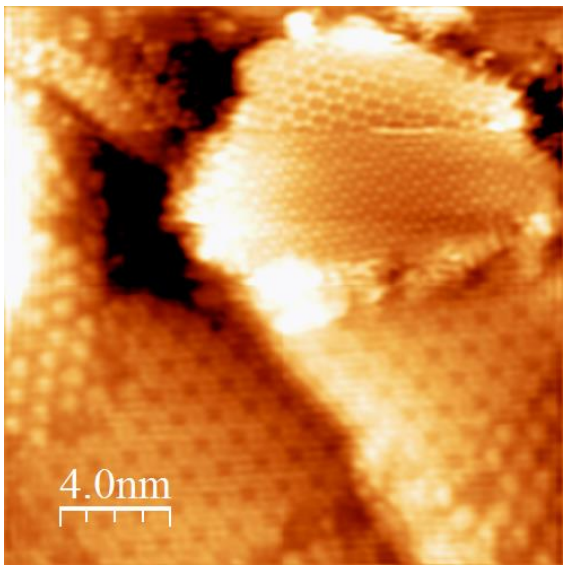

Figure 5: 20nm×20nm silicene STM image provided by *SCALA*
I = 0.14 nA, V = -1.6 V

These “pseudo-raw” images present lots of imperfections, ranging from real physical defects, such as contaminants, vacancies, interstitial defects etc. to non-existent entities due to the electronic noise, vibrations, defects on the tip etc.

With the purpose of dealing with these distortions and enhancing the quality of the images, the freeware *WSXM 4.0 Beta 8.0* was used. *WSXM*[7] is a program widely used by the STM community able to read most of file formats. It includes an enormous amount of features to process STM images. Below there’s a brief explanation of the standard procedure used for improving the images of this thesis.

The first step is cropping the image. The default contrast scale spans the whole interval of intensities (and equivalently all the heights). This can seriously mitigate the visibility of the structure. For example, if the subject of study were the corrugation of silicene[6], that is around 0.07 nm, and if there were some step terraces (each atomic layer accounting for around 0.2 nm), the contrast imposed by the terraces would render the corrugation barely visible, if at all. Cropping the images allows the suppression of unnecessary and problematic regions.

After the selection of the pertinent part of the image, the goal is the reduction of the noise. It depends on the scale, but usually the interesting structures in high resolution images span several tens of pixels, whereas the electronic noise arises from a point process. This suggests some type of Fast Fourier Transform (FFT) filtering. Indeed, the reduced size of the noise implies an associated high frequency while the relevant information is enclosed in the low frequency region of the two-dimensional FFT. Therefore, an elliptic low-pass filter is the suitable choice.

Finally, the image should be flattened. In effect, the STM images often reflect a regular slope even over narrow terraces. This is obviously an artefact derived from the data acquisition and can be solved by the *Flatten* function of the software. It picks regions that are supposed to be at the same level (input given by the user) at effectively puts them at the same height.

For aesthetic purposes the user may use the equalizer in the end to enhance the contrast scale and make the image more apparent. Unlike the previous steps, this one doesn’t modify at all the matrix of data.

The following figure shows one example of the same image of hydrogenated (4×4) silicene before and after the treatment by means of *WSXM*.

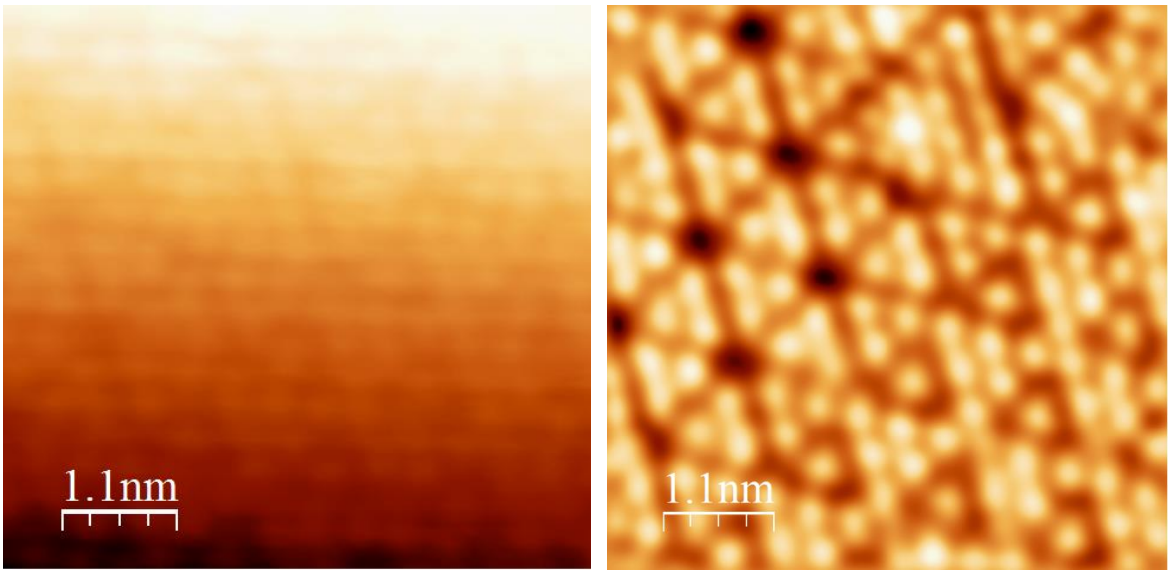

Figure 6: Hydrogenated (4×4) silicene STM image 5.6 nm × 5.6 nm 0.55nA -515mV before correction (left) and after correction (right)

References :

1. Binnig G. et al. Surface Science 126, 236-244 (1983)
2. Hansma, P. K. et al. J. Appl. Phys. 61, 2, (1987)
3. Bardeen J., Phys. Rev. Lett. 6, 57 (1961)
4. Tersoff J. and Hamann D. R., Phys. Rev. B 31, 2 (1985)
5. *The VT SPM User's Guide*
6. Bai C., *Scanning Tunneling Microscopy and its applications*, Surface Sciences, Springer-Verlag (1996)
7. Horcas I., et al., Rev. Sci. Instrum. 78, 013705 (2007)

High-resolution electron energy loss spectroscopy

1. Theoretical basis

In the second half of the 20th century, the progress in the field of the technology of vacuum made the preparation and characterization of surfaces possible in a reproducible way. In this context, several different techniques were conceived for the study of the outermost layers of a surface, among which the high-resolution electron energy loss spectroscopy (HREELS) is included.

This technique relies on a beam of electrons that is sent onto a surface in order to take a look at the vibrational modes of its atoms and molecules, some electronic transitions, the plasmons etc. These phenomena require a part of the energy of the incoming electrons to occur, and so, after the scattering process the outgoing leptons emerge with a different energy given by the following equation:

$$E_F = E_I - \hbar\omega$$

In this expression, which accounts for the law of conservation of energy in the process, E_F represents the energy on the electron after the scattering event, E_I its energy before it (around a few electronvolts to ensure an insignificant penetration in the sample) and ω stands for the frequency of the mode activated in the process.

The inverse phenomenon is also possible, that is the annihilation of an existing mode inducing an increase in the energy of the emerging electron, in which case it shouldn't be called an "energy loss", but an "energy gain".

Consequently, if a spectrum of the electrons after interacting a surface is registered, it is possible to have access to its modes, and ultimately to its nature.

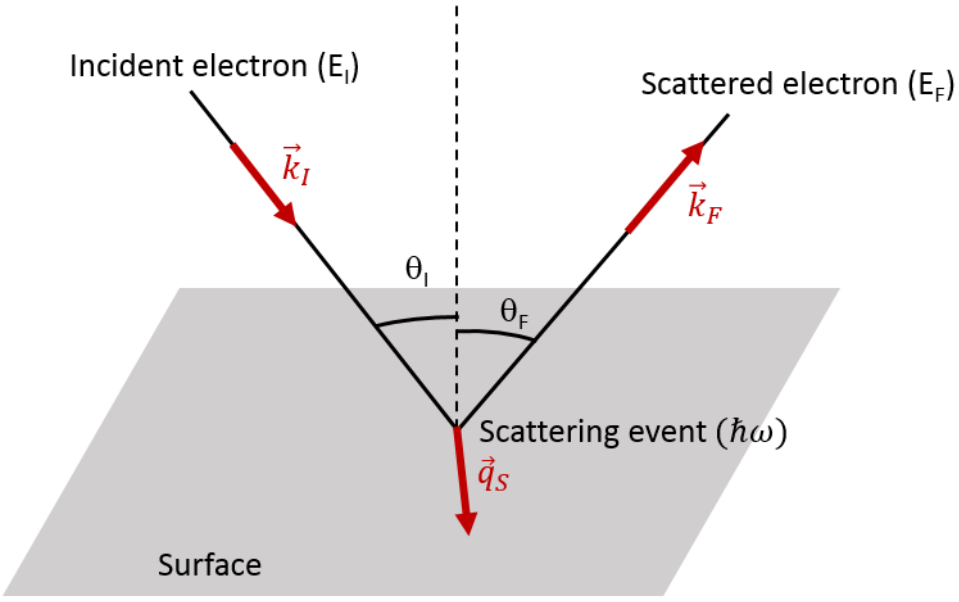

Figure 1: Principle of operation of HREELS

It is also possible to analyse the scattering by applying the law of conservation of momentum by means of the wavevectors of the incident beam $\vec{k}_I$, the scattered beam $\vec{k}_F$, and the quasimomentum exchanged with the surface $\hbar\vec{q}_S$:

$$\vec{k}_I = \vec{k}_F + \vec{q}_S$$

The study of the inelastic dispersion that gives rise to the apparition of peaks on the spectra needs a careful consideration on the interaction between the solid and the incoming electrons. This a cumbersome problem, although two distinct scenarios are usually considered to reduce the complexity of the question: the dipolar regime and the impact scattering regime.

In principle, both mechanisms lie at the extremes of the range of possible values for the deflection angle; indeed, for low values of this parameter the dipolar mechanism is prevalent whereas the impact mechanism becomes more relevant for high values of the deflection. However, the border between both scenarios is dim and the actual situation usually requires an explanation that lies somewhere in-between. Still, these approximations are notably helpful and can be successfully applied in a great number of situations.

Suppose a set of atoms labelled with the index j at the positions given by $\vec{R}_j$ and the potential created by them at some point $\vec{r}$:

$$V(\vec{r}) = \sum_{atoms} V_j\left(\vec{r} - \vec{R}_j\right)$$

If the dispersion of one electron involving a change of wavevector $\vec{q} = \vec{k}_f - \vec{k}_i$ is taken into account and since the scattered beam is much less intense than the incident one, the first Born approximation provides us with the matrix element of the process:

$$M(\vec{q}) = \int \frac{dxdydz}{\xi} e^{i\vec{q}\cdot\vec{r}(x,y,z)} V(\vec{r})$$

In this expression, ξ represents a volume of quantization. Hereinafter the contribution of every atom is separated:

$$M_j(\vec{q}) = \int \frac{dxdydz}{\xi} V_j(\vec{r}) e^{i\vec{q}\cdot\vec{r}(x,y,z)}$$

And the conclusion is:

$$M(\vec{q}) = \sum_j M_j(\vec{q}) \cdot e^{i\vec{q}\cdot\vec{R}_j}$$

The dipolar scattering mechanism

The series expansion of the exponential to first order shows that for scatterers of a given size d in the limit of small deflection angles ($|q| \cdot d \ll 1$) the cross section of the interaction depends only on the oscillating dipolar moment.

These conditions along with the requirement for the excitation to generate a dipolar moment perpendicular to the surface (which will be enhanced by the image charges, instead of screened) are the starting point to analyse the scattering phenomenon from the dipolar mechanism. More precisely, the selection rules observed when a scattering event occurs as a result of the dipolar mechanism can be seen as the same ones that rule infrared spectroscopy[1]. Only vibrations that belong to the totally symmetric representations A_1, A' and A are observed as fundamentals in dipole scattering.

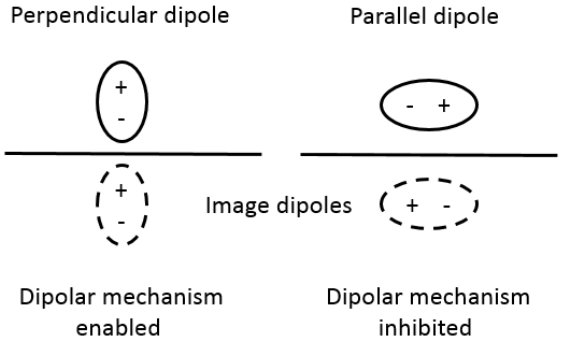

Figure 2: Two dipoles on a surface (one perpendicular and one parallel) and the image charge distribution that they induce.

Such mechanism is not only activated by vibrations of atoms and molecules on the surface. There are contributions as well from the free carriers in metals and semiconductors, from the inter-band transitions etc.

It can be shown[1] that whenever the dipolar scenario is dominant, the probability that an electron undergoes scattering per unit of solid angle and per unit of energy prior to the event obeys the equation below:

$$\frac{d^2S}{d\Omega d(\hbar\omega)} = \frac{2m^2e^2v_\perp^4}{\pi\hbar^5\cos\theta_I}\left(\frac{k_F}{k_I}\right)\frac{|R_I|^2 q_\parallel}{\left[v_\perp^2 q_\parallel^2 + (\omega - v_\parallel \cdot q_\parallel)^2\right]} \cdot \left[1 + \frac{1}{e^{\hbar\omega/k_BT} - 1}\right] Im\left(\frac{-1}{\varepsilon + 1}\right)$$

With the following parameters:

m: mass of the electron

e: charge of the electron

$v_\perp, v_\parallel$: components of the velocity of the electron perpendicular and parallel to the surface.

θ_I: angle of incidence

k_F, k_I: final and initial electron wavevectors

R_I: probability of reflection of the incoming electron on the surface

$q_\parallel$: parallel component of the variation of the wavevector

T: temperature

ε: electric permittivity of the material

ω: frequency of the mode.

In practice, all these parameters could be directly measured during the progress of the experiment.

The impact scattering mechanism

So far, the study was restricted to the scattering with small deflection angles by using the dipolar approximation. In the case of greater deflection angles this simplification is no longer correct and a precise microscopic model of the surface becomes necessary in order to describe the process. The reason is the distance from the surface at which the interaction takes place: while the onset of the dipolar scattering can happen as far from the surface as hundreds of angstroms, the impact mechanism is only triggered at a few angstroms. Additionally, a different theoretical framework is required to explain the scattering events produced by dipoles parallel to the surface.

The magnitude at the centre of this phenomenon is the amplitude of dispersion $f(\vec{k}_F, \vec{k}_I, \vec{R}_j)$, which characterises the amplitude of the wave that emerges from the process from the incident wave and the positions of the atoms within the solid. This function can be expanded in series to first order in terms of the separation of the atoms from their respective positions of equilibrium $\vec{u}_{j\alpha}$:

$$f(\vec{k}_F, \vec{k}_I, \vec{R}_j) = f(\vec{k}_F, \vec{k}_I, \vec{R}_j^0) + \sum_{j,\alpha} \left(\frac{\partial f}{\partial R_{j\alpha}}\right)_0 u_{j\alpha} + O(u_{j\alpha}^2)$$

The term of zeroth order corresponds to the scattering amplitude of the lattice under equilibrium conditions, that is, the elastic scattering that has already been explained for the discussion of the LEED technique. On the other hand, the first order terms are related to excitations of vibrations of the system whose activation needs energy provided by the beam of electrons.

The following step is the calculation of the respective matrix elements:

$$M(\vec{k}_F, \vec{k}_I; +s) = \langle n_s + 1 | f(\vec{k}_F, \vec{k}_I, \vec{R}_j) | n_s \rangle$$

From them, it's possible to deduce the scattering cross sections and the probabilities of excitation. Therefore, the key element is the variation of the amplitude of scattering and the modification in the system's potential when the nuclei are displaced slightly from the positions of equilibrium.

This is generally a complex problem, because the usual simplifications, such as the so-called "muffin-tin" potentials[2], are not useful given their inability to generate distortions of the electron cloud responsible for the scattering events under impact conditions.

The basic concepts related to the selection rules of this regime should nonetheless be emphasised.

For example, if the plane that contains the trajectory of the electron is a symmetry plane and a mode has an odd symmetry with respect to that plane, such a mode is forbidden by the selection rules along the specular direction.

Similarly, if the normal to the surface is a binary rotational symmetry axis and a mode has an odd symmetry with respect to that axis, that mode is forbidden along the specular direction as well.

Additionally, if the plane perpendicular to both the surface and the trajectory is a plane of specular symmetry and a mode has odd symmetry with respect to the reflection on that plane, the mode's amplitude vanishes for any direction of the emergent beam according to the selection rules.

The consideration of the selection rules for both mechanisms (the dipolar and the impact ones) can turn into a useful tool for identifying the normal modes of the chemical species adsorbed when the geometry is simple enough.

Finally it should be noted that the vast majority of the HREELS spectra that have been registered during this thesis have been obtained with the detector placed on the specular direction. Given that the loss energies were at every time small compared to the primary energy (below one tenth) and that the studied surfaces were reasonably well ordered, the obtained data can therefore be analysed within the framework of the mechanism of dipolar dispersion.

2. Experimental device[3]

The following images include a picture and a diagram of the spectrometer that has been used for the elaboration of this thesis.

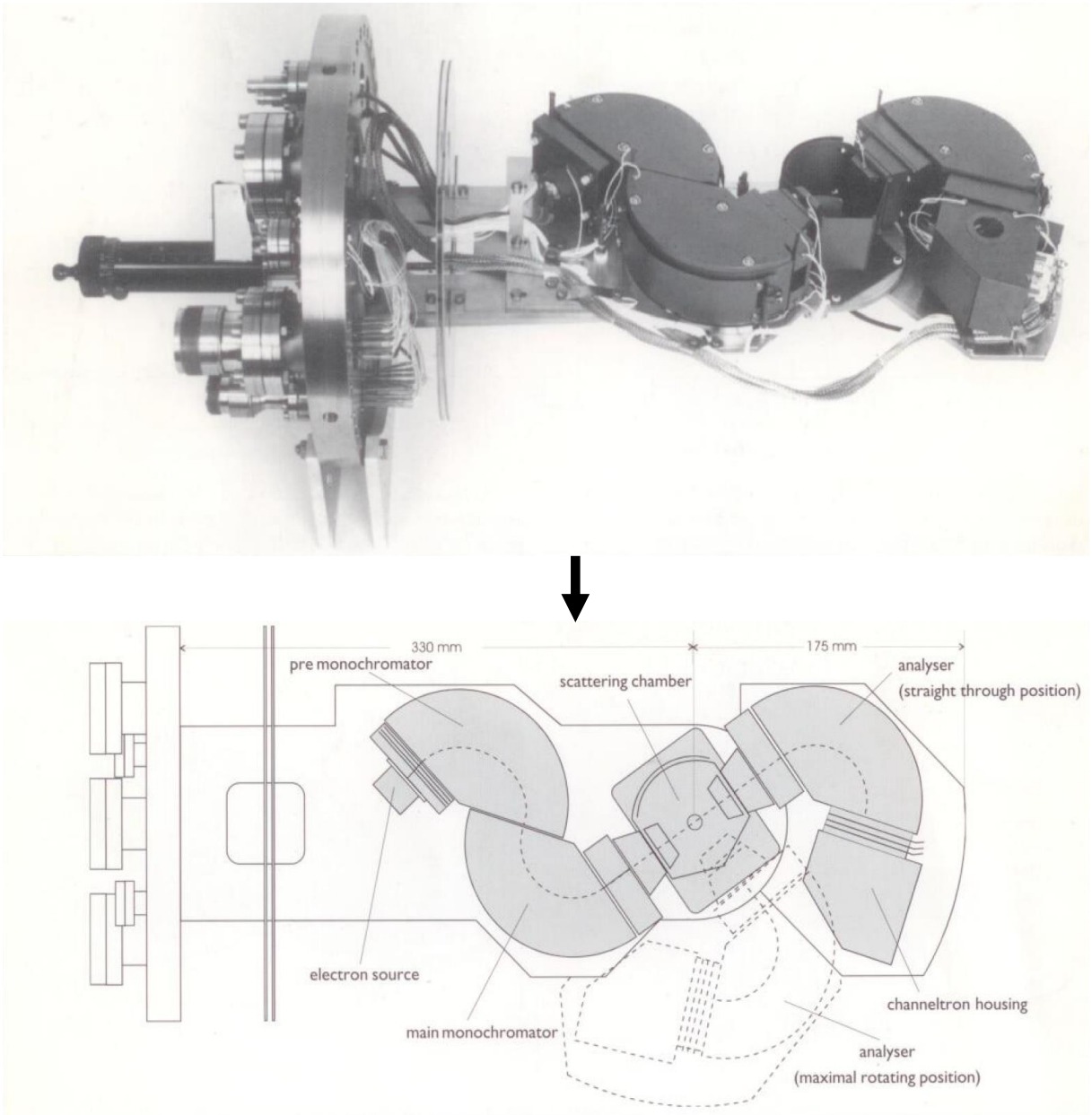

Figure 3: Picture of the HREELS DELTA 0.5 spectrometer and draft of the fundamental components

It consists in a *DELTA 0.5* spectrometer made by *Vacuum Science Instruments*. The source of electrons is a LaB_6 filament through which a current circulates. The emitted electrons are directed into a concentrated beam by an electrostatic lens. The beam is then focused on a monochromator which prevents the dispersion induced by the spatial charge effect, that is to say the widening of the energy distribution. The next stage takes place in the cylindrical monochromator, which selects more rigorously the energy of the electrons until achieving dispersions below 4 meV.

The two subsequent electrostatic lenses focus the beam onto the sample, and after the scattering, two additional lenses drive the electrons to the analyser. The analyser itself contains one more monochromator whose purpose is the separation of the dispersed electrons depending on their kinetic energy. The position of the analyser can also be modified to choose the direction of dispersion in the plane of incidence.

In the last stage, the channeltron amplifies the signal that is then transmitted to the analog-to-digital converter to be registered by the system.

Regarding the operation, the high spectral resolution impose the use of low energy electrons (around a few electronvolts). With this in mind, in principle it would be interesting to get a signal as powerful as possible to increase the signal to noise ratio, however there are two undesirable effects that would hinder the correct operation of the device.

Indeed, it would be ideal to increase to current so as to amplify the number of electrons and hence the final signal. Nevertheless this would increase the optic size of the filament producing a flux that would escape the monochromator. Apart from that, the density of electrons in the monochromator would rise, reducing its efficiency and widening the energy distributions. Generally, the latter effect is more serious than the former one.

Moreover there is the so-called Boersch effect, which is negligible in the typical conditions of operation but relevant when the flux is very intense or if the electrons need to be transported over long distances.

Some other factors that could have an impact on the measurements would be the appearance of ghost peaks (whose origin is the collisions of dispersed electrons with the deflection plates) or the background signal (around 10^6 times less intense than the elastic peak).

The design of the monochromators (usually in the shape of cylinders that span 127 degrees, achieving perfect focalisation to first order) is optimal for obtaining the best performance from the spectrometer by counteracting as much as possible the aforementioned unwanted effects.

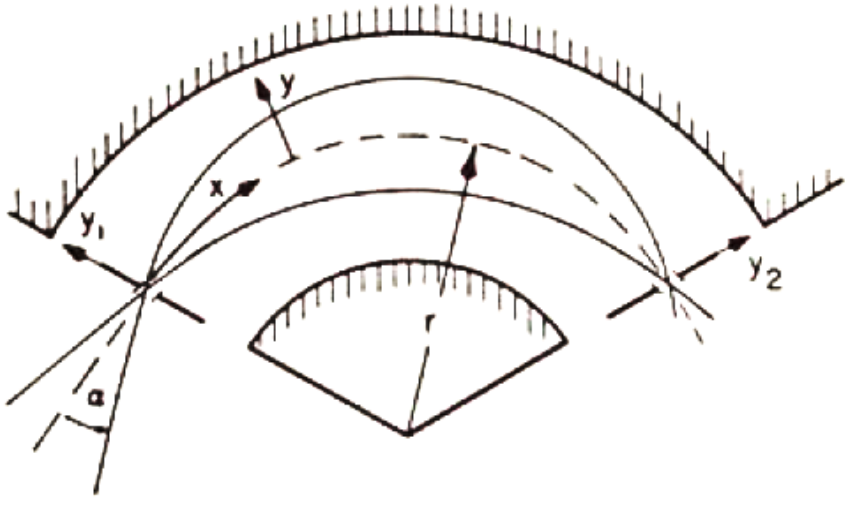

Figure 4: Trajectories of the electrons within a cylindrical monochromator that spans 127 degrees.

3. Analysis of HREELS data

The following figure contains one example of spectrum, namely the spectrum of a hydrogenated (4×4) silicene sample registered under specular conditions.

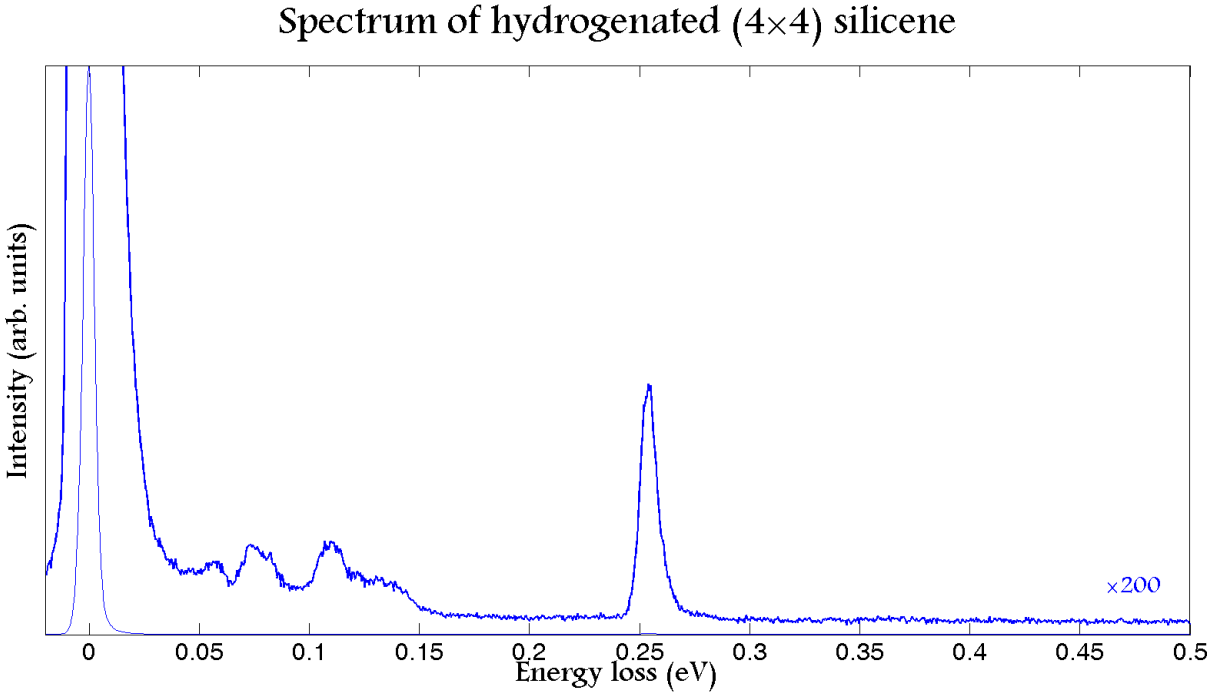

Figure 5: HREELS spectrum of hydrogenated (4x4) silicene

The loss energies probed by the analyser are indicated on the x-axis (if they are negatives, they are accounted as "gains" instead). On the other hand the y-axis corresponds to a magnitude proportional to the number of electrons detected by the analyser for each probed value in the energy interval.

The most intense peak, centred on 0 eV, is the so-called elastic peak. The rest of the features, with intensities around 1000 times lower than the elastic one in specular conditions, are related to different oscillations of the system. For example, the peak recorded at around 260 meV has its origin in the Si-H stretching mode.

In order to perform a quantitative analysis of the spectra, the following procedure has generally been followed:

Since the features are expected to have approximately the same shape, the first objective is the translation of that shape into a mathematical function that will only admit further variations in its position and amplitude, keeping constant the other parameters, such as the asymmetry or the width.

The theoretical profile for the peaks would be:

$$p(E) \propto \frac{1}{E}\,\mathrm{Im}\left(\frac{-1}{\varepsilon(E)+1}\right)$$

This usually gives rise to a lorentzian or Voigt profile in the end.

However, during the data treatment it was systematically seen that, probably due to some instrumental characteristics of the spectrometer, the elastic peak was highly asymmetric, suggesting the use of a more appropriate function for the fitting procedure.

Stancik and Brauns[4] have proposed asymmetric variants of the lorentzian and gaussian profiles for the analysis of spectra in the infrared range. Those expressions have been successfully combined in this work for obtaining the best non-linear fits in the least-squares sense.

In particular, the considered profile consists in the addition of an asymmetric lorentzian and an asymmetric gaussian. The mathematical expression is:

$$p(E) = G_{asy}(E) + L_{asy}(E)$$

The asymmetric profiles are characterised by the equations below:

$$G_{asy}(E) = A_1 e^{-\frac{(E-E_0)^2}{2\sigma_1^2}} \cdot \left[\mathrm{erf}\left(k_1 \frac{E-E_0}{\sigma_1}\right) - 1\right]$$

$$L_{asy}(E) = A_2 \frac{e^{-k_2 \cdot (E-E_0)} + 1}{(e^{-k_2 \cdot (E-E_0)} + 1)^2 \cdot (E-E_0)^2 + 4\sigma_2^2}$$

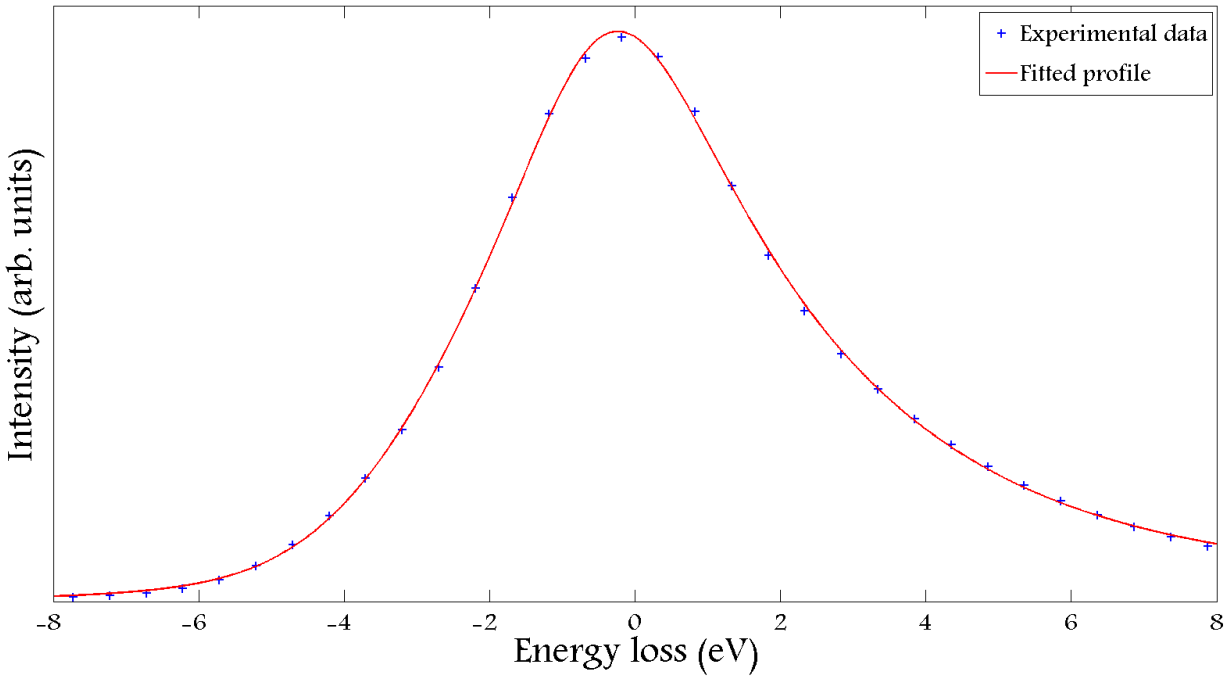

Figure 6: Example of the fitting result for the elastic peak of a HREELS spectrum

After the determination of the features' profile, the fits of the rest of the peaks were performed even allowing several blended components when it was necessary. This step provides the positions and the amplitude of peaks with their respective uncertainties.

These data open the way for the quantitative comparison of the spectra (as long as they have been registered in the same conditions of operation) because all the values of the parameters are relative to the elastic peak.

References:

1. Ibach, H. and Mills D. L., *Electron Energy Loss Spectroscopy and Surface Vibrations*, Academic press, New York, (1982)
2. Feng D. and Jin. G. *Introduction to Condensed Matter Physics*, World Scientific (2005)
3. *DELTA VSI 0.5, VSI Vaccum Science Instruments GmbH*
4. Stancik A.L. and Brauns E.B., Vibrational Spectroscopy 47, 66–69 (2008)
5. Ibach H., *Electron Energy Loss Spectrometers, the technology of high performance*, Springer-Verlag, (1991)
6. Tong S. Y. et al., Phys. Rev. B 21, 3057 (1980)
7. Salomon E., Ph.D. thesis *Propriétés physiques de films minces de phthalocyanines adsorbées sur des semi-conducteurs III-V* Aix-Marseille Université (2005)

Photoelectron diffraction

1. Theoretical basis

The comprehension of any surface phenomenon is tightly related to the knowledge of bond distances, crystallographic directions, coordination numbers etc. From the beginning of the 20th century, several experimental techniques were developed to extract that information from the systems under study. One of those techniques is the photoelectron diffraction, which was used for the execution of this thesis and will be explained in the following pages.

In short, the photoelectron diffraction starts with the excitation of an electron from an atomic core level into an unbound state. Then, the peak intensity is registered as a function of the polar angle, the azimuth and/or the kinetic energy of the outcoming electrons. The modulations in the flux of electrons are due to scattering events from close neighbouring atoms and interference among the resulting scattered waves. The diffraction patterns offered by these experiences are analysed later so as to infer information from them.

One typical magnitude of this technique is the so-called anisotropy χ, which reflects the variations of intensity depending on the direction of observation. Later on, a small discussion of possible definitions of the anisotropy will be included, but for now the following simplification will be appropriate enough:

$$\chi_{\max} = \frac{I_{\max} - I_{\min}}{I_{\min}}$$

This means that the maximum anisotropy over one pattern is the subtraction of the minimum intensity from the maximum one divided by the minimum.

The modulation throughout the patterns is quite significant as it yields anisotropy values even over 0.7. This implies variations of the peak intensity (in the best cases) around 40%, which are easy to measure.

It should be noted that the process is strongly dependent on the kinetic energy of the electrons[1]. For energies in the range from 50 to 200 eV the amplitude for scattering into any angle is high. Between 200 and 500 eV, only the forward scattering ($\theta = 0°$) and the backscattering keep their high intensity. Beyond 500 eV, the only significant amplitude is found very peaked around the forward direction and it becomes narrower as the energy is increased ("forward focusing").

One last relevant aspect of photoelectron diffraction is that it probes specifically one type of atom (one chemical species) and it has a very convenient short range. Even atoms of the same element at inequivalent sites will show different signatures by virtue of their neighbouring atoms. Actually, the main features on the patterns will be produced by the closest scatterers around a given emitter. On the other hand, fine structure may reveal the geometry as far as 2 nm away from the emitter[2].

Since the first article with a theoretical description of low energy photoelectron diffraction by Liesbsch[3], several studies have improved the knowledge about this technique. Hereinafter, the simplest approach will be explained, which relies on the simplification of considering only single scattering processes.

The following figure shows the single-scattering cluster model, that is to say the basis for the explanation of the phenomenon.

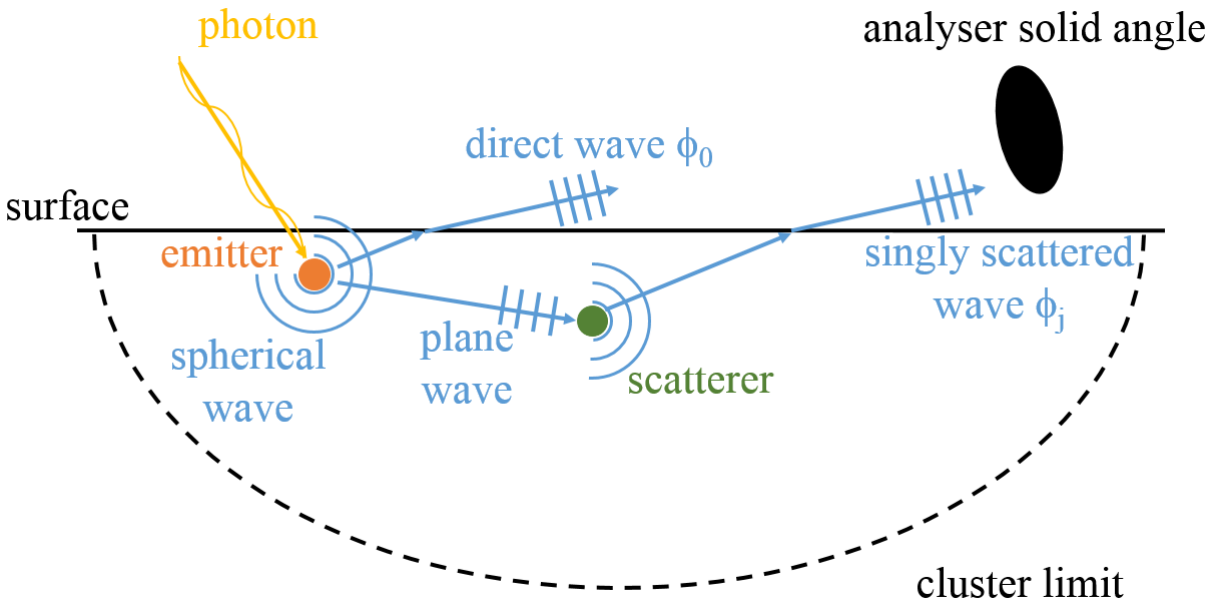

Figure 1: Single scattering cluster model

The origin of the diffraction patterns is some radiation characterised by a polarization vector $\vec{p}$ that is cast onto a surface, ejecting a core-level photoelectron from an atom. The dipole approximation allows to determine the intensity of the emission as a function of the initial core-electron wave function ψ_i and the final photoelectron wave function with wave vector $\vec{k}$:

$$I(\vec{k}) \propto \left|\langle \psi(\vec{r},\vec{k})|\vec{p}\cdot\vec{r}|\psi_c(\vec{r})\rangle\right|^2$$

The final wave function is obtained by superimposing a direct wave from the emitter ϕ_0 and all the possible singly scattered waves ϕ_j:

$$\psi(\vec{r},\vec{k}) = \phi_0(\vec{r},\vec{k}) + \sum_j \phi_j\,(\vec{r},\vec{r}_j \to \vec{k})$$

Since the detector is sufficiently far away, all the waves in the previous equation can be considered as plane waves. Flux conservation also imposes the decay of the direct wave that enables the production of scattered waves as r_j^{-1}. This is the very reason why photoelectron diffraction only probes short ranges, even before taking into account the inelastic effects.

To elaborate on the dipole matrix element, the usual approach is the consideration of a p-wave final state resulting from the excitation of an s-orbital. More complicated expressions can be obtained if the starting level is a different orbital (in particular they would involve both the increase and the decrease of the angular momentum) but the approximation still yields reasonably correct results, particularly in the range of energies over 200eV[4].

Generally, the following statements hold for typical photoelectron diffraction patterns:

1) Higher values of the final angular momentum produce a lower intensity of forward scattering, hence the approximation of the emission from an s-level overestimates the anisotropy of the pattern.

2) The differences due to angular momenta become less significant as the energy is increased because of the enhancement of the forward scattering. Indeed, for energies over 500 eV, the discrepancies between different final states are minimal[5].

Regarding the scattering events, the waves that arise from them are characterised by their corresponding plane-wave scattering factors *f(θ)*. Such factors are associated with phase shifts δ_l and are given by the expression below:

$$f(\theta) = (2ik)^{-1} \sum_{l=0}^{\infty} (2l+1)\left[e^{2i\delta_l} - 1\right] P_l(\cos\theta)$$

where P_l represents the Legendre polynomials.

As it has already been stated, the chosen approach considers plane waves. It could be refined through the introduction of spherical waves, but for the sake of discussion the effects of that improvement will be mentioned later.

The next step is the calculation of these factors for example by applying the partial-wave method to an appropriate potential, such as the muffin-tin model.

The introduction of the potential models reveals two trends for the scattering factors linked to the atomic number:

1) The forward scattering amplitude is sensitive to the size of the atom, and so, the forward scattering amplitudes from free atoms are always greater than the ones from the muffin tin counterparts, being the latter smaller in size.

2) As for the back-scattering, its amplitude at high energies increases monotonically with the atomic number.

The inelastic scattering effects also need to be included. These inelastic processes, which only take place within the material, reduce exponentially the intensity accordingly to a parameter called inelastic attenuation length Λ, which is around 1.4 times smaller than the inelastic mean free path. Consequently, the amplitude of a wave at a distance *L* from its source obeys the expression:

$$\phi(L) = \phi_0 e^{-\frac{L}{2\Lambda}}$$

Fortunately, this parameter seldom plays a significant role in the formation of the patterns other than vary the overall intensity of the emission[6].

In respect to the vibrational effects, they add one additional contribution to the attenuation of the interference effects and this one is more relevant than the former. The simplest way to deal with this phenomenon is to multiply each wave by the corresponding Debye-Waller factor, which takes into account the mean-squared vibrational displacement of atoms. It can be shown nonetheless that in forward scattering dominated regimes, vibrational effects are not significant to first order.

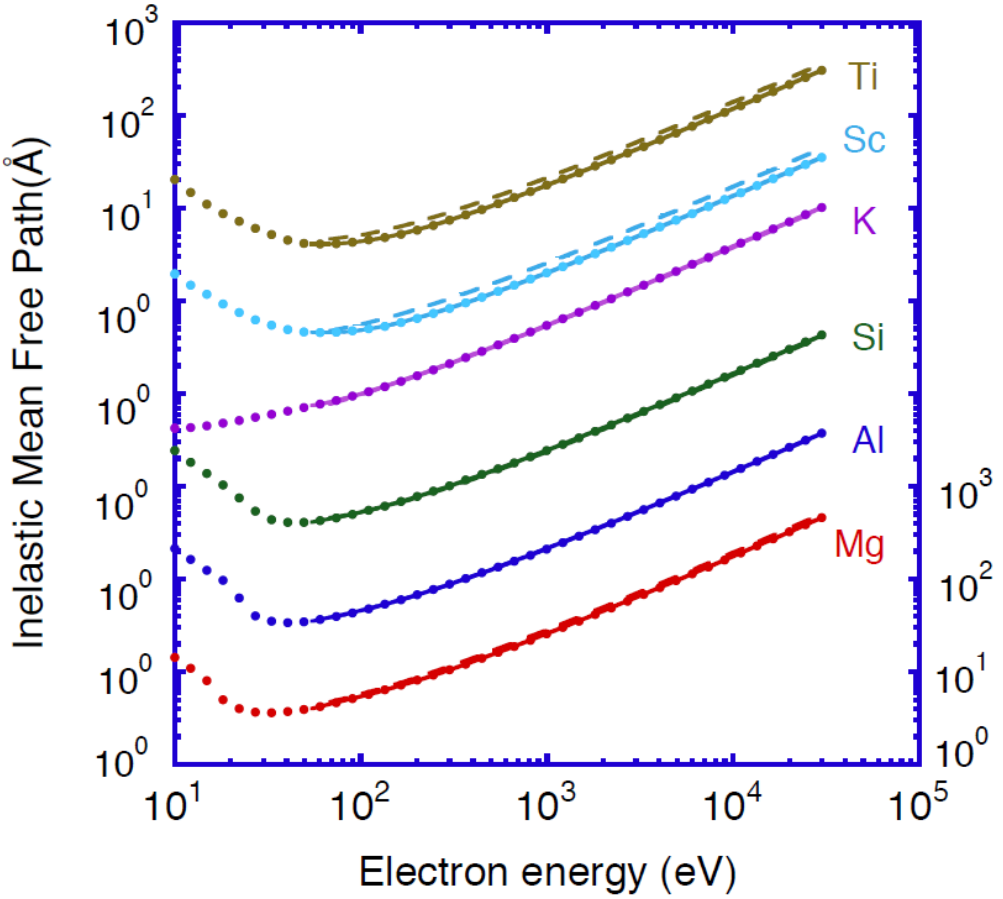

Figure 2: Plots of electron inelastic mean free paths as a function of electron energy[7]. The ordinate scale on the right indicates the IMFP for Mg. Successive plots have been displaced vertically for clarity, and the ordinate scale at the left indicates these displacements.

In the end, after considering all of the aforementioned effects, the intensity is found to be proportional to:

$$I(\vec{k}) \propto \sum_{\vec{p}} \left(\vec{p}\cdot\vec{k} e^{-\frac{L}{2\Lambda}} + \sum_j \frac{\vec{p}\cdot\vec{r}_j}{r_j} f_j(\theta_j) W_j e^{-\frac{L_j}{2\Lambda}} e^{i\cdot[kr_j(1-\cos\theta_j)+\psi_j(\theta_j)]} + \sum_j (\vec{p}\cdot\vec{r}_j)^2 \frac{|f_j(\theta_j)|^2}{r_j^2} (1-W_j^2) e^{-\frac{L_j}{\Lambda}} \right)$$

where the terms included have the meanings shown below:

-$\vec{p}\cdot\vec{k}$ and $\vec{p}\cdot\vec{r}_j$: photoemission matrix-element modulations along the unit vectors $\vec{k}$ and $\vec{r}_j$.

-$e^{-\frac{L}{2\Lambda}}, e^{-\frac{L_j}{2\Lambda}}$ and $e^{-\frac{L_j}{\Lambda}}$: inelastic attenuation factors

-$(\vec{p}\cdot\vec{r}_j) f_j(\theta_j) W_j e^{-\frac{L_j}{2\Lambda}}/r_j$: effective amplitude of ϕ_j after allowance for vibrational and inelastic effects.

-$e^{i\cdot[kr_j(1-\cos\theta_j)+\psi_j(\theta_j)]}$: Total final phase shift between the direct and the singly scattered waves.

The summation is performed over two wisely chosen perpendicular polarizations. It is also interesting to remark that the terms that run over the cluster (that is those that include the index *j*) do not require any periodicity, and therefore reciprocal lattice vectors don't intervene in any step of the resolution.

Finally, some weak refraction should be introduced at the surface of separation between the material and the exterior volume. The change in the direction of the waves in the most serious conditions (grazing incidence) does not go beyond a few degrees, yet it's observable. Additionally, the finite resolution of the analyser is responsible for the loss of some image sharpness in the experimental diffraction patterns.

Some improvements of the treatment can be made by introducing the spherical character of both the primary and the singly scattered waves. The main effect is a decrease in the forward scattering direction intensity, which becomes more noticeable as the energy increases.

Another additional refinement necessary in some cases is the inclusion of correlated vibrational motions, which results in a reduction of the Debye-Waller factors[8].

Lastly, a more robust approach of the phenomenon should consider multiple scattering. In that case, the final wave would not only consist of the direct wave and the singly scattered ones, but there would also be twice scattered waves, thrice scattered waves etc. The calculations can be performed by means of translational symmetry arguments[9], Taylor series by means of the magnetic quantum number expansion (MQNE) method[10], Green functions[11] etc. The multiple scattering produces some defocusing along compact directions as well as a strengthened backscattering[12].

2. Experimental devices

The photoelectron diffraction patterns included in this thesis were registered in two synchrotron facilities: the *Elettra* synchrotron in Trieste (Italy) and the *SOLEIL* synchrotron in Saint-Aubin (France). Hereinafter their characteristics will be described briefly for the sake of comparison.

The *ANTARES* beamline

At the *SOLEIL* facilities, the experiments were performed on the *ANTARES* (A New Tailored Angle RESolved Spectroscopies) beamline[13]. This beamline was devised for the complete determination of the electronic structure of condensed matter angle-resolved photoemission spectroscopy (ARPES) and photoelectron diffraction.

The usual operation of the source involves an electron energy of 2.5 GeV and injection currents in top-up mode of 500 mA. The main experiments targeted during its conception (nano-ARPES, core level imaging and x-ray absorption spectroscopy) can be performed in the energy range between 10 and 900 eV. The two undulators, installed in tandem configuration, enable the production of linearly and circularly polarized x-rays.

The following stage of the beamline includes a plane-grating monochromator, whose transmission remains relatively high despite its ability to suppress higher orders light.

The whole design, shown in the following figure, ensures an illumination coherent and homogeneous over the Fresnel Zone plates. The strong point of the beamline is its remarkable momentum and energy resolutions, below 0.05 $Å^{-1}$ and 200 meV respectively.

Generally, the flux of photons on the sample is $6.4 \cdot 10^{12}\ s^{-1}$ during micro-spot operation and $5.4 \cdot 10^{10}\ s^{-1}$ for nano-spot experiments. In both cases, the habitual resolution power is 32000 at a typical photon energy of 200 eV.

The analysis chamber contains nano-spot focusing optics and the electron analyser. The effect of the thermal drift and the mechanical vibrations is reduced to a marginal magnitude by means of an interferometric system. The positioning of the sample and the analyser allow measurements with high precision.

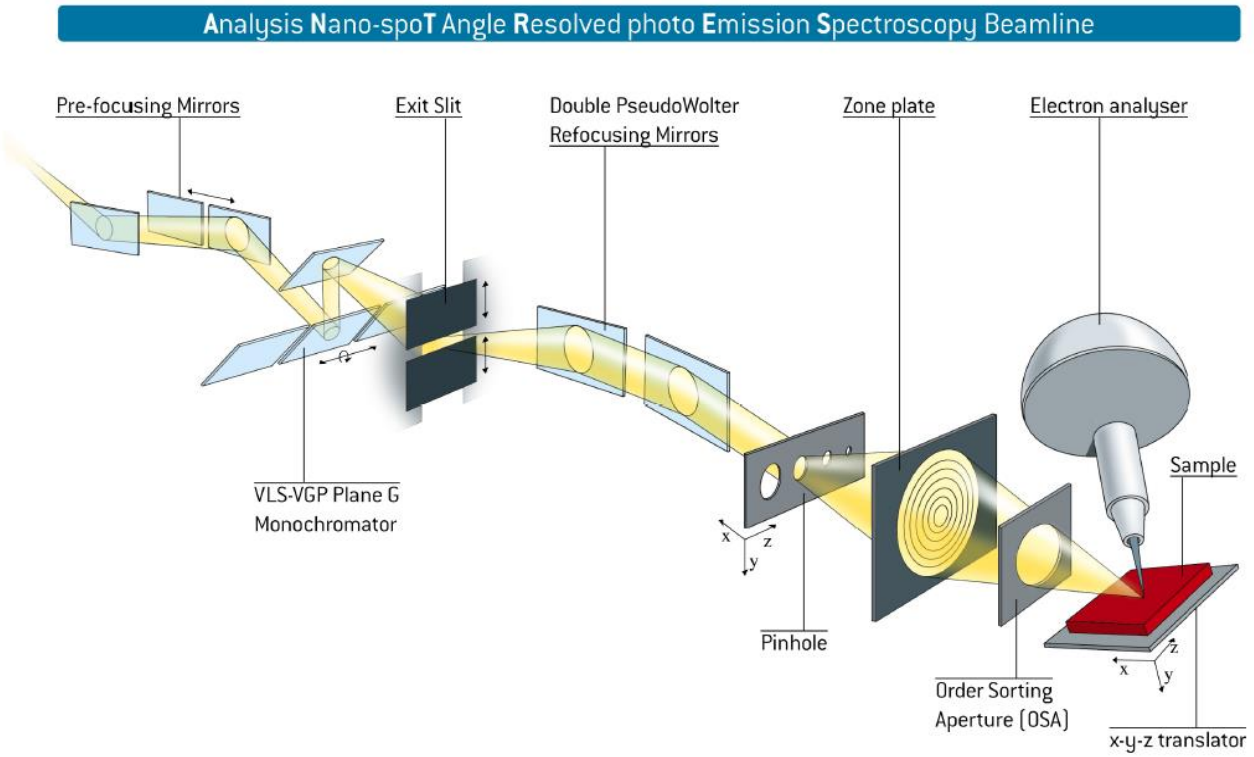

Figure 3: Schematic representation of the basic components of the ANTARES beamline

The *ALOISA* beamline

The photoelectron diffraction data that will be analysed in the third chapter were obtained at the *ALOISA* beamline of the Elettra Synchrotron Light Source in Trieste, Italy[14]. *ALOISA* is a multipurpose beamline devoted to surface science experiments. The possible photon energies range from 130 eV to 8 keV and the available experimental techniques are X-ray photoemission spectroscopy and diffraction (both ordinary and resonant), near edge X-ray absorption fine spectroscopy, surface X-ray diffraction and Auger photoelectron coincidence spectroscopy.

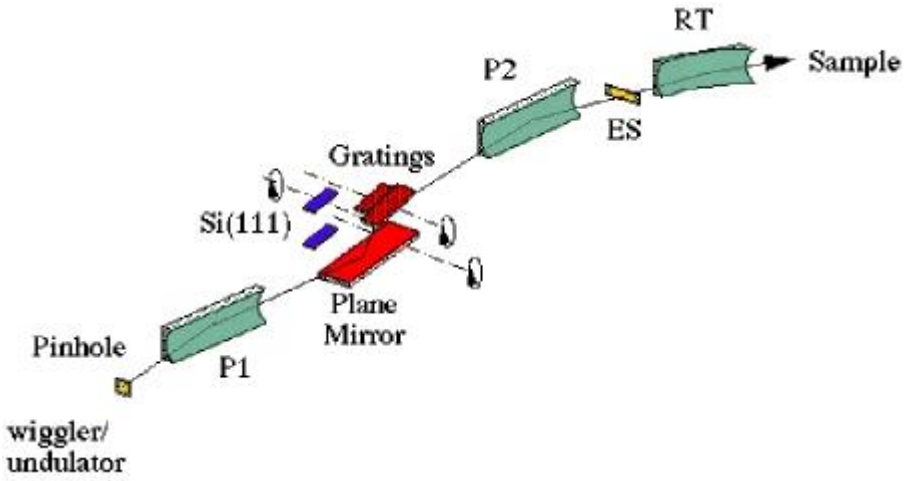

Figure 4: Scheme of the monochromator at *ALOISA* beamline

The monochromator (see figure 4) was designed to cover the whole range of energies. Synchrotron light obtained from the wiggler/undulator is collimated by the paraboloidal mirror P1. Then, there are two dispersing elements, a plane mirror for the low energy range (below 1500 eV) and a silicon channel-cut for high energies. The light is focused again onto the exit slits by the paraboloidal mirror P2 and reaches a toroidal mirror that redirects the light towards the centre of the experimental chamber. Resolutions go beyond 10000 for energies about 400 eV and are around 7500 the rest of configurations. The spot has a size of 20-30nm × 150-200 nm and receives fluxes ranging from more than 10^{11} photons in the low energy range to $5 \cdot 10^{10}$ in the high energy end.

The experimental chamber contains 6 hemispherical electron energy analysers movable along two angular directions and with resolutions around 2 degrees. The sample manipulator's position can be modified through 6 degrees of freedom. Importantly, live RHEED allows the user to control the epitaxy in real time.

The table below offers a glimpse of the extensive geometrical parameter space of the manipulator.

Rotating element	Rotation axis	Range	Resolution
Experimental chamber	Beam	$\pm 120°$	0.00015°
Axial frame	Beam	$\pm 120°$	0.0002°
Bi-modal frame	Perpendicular to the beam	$\pm 100°$	0.0002°
Sample holder	Beam	[-90,185]º	0.001°
Sample holder	Grazing angle	[-2,15]º	0.001°
Sample holder	Surface normal	$\pm 95°$	0.001°

Table 1: Adjustable geometrical parameters of the sample manipulator

Regarding the data acquisition, the plane of scattering was chosen perpendicular to the surface and the angle of incidence of the X-ray was kept fixed at 4º in the transverse magnetic condition. The level selected for the acquisition of the diffraction patterns was the cobalt line $2p_{3/2}$. A good compromise between spectral resolution and signal-to-noise ratio was reached for a kinetic energy of the outcoming electrons set to 160 eV. As for the scan, it was performed over the region spanned by the intervals 0-67º for the polar angle θ, and 0-107º for the azimuth ϕ (including the directions $\langle 011 \rangle$ and $\langle 010 \rangle$ of the substrate).

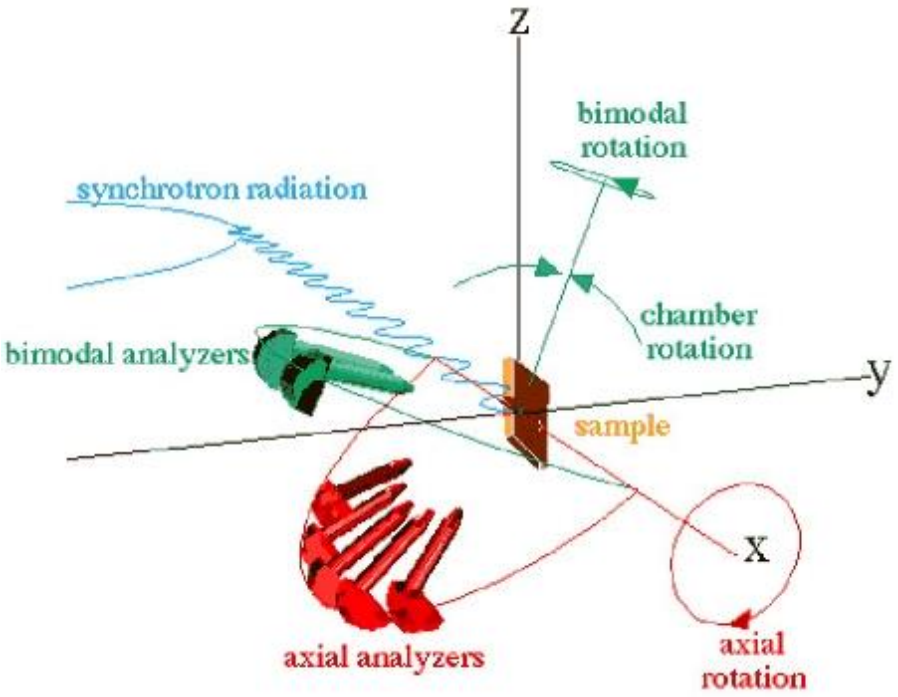

Figure 5: Scheme of the degrees of freedom of the manipulator at the *ALOISA* beamline.

3. Data treatment

The measurements consist in registering the photoemission spectrum of interest, which is the intensity of the flux of emitted photoelectrons as a function of the kinetic or the binding energy. Both magnitudes are closely related through the following equation that involves also the work function ϕ and the energy of the photon:

$$E_{photon} = E_{binding} + E_{kinetic} + \phi$$

The objective is to register as many spectra as possible varying only the direction of observation. In this manner, the device will detect any anisotropy that could reveal valuable information about the sample.

After the data acquisition, the measurements produce basically three dimensional matrices I_{ijk}. The first index i runs over all the possible values of the azimuthal angle ϕ, the index j spans the interval of polar angles θ, and finally k makes reference to each sampled value of the energy during the acquisition of the spectra.

The following figure shows one example of a photoemission spectrum for fixed values of the azimuthal and polar angles.

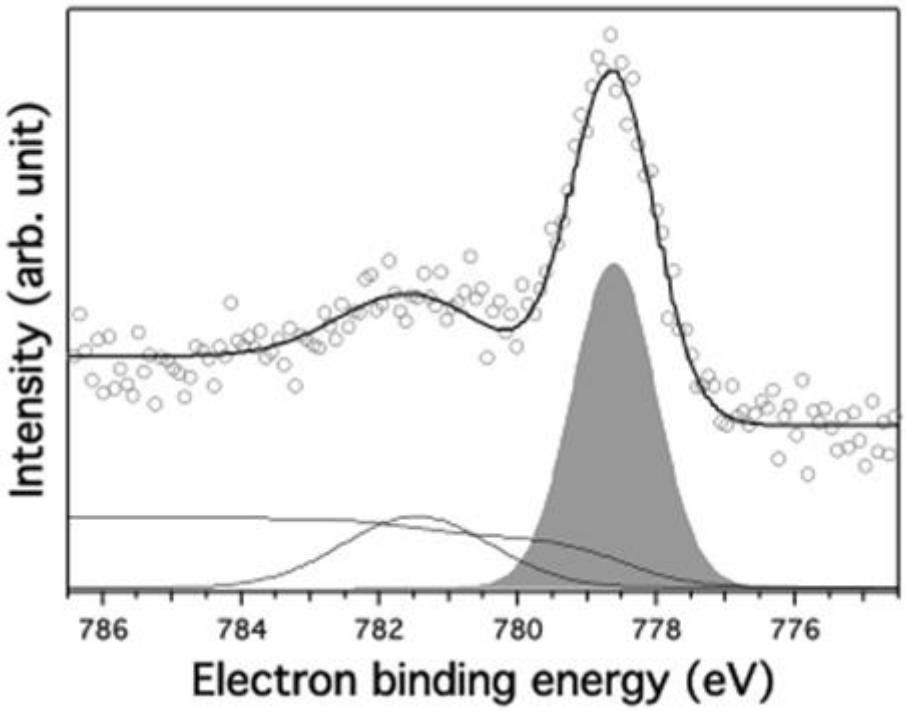

Figure 6: Photoemission spectrum of the Co $2p_{3/2}$ level of a sample of cobalt phthalocyanine on Ag(100).

In order to lower the dimension of the data so as to obtain the two-dimensional (*i*,*j*) matrices which are then represented as the diffraction patterns, the selected features are integrated (for example the grey peak in the figure above).

The result of this operation is a *raw* diffraction pattern that would need a further normalisation if any quantitative comparison were to be performed.

The normalisation procedure admits multiple "translations" into mathematical operations. This choice has a serious impact on the values of numerical coefficients that are calculated to quantify the similarity or the agreement between two different patterns.

In any case, there are two main objectives for the normalisation: the first one is the suppression of the background signal from the raw patterns, which tends to cover the actual features of the diffraction. As for the second one, the idea is to make the statistics of different images as similar as possible to ensure that differences in the matrices come really from anisotropy effects and not so much from factors such as the instrument. It is also important to prevent the adulteration of the data as much as possible, and consequently only the mean of the intensity over the pattern was set to one in this thesis. Both stages will be described in more detail in the next paragraphs.

Regarding the removal of the background, it should be noted that the background itself should present rotational symmetry around the direction perpendicular to the surface. In effect, if the background is not related to the structure of the material and that very structure is the only element without rotational symmetry, then it follows that the background must depend exclusively on the polar angle. The following figure with polar profiles shows the plausibility of this assumption.

The background level $I_{min}(\theta)$ for each value of the polar angle θ was taken as the minimum value of the signal over the respective azimuthal profile of intensity $I_\theta(\phi)$. This strategy relies on one reasonable consideration: since the background has rotational symmetry, the signal over an azimuthal profile can never be lower than the background. Moreover, for a given azimuthal profile the diffraction features shouldn't span the whole range of azimuths. Be that as it may, such features would be undistinguishable from a background level. The images below summarise this first part.

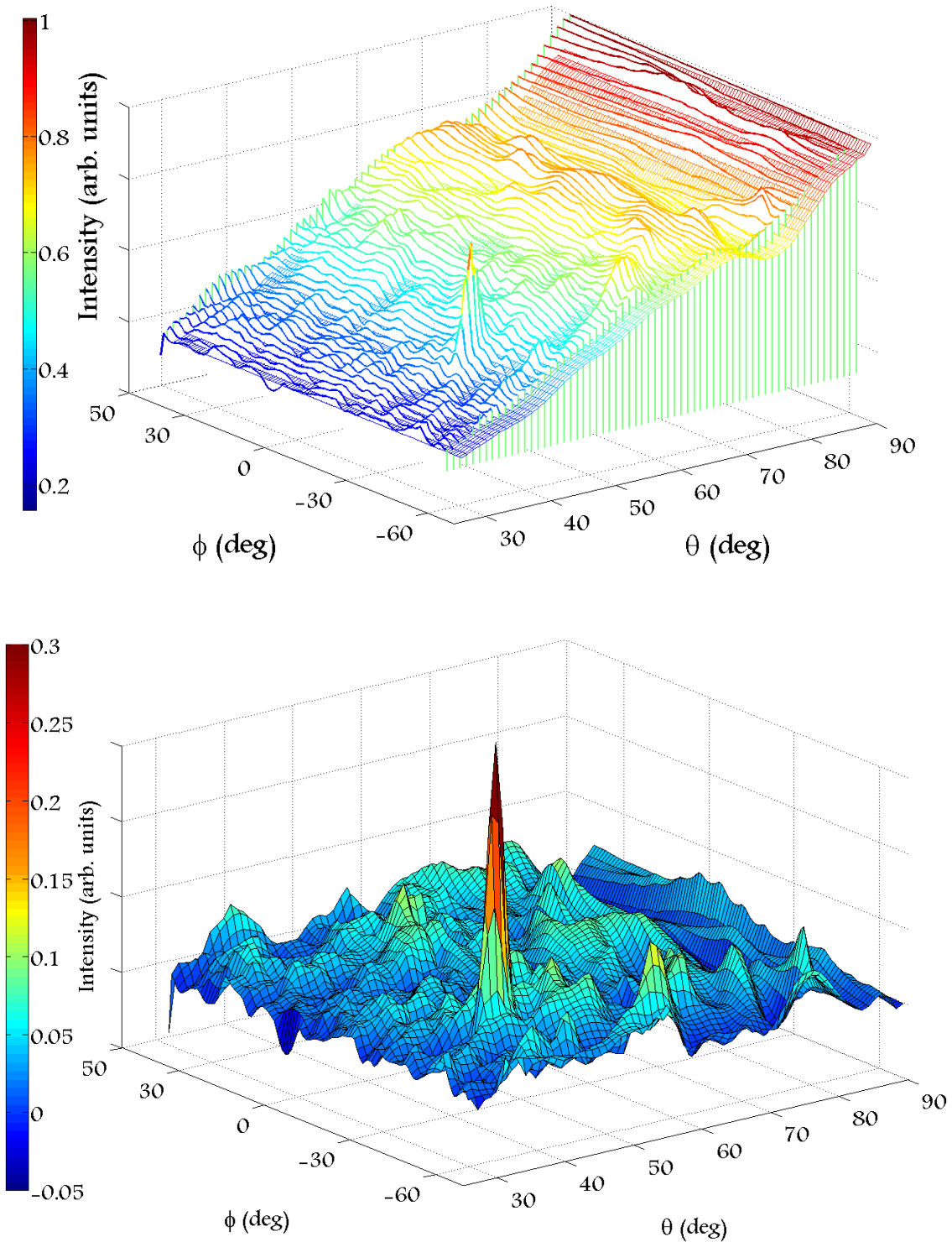

Figure 7: *Raw* diffraction pattern and determination of its corresponding background level. The waterfall plot shows every azimuthal profile with thick lines while the background signal is represented by the finer, thinner grid. The lower figure includes the same data after the subtraction of the background.

With respect to the normalisation, there are several possibilities. García de Abajo[15] chooses the following normalisation for the anisotropy:

$$\chi_1(\phi,\theta) = \frac{I(\phi,\theta) - I_0(\theta)}{I_0(\theta)}$$

where $I_0(\theta)$ represents the average of the intensity over azimuthal angles.
While Auwärter[16] has proposed the following variant:

$$\chi_2(\phi,\theta) = \frac{I(\phi,\theta) - I_0(\phi)}{I_0(\phi)}$$

where $I_0(\phi)$ stands for the average of polar scans for each angle ϕ.

Both can be tested on some produced data to evaluate which one is the best option. Consider the test pattern given by the expression:

$$I_{signal} = \theta \cos^2(3\phi) \sin^2(4\theta)$$

And the background specified by:

$$I_{background} = (\pi/2 - \theta)\,\mathrm{erf}\left(\frac{\pi/2 - \theta}{\pi}\right)$$

Then, the signal that should be obtained after the normalisation is well-known. After applying the aforementioned definitions the results are different as shown in the comparison below.

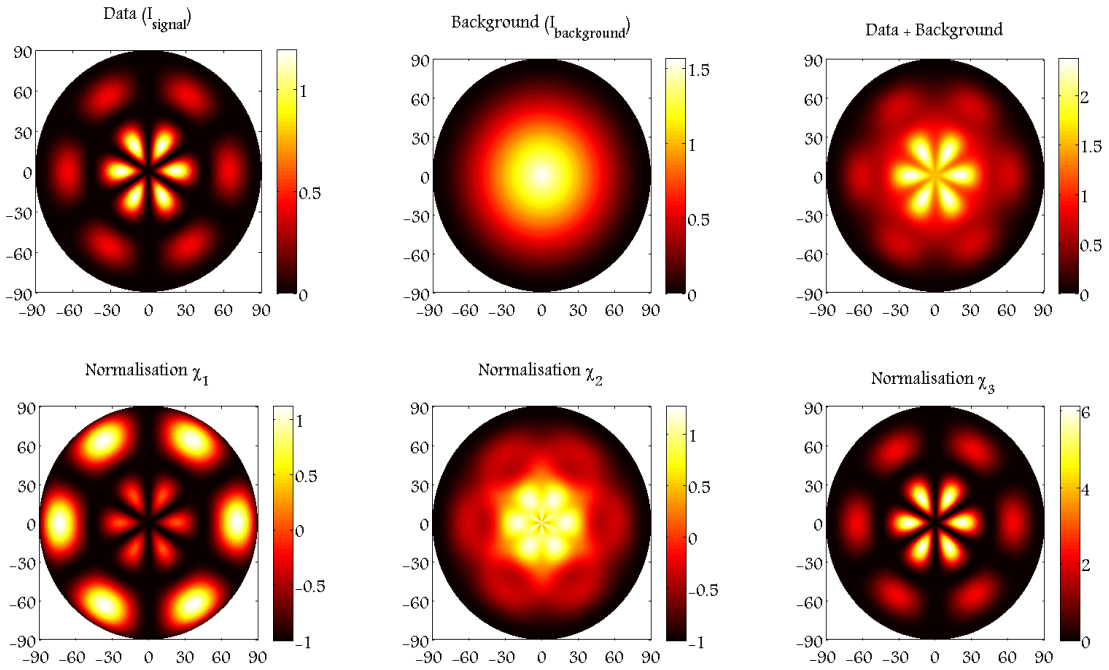

Figure 8: Polar plots of the test pattern, the background and the proposed normalisations. The radial coordinate is the polar angle θ and the azimuthal one is the angle ϕ. The angles on the axes are specified in degrees

Nevertheless, in this thesis, the following variation of χ_1 has been considered:

$$\chi_3(\phi,\theta) = \frac{I(\phi,\theta) - I_{min}(\theta)}{\langle I(\phi,\theta) - I_{min}(\theta)\rangle}$$

Here, $I_{min}(\theta)$ is the minimum value of the intensity for a given polar angle θ and the angle brackets in $\langle I(\phi,\theta) - I_{min}(\theta)\rangle$ denote an average over the whole set of data. The reasons behind this choice are mainly two:

1) By subtracting a polar or azimuthal average (as the first two definitions do) instead of the minimum value, some signal is necessarily being subtracted. This should be avoided as much as possible.
2) It should be noted that with the third definition the whole pattern is divided by the same value, whereas the other two involve divisions by a factor dependent on one parameter, either the azimuth or the polar angle. This means that every "row" or "line" of the data is being weighted differently and some artificial anisotropy may be introduced.

The chosen approach produces less modifications on the data and yields a better representation of the original physical signal as the second row of figure 8 reveals. For these reasons the third option will be used throughout this work.

References:

1. Fadley, C. S., *The study of surface structures by photoelectron diffraction and Auger electron diffraction*, Plenum Press, New York, (1993)
2. Terminello, L. J. et al. Phys. Rev. B38, 3879, (1988)
3. Liebsch, A., Phys. Rev. Lett. 32, 1203, (1974)
4. Friedman, D. J. et al., J. Electron. Spectrosc. 51, 689 (1990)
5. Parry, D. E., J. Electron. Spectros. Relat. Phenom. 49, 23 (1989)
6. Kono, S. et al., Phys. Rev. Lett. 41, 1831 (1978)
7. Tanuma, S. et al., Surf. Interface Anal. 43, 689 (2011)
8. Sagurton, M. et al., Phys. Rev. B30, 7332 (1984)
9. Poon, H. C. et al., Phys. Rev. B30, 6211 (1984)
10. Barton, J. J. et al., Phys. Rev. B32, 1892 (1985)
11. Rehr, J. I. et al., Phys Rev. B34, 4350 (1986)
12. Xu, M. L. et al. Surf. Sci. 207, 215 (1989)
13. Avila, J. et al. *ANTARES, a scanning photoemission microscopy beamline at SOLEIL*, Journal of Physics: Conference Series 425 192023 (2013)
14. https://www.elettra.trieste.it/it/lightsources/elettra/elettrabeamlines/aloisa/aloisa.html
15. García de Abajo, F. J. et al., Phys. Rev. B, 63, 075404 (2001)
16. Auwärter, W. et al. Phys. Rev. B, 81, 245403 (2010)

The experimental device

The study and the characterisation of surfaces and interfaces require the so-called ultra-high vacuum environments, that is, pressures below the threshold of 10^{-10} torr. The reasons behind this need are two. The first one is the existence of contaminant species that could spontaneously get adsorbed onto the surface or even worse, react with it. The second reason is the increasingly longer electron mean free paths as the pressure is reduced, which for example enhances the performance of the HREELS spectrometer.

Most of the measurements included in this thesis have been registered under such conditions. To obtain the necessary pressure levels, a volume has been kept isolated from the atmosphere by means of a group of stainless steel chambers and several pumps. The latter have been the active elements in charge of initially decreasing the pressure and maintaining it once the stationary value (around $3\text{-}5\cdot10^{-10}$ torr) was reached. The pumping system consists of primary pumps, turbomolecular pumps and ion pumps. For some experiments, liquid nitrogen has been added to the system through an isolated circuit to cool down the chambers inducing a lower pressure.

The device used throughout this thesis is located at the *Physique des Interactions Ioniques et Moléculaires* team (*Aix-Marseille Université*). It includes a fast introductory system (load-lock), which allows to transfer samples between atmospheric pressure and ultra-high vacuum in around 30 minutes; a preparation chamber where the preparation of the samples and the LEED measurements take place, a STM chamber, a HREELS chamber and a molecular chamber where molecules are evaporated onto the sample to prevent the contamination of the rest of the device.

The transfers between the chambers are carried out with the help of ferromagnetic bars (inside) and permanent magnets (outside) kept in magnetic contact. This system allows manipulations without the need to break the vacuum.

The next figures show an actual picture and a diagram of the device.

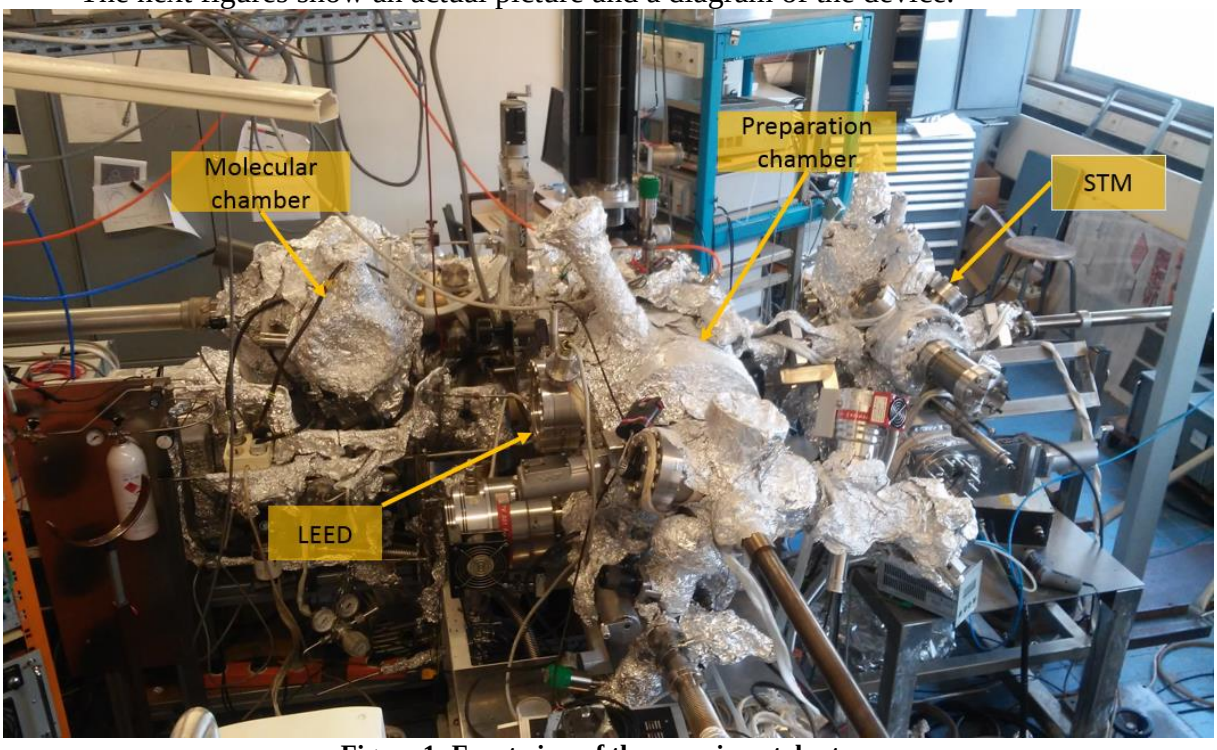

Figure 1: Front view of the experimental setup.

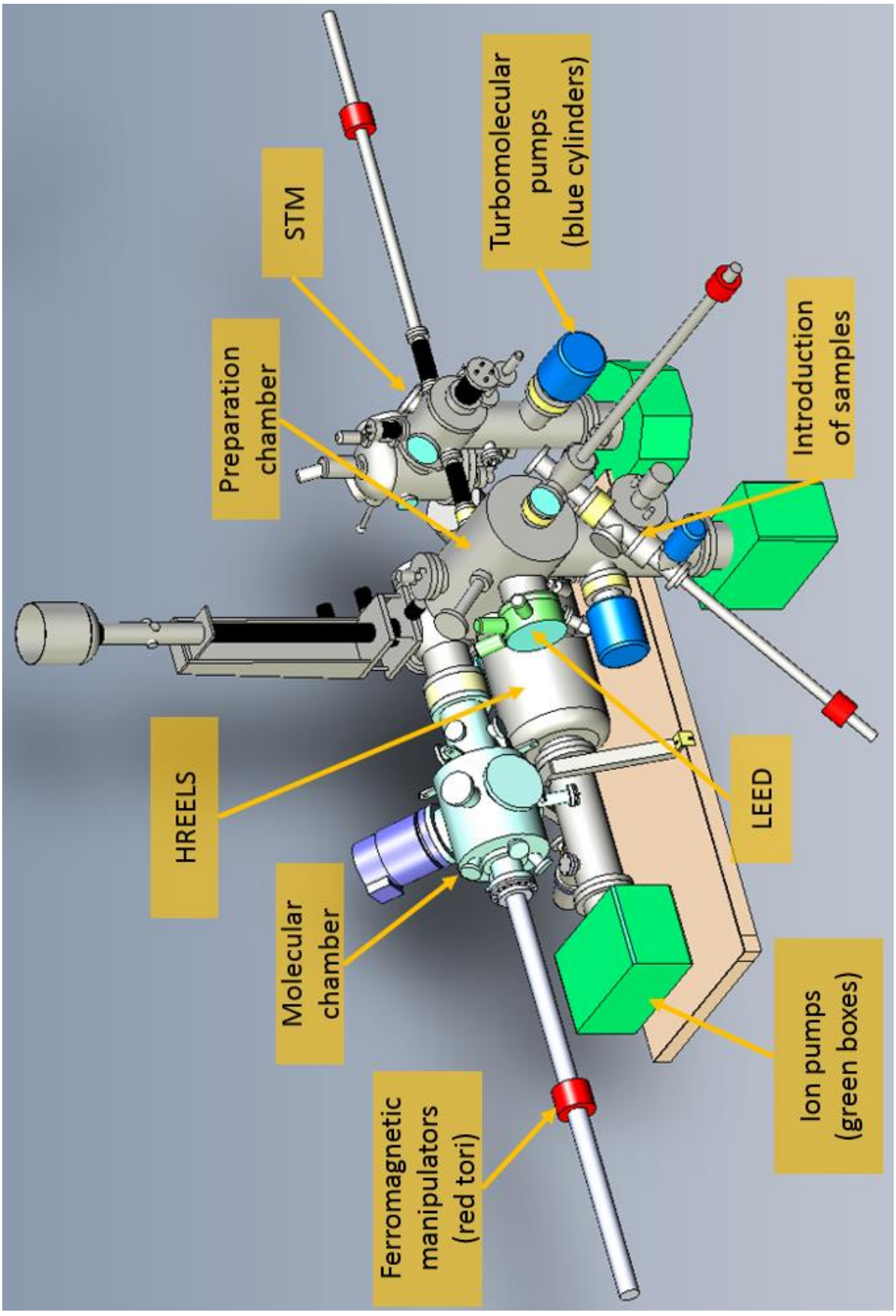

Figure 2: Diagram of the device

The system also includes an Ar^+ ion gun whose purpose is the preparation of the surfaces, and two sources connected to the preparation chamber for performing hydrogenations: one high energy capillary (0.2 eV) source and one low energy (25 meV) plasma source.

The molecular epitaxial growths are done with the help of several evaporators of molecules in the molecular chamber. They consist of a quartz crucible that is meant to contain the molecules during the evaporation. This crucible is surrounded by a wolfram filament whose purpose is to heat the crucible by means of the Joule effect. A temperature higher than a fixed threshold for each molecule triggers the evaporation.

The molecular chamber is also equipped with an additional LEED device that enables the simultaneous acquisition of LEED patterns as the evaporations progress. In this manner, it is possible to control precisely the extent of the evaporation providing more accuracy in the preparation of the samples.

The figure below shows a scheme of one evaporation unit.

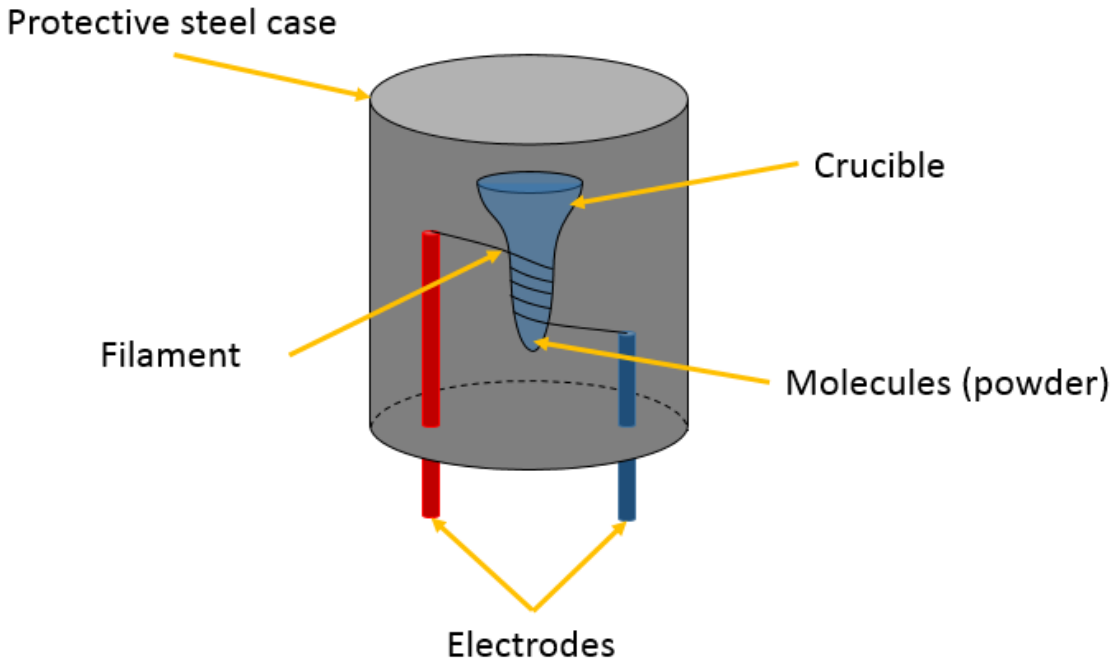

Figure 3: Diagram of one evaporation cell

Finally, the growth of silicene layers is slightly different and takes place in the preparation chamber instead. The temperatures for evaporating the molecules are significantly lower than those needed to produce a flux of silicon atoms from a wafer. Moreover, in order to keep the substrate at the desired temperature, the sample can be heated with the help of an additional incandescent filament located 1 cm above.

When preparing silicene, a current ranging between 12 and 14 A is maintained through the wafer. The high temperature reached on the silicon along with the chosen distance to the silver substrate (around 6 cm) ensure a flux of atoms appropriate for producing silicene in a reasonable time (between some tens of minutes and a few hours). The high intensity of the current induces a significant deterioration over periods of a few months, so the wafer has to be replaced from time to time and the flux must be recalibrated again.

A scheme of the device that allows to make a current circulate through the silicon wafer is displayed in figure 4.

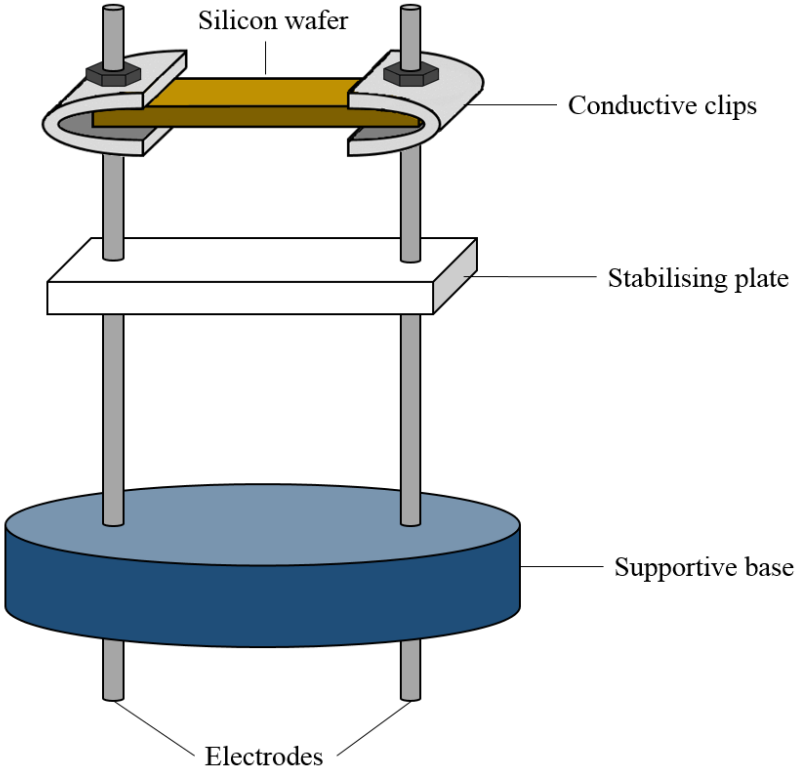

Figure 4: Schematic view of the silicon evaporator

The EDAC code

In order to test structural models of interfaces (for instance cobalt phthalocyanines on Ag(100)), the experimental photoelectron diffraction patterns needed to be compared with a priori sets of equivalent data. The latter have been obtained by means of the software *Electron Diffraction in Atomic Clusters*[1] (EDAC), which is the central element of this section.

EDAC is a program written in the *C++* language. It simulates photoelectron diffraction patterns, electron scattering in molecules and low energy electron diffraction in the framework of multiple scattering theory. It doesn't take into account any approximations apart from the muffin-tin model and the free-electron Green function is implemented through an exact representation that consists of rotations matrices and translations along the axis perpendicular to the surface.

1. Theoretical basis[1]

In the previous XPD section, the most simplified theoretical model of the technique was described and the multiple scattering was cited as one of the most promising ways to improve its overall agreement with experimental data.

Several approximations can be considered when characterising multiple scattering, but since electrons with energies higher than 50 eV barely interact if at all with the outermost region of the atomic potentials, those can be replaced by the muffin-tin models[2].

On a different aspect, computational calculations of these processes can be separated in two types regarding the symmetry: cluster and layer-by-layer schemes. The latter require in general a stricter periodicity and is usually reserved to LEED patterns[3]. On the other hand, the former exploits the fact that electrons cannot propagate over long distances due to inelastic processes. These are implemented by means of a complex (as opposed to real) optical potentials, that is to say inelastic mean free paths. So in the end, the clusters are restricted to a small region of a radius comparable to the inelastic mean free path.

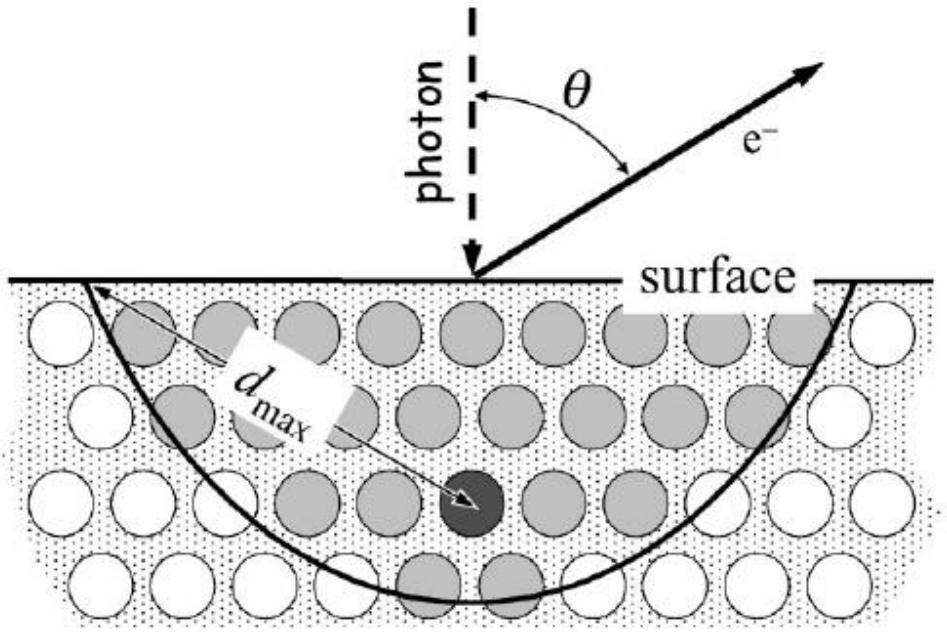

Figure 1: Example of one reduction of the simulated sample to a parabolic cluster. The emitter is highlighted in black and the region accessible to its emitted electron is enclosed within the parabola.

The multiple scattering calculations are very demanding, so several approaches have been developed to increase the efficiency of the simulations. In particular, the EDAC software, with its exact representation of the Green function propagator and its fully convergent recursive method, carries out $N^2(l_{\max}+1)^3$ multiplications, where N is the number of atoms in the cluster, and $l_{\max}$ represents the cut-off of the orders considered when performing the multipole expansion (it must be noted that the physical magnitudes are represented through their spherical harmonics in the code). The exact method is also available but the computation time in that case scales as $N^3(l_{\max}+1)^6$, which makes the simulation of any cluster of a reasonable size almost unfeasible.

In any case, the theoretical framework of multiple scattering has its origin in the time-independent Schrödinger equation (in this section atomic units will be used $e = \hbar = m_e = 1$):

$$(H_0 + V - E)\varphi = 0$$

where H_0 stands for the kinetic energy ($H_0 = -\nabla^2/2$), V represents the sum of the atomic potentials (equal to a constant outside of the muffin-tin spheres) and E the energy of the wave function in question.

If φ_0 is the wave function that satisfies free-electron Schrödinger equation, the actual wave function can be separated in two parts that fulfil the following expressions:

$$\varphi = \varphi_0 + \phi$$
$$\phi = G_0 T \varphi_0$$

where G_0 is the free-electron propagator:

$$G_0(r - r') = -\frac{1}{2\pi}\frac{e^{ik|r-r'|}}{|r-r'|}$$

and T represents the atomic cluster matrix:

$$T = \sum_{\alpha}\left(T_\alpha + \sum_{\beta\neq\alpha} T_\beta G_0 T_\alpha + \sum_{\gamma\neq\beta}\sum_{\beta\neq\alpha} T_\gamma G_0 T_\beta G_0 T_\alpha + \cdots\right)$$

This expression[3] is an infinite series expansion (as it accounts for any possible scattering path) written in terms of the matrices of the individual muffin-tin potentials V_α, which obey the self-consistent equation below:

$$T_\alpha = V_\alpha + V_\alpha G_0 T_\alpha$$

After the expansion of the magnitudes in spherical harmonics, the series can be rewritten in terms of the scattering phase shifts[4] δ_l^α through the scattering matrix:

$$t_\alpha = \sum_l \sin\delta_l^\alpha \, e^{i\delta_l^\alpha}$$

and the translation formula of spherical harmonics:

$$G_{\alpha\beta} = \sum_{L,L'} 4\pi \sum_{L''} h_{L''}\left[k\left(R_\alpha - R_\beta\right)\right] \int d\Omega \cdot Y_L(\Omega)\, Y_{L''}(\Omega) Y_{L'}^*(\Omega)$$

In this expression, $Y_L(\Omega)$ is the spherical harmonic characterised by the degree and order specified by L, h_L represents the radial part of the spherical wave and k the wave vector of the electron.

Keeping all these elements in mind, the self-consistent equation that is solved by the EDAC code is:

$$\phi_\alpha = \phi_\alpha^0 + t_\alpha \sum_{\beta \neq \alpha} G_{\alpha\beta}\phi_\beta$$

With:

$$\phi_\alpha^0 = G_0 T_\alpha \varphi^0$$

As it has been stated before, the inversion of the system of equations is possible, but involves too many operations (they scale as $N^3(l_{\max}+1)^6$). There are several faster solving procedures such as the direct Jacobi iteration, the simultaneous relaxation method or the modified recursion method. The last one has the best performance, as it yields exact results after $N(l_{max}+1)^2$ iterations. Fortunately, for typical clusters, reasonable convergence is reached after around 20 iterations.

Another interesting feature of the code is that in principle, the calculations should be performed for every direction. Yet, by means of a convenient storage in memory of partial results, it is able to compute intensities along multiple directions at the same time, hence speeding up the process.

In effect, the Green function is calculated along the z axis after rotating the bond vector between the atoms α and β $d_{\alpha\beta}$ until obtaining alignment with the aforementioned axis:

$$G_{\alpha\beta}^z = \delta_{mm'}\sqrt{4\pi} \sum_{l''} \sqrt{2l''+1} \cdot i^{l''} \cdot h_{l''}^{+}\left(kd_{\alpha\beta}\right) \int d\Omega \cdot Y_{lm}(\Omega)\, Y_{l''0}(\Omega) Y_{l'm}^*(\Omega)$$

In the end, the vector is inversely rotated back to its original position so the final green function is:

$$G_{\alpha\beta} = R_{\alpha\beta}^{-1} G_{\alpha\beta}^z R_{\alpha\beta}$$

Since the considered cluster is not infinite and there is a significant degree of symmetry in it, there are many coincidences in the rotations and translations. Therefore the storage of these values allows to circumvent redundant calculations.

2. Simulation settings

This section is intended to be a brief description of the main parameters that must be specified to run a simulation. The effects of modifying them are also commented hereinafter.

The first part is devoted to the structure and the geometrical properties of the cluster. Its shape must be chosen between two options: spherical or parabolic. The advantage of the parabolic cluster is its larger coverage of the surface at the expense of not going as deeply into the material as a spherical cluster would do. Another parameter is the size of the cluster, which is around 20 Å for the simulations included in this thesis. The next step is the actual specification of the cluster, which can be achieved by selecting directly a semi-infinite cluster (later restricted to the specified size), layer by layer, or introducing the position of each individual atom.

The second part includes the enumeration of the atoms whose emission will be simulated. At this moment, the user may select either the built-in muffin-tin potentials or some other custom potentials. In general the results of this thesis have considered more accurate models than the built-in ones provided by the member of the *ALOISA* beamline Alberto Verdini.

Regarding the emission itself, it's mandatory to select one core level. The polarization of the photons as well as its direction can also be fixed. It's also possible to specify the operation mode of the device, that is to say, if only the analyser moves, if only the sample moves or if both move. Some other needed parameters are the kinetic energy of the electrons and the region of solid angle whose photoemission will be simulated.

The last part is devoted to additional data such as the energy of the vacuum level. Although it has usually a limited effect, the inelastic mean free path can be introduced. Both the temperature and the Debye temperature of the sample can be set. A higher temperature produces a broadening of the features that causes blurrier patterns.

The last parameter is the maximum effective angular momentum number l_{max}, and is crucial for two reasons: firstly, it modifies the time of simulation more than any other parameter (the simulations included in this work have been running for times ranging from a few days to more than a week on an ordinary computer) so low values would be desirable. However, choosing a too low value can make the simulation converge to a false result due to the lack of higher order spherical harmonics. Reasonable values of this parameter used during this thesis have been in the interval 15-20.

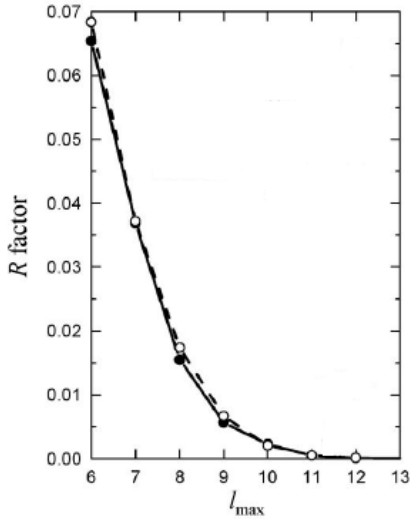

Figure 2: One example of the evolution of the accuracy of simulations with increasing l_{max}. The R factor is a measurement of the discrepancy between the exact solution and the one obtained by means of the recursion method. Perfect match is attained when $R = 0$. The two curves account for alternative definitions of the R factor. As it's evident, the result becomes more accurate for higher l_{max}.

3. Testing the EDAC code

Before being able to perform simulations with ease, it was necessary to dive into the code and understand how to use it in order to obtain sensible results. With this aim, some preliminary studies on well-known systems were tackled. Chambon[5] studied the early stages of formation of the Ag-Ni(111) interface by grazing incidence x-ray diffraction and x-ray photoelectron diffraction.

In the article, they probed the structure with electrons emitted from the Ag $3d_{5/2}$ core level with a kinetic energy close to 530 eV. They also simulated with the MSCD code[6] the diffraction pattern corresponding to the model they devised for the system and obtained a rather satisfying agreement, as shown in the figure below[5].

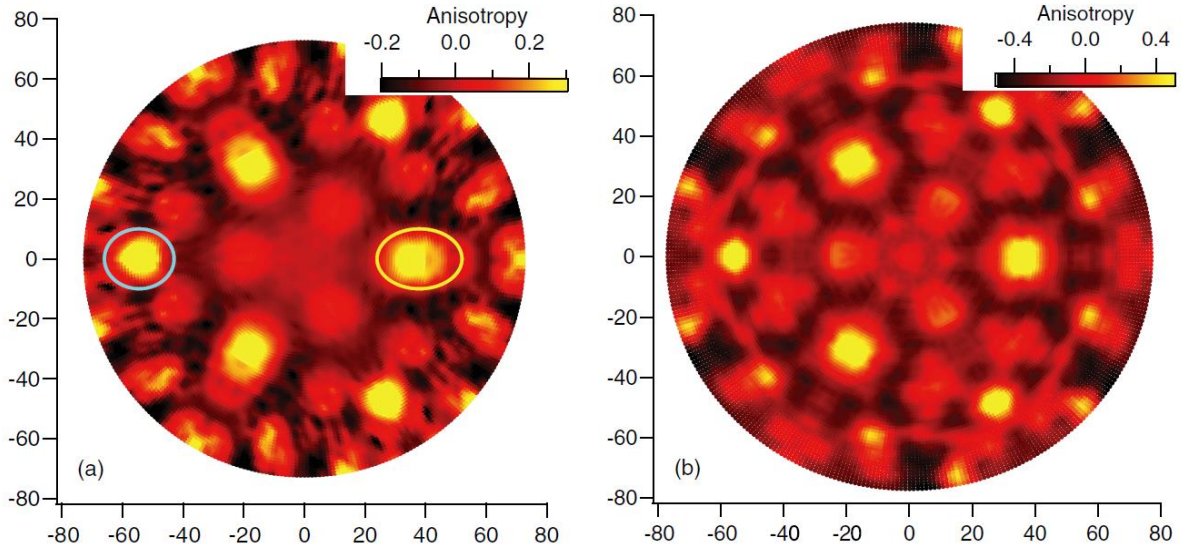

Figure 3: Experimental XPD pattern of a 2.9 monolayers deposit of Ag on a Ni(111) substrate (left) and equivalent simulated pattern (right). The electrons were emitted from the Ag $3d_{5/2}$ level with a kinetic energy equal to 530 eV.

During the first stage of "discovery" of the EDAC software, it was deemed as convenient to try to reproduce the results from the chart above. Several attempts were necessary to tune adequately the simulation parameters so as to produce a simulated pattern similar enough to the published results. As a guide, an explained version of the configuration file is included in the following lines.

* * *

Example of a parameter file

`cluster surface off`

Specification of the cluster's shape, either *off* (spherical) or *on* (parabolic)

`cluster reference-point l(A) 0 0 0`

Position of the point of reference (x,y,z) in terms of the units written as the third word, in this case *l(A)*, which means "distances measured in Å". The cluster will be generated starting from this point, so it becomes the centre of the sphere or the focus of the paraboloid

```
cluster Rmax l(A) 18
```
Size of the cluster in the specified units, 18 Å in this example

```
add cluster layer Ag l(A) 1.4387 0 2.5 5.0035 2.8888 0 30
add cluster layer Ag l(A) 3.1066 0 4.8587 5.0035 2.8888 0 30
add cluster layer Ag l(A) 4.7745 0 7.2174 5.0035 2.8888 0 30
```
Three atomic layers are introduced in the cluster. They are made of silver atoms, and the coordinates are written in Å as before. The sixth, seventh and eighth words of each line correspond to the position of the reference atom of the corresponding layer. The ninth and tenth parameters determine size of the lattice vectors. The eleventh parameter is the angle between the first basis vector and the x-axis (0º). The last one if the angle between both basis vectors (30º).

```
add cluster surface Ni l(A) 0 0 0 3.52 fcc111
```
The intersection of one semi-infinite face-centered cubic cluster with the sphere of radius equal to 18 Å is added. The atoms are nickel ones, the reference atom is located at (0,0,0) Å and the lattice parameter is 3.52 Å. The orientation of the cluster is (111).

```
cluster natoms 350
```
The cluster is further reduced to 350 atoms.

```
cluster output l(A) cluster_AgNi10
```
The positions of the atoms in Å will be written in a file called *cluster_AgNi10*

```
emitters 6 11 47 12 47 13 47 46 47 47 47 50 47
```
Selection of 6 emitter atoms. They are selected according to the order included in the previous output file. *47* is a reference to the chemical species, in particular the atomic number 47 is silver's one.

```
initial state 3d5/2
```
Core level from which the electrons are emitted

```
polarization LPx
```
Polarisation of the beam, in this case *LPx* stands for p-polarisation.

```
incidence 90 0
```
Spherical angles of incidence of the beam (θ,ϕ)

```
semi-movable cluster
```
Type of acquisition. This choice implies that the angle between the incoming beam and the analyser is not kept constant, The cluster rotates around *z* with φ, and φ=0 stands for the analyzer lying in the *x*-*z* plane toward *x*>0.

```
emission energy E(eV) 530 530 1
```
The simulations is performed with electron energies ranging from 530 eV to 530 eV. The interval is sampled 1 time. In other words, there will be only one simulation with 530 eV of kinetic energy.

`emission angle theta 2 90 45`

The sampled interval of polar angle will be [2,90]º. It will be split in 45 equal parts. This means there will be a pixel at 2º, 4º, 6º etc.

`emission angle phi 3 360 120`

Equivalent instruction for the azimuthal angle

`V0 E(eV) 4.5`

Energy of the vacuum level in eV

`imfp inline 1 l(A) 9.26`

Inelastic mean free path

`lmax 15`

Sets the maximum (global) effective orbital angular momentum number lmax to be used in scan in the simulation

`orders 4 5 10 15 20`

The specified 4 orders of iteration will be written in the output file.

`muffin-tin`

Chooses to use the built-in muffin-tin potentials for the atoms.

`temperature 300 330`

Specification of the temperature and the temperature of Debye of the sample.

`emission angle window 0`

Simulates a limited angle of acceptance of the detector (of 0º in this case)

`scan pd outputAgNi10.dat`

Output file

`End`

End instruction, the simulation doesn't run without it.

* * *

The output file is a table whose first column specifies the polar angle of the pixels. The second one is the azimuth of said pixels. The rest of the columns contain the intensity of the related pixel found after the n-th iteration specified by the user in the parameter file and written again on top of the output file.

After treating de data following the procedure explained in the photoelectron diffraction section of the experimental techniques, a normalised diffraction pattern is obtained. A graphic representation of the anisotropy map corresponding to the system presented by Chambon[5] is included below.

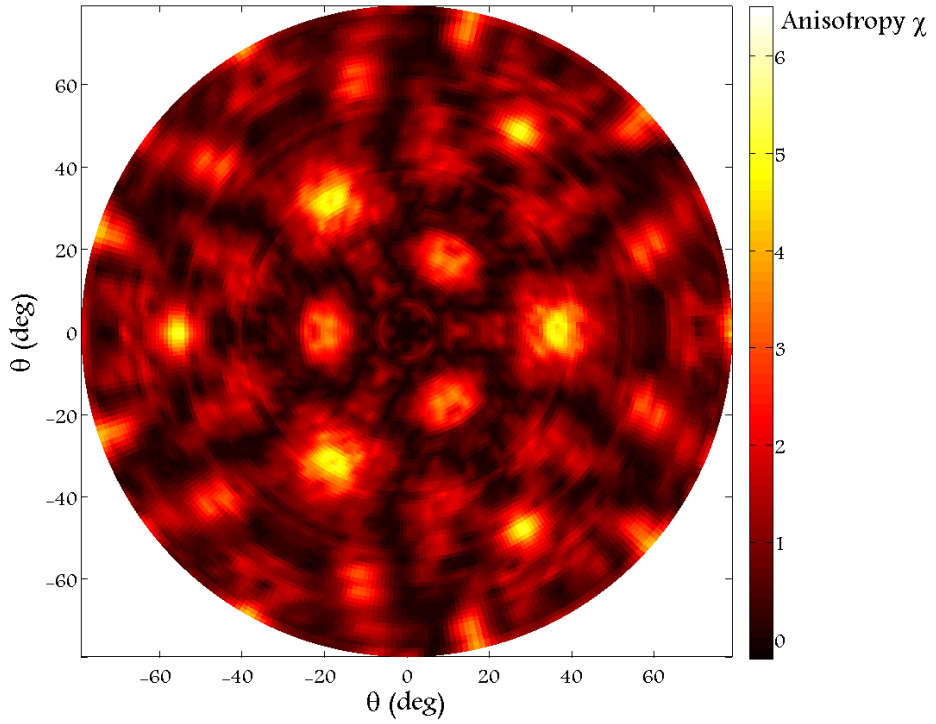

Figure 4: Simulated XPD pattern by means of the EDAC code of the system whose diffractive patterns are displayed in figure 3.

In the third chapter a numerical tool for determining the similarity between two patterns in a quantitative manner will be introduced. For now, the direct visual comparison suffices to conclude that the attained command of the EDAC software is good enough to investigate the systems of interest of this thesis.

References:

1. García de Abajo F. J. et al., Phys. Rev. B, 63, 075404 (2001)
2. Pendry J. B., *Low Energy Electron Diffraction*, Academic Press, London, (1974)
3. Lee P. A. and Pendry J. B., Phys. Rev. B 11, 2795 (1975)
4. Messiah A., *Quantum Mechanics*, North-Holland, New York (1966)
5. Chambon C. at al., Phys. Rev. B, 84, 165446 (2011)
6. Chen Y., et al., Phys. Rev. B 58, 13121 (1998).

Chapter II:
Components of the systems

Silicene

In 2010, Andre Geim and Konstantin Novoselov were awarded the Nobel Prize in Physics for their ground-breaking experiments regarding the two-dimensional material graphene[1]. Graphene is a two-dimensional material made of atoms of carbon arranged in a regular honeycomb pattern similar to the one of graphite. It's extremely light and tough, displaying a resistance 200 times greater than steel for a 5 times lower weight. Some other of its astounding properties are its flexibility, its transparency, the heat and electric conductivities, its reactivity etc.

Since the discovery of graphene, a great effort has been put in finding analogue two-dimensional materials made of elements from the group IV. The most immediate one would be a sheet of atoms of silicon, the so-called silicene. In 1994, Takeda and Shiraisi[2] proposed theoretically the plausibility of such a material and it was finally synthesised by several groups[3,4,5] within the last five years. Monolayer allotropes of germanium[6] and tin[7] have also been proposed, and they are attracting more and more attention lately as they have recently been synthetized and may also show interesting physical properties.

Although silicene shares several properties with graphene, there are also remarkable differences. Perhaps, the most immediate one is related to its production. While graphene is a natural allotrope of carbon and can be obtained simply by exfoliating it from graphite (even with adhesive tape), silicene does not exist in nature and has to be synthesised through more innovative ways. From its first synthesis, it is usually produced by an epitaxial growth of silicon on a Ag(111) substrate[3], though it is also possible to evaporate it on iridium[8] or ZrB_2[9].

The reason why silicene cannot be exfoliated lies on the hybridization of the orbitals. The sp^2 hybridization of carbon atoms (in graphite) along with their four valence electrons per atom favour the formation of weak π-bonds that involve the remaining p_z orbital which happens to be perpendicular to the graphene-like planes. These bonds can readily be broken to separate layers of graphene. On the contrary, the atoms of silicon are always sp^3-like hybridized. As a result, there's no material made of silicon akin to graphite, the structure is sustained by σ bonds and it's no longer possible to separate layers of silicene from a silicon sample. In the case of silicene obtained through epitaxial growth, the hybridization of atoms is somewhere between the two situations, as some of them present a superposition of sp^2/sp^3 orbitals, while the rest are purely sp^2-like hybridized[3].

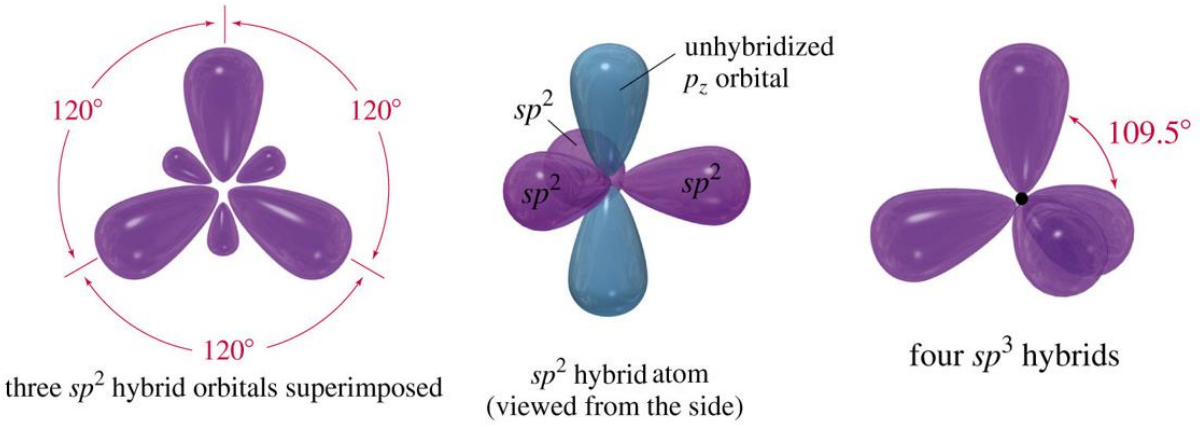

Figure 1: View of sp^2 and sp^3 hybridization

Although all the silicene samples analysed throughout this work lie on a Ag(111) substrate, it is worth introducing the Si/Ag systems in general, that is, Si patches grown on Ag(100), Ag(110) and Ag(111) surfaces as the former have been used as substrates before the latter and form better understood systems.

In any case, when depositing a semiconductor on a metallic surface (for instance Si and Ag respectively) there are three elements considered to play a fundamental role in the arrangement of the atoms: the relative surface stress of pure elements, the chemical interactions among them and the size mismatch of the chemical species.

Some systems give rise to surface alloys, such as the Si/Cu(110)[10]. 0.5 monolayers of Si atoms on a Cu(110) surface originate a $c(2 \times 2)$ superstructure. There, both chemical species are orderly intercalated on the last layer following the pattern included in figure 2.

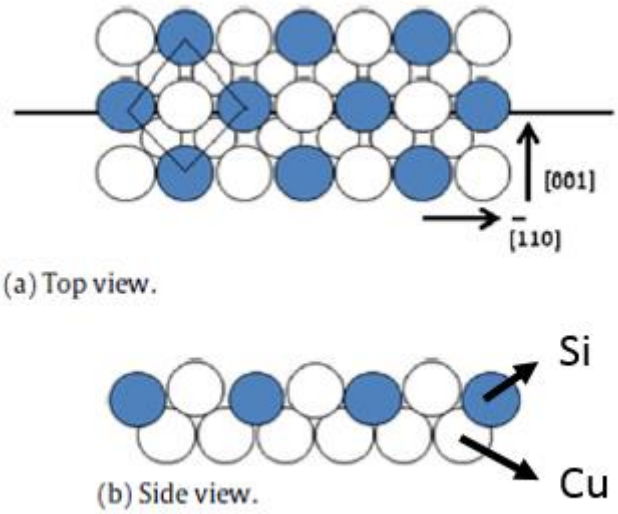

Figure 2: Structure of the Si/Cu(110) surface alloy[13]

The other usual tendency is the phase separation. In those systems, the atoms tend to surround themselves with as many analogue atoms as possible in a close-packed structure. One prototype that shows such a behaviour is Ge/Ag[11], and to a slightly lesser extent the subject of this discussion Si/Ag. Keeping this in mind, the following paragraphs will introduce briefly the three Si/Ag systems mentioned at the beginning of this page.

1. System Si/Ag(100)

The low solubility of Si in Ag contribute to the preference for the tendency to the phase separation. On the Ag(100) surface, the growth of a silicon monolayer at a temperature of about 230ºC induces the formation of a $p(3 \times 3)$ superstructure. Beyond that point, the long-range order vanishes and instead, the previous phase coexists with stripes of hexagons following [110] directions.

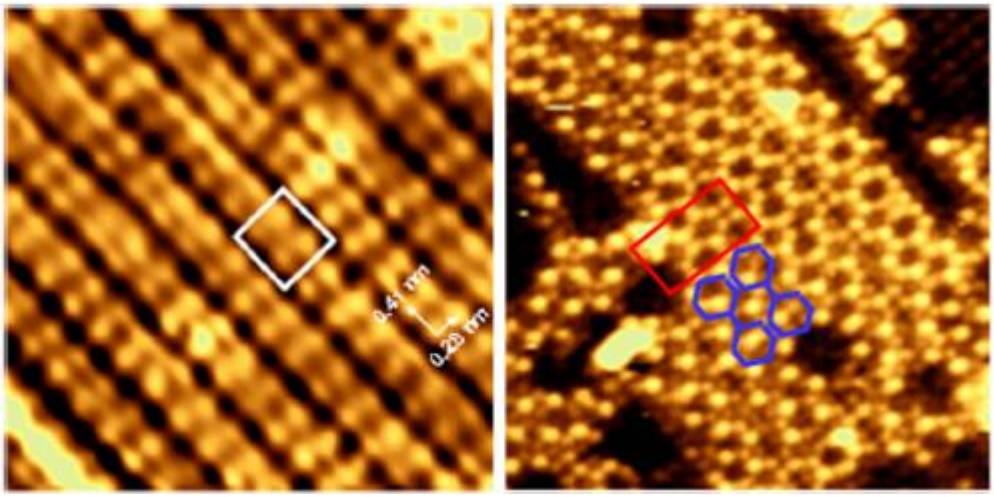

Figure 3. Left: Filled states STM image (6.4 nm × 6.1 nm, V=-1.02 V, I=1.14 nA) of the Si/Ag(100) system at monolayer coverage. The white rectangle indicates the unit cell. Right: Filled states STM image (6.4 nm × 6.4 nm, V=-1 V, I=1 nA) of the Si/Ag(100) system beyond one monolayer. The pattern of two joined chains of hexagons is drawn in blue.[12]

2. System Si/Ag(110)

When depositing silicon on a Ag(110) substrate below the monolayer coverage, the silicon atoms tend again to the phase separation in the form of nanowires[13] of silicon atoms following a honeycomb arrangement. These nanowires are assembled parallel to the [-110] direction of the silver, and they display a width equal to four times de lattice parameter of the silver (1.6 nm in total) and a height of 0.2 nm. Regarding their length, it lies in a large interval, ranging from 1.5 nm to even beyond 100 nm. Upon annealing, the shortest nanowires (which could be more accurately described as nanodots) usually disappear, or rather diffuse along the [-110] direction of the surface until they find a longer nanowire to cling to, hence extending it. This process has been captured in the figure 4.

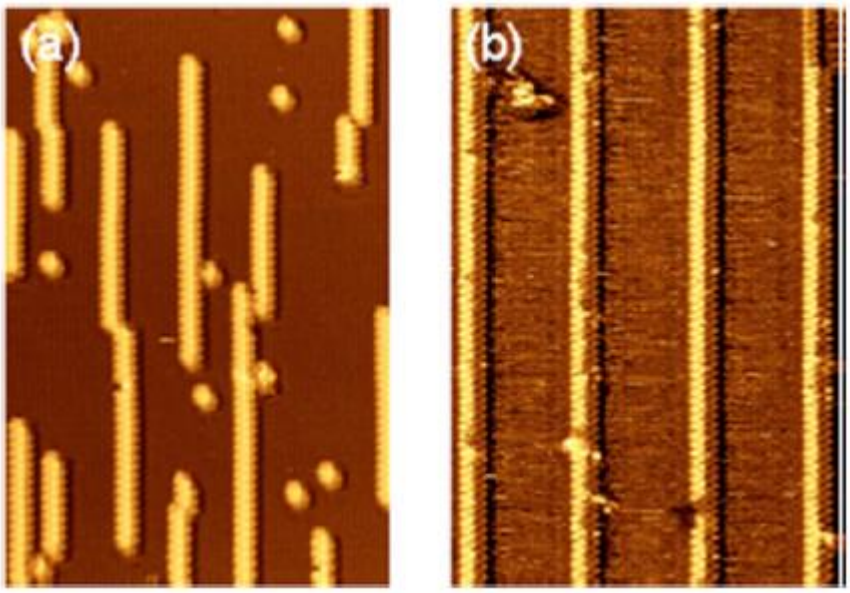

Figure 4: STM images (24.3 nm × 36.1 nm) of Si/Ag(110) at low coverage a) before annealing and b) after annealing. The lengthening of the nanowires as well as the disappearance of the shortest units are evident.[12]

After an evaporation of one monolayer of silicon, a 5×2 superstructure (apparent on the LEED pattern shown below) is revealed. In these conditions, the substrate is completely covered by the aforementioned nanowires with a regular spacing of 2.05 nm (five times the lattice parameter of the silver). The two-fold periodicity corresponds to the [-110] direction.

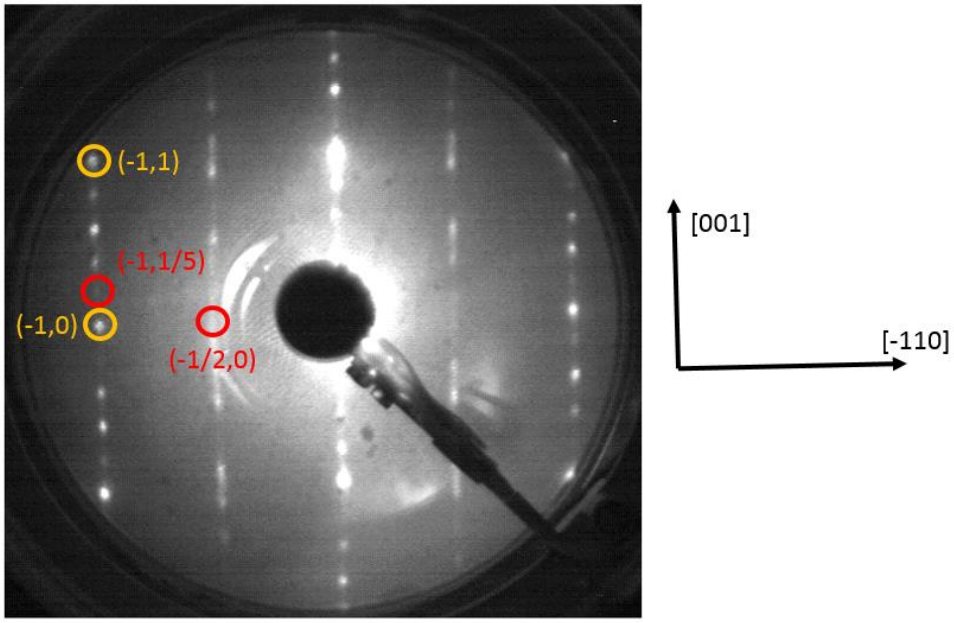

Figure 5: LEED pattern of Si nanowires on Ag(110). Energy of the electrons: 45.6 eV. The yellow circles indicate spots from the silver and the red ones spots from the silicon.

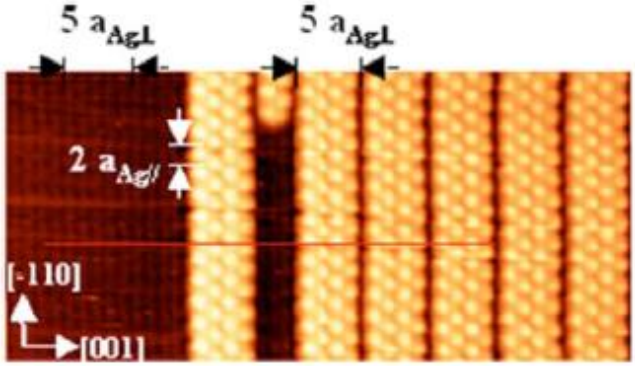

Figure 6: STM image (17.4 nm × 8 nm, -1.7 V, 0.3 nA) of one monolayer of Si nanowires on Ag(110)[12].

After more precise STM measurements and comprehensive Density Functional Theory calculations both the structure of the nanowires and their position relative to the substrate were discovered[14]. The ab initio simulations manifested a tendency of the Si atoms towards the adoption of a configuration with a notable buckling (0.2 nm). Such a feature explained perfectly the asymmetric STM profiles that had been observed before as well as some distortions in the substrate (noticeable only at one side of the nanowires). The coupling between the silicon and the substrate is linked to the existence of micrometric domains where the chirality (left-handed or right-handed) stays constant.

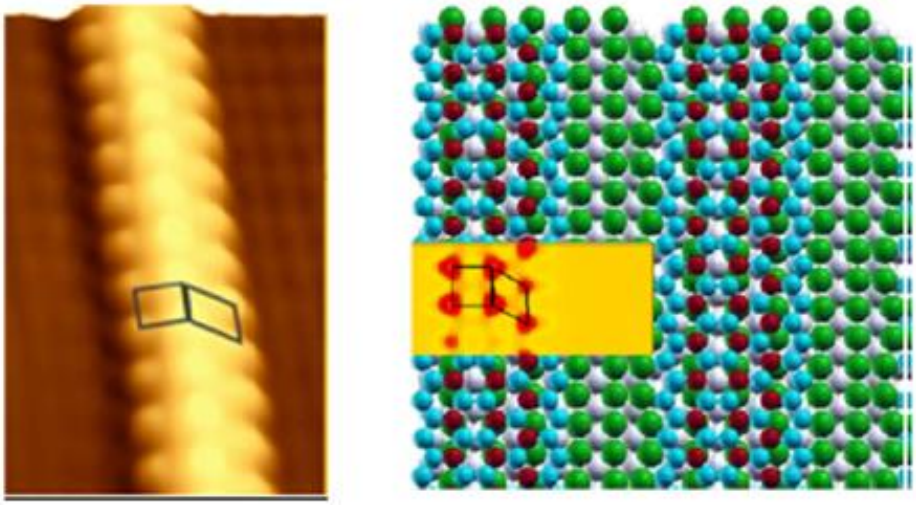

Figure 7. Left: 10.2 nm × 6.4 nm STM image of one silicon nanowire which evokes their asymmetry. Right: Structural model of the nanowires. Red and blue spheres represent Si atoms (upper and lower ones respectively). Green spheres correspond to Ag atoms in the last layer. The yellow detail emphasizes the origin of the structure shown on the STM images: the upper silicon atoms[12].

Regarding the electronic properties, Si nanowires are reported to have a metallic character expressed through their asymmetric Si 2p core levels, in particular, the peaks may be even more asymmetric than the Ag 3d ones from clean silver[13]. Interestingly, thicker nanowires with diameters between 1.3 and 7 nm obtained through chemical synthesis or lithographic patterning are semiconducting.

Furthermore, four new discrete electronic states particular to the nanowires (with binding energies between 0.9 and 3.1 eV) were detected due to the confinement into the nanowires[12] or possibly caused by edge effects.

Finally, the oxidation of this type of structures is possible but progressive. It starts at the ends of the nanowires and extends later along the [-110] direction, making the material semiconducting (with a small gap of 0.35 eV) in the process.

The previous structures present limited versions of the honeycomb arrangement seen in graphene. For this reason, after these surprising findings the scientific community turned its attention toward Ag(111) substrates, where it was expected that these structures could cover long-range distances.

3. System Si/Ag(111): Silicene (structural properties)

The deposition of Si on a Ag(111) substrate is more recent and has paved the way for the synthesis of silicene. Indeed, in 2012 several groups claimed the experimental production of silicene for the first time[3,4,5]. Different experimental techniques have revealed the formation of a buckled honeycomb lattice with atoms at two different distances from the substrate.

In any case, the preparation of silicene samples usually follows a common process that has to be carefully respected, since small variations of parameters such as the temperature, can lead to very different outcomes as it will be referred in the subsequent paragraphs.

In order to obtain Ag(111) substrates with the desired quality, they are subjected to Ar^+ ion bombardment (the usual procedure used for this thesis involves pressures around $5 \cdot 10^{-7}$ Torr and energies per ion between 0.6 and 3 keV) and then annealed at 700 K for 20 minutes under ultra-high vacuum conditions. The last step is the evaporation of the silicon atoms from a hot wafer while the sample is kept at a temperature around 200ºC.

If the guidelines are respected and the state of the substrate is good enough, the synthesis of the monolayer can be done in the conditions of the PIIM's laboratory within 20 minutes.

One common question at the very first stages of the research on silicene has been how similar the two-dimensional allotropes of silicon and carbon would be. The answer requires among other elements, a solid structural model.

The (4×4) reconstruction proposed by Vogt[3] has been deemed correct as it's not only robust from the DFT point of view, but it also successfully explains the LEED patterns, the STM images and more recently the reflection high-energy positron diffraction[15].

The figures below contain the basic information about the model[3].

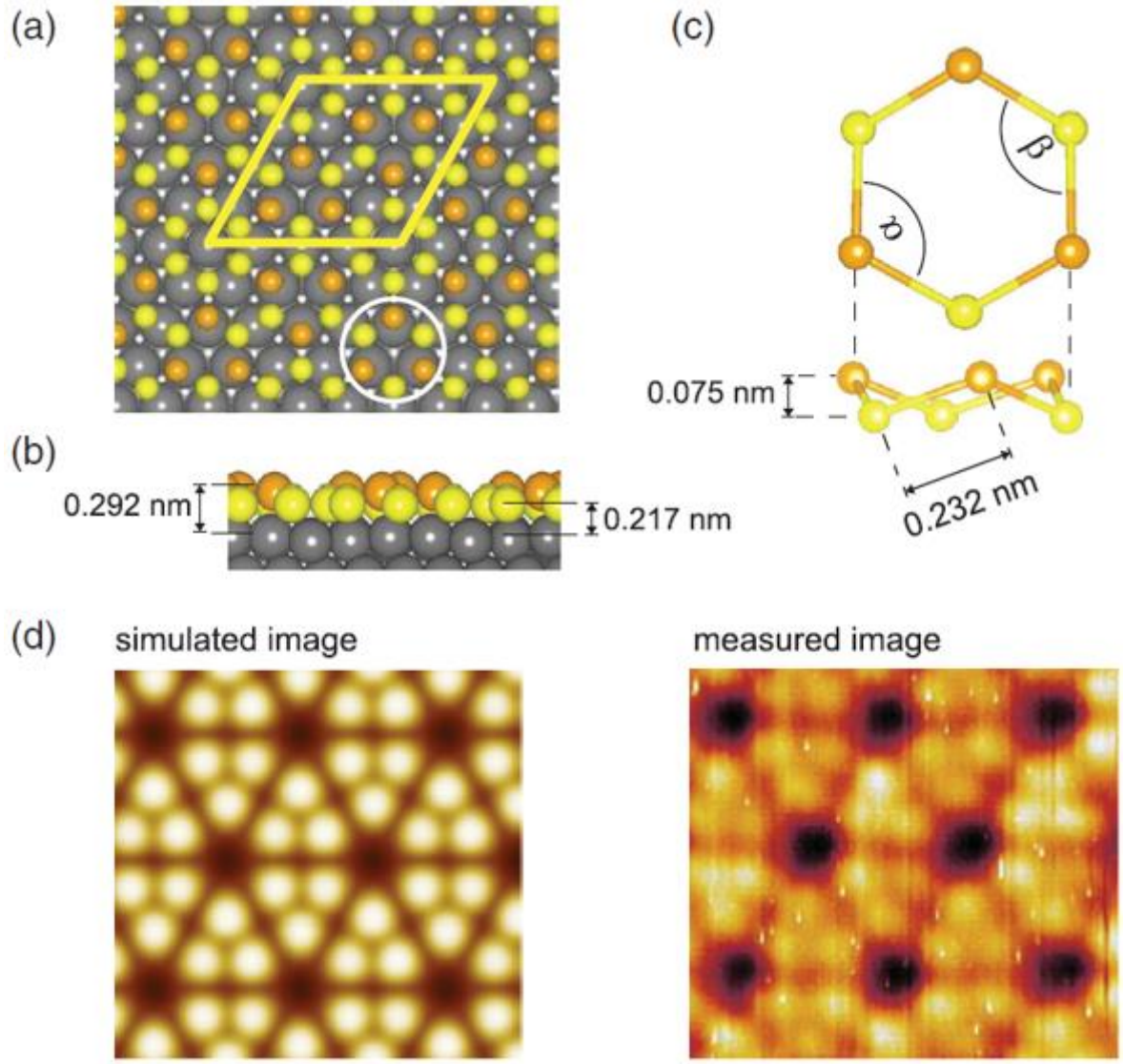

Figure 8. a) Top view of the structure of silicene on top of the last layer of Ag(111). The grey balls represent silver atoms, the yellow ones correspond to the lower silicon atoms and the orange spheres stand for the upper silicon atoms. The unit cell of silicene is enclosed in the yellow rhombus. b) Side view of silicene. c) Detail of the geometry of the hexagon surrounded by the white circle. d) Simulated STM image of the model (left) and actual STM image of the monolayer silicene (right).

As it's evident, the Si atoms lie on two parallel planes separated by 0.075 nm giving rise to the buckling of silicene. The experimental Si-Si distance is measured to be about 0.22 nm, which is slightly shorter than the equivalent distance in bulk silicon (0.235 nm).

The difference in height induces also differences in the bond angles. In effect, if one unit cell is considered, the six upper atoms display bond angles of 110º (α in figure 8), which could be interpreted as sp^3-like since the theoretical value for them is 109.5º. As for the lower atoms, six of them are purely sp^2-like hybridized (bond angle = 120º) whereas the remaining six atoms show bond angles between 112º and 118º (β in figure 8), therefore revealing a hybridization somewhere between sp^2 and sp^3-like orbitals.

As it was mentioned before, small changes in the parameters (temperature, coverage, state of the surface…) can produce different results. For a low coverage Arafune[5] stated that there seems to be a unique phase (of course only if any long-range order is attained): the (4×4). If the epitaxy is not stopped after monolayer completion, the system evolves being able to adopt a plethora of new arrangements such as: $\left(\sqrt{13} \times \sqrt{13}\right)R13.9°$, $\left(\sqrt{3} \times \sqrt{3}\right)R30°$, (3.5×3.5) etc. The following figure[5] summarises the possibilities as a function of the coverage and the temperature.

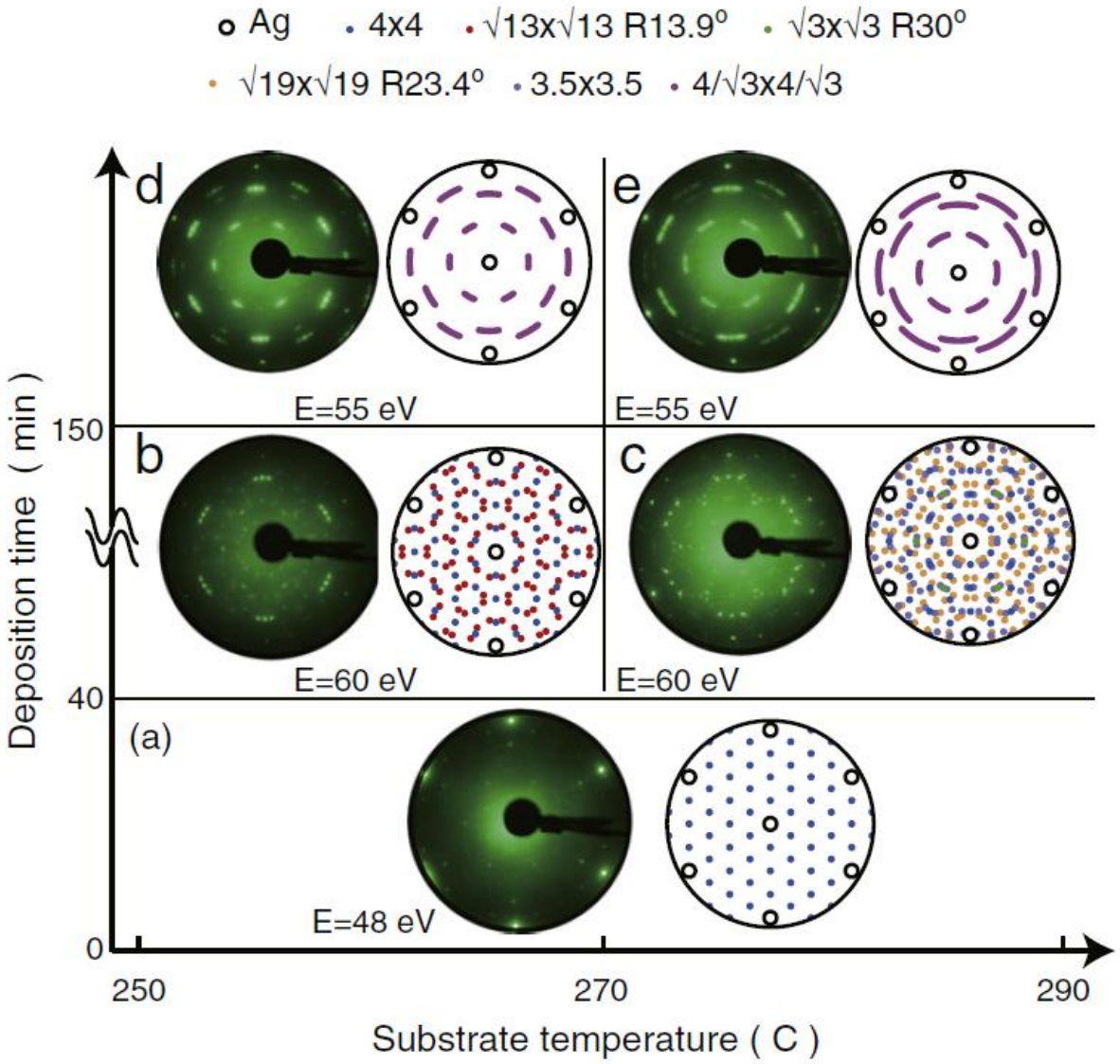

Figure 9: LEED patterns of silicene samples as a function of both the temperature of the substrate during the epitaxial growth and the coverage. On the right side of each cell the simulated LEED patterns of the identified phases are shown for comparison.

The image below[16] emphasizes the coexistence of multiple phases of silicene in a small zone of one sample. This strongly supports the fact the minimal differences in the evaporation conditions can trigger the formation of distinct phases.

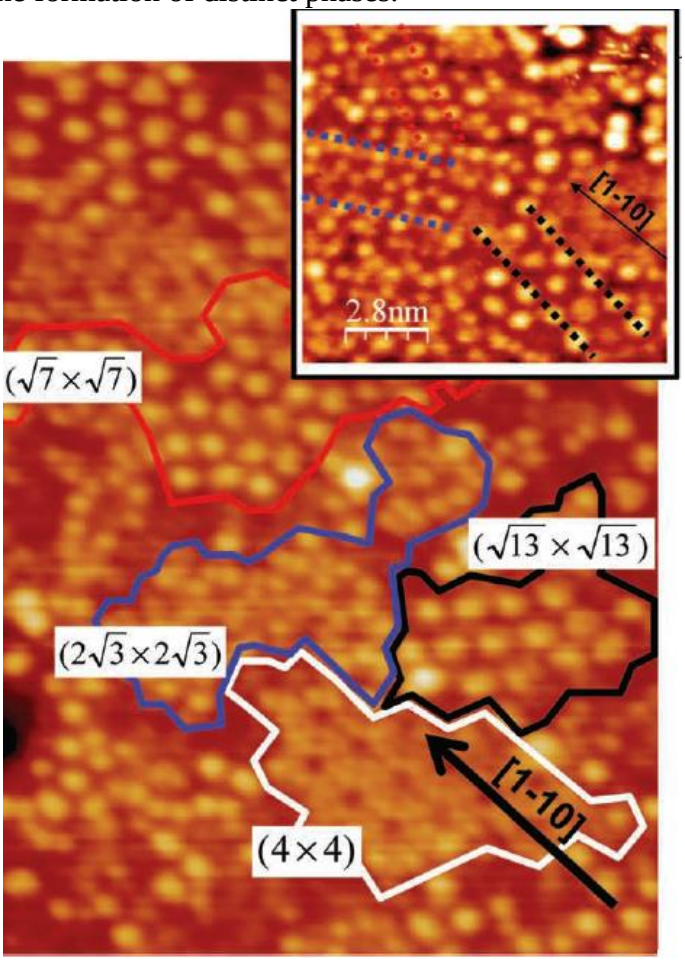

Figure 10: STM image (16.3 nm × 20.6 nm, V = -1.5 V, I = 0.2 nA) of silicene displaying different phases. The square in the upper right corner stresses the different orientations of several domains.

If the coverage is increased significantly (beyond the second or third layer) the system starts becoming "less two-dimensional" and some of its properties change. From this point, the material will be considered multilayer or thick silicene.

The characteristic phase is the $(\sqrt{3} \times \sqrt{3})R30°$, although it appears with four additional possible orientations that can be obtained by performing rotations of $\pm 5°$ and $\pm 33°$ on the original geometry. Salomon[17] showed that those orientations are due to the structural properties of the initial wetting monolayer. So even if the last layer would display a $(\sqrt{3} \times \sqrt{3})$ reconstruction, the geometry of the first layer of silicene would have an impact on the orientation of the last layer.

Actually there is an open debate on the nature of multilayer silicene. The most direct assumption is a "complete" $(\sqrt{3} \times \sqrt{3})R30°$ silicene. However, Fu[18] has recently claimed that by adding more layers on bilayer silicene, the diamond bulk Si structure spontaneously forms, and that the only remnant from silicene lies in the last layer, which displays nonetheless a weak buckling responsible for the $(\sqrt{3} \times \sqrt{3})$ surface arrangement. There are also articles that claim that thick silicene is in fact bulk Si(111) with a Ag $(\sqrt{3} \times \sqrt{3})R30°$ surface reconstruction. A recent article by De Padova[19] accepted for publication claims that all those scenarios are possible depending on the growth conditions, being the temperature the most important parameter.

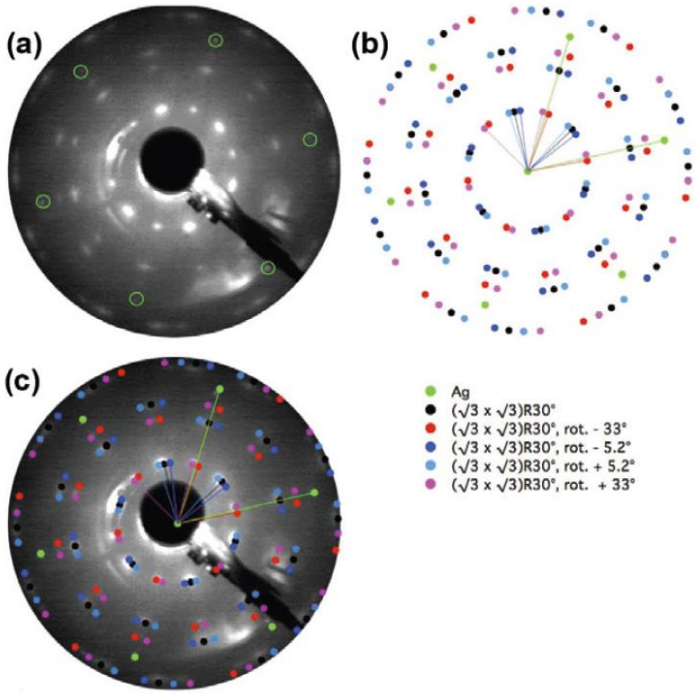

Figure 11. a) Experimental LEED pattern of silicene's $(\sqrt{3} \times \sqrt{3})$ reconstruction. The Ag spots are indicated with the green circles. b) Simulated LEED pattern of the system Ag(111) + multilayer silicene with all its possible orientations. c) Superposition of the expected pattern with the experimental one. The colour code identifies the spots due to the different orientations[17].

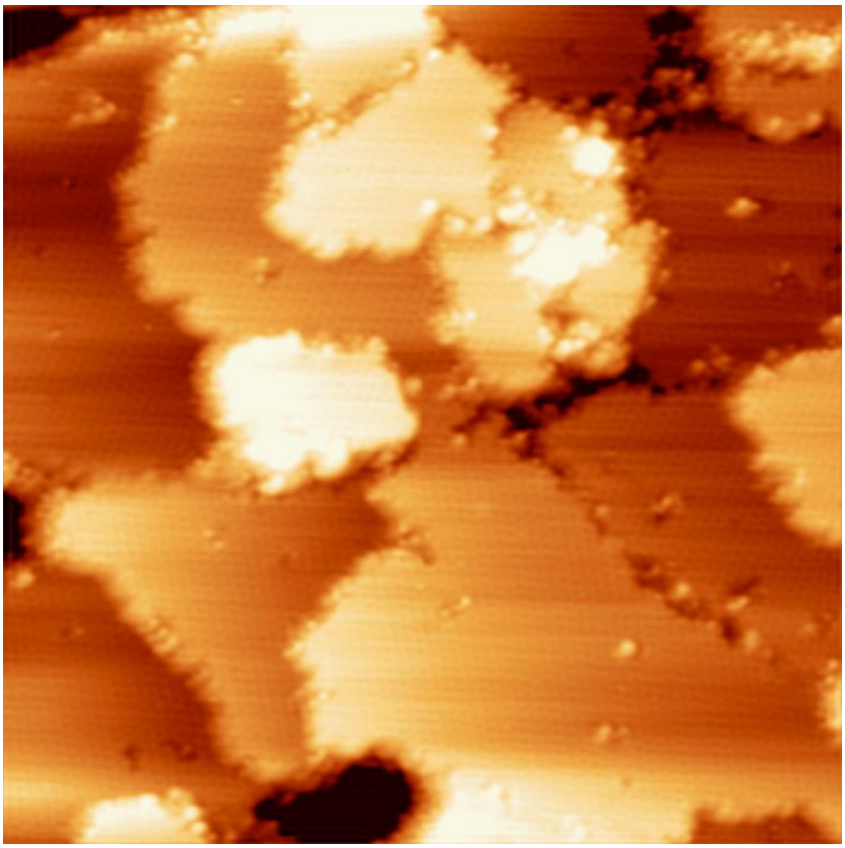

Figure 12a: STM image of multilayer silicene $(\sqrt{3} \times \sqrt{3})$, 50nm×50nm, V = -2.2 V (filled states), I_t = 0.19nA

From a closer distance, the unit cell can be seen more easily. The following figure includes a high resolution image of the surface and profiles measured along selected directions.

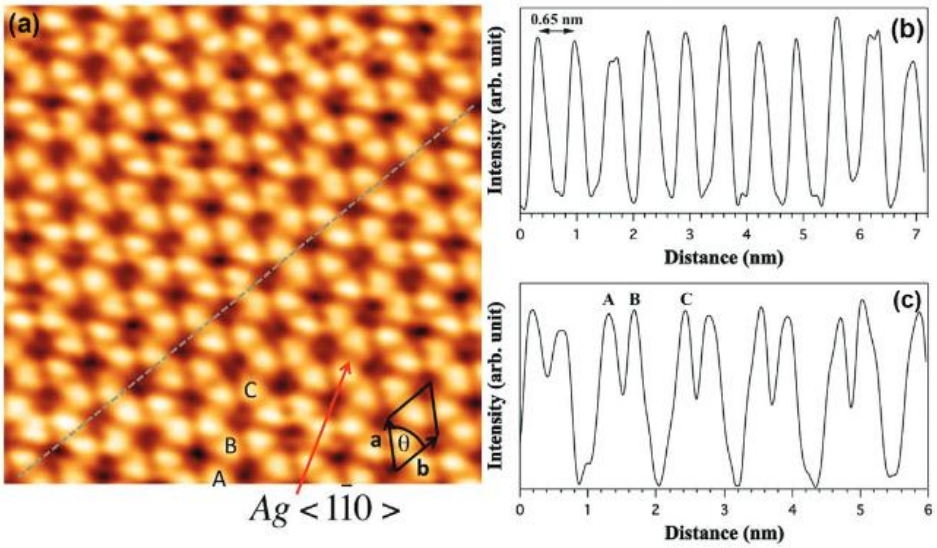

Figure 12b: a) 5.7 nm × 5.7 nm high resolution STM image of multilayer silicene. Tunnelling parameters: I_t= 0.16 nA, V = -560 mV (occupied states). The unit cell appears highlighted by the black rhombus. b) Topography profile along the dashed grey line on the image. c) Topography profile along the Ag [$1\bar{1}0$] direction.

4. Electronic properties of silicene

Many of the outstanding characteristics of silicene are related to its electronic bands. One of the most often referred facts about silicene is the existence of the Dirac cone, which implies the presence of "massless" Dirac fermions as a result of the linearity of the bands near the Fermi level. The figure below[3] shows the Dirac cone of monolayer silicene.

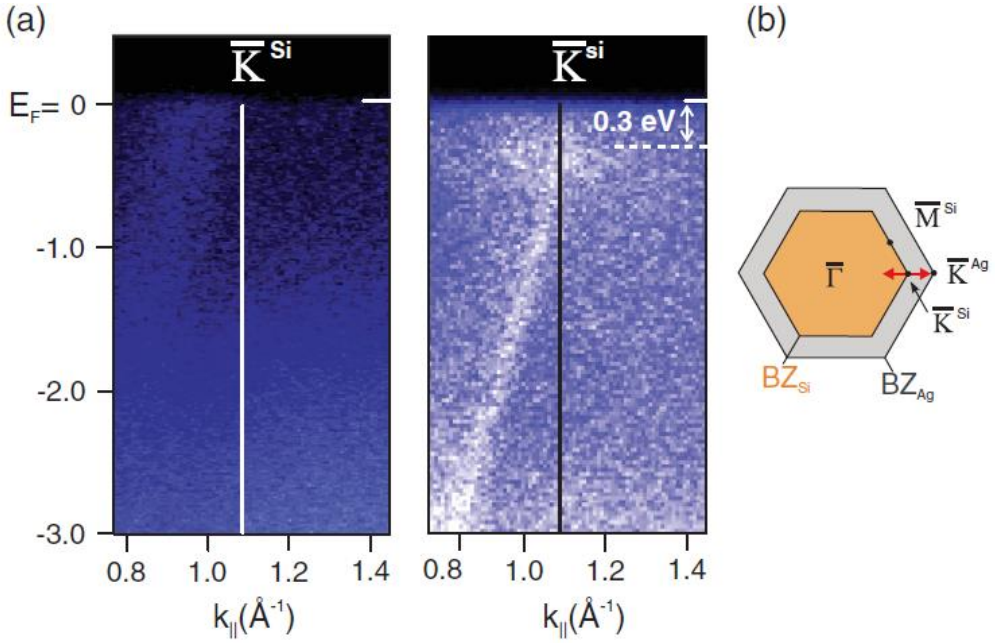

Figure 13: a) ARPES intensity map of a clean Ag(111) surface (left) and after the formation of the 2D Si adlayer (right), taken along the Ag Γ–K through the silicene K (E = 126 eV). (b) Brillouin-zone scheme of the Si layer with respect to the Ag (111)-(1×1) surface. The red arrows indicate the ARPES measurement direction

Vogt[3] estimated a Fermi velocity around $1.3 \cdot 10^6$ m/s for the electrons, comparable to the one measured in graphene. In the same work, the sp states from the silver substrate were proposed as the origin of the linear dispersion, however, this topic is still controverted. Cahangirov[20] stated that the phenomenon arises from the combined hybridization of Ag and Si, since those states don't exist on the clean substrate and become parabolic on freestanding silicene according to their DFT calculations. Similarly, Gori[21] argued that the Dirac cone is due to the silver substrate, appearing as an effect of band folding induced by the Si overlayer periodicity. Requist[22] has proposed that these band structures can also be obtained by depositing Ag on a Au(111) substrate. This leads to the appearance of surface states which involve the deeper d orbitals. It has even been claimed that the Dirac cone exists only for freestanding silicene and it fades out because of the delocalisation of the involved states when a supporting substrate is added[23]. Any robust conclusion on this topic will need further investigation in the future.

There seems to be a greater consensus on the electronic gap of different materials that involve silicene. Whether the band structure be obtained by means of DFT calculations[20] or with some other methods (for instance tight-binding theory[12]), the values of the gap appear to be less controverted even if all the available values so far are theoretical.

Indeed, freestanding or unsupported monolayer silicene is reported to be a gapless material. The valence and conduction bands are predicted to be in contact only through the Dirac cone's vertex, whence its appeal for fast microelectronic applications. The figure 14 illustrates this information[20].

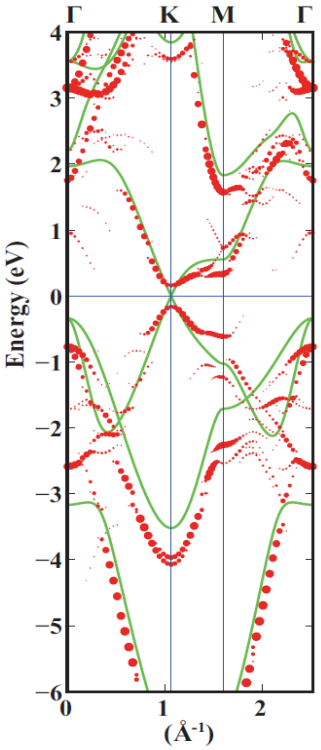

Figure 14: Bands of freestanding (4×4) silicene unfolded to the Brillouin zone of (1×1) silicene indicated by the red dots. The band structure of ideally buckled silicene is shown by the green curves.

As for the silicene monolayer grown on an Ag(111) substrate, from ARPES measurements Vogt[3] estimated a gap of approximately 0.6 eV. One additional effect of the presence of the Ag(111) substrate on silicene is the likely charge transfer from the former to the latter, which is considered to be of 0.5 electrons per (4×4) supercell[20].

Finally, nearly parallel to the discovery of silicene, there have been some proposals for functionalizing it by adding some chemical species to the surface, being the easiest and most immediate one the hydrogenation. Such a procedure when performed on freestanding silicene is supposed to produce the so-called silicane, which is thought to have an indirect gap (contrary to the previous cases) between 3 and 4 eV[12].

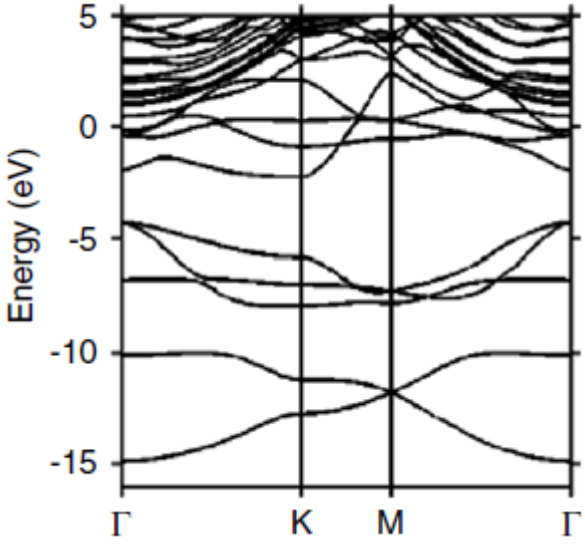

Figure 15: The band structure of hydrogenated freestanding silicene obtained by means of the DFT-LDA method[13].

References:

1. Geim A. K. and Novoselov K. S., Nature Materials 6, 183 - 191 (2007)
2. Takeda K. and Shiraishi K., Phys. Rev. B, 50, 14916 (1994)
3. Vogt, P. et al., Phys. Rev. Lett. 108, 155501 (2012)
4. Lalmi, B. et al., Appl. Phys. Lett., 97, 223109 (2010)
5. Arafune, R. et al., Surface Science, 608, 297–300 (2013)
6. Houssa, M. et al., Appl. Phys. Lett. 96, 082111 (2010)
7. Balendhran, S., et al., *Elemental Analogues of Graphene: Silicene, Germanene, Stanene, and Phosphorene*. Small, 11: 640–652. doi:10.1002/smll.201402041 (2015)
8. Meng, L. et al., Nano Letters, 13 (2), 685–690 (2013)
9. Fleurence, A. et al., Phys. Rev. Lett., 108 (2012)
10. Polop C. et al., Surf. Sci. 402-404, 245–248 (1998)
11. Olesinski, R.W. and Abbaschian G.J., Bull. Alloy Phase Diagr. 9 59 (1988)
12. Kara, A. et al., Surf. Sci. Reports, 67, 1–18 (2012)
13. Léandri C. et al., Surf. Sci. 574 (2005)
14. Kara, A. et al., J.Phys.: Condens. Matter 22, 045004 (2010)
15. Fukaya Y., et al., Phys. Rev. B 88, 205413 (2013)
16. Chiappe, D. et al., Adv. Mater., 24, 5088–5093 (2012)
17. Salomon, E. et al., J. Phys.: Condens. Matter 26, 185003 (2014)
18. Fu, H. et al., Nanoscale, 7, 15880 (2015)
19. De Padova, P. et al, to be published in 2D materials.
20. Cahangirov, S. et al., Phys. Rev. B 88, 035432 (2013)
21. Gori, P. et al., J. Appl. Phys. 114, 113710 (2013)
22. Requist, R. et al., Phys. Rev. B 91, 045432 (2015)
23. Mahatha, S. K. at al., Phys. Rev. B89, 201416(R) (2014)

Molecules involved in the experiments

With the aim of elaborating and studying two-dimensional materials and interfaces, different molecules have been evaporated on the used substrates (namely silver and silicene surfaces). The following pages will briefly introduce the molecules involved in the experiments: the 2,3,5,6-tetrafluoro-7,7,8,8-tetracyanoquinodimethane (F_4TCNQ) and the cobalt phthalocyanine (CoPc).

1. Cobalt phthalocyanine

After their first synthesis at the dawn of the 20th century, phthalocyanines (as a family of molecules) have been mainly used in the industry of dyes. However they have also found a place in numerous domains ranging the chemical sensors to photovoltaic cells and photodynamic reagents for cancer therapy.

The phthalocyanines (tetrabenzotetraazaporphyrin) were synthesised for the first time in 1907 by Braun and Tcherniac[1] through the heating of o-cyanobenzamide to a high temperature. It would still take 25 additional years to understand the structure of both the metal-free phthalocyanine and the metallophthalocyanines[2,3].

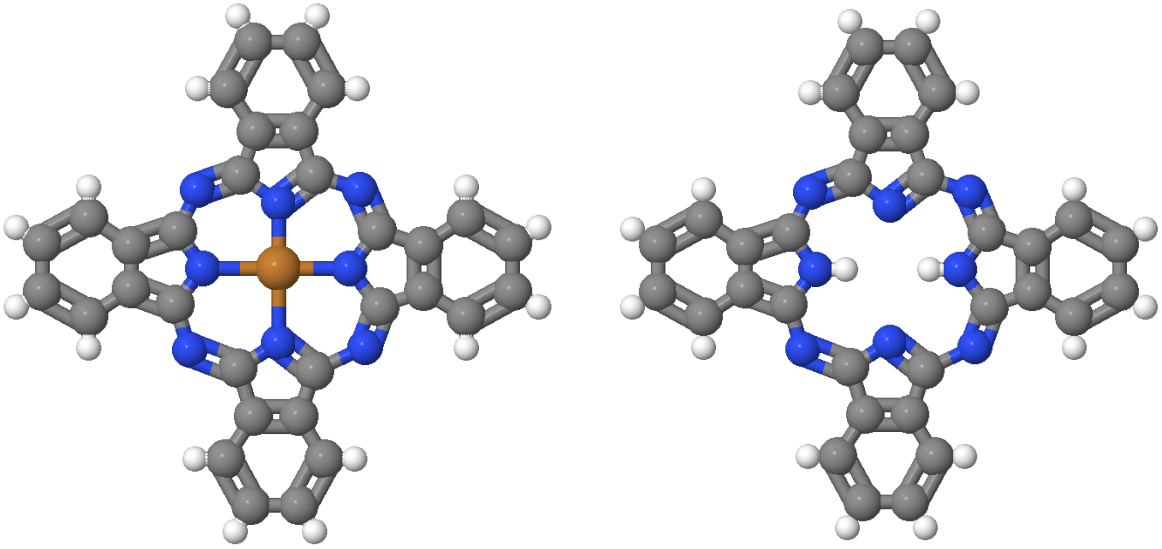

Figure 1: Top view of a metallophthalocyanine (left) and a metal-free phthalocyanine (right). The colours of the spheres are linked to the different chemical species (white: H, blue: N, grey: C and brown: a metal, for example Co).

The phthalocyanines are formed from four units of isoindole connected among them through atoms of nitrogen giving rise to an aromatic macrocycle. At the centre there can be either two atoms of hydrogen, one metallic atom or a more complex species such as $Si(OH)_2$. The structure of the macrocycle is supported by covalent bonds whilst the bonds with an eventual metallic centre are at least partially ionic. In that case, the metal tends to transfer two electrons to the rest of the molecule, so the oxidation states would read $M^{2+}Pc^{2-}$.

The CoPc molecule, like most of the metallophthalocyanines, is considered to be flat and belong to the D_{4h} symmetry group[4] although its geometry could change upon the adsorption on a substrate. This might produce a slight displacement of the central atom out of the plane of the molecule effectively lowering the symmetry group to C_{4v}.

Regarding the formation of layers, the cobalt phthalocyanines stack within columns forming two main phases[5] whose difference lies on the stacking angles (the angle between the surface and the line that connects equivalent atoms from two consecutive layers). Indeed, the so-called α-phase CoPc displays a stacking angle of 65.8º and is metastable, whereas the more stable β-phase stacks with an angle of 42.9º.

1.a) Synthesis

The very first synthesis of phthalocyanine was performed by heating o-cyanobenzamide in refluxing ethanol. The reaction produced a bluish substance (the molecule) in low yield. After that, about ten different mechanisms were also conceived for synthesising phthalocyanine. The most usual precursors are phthalonitrile, 1,3-diiminoisoindoline and phthalic anhydride. One of the most common schemes[6] is the synthesis of CoPc performed by reacting finely divided cobalt metal with phthalonitrile in ethylene glycol at 190ºC. This procedure doesn't provide the highest yield but the purification of these chemical species has been thoroughly studied and satisfactorily mastered.

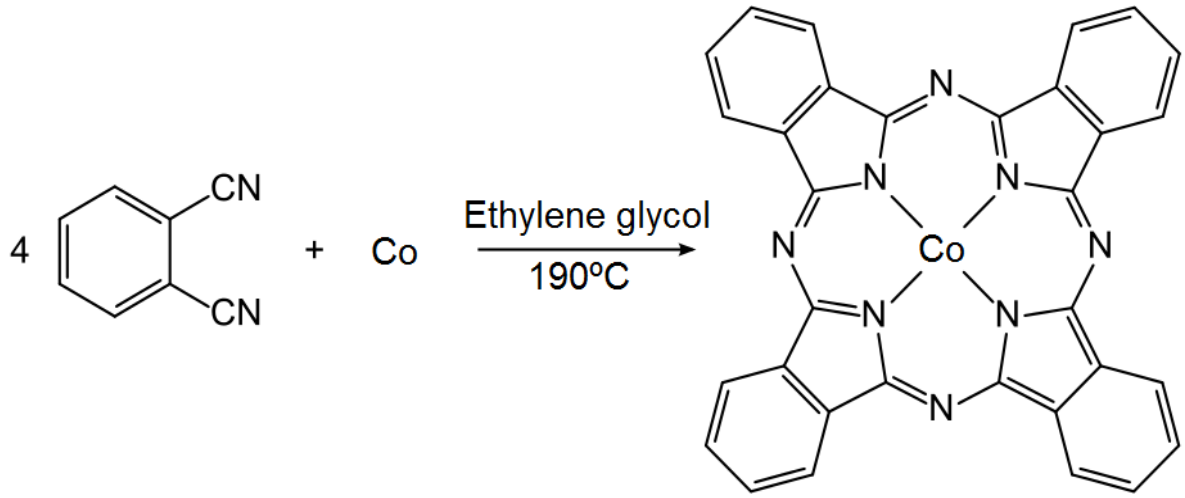

Figure 2: Typical synthesis of cobalt phthalocyanine from phthalonitrile.

The most usual methods to purify the unsubstituted phthalocyanines are the sublimation and the dissolution in sulphuric acid followed by precipitation on ice. None of them is normally suitable for organic compounds but they work for unsubstituted phthalocyanines because these compounds are generally extremely stable to strong acid and high temperatures (up to 550ºC). Finally, although most of these molecules are rather insoluble, some of them can still be purified by extraction and recrystallization with the help of sulphuric acid or in the least favourable cases, organic solvents.

1.b) Vibrational characterization

A significant part of the results of this thesis is related to the vibrational spectrum of CoPc. A useful technique to have access to the normal modes of vibration of a molecule would be an absorption spectrum in the range of infrared (IR) wavelengths. The following figure[7] shows such a spectrum of CoPc.

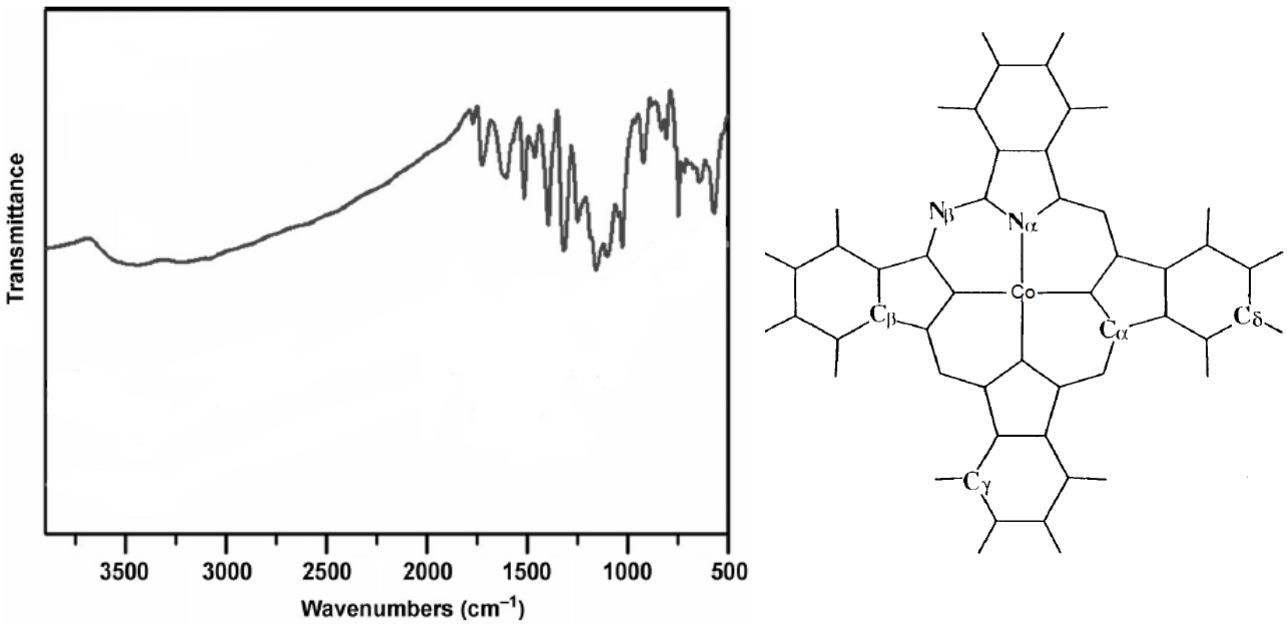

Figure 3: Typical IR absorption spectrum of CoPc (left) and atom designations for the identification of the vibrational modes[7]

The main features of CoPc's IR spectrum have been included in the following table from several works on IR and HREELS spectroscopy, as well as from some theoretical calculations[8,9].

Wavenumber (cm^{-1})	Energy (meV)	Type of vibration
436	54	C_β, C-H, N_β out of plane
725	90	Out of plane C-H deformation
742	92	Out of plane C-H deformation
770	95	C-N-C deformation
880	109	C-C-C from benzene, C_α and N_α out of plane
980	121	In-plane C=N and C=C stretching
1059	131	In-plane C-H deformation
1079	134	In-plane C-H deformation
1115	138	In-plane C-H deformation
1160	144	C-C-C from benzene, H-C-C
1280	159	C-C from benzene, H-C-C, C_β
1330	165	Out of plane C-C deformation
1480	184	Out of plane C-C deformation
1512	187	C-N_α and C-N-C
1555	193	H-C-C, C-C and C-C-C from pyrroles
1601	198	C-C from pyrroles, C-N-C

Wavenumber (cm^{-1})	Energy (meV)	Type of vibration
1712	212	C-C-C from pyrroles and benzenes, C-N
1741	216	C-C from benzenes, pyrroles bending
1768	219	C-C from benzenes, pyrroles bending, N_β

Table 1: Main vibrational modes of CoPc

1.c) Electronic characterization

Any general description of the CoPc molecule should include some information about its electronic structure. The figure below[10] shows one absorption spectrum of CoPc dissolved into ortho-dichlorobenzene. The peaks that appear on it correspond to missing photons absorbed by the solution to promote allowed electronic transitions between close molecular orbitals.

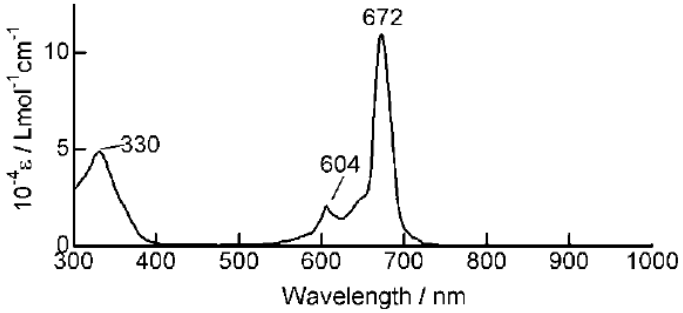

Figure 4: Electronic absorption spectrum of CoPc dissolved in ortho-dichlorobenzene.[10]

The distinguishable features of the spectrum are classified according to a nomenclature of the underlying bands[11]. The following figure and table summarise respectively the molecular orbitals and the spectroscopic bands associated to the CoPc molecule.

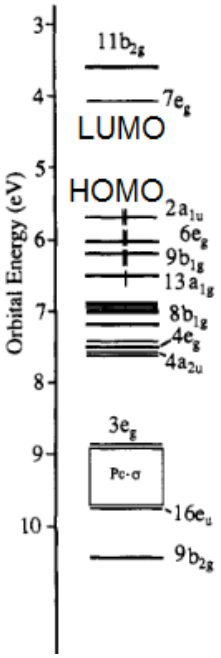

Wavelength (nm)	Energy (eV)	Band	Type and transition
672	1.8	Q	$\pi(C) \rightarrow \pi(C, N, d_z)$ $2a_{1u} \rightarrow 7e_g$
604	2.1	Extra band	$\pi(C, N_b) \rightarrow \pi(C, N, d_z)$ $5a_{2u} \rightarrow 7e_g$
415	3.0	Extra band	$\pi(C) \rightarrow \pi(C, N, d_z)$ $2b_{2u} \rightarrow 7e_g$
313	3.9	B	$\pi(d_z) \rightarrow \pi(C, N_p)$ $6e_g \rightarrow 4b_{1u}$
274	4.5	Extra band	$\pi(C) \rightarrow \pi(C, N_p)$ $5e_g \rightarrow 4b_{1u}$
240	5.2	L	$\pi(C) \rightarrow \pi(C)$ $2b_{2u} \rightarrow 8e_g$
210	5.9	C	$\pi(d_z) \rightarrow \pi(C)$ $6e_g \rightarrow 3a_{1u}$

Figure 5 and table 2: Energy level scheme of CoPc (left) and main spectroscopic bands caused by electronic transitions between the molecular orbitals (right). The extra bands are missing on the H_2Pc spectrum. N_p: pyrrolic nitrogen, N_b: bridge nitrogen, d_z: d_z orbital from the Co atom, Pc-σ: In-plane orbitals without significant contribution from cobalt.

The so-called "Q band" around 1.8 eV is caused by the least energetic possible transition from the Highest Occupied Molecular Orbital (HOMO) to the Lowest Unoccupied Molecular Orbital (LUMO). This value is the optical gap associated to the molecule.

2. F_4TCNQ

F_4TCNQ is an abbreviation for the organic molecule 2,3,5,6-tetrafluoro-7,7,8,8-tetracyanoquinodimethane. It is one of the most efficient electron acceptors[12], and that fact is exactly the reason why it has taken part in some of the results included in this thesis. Substituted 7,7,8,8-tetracyanoquinodimethanes are usually synthetized following the methods included in the first documents on the matter, some DuPont patents[13] whose most common precursors are p-xylylene dihalides.

The structure of the molecule according to ab-initio calculations belongs to the D_{2h} symmetry group[12]. Its main features are four electron-withdrawing cyanide groups attached to the terminal carbons, and four highly electronegative fluorine atoms linked to the central benzene ring. The molecule also displays a significant distortion that strengthens the charge transfer so as to make the ring more stable. The figure below is a simple sketch of the molecule.

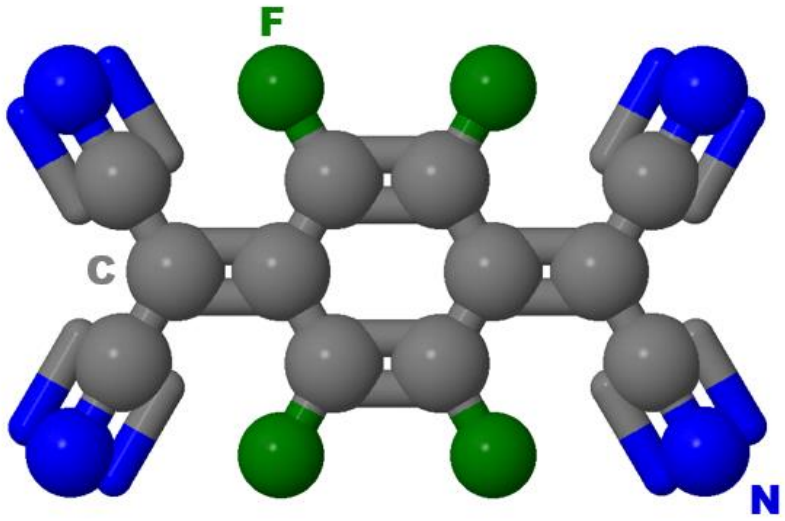

Figure 6: Chemical structure of the F4TCNQ molecule

2.a) Synthesis

The synthesis of F_4TCNQ usually starts with hexafluorobenzene. In order to obtain this first reagent, an electrophilic chlorination of benzene is performed with the necessary participation of a suitable catalyst such as ferric chloride ($FeCl_3$).

The following stage consists in the preparation of hexafluorobenzene. This is achieved by means of the anhydrous action of KF on C_6Cl_6 in an autoclave at around 475ºC without any solvent[14]. The reaction evolves according to the mechanism:

$$C_6Cl_6 \rightarrow C_6Cl_5F \rightarrow 1{,}3-F_2C_5Cl_4 \rightarrow 1{,}3{,}5-F_3C_6Cl_3 \rightarrow 1{,}2{,}3{,}5-F_4C_6Cl_2 \rightarrow C_6ClF_5 \rightarrow C_6F_6$$

Once the perfluorobenzene has been synthesised, the subsequent step is the nucleophilic displacement of two opposed fluorine atoms by the tert-butyl malonitrile anion. A further thermolysis of the products will produce the loss of isobutylene and the process is concluded with a last oxidation by bromine[15]. The scheme of these last stages in the production of F_4TCNQ is shown in the following figure:

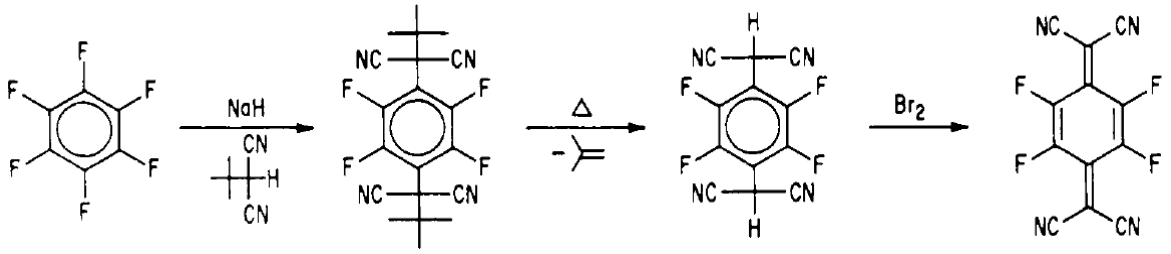

Figure 7: Synthesis of F_4TCNQ from hexafluorobenzene

2.b) Vibrational characterization

The vibrational normal modes of this molecule can again be accessible through an infrared spectrum. The following figure[16] shows such a spectrum of neutral F_4TCNQ.

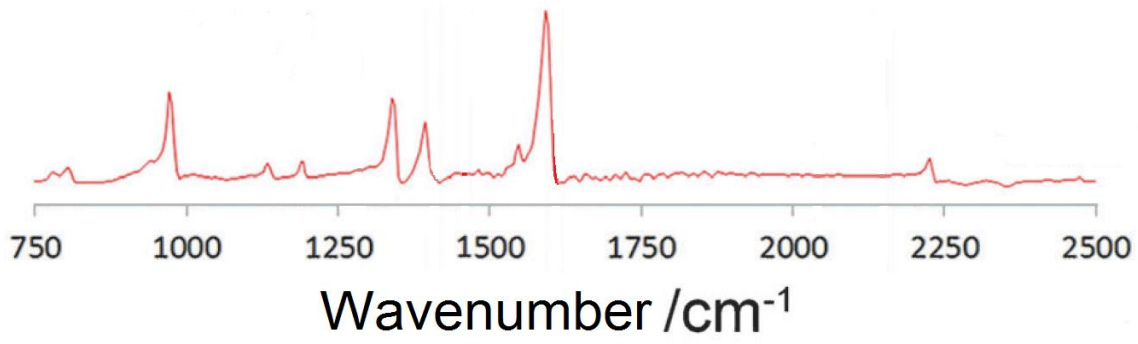

Figure 8: Infrared spectrum of F_4TCNQ[20]

The identification of the features[17] is possible with the help of the following table, which includes the most prominent normal modes of the molecule among all the existing ones.

Mode	Wavenumber (cm^{-1})	Description
1	775	Ring substituent bend
2	804	Ring mode
3	886	Ring stretch
4	988	Ring stretch
5	1142	Ring stretch
6	1150	Ring stretch
7	1194	C-CN stretch
8	1192	C-CN stretch
9	1305	C-F and ring C-C stretch
10	1358	C-F and ring C-C stretch
11	1390	C-F and ring C-C stretch
12	1452	C-F and ring C-C stretch

Mode	Wavenumber (cm^{-1})	Description
13	1485	Exocyclic C=C stretch
14	1553	Exocyclic C=C stretch
15	1608	Ring C=C stretch
16	1679	Ring C=C stretch
17	2213	C≡N stretch
18	2214	C≡N stretch
19	2231	C≡N stretch
20	2234	C≡N stretch

Table 3: Main normal modes of F_4TCNQ (see figure 8)

The figure below depicts the motion of the molecule for each normal mode included in the previous table. The blue diamonds indicate the equilibrium positions of the atoms while the red circles show the amplitude and the direction of the vibrations.

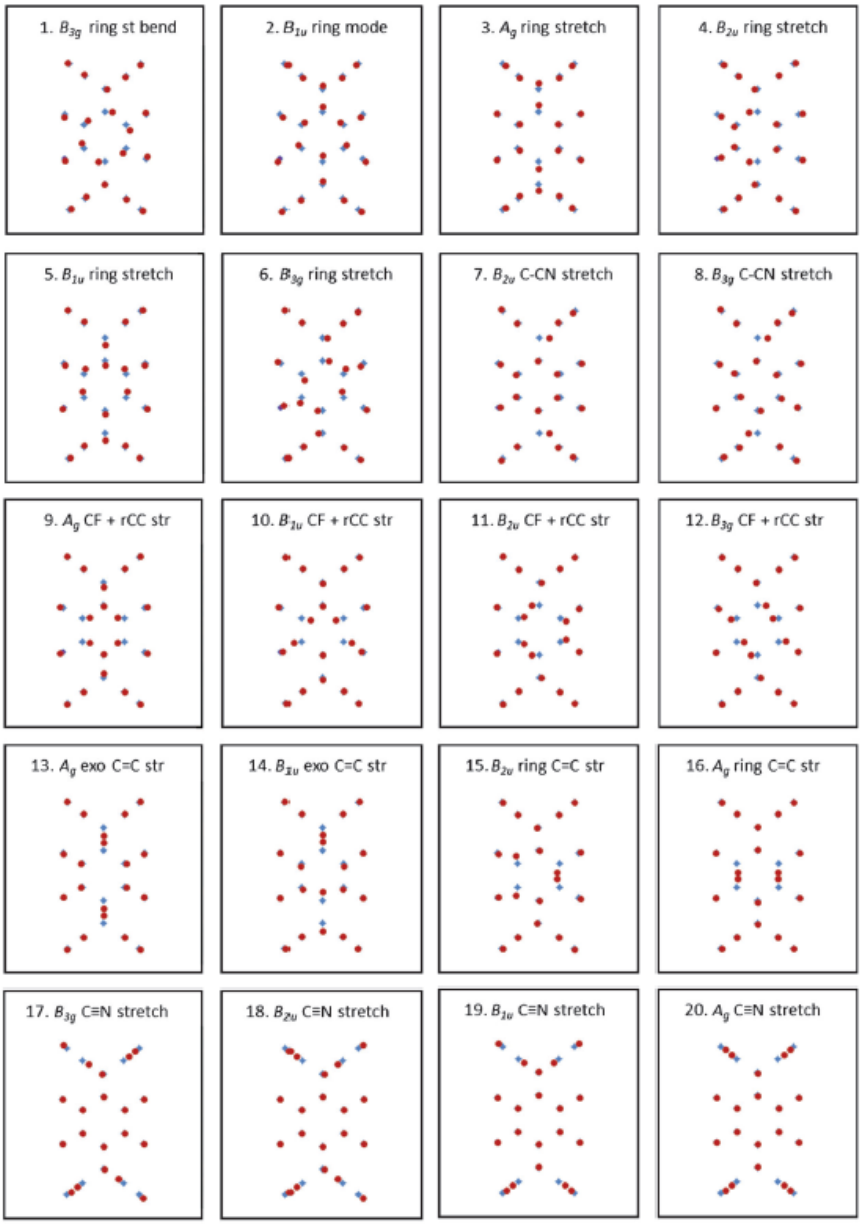

Figure 9: Motion schemes of some selected normal modes of the F_4TCNQ molecule.

2.c) Electronic characterization

The high electronegativity of the F_4TCNQ molecule frequently causes the capture of one or even two electrons (for instance from a possible substrate) by the molecule. Because of this, the studies about its anions are more common nowadays than the ones of the neutral species. However, in order to confine the discussion to its intrinsic properties, the following information will be devoted to the neutral molecule.

The figure 10 includes one absorption spectrum[18] of F_4TCNQ in the optical range.

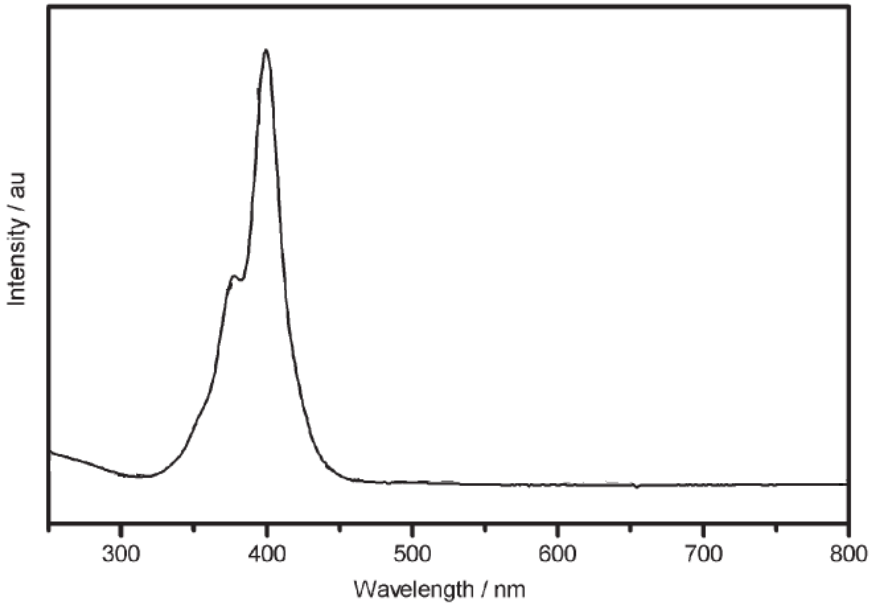

Figure 10: Absorption spectrum of F_4TCNQ.

The spectrum features a main peak at around 391nm with a remarkable hump at 371nm. The origin of this structure is the transition from the HOMO to the LUMO. The following DFT calculation[19] shows the density of states and where the energy levels are predicted to lie for an interface of F_4TCNQ on aluminium oxide.

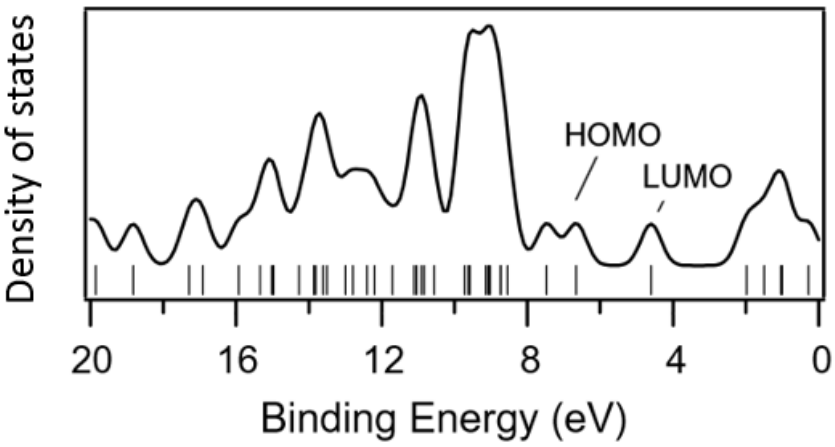

Figure 11: Density of states of F_4TCNQ on an aluminium oxide substrate with the underlying energy levels of the molecular orbitals.

Among all the orbitals, only a few of them play a significant role when it comes to the bonding between the molecules and the metallic substrate. The reason behind this lies in the orbital overlap populations: while some orbitals hardly share their space with the substrate, some others are spread over regions strongly influenced by the substrate[20]. In that regard, the depiction below, obtained in the framework of the DFT, includes the most relevant molecular orbitals of the F_4TCNQ molecule[21].

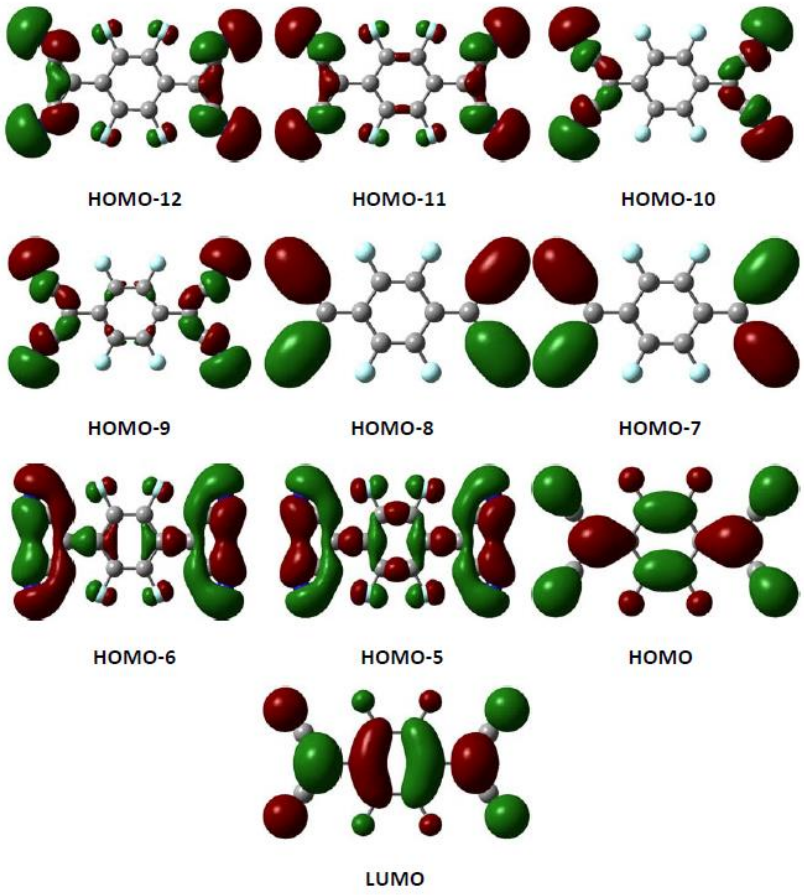

Figure 12: Isodensity plots of the molecular orbitals of F_4TCNQ with relevant overlap with the substrate.

References:

1. Braun A. and Tcherniac J., Ber. Deut. Chem. Ges., 40, 2709 (1907)
2. Linstead R. P. and Lowe A. R., J. Chem. Soc., 1022 (1934)
3. Robertson J. M., J. Chem. Soc., 615 (1935)
4. Chen, X. et al., Phys. Rev. Lett. 101, 197208 (2008)
5. Serri, M. et al., Nature Communications 5, 3079 (2014)
6. Ebert A. A. and Gottlieb H. B., J. Am. Chem. Soc., 74, 2806 (1952)
7. Kumar, P. et al., Chem. Eur. J., 20, 6154 – 6161 (2014)
8. Salomon, E. Ph.D. thesis *Propriétés physiques de films minces de phthalocyanines adsorbées sur des semi-conducteurs III-V* Aix-Marseille Université (2005)
9. Palys, B. J. et al., Journal of Raman spectroscopy, Vol. 26, 63-76 (1995)
10. Kobayashi, N. et al., Chem. Eur. J., 10, 6294 – 6312 (2004)
11. Rosa, A. and Baerends, E. J., Inorg. Chem. 1994, 33, 584-595
12. Horke, D. A., et al., J. Phys. Chem. A 2011, 115, 8369–8374

13. U .S. Patents 3115506, 3226389, 3526497, 3558671, 3687987, 3739008
14. Maynard, J., J. Organ. Chem. 28, 112 (1963).
15. Wheland, R. C. and Martin, E. L., J. Org. Chem., Vol. 40, No. 21, 1975
16. Haworth N. L. et al, ChemPlusChem 2014, 79, 962 – 972
17. Meneghetti, M. and Pecile, C. J. Chem. Phys. 1986, 84, 4149 –4162.
18. Gao, Z. Q. et al. Chem. Commun. 2008, 117-119
19. Braun, S. and Salaneck W. R., Chemical Physics Letters 438 (2007) 259–262
20. Koshino, M. et al., Journal of Electron Spectroscopy and Related Phenomena 135 (2004) 191–200
21. Rangger, G. M. et al., *J. Chem. Theory Comput.*, 2010, 6 (11), pp 3481–3489
22. Leznoff C. C. and Lever A. B. P., *Phthalocyanines. Properties and Applications*, VCH, Cambridge, vol. 1–4 (1996)

Chapter III:
Influence of local structure on the properties of CoPc adsorbed on Ag(100) substrates

Influence of local structure on the properties of CoPc adsorbed on Ag(100) substrates

1. Introduction

The roots of organic electronics probably lie in the discovery of the photoconductivity of anthracene in 1906 by Pochettino[1]. His experiments showed for the first time that it was possible to establish a current by casting light on this organic compound. A more comprehensive approach to the domain would be done more than half a century later, when Kearns and Calvin[2] studied the photovoltaic effect on magnesium phthalocyanine, a close analogue of the chemical species central to this chapter. One of the first organic devices ever devised was a field-effect transistor produced from H_2Pc in 1970 by Barbe[3].

Ever since, the field has experienced a remarkable progress that has boosted the conception of countless electronic, magnetic and optical devices[4,5,6].

Despite the development in the field, even if it's clear that many mechanisms (such as dispersive interactions, Pauli repulsion, interface states and dipoles, the nature of the bonds etc.) have a significant impact on the properties of organic-metal systems, their influences at a fundamental level are not only unknown quantitatively, but sometimes at the qualitative level too.

Some of the most common organic-metal interfaces are those involving phthalocyanines. They form well-ordered films on many substrates and some properties, mainly the magnetic ones, can be modified by changing the central atom. Besides, these chemical species are widely used in the production of optical, electronic and magnetic devices[7,8]. All these reasons attract a significant interest both from the most theoretical and the most applied standpoints.

This study will be restricted to CoPc evaporated on Ag(100) substrates. It has been shown that when metal phthalocyanines are deposited on silver, the nature of the central atom of the molecule is strongly related to the mechanism of charge transfer between the substrate and the molecules. In effect, for instance ZnPc and CuPc are reported to induce a charge transfer between the LUMO and the metal, hence causing the partial filling of the LUMO. This is manifested in the apparition of a new state in the gap.[9,10]

On the other hand, CoPc and FePc, due to the specific occupation of their 3d orbitals, undergo a charge transfer from the substrate not towards the LUMO as it happened before, but towards some molecular orbitals highly concentrated on the metallic atom and hence with a strong contribution from the original electronic states of cobalt or iron[11,12,13].

The purpose of the present chapter is the demonstration that the charge transfer mechanism in the MPc-metal systems is not only affected by the nature of the metallic centre of the molecule, but also by less drastic changes on the geometry, i.e. the sites of adsorption, the substrate-adsorbate relative orientation and the distances between the different elements, in particular the height of the molecules over the last layer of Ag(100)

2. Experimental procedure

The system CoPc/Ag(100) was studied by means of STM, LEED, HREELS and X-ray photoelectron diffraction.

The preparation of the Ag(100) single-crystal that was used as substrate was performed through several sputtering cycles with Ar^+ ions with energies of 1.5 keV and the respective subsequent annealing periods to 730K. The CoPc molecules were thermally evaporated at room temperature and 10^{-10} mbar from a quartz crucible with rates of about 0.4 monolayers per minute. These conditions originated two different results (as it will be shown in the following pages they correspond to two different surface reconstructions) depending among other parameters on the coverage: 0.80 ± 0.05 monolayers in one case and 0.95 ± 0.05 for the second possibility.

3. The surface arrangements

Upon producing organometallic interphases, different conditions (temperature, coverage, evaporation rate, crystallographic planes…) of the epitaxy can lead to the growth of different reconstructions.

In the case of CoPc on a Ag(100) substrate, a (5×5) arrangement has been reported and examined by some authors[14,15]. During the experiments referred here, that structure has also been observed. Its characteristics have been analysed in the light of its LEED pattern, some STM images and the corresponding HREELS spectra, which will be shown later.

However, another phase previously unreported has been identified: the (7×7). This section is devoted to the characterization of the latter and the comparison between both of them. As it will be demonstrated in the following pages, the charge transfer mechanism is not the same for the two phases. Indeed, the X-ray photoelectron diffraction patterns, which happen to be very sensitive to fine geometrical details (e.g. variations of 0.1 Å in the height of the molecules over the substrate), will allow to clearly establish the structural differences between both reconstructions. These are most likely at the origin of the charge transfer particularities and reveal that the nature of the cobalt atom is not enough to fully explain the charge transfer mechanism.

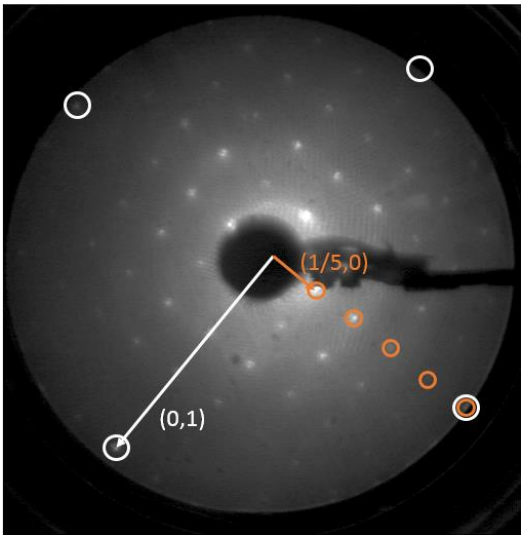

Figure 1: LEED pattern (E = 32.1 eV) of the (5×5) phase of CoPc on Ag(100). The white circles enclose the Ag spots while the orange ones surround 5 consecutive spots of the CoPc (5×5) reconstruction along the $\langle 011 \rangle$ and $\langle 01\bar{1} \rangle$ directions.

The figure above contains the LEED pattern with electrons with energies of 32.1 eV corresponding to the (5×5) phase after an evaporation of approximately 0.8 monolayers. The quintuple periodicity of the substrate is evident as well as the fact that there is not any rotation between the crystalline lattices of the molecular superstructure and the underlying silver.

Regarding the appearance in the real space, the same phase is depicted in the following STM image. The directions of silver and the axes of symmetry of the isoindole groups are also highlighted for the sake of clarity.

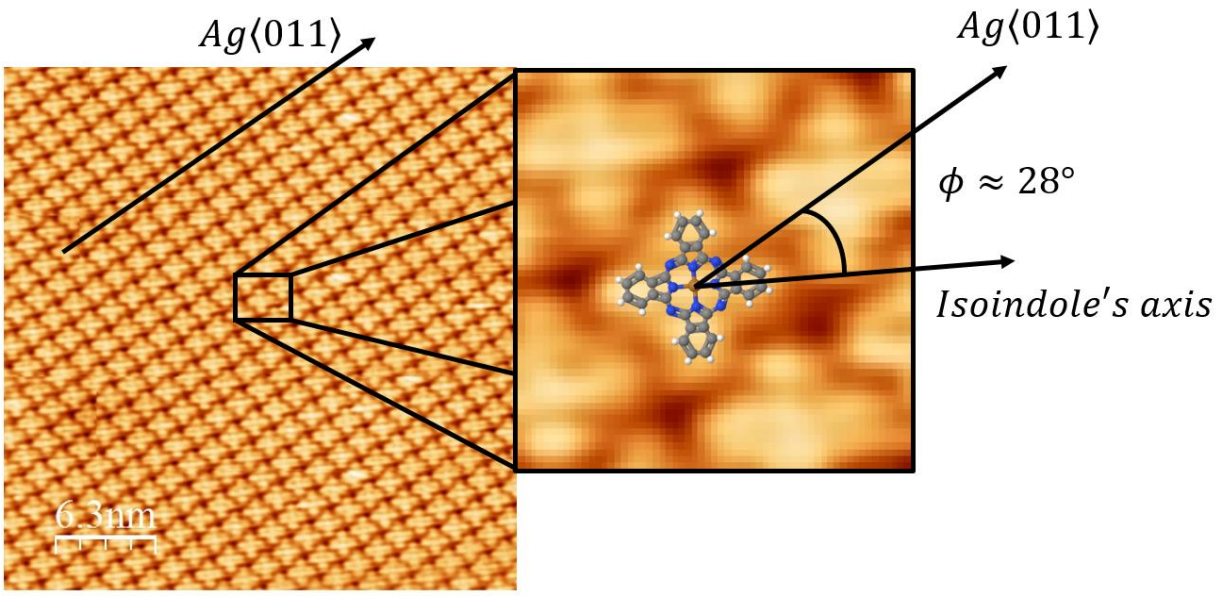

Figure 2: 34.4 nm×34.4 nm STM image of the (5×5) phase of CoPc on Ag(100) obtained with the tunnelling conditions specified by $V = -317\ mV$ and $I = 0.172\ nA$.

On the micrograph, each CoPc molecule appears as a cross with a bright centre. Regarding their orientation, the angle spanned between the direction ⟨011⟩ of the silver substrate and the symmetry axis of the isoindole group of CoPc is equal to 28º. This parameter will be taken into account when trying to reproduce experimental XPD patterns with numerical simulations provided by the EDAC code. As for the distance between molecules, in the following paragraphs the height profiles will reveal a periodicity equal to 14.45 Å. This value is consistent with the van der Waals radius of the molecule, suggesting that the identification of the crosses with the molecules is correct.

As it has already been stated, this structure was observed for a coverage around 0.80 monolayers. In some cases, when the amount of molecules deposited was higher, close to 0.95 monolayers, an additional surface arrangement was formed: the (7×7) phase. It must be stressed that the coverage is not the only magnitude that determines the surface reconstruction of the molecules and consequently conditions such as the surface state or the temperature could be of foremost importance in the formation of the (7×7) phase.

The LEED pattern below reveals the sevenfold commensurability of the new system. The molecular arrangement is once again aligned along the highest symmetry axis of the Ag(100) surface so the only difference seems to come from the distance between molecules.

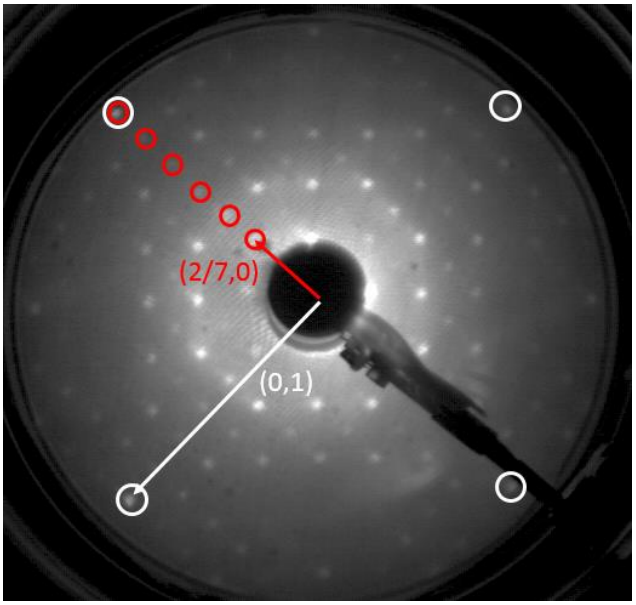

Figure 3: LEED pattern (E = 31 eV) of the (7×7) phase of CoPc on Ag(100). The white circles highlight the Ag spots while the red ones enclose 6 consecutive spots of the CoPc (7×7) reconstruction along the $\langle 011 \rangle$ and $\langle 01\bar{1} \rangle$ directions (one red circle is missing because the corresponding diffraction spot lies hidden behind the electron cannon).

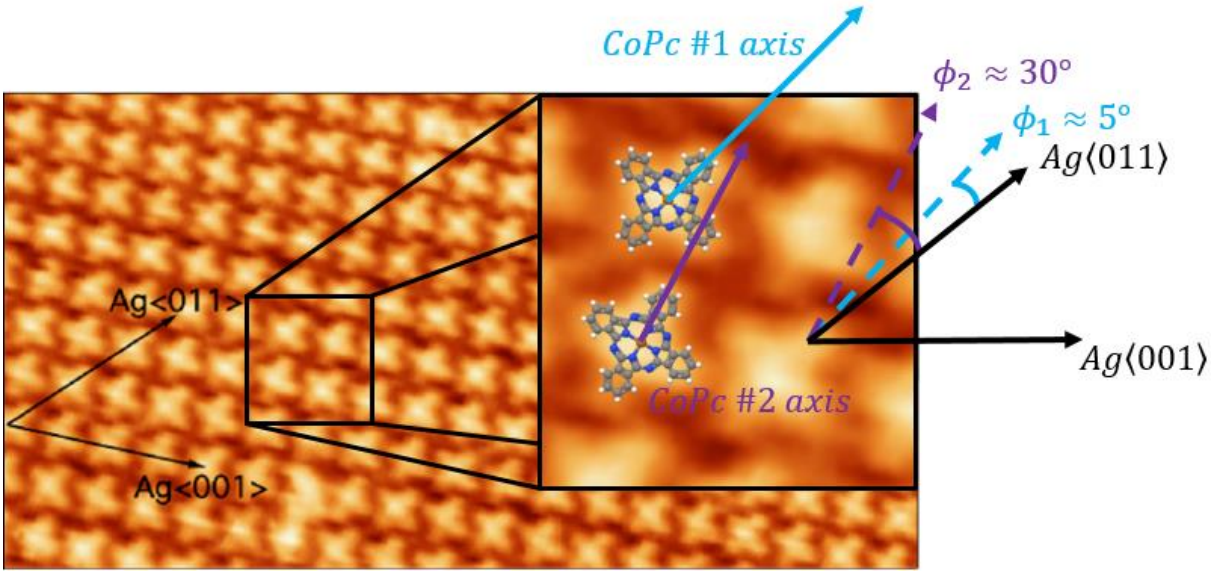

Figure 4: 24.6 nm×20.3 nm STM image of the (7×7) phase of CoPc on Ag(100) obtained with the tunnelling conditions specified by $V = -758\ mV$ and $I = 0.228\ nA$. The axis of two adjacent molecules have been traced in order to make clearly distinguishable the two orientations of the molecules present in this reconstruction.

The respective STM image (shown above) reveals some interesting differences when comparing to the (5×5) phase.

There are two different orientations of the molecule. Both lie on the same plane but while half of the molecules present their axes rotated approximately 5 degrees with regard to the $\langle 011 \rangle$ direction of the substrate, the other half shows a rotation of about 30 degrees with regard to the same reference. This points beyond doubt at the existence of two inequivalent sets of molecules (at the very least from the geometrical point of view).

Furthermore, the molecules of the (5×5) phase display a 4-fold symmetry which is lost in the (7×7)[16]. In effect, the molecules in the latter phase rather exhibit a 2-fold symmetry instead.

Another meaningful comparison between both structures can be performed by analysing height profiles of the STM images along selected directions. Three of those profiles are reproduced below:

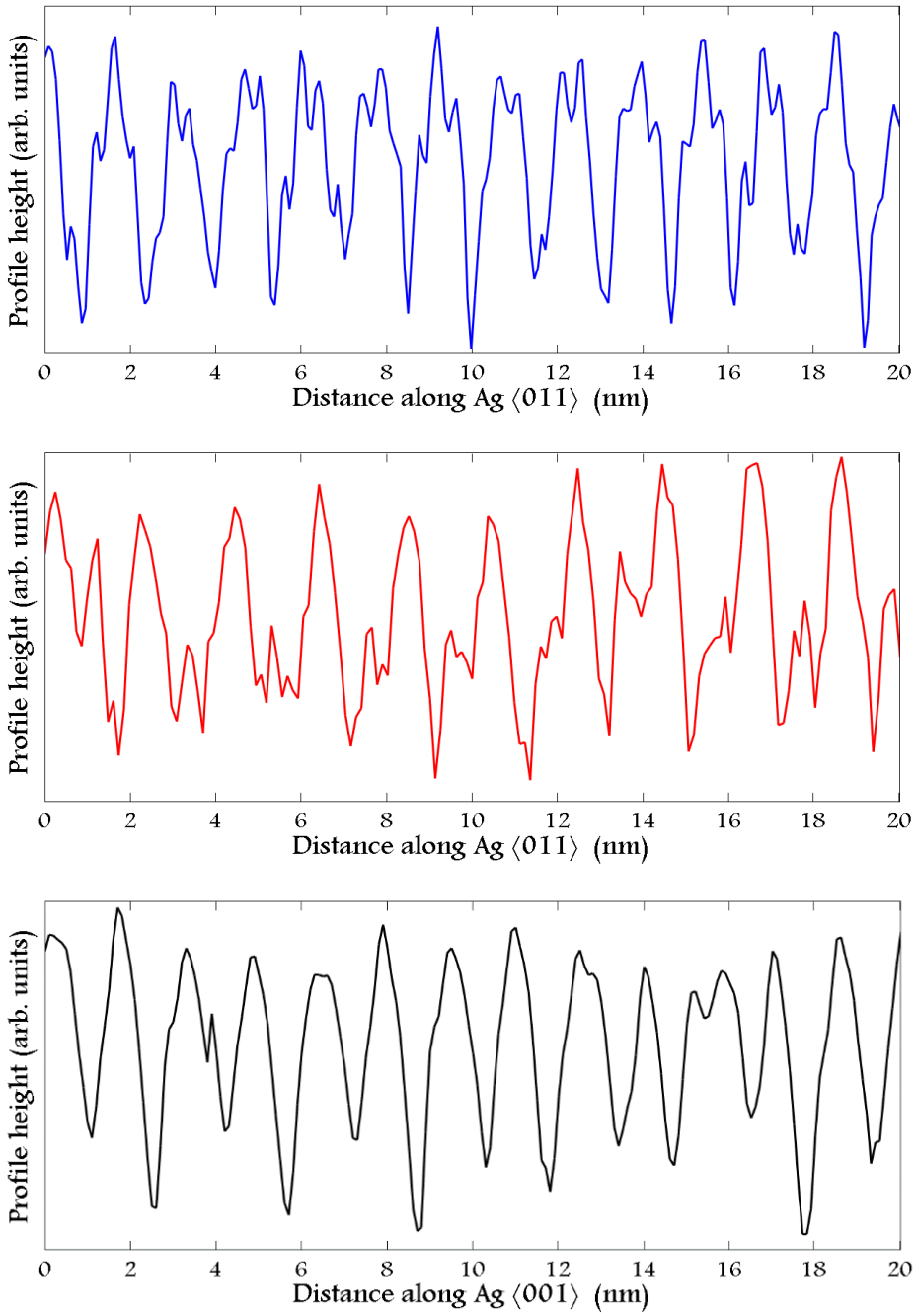

Figure 5: Examples of height profiles of CoPc/Ag(100). Blue: (5×5) along direction ⟨011⟩. Red: (7×7) along direction ⟨011⟩. Black: (7×7) along direction ⟨001⟩.

The highly periodic character of the height profiles and the large domains allow to obtain very finely sampled Fourier transforms of the profiles. The following chart includes the normalised power spectral density corresponding to a much larger sample of the data in figure 5.

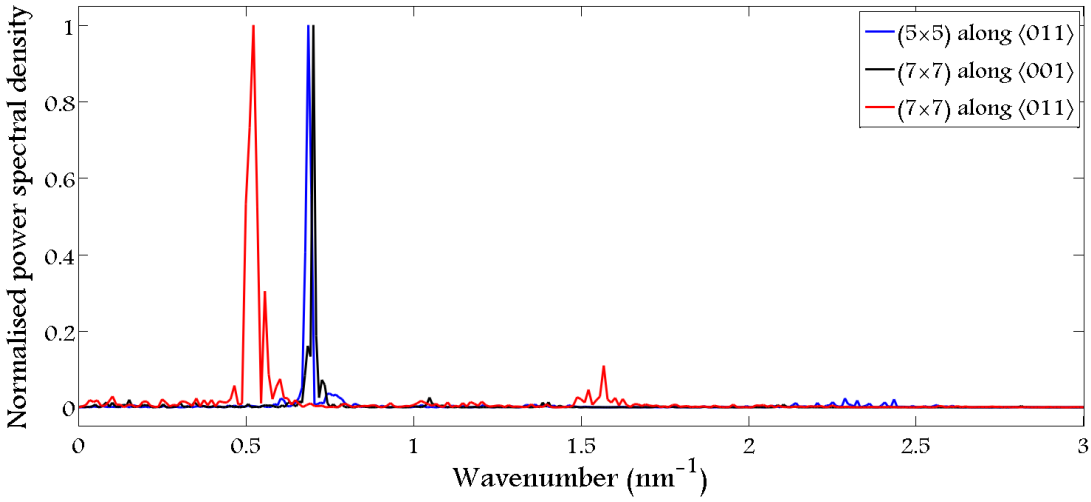

Figure 6: Normalised power spectral density of the profiles obtained along the directions specified in the legend.

The Fourier transform clearly identifies the periodicity of the lattices. The spatial frequency (that is, the related wavenumber) and also the distance between consecutive molecules are listed in the table below. These values already shed some light on the comparison between both phases as it will be explained in the subsequent paragraphs.

Phase and direction	Spatial frequency of the molecules (nm^{-1})	Intermolecular distance (nm)	Expected distance (nm)
(5×5) along direction ⟨001⟩	0.484	2.06 ± 0.03	2.05
(5×5) along direction ⟨011⟩	0.686	1.46 ± 0.02	1.45
(7×7) along direction ⟨001⟩	0.701	1.43 ± 0.02	2.86
(7×7) along direction ⟨011⟩	0.505	1.98 ± 0.04	2.02

Table 1: Experimental and calculated (according to the LEED periodicity) distances between consecutive CoPc molecules for the two studied phases along the selected directions

The inspection of the results in table 1 leads to a coherent conclusion. Regarding the (5×5) phase, the experimental values are compatible within the intervals of uncertainty with the distances deduced from the surface reconstruction and the lattice parameter of silver. On the other hand, the (7×7) arrangement has an unexpected point. The separation between molecules along the Ag ⟨011⟩ direction reasonably matches the expected value, however, following the Ag ⟨001⟩ direction the experimental spatial frequency surpasses the expectation by a factor of approximately 2.

In summary, a larger evaporation of molecules can produce the formation of the (7×7) reconstruction. This structure is interestingly less compact (despite the greater deposit) along the Ag⟨011⟩ direction and more compact along the Ag⟨001⟩ one. The immediate conclusion is that the latter arrangement has two molecules per unit cell, whereas the former has only one.

This explanation reconcile a higher compactness on a bigger structure and also justifies the existence of two possible orientations for the molecules as seen in figure 4.

4. A vibrational study

Further insight into the system can be gained by means of the HREELS spectra of both phases. Such data are reproduced below:

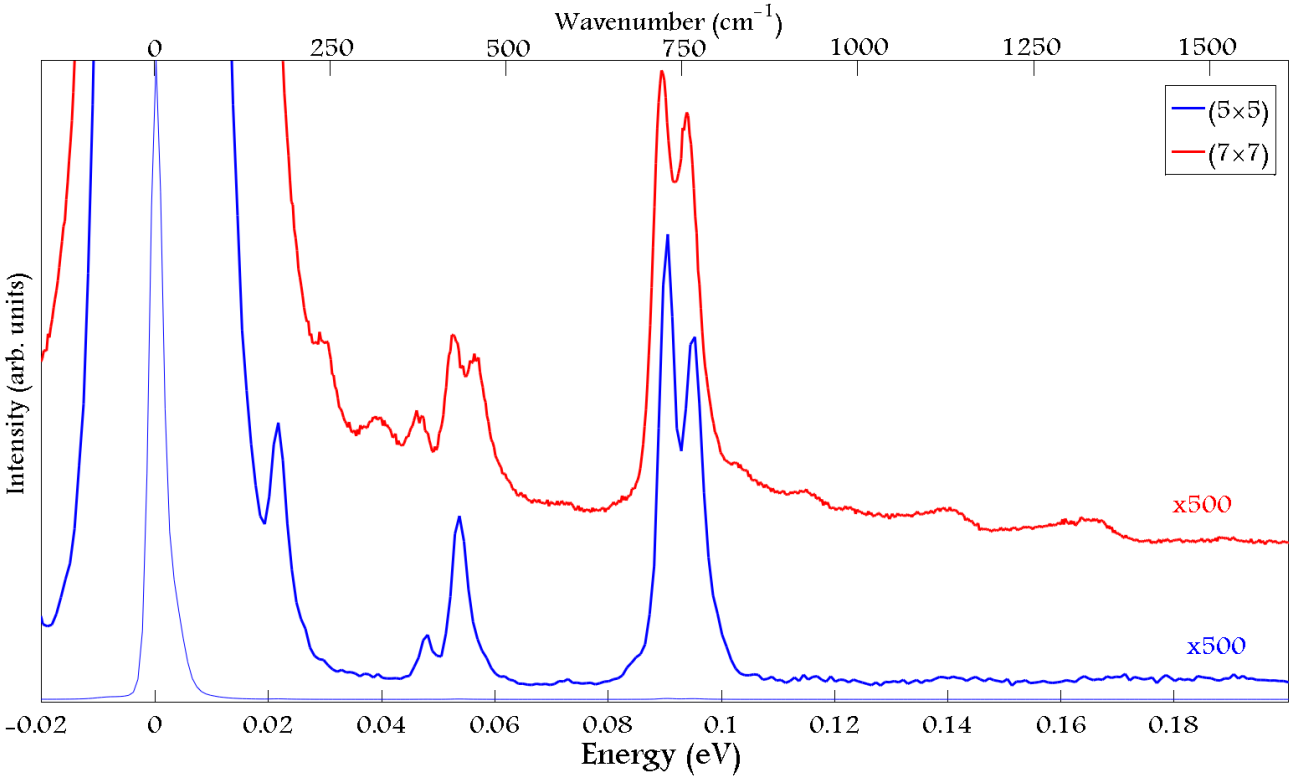

Figure 7: HREELS spectra recorded in specular condition ($\theta_{incidence} = \theta_{scatter} = 62°$) and at 3.0 eV of primary energy, for the (5 × 5) and the (7 × 7) phases of CoPc/Ag(100).

The vibrational modes featured in the spectra have been summarised in the following table[17]:

Mode	Position (cm^{-1})	Type of activity	Symmetry group
Isoindole out of plane	175	Infrared	A_{2u}
Ring breathing	248	Raman	A_{1g}
Nitrogen atoms out of plane	321	Infrared	A_{2u}
Ring N-C out of plane bending	382	Infrared	A_{2u}
Indole middle C, C-H and external N out of plane bending	430	Infrared	A_{2u}
Macrocycles in-plane bending	461	Raman	B_{2g}
Pyrroles out of plane bending	727	Infrared	A_{2u}
C-H out of plane bending	761	Infrared	A_{2u}
Macrocycle bending, C-C-C benzene in plane	940	Raman	B_{2g}
H-C-C in plane bending	1134	Raman	A_{1g}
Central N and C-C in plane stretching	1340	Raman	A_{1g}

Table 2: Vibrational modes present in the HREELS spectra.

Upon examination, the (7×7) surface arrangement displays a spectrum richer in peaks. In particular, the features located at 248, 321, 461, 940, 1134 and 1340 cm^{-1} are absent in the spectrum of the (5×5). As it can be checked on table 2, those modes are mostly Raman active.

The selection rules for HREELS spectroscopy in the specular direction and under the appropriate conditions can be seen as the same as the ones ruling in infrared spectroscopy[18]. As a result, it's useful to consider the common rule of thumb when studying infrared and Raman modes, the so-called rule of mutual exclusion. It states that the normal modes cannot display both infrared and Raman activity in the case of a molecule with a centre of symmetry[19] if the signal from the impact mechanism can be neglected. The reason for this mutual exclusion arises from the nature of the centrosymmetric point group. In effect, on one hand infrared active modes require a change of sign under inversion when transformation occurs according to the irreducible representation generated by one of the components of the dipole moment. On the other hand, Raman active modes, whose transformation depends on the polarizability tensor, must possess an even character under inversion. As it's obvious, both conditions cannot be fulfilled at the same time if the molecule has a centre of symmetry.

The apparition of Raman active modes on the HREELS spectrum of the (7×7) is remarkable, since it involves the expression of such modes but by means of a mechanism akin to the infrared one. As it has just been shown this is impossible in light of the rule of mutual exclusion. The impact mechanism is not responsible for the Raman modes either since they would also be manifest on the (5×5) phase. The way to circumvent this impediment is the lowering of the molecular symmetry because of the interactions between the molecules and the substrate. Considering the correlation tables and according to the symmetry of the observed vibrational modes, the D_{4h} molecular symmetry is most probably reduced to C_{2h} or C_{2v} for CoPc in the (7 × 7) phase. This assumption turns out to agree with the "distorted" appearance of the CoPc revealed on the STM image of the (7×7) phase.

Another particularity of this reconstruction's spectrum can be found in the region between 1000 and 1500 cm^{-1}. In between, there are two Raman peaks at 1134 and 1340 cm^{-1} that display highly asymmetric profiles.

The shape of those lines strongly resembles Fano-like profiles. A Fano line arises when a resonant scattering process occurs. In a nutshell, this kind of resonance happens when there's interference between one scattering originated at the continuum of states and another dispersion from a discrete state[20]. When both energies overlap, in the vicinity of the discrete level the scattering from the continuum changes slowly in amplitude and phase with the increasing frequency, whereas the discrete state's scattering undergoes a shift of π radians in phase over the characteristic width of the level. For this very reason, if both processes are in phase on one side of the discrete level, they will be in antiphase in the equivalent point of the other side, thus partially cancelling out. Constructive interference on one side along with destructive interference on the other side are at the origin of the asymmetric line shape.

Such features are described by the equation below in the domain of angular frequency:

$$L(\omega) = L_0 + c\gamma\omega_r\omega\frac{\left[1 - \frac{\tau}{\gamma}\cdot(\omega^2 - \omega_r^2)\right]^2}{\gamma^2\omega^2 + (\omega^2 - \omega_r^2)^2}$$

This expression is written in terms of the following parameters:

L_0: Background level

c: Normalisation factor (amplitude)

γ: Value related to the width of the distribution

τ: Tunnelling rate

ω_r: Fully renormalised Born-Oppenheimer vibrational frequency.

The fitting procedure of the spectrum with two components of this type yields a satisfactory result as it can be verified below:

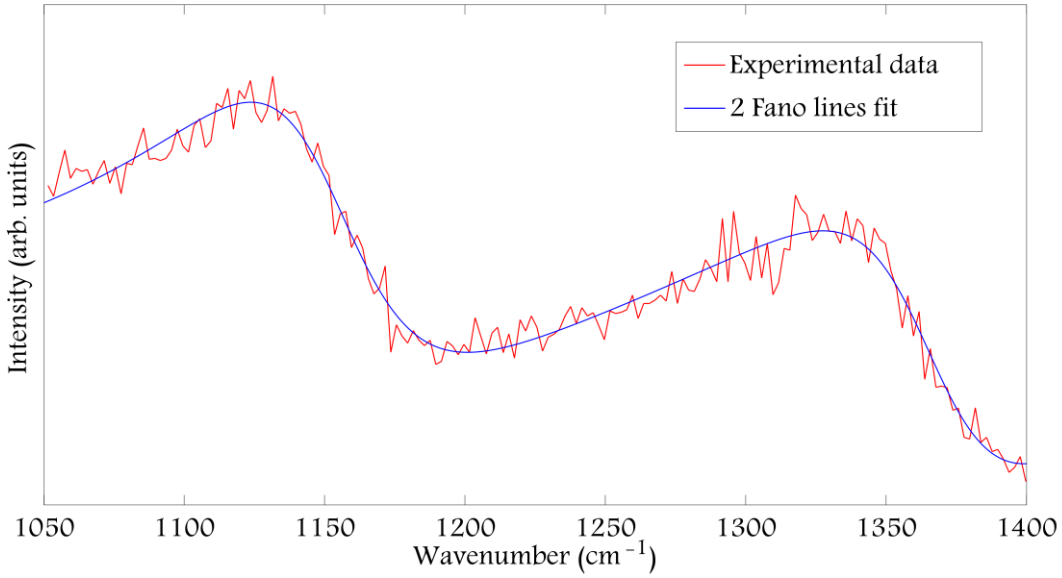

Figure 8: Zoom of the spectrum of the (7×7) phase between 1050 and 1400 cm^{-1}. The best fit with 2 Fano lines is superimposed.

The best match was obtained for the values of the parameters included in the following table.

Parameter (units)	First peak	Second peak
c (arb. units)	3.6 ± 0.6	2.1 ± 0.9
γ (cm^{-1})	85 ± 7	80 ± 15
λ^{-1} (cm^{-1})	1153 ± 4	1367 ± 5
τ (μm)	6.5 ± 0.9	8 ± 1

Table 3: Parameters of the best Fano fit for range of spectrum shown in figure 8.

These values are comparable to the ones calculated from spectra of ZnPc on Ag(110) substrates, and suppose a robust evidence of the coupling between electrons and phonons[21]. In particular, the reason behind the asymmetric line shape lies at the non-adiabatic character of the energy transfer towards the vibrational modes of the substrate from the excited vibrations of the molecules. Resuming the discussion about resonant scatterings, this coupling can only take place when there's a significant overlap between the Fermi level of the substrate (the continuum of states that was being mentioned in the previous page) and the lowest unoccupied molecular orbital of the molecules[22].

If the interference between both states is observed, that inevitably implies at least the partial filling of that orbital, and hence, a charge transfer from the metallic substrate into it.

As for the (5×5) CoPc/Ag(100), it has been proved[23] that no electrons are effectively promoted into the LUMO. Furthermore, numerical simulations in the frame of the GW approximation rather support a charge transfer from the substrate towards the previously unoccupied a_{1g} molecular orbital, which is formed mainly with the contribution of the Co d_z orbital. As a result the transferred charge is fundamentally concentrated in the region close to the cobalt atom.

It's possible to asseverate now that the presence of Fano-like peaks in the spectrum of the (7×7) CoPc on Ag(100) and their absence in the case of the (5×5) phase demonstrate the existence in the former system of a charge transfer mechanism involving the LUMO which is missing in the latter.

5. The XPD data

Up to this point, several independent evidences have supported the existence of a previously unreported phase of CoPc on Ag(100). The LEED patterns are a robust proof of the new (7×7) commensurability. Additionally, the geometrical constraints revealed by the STM images, that is to say the two molecules per unit cell and the two possible orientations of the molecule, suggest the existence of two sets of inequivalent molecules that could readily leave an imprint on some other properties, such as the charge transfer between the substrate and the molecules.

The HREELS spectra are not at odds in the slightest with that assumption, given that the vibrational signatures of the two aforementioned phases are remarkably different and exhibit the activation of modes coherent with a change in the symmetry of CoPc as well as distinct mechanisms of charge transfer.

In a previous work[24], Mugarza found that these molecules get adsorbed on hollow sites when they are evaporated sparsely on Ag(100) surfaces. The existence of two different molecules in the unit cell of the (7×7) phase with their respective orientations hints at the possibility of two distinct adsorption sites. This might be closely related with the observation of a charge transform mechanism that was absent in the case of the (5×5) reconstruction. At this stage, the photoelectron diffraction appears as a suitable tool for delving into this question.

X-ray photoelectron diffraction effectively probes a part of the parameter space that has heretofore been out of reach: the local coordination of the molecules on the substrate. There have been several evidences in the previous discussion that support inequivalent molecules in the (7×7) arrangement, so there's no reason to think they shouldn't resurface again in the light of this technique. Even more when it can excel at differentiating among tiny variations in the structural parameters and the STM images already manifest that those variations exist.

The downside of the photoelectron diffraction lies at the difficulty in interpreting the results. It is true that under suppositions such as single scattering regime or eminent forward and backscattering it is possible to associate the bright, fine spots to the closest neighbours. However those approximations require quite high electron energies that weren't selected for the experiments referred in this section because they would have a negative impact on the performance of the spectrometer (a higher energy implies a worse resolution) and on the surface specificity (higher energies involve longer mean free paths and thus a greater signal coming from the bulk). As a result, in the subsequent pages rather than directly interpreting the experimental pattern, it will be compared with the numerically simulated patterns corresponding to several structural models.

The low anisotropy of the signal inherent to low energies (as the electrons are weakly focused by the atoms of the lattice) caused a high background that may easily mislead the observer upon the first vision into thinking that no significant diffraction pattern was present and that no useful information could be garnered from the data.

For this very reason, the *raw* data had to be carefully treated and analysed as the following pages will show.

Continuing with what has already been mentioned, the photoelectron diffraction patterns were actually registered as photoemission spectra at the ALOISA beamline of the Elettra Synchrotron Light Source in Trieste, Italy. The PED polar scans were measured by collecting the photoemission signal as a function of both the polar emission angle and the kinetic energy of the electrons by rotating the electron analyser in the scattering plane for different orientations of the azimuth. The angle of incidence of the X-rays was kept at 4º under the transverse magnetic condition for the polarization, and the direction perpendicular to the surface was contained in the plane of incidence.

The spectral feature that was selected for the technique was the Co $2p_{3/2}$ level and it was set to emerge with a kinetic energy of 160 eV per electron. The parameters were fixed so as to guarantee an optimal compromise between photon flux, energy resolution and signal-to-noise ratio.

The hemispherical region chosen for the experiment spans the solid angle comprised between 0º and 67º in polar angle and 107º degrees of azimuth. The symmetry directions of the substrate had been previously checked in order not to leave out of the probed section the directions ⟨010⟩ and ⟨011⟩.

Additionally, no difference in the XPS spectra of Co, C, and N was detected after several hours of illumination with X-rays' energies around 1 keV.

The figure below shows a typical X-ray photoemission spectrum of the aforementioned level of cobalt. There were one of those spectra per pixel to assemble the final photoelectron diffraction pattern.

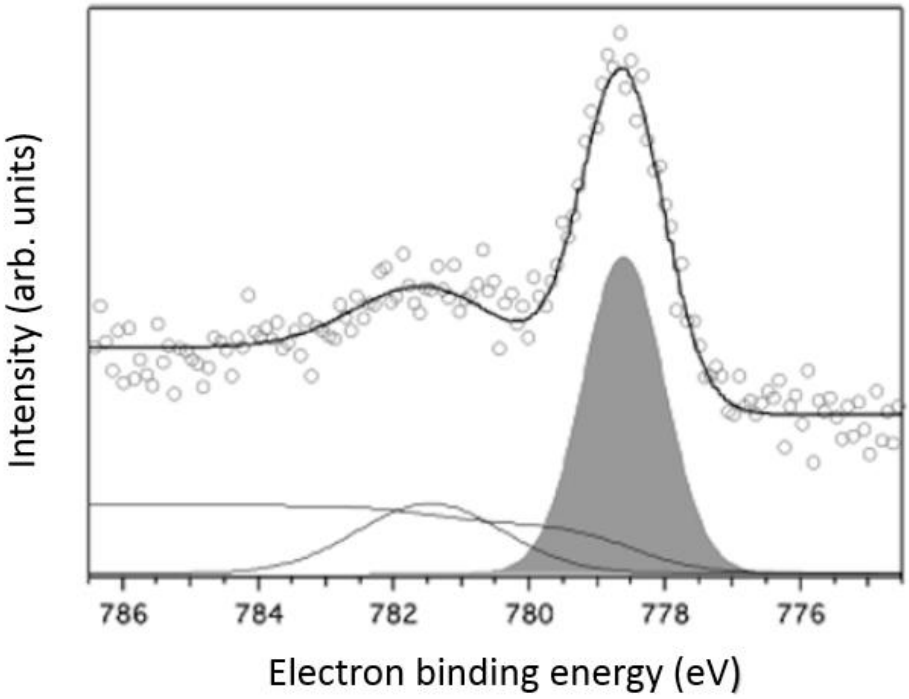

Figure 9: X-ray photoemission spectrum with a beam energy of 940 eV of the Co $2p_{3/2}$ level from a system composed of CoPc molecules adsorbed on Ag (100). The best fit is shown in the lower part. The greyed peak corresponds to the Co $2p_{3/2}$ level that was separately considered in the end to obtain the diffraction pattern.

The previous graph depicts the photoemission from the cobalt 2p level as a function of the binding energy. As it has been stated in the previous page, the kinetic energy of the emitted electrons after the impact of photons of 940 eV was around 160 eV.

The spectroscopic signal was decomposed in the three parts that are apparent on the figure: the split $2p_{3/2}$ peak of cobalt (gaussian) and a Shirley background[25]. The apparition of two and even more features stemming from Co^{2+} ions is common and can be interpreted as shifts produced by uneven chemical environments (deteriorated molecules, monolayer vs. multilayer etc.).

The Shirley background is a common procedure to account for the presence of a background level dependent on the kinetic energy of the electrons that appears frequently on raw x-ray photoemission data. It includes a first straightforward step which is the subtraction of the constant value at kinetic energies beyond the Fermi level. This contribution is usually rooted in photoelectrons ejected by high-energy bremsstrahlung undergoing subsequent energy losses in the sample. Its removal brings the baseline to zero on the high kinetic energy side of the peaks, but in general the low energy side lies at a higher level. Obviously a rigid shift cannot deal with 2 different background levels, so an energy-dependent correction is necessary.

The reason behind the second correction is the inelastic scattering. The general treatment involves the use of a response matrix, but if the peaks of interest are isolated and the low-energy tail is constant enough, a simpler approach is possible. The difference in intensity of both tails is assumed to arise from outcoming photoelectrons inelastically scattered on its way out of the sample. The second correction of the background is then performed through subtraction of a quantity proportional to the cumulative distribution of the peaks up to each energy (whence the energy-dependent character of the background comes) imposing zero intensity on both tails. The final intensities are generally computed by numerical algorithms.

Once the spectrum is supposedly free of any background, the cobalt $2p_{3/2}$ can be fitted. The mandatory expected binding energy of the orbital is around 778 eV and in some circumstances the values can shift away as far as to 782 eV depending on the chemical environment.

The integral of the most intense peak was computed with the help of the fit for each pixel, which yielded a matrix of intensity in the region of hemisphere probed. The heat map that results from assigning a colour scale to the integrated area is shown in figure 10. Hereinafter this matrix will be referred as the "raw data" even if a background subtraction has already been performed on the spectra. The reason is that this is the first stage at which it's already possible to visually apprehend the diffraction pattern.

At first sight, the observer can appreciate that the raw diffraction pattern displays some undesired characteristics:

First of all, there's one hot spot at $\phi \approx 25°$ and $\theta \approx 49°$ that seems to be out of place, like the signal produced by a hot pixel. Notwithstanding, it must be noted that this bright spot has some extension so such an explanation is ruled out. Probably there is some physical signal behind it, but two reasons lead to the conclusion that the signal from that point is at least over magnified. Indeed, the statistical significance of the spot is clearly unparalleled over the whole range of data thus reducing the likelihood of such an event. Moreover, the system possesses 4-fold symmetry and the $\langle 001 \rangle$ axes should be mirror axes if the discussion is restricted to the substrate. In any case the scattering cross section of N, C, and H is very small when compared to Ag or Co atoms so the assumption of the persistence of the mirror axis in the CoPc/Ag(100) system is reasonably sensible. If the $\langle 001 \rangle$ direction is still a bilateral axis, a similar bright spot (the mirrored one) should be manifest at $\phi \approx 75°$ and $\theta \approx 49°$, yet it's missing.

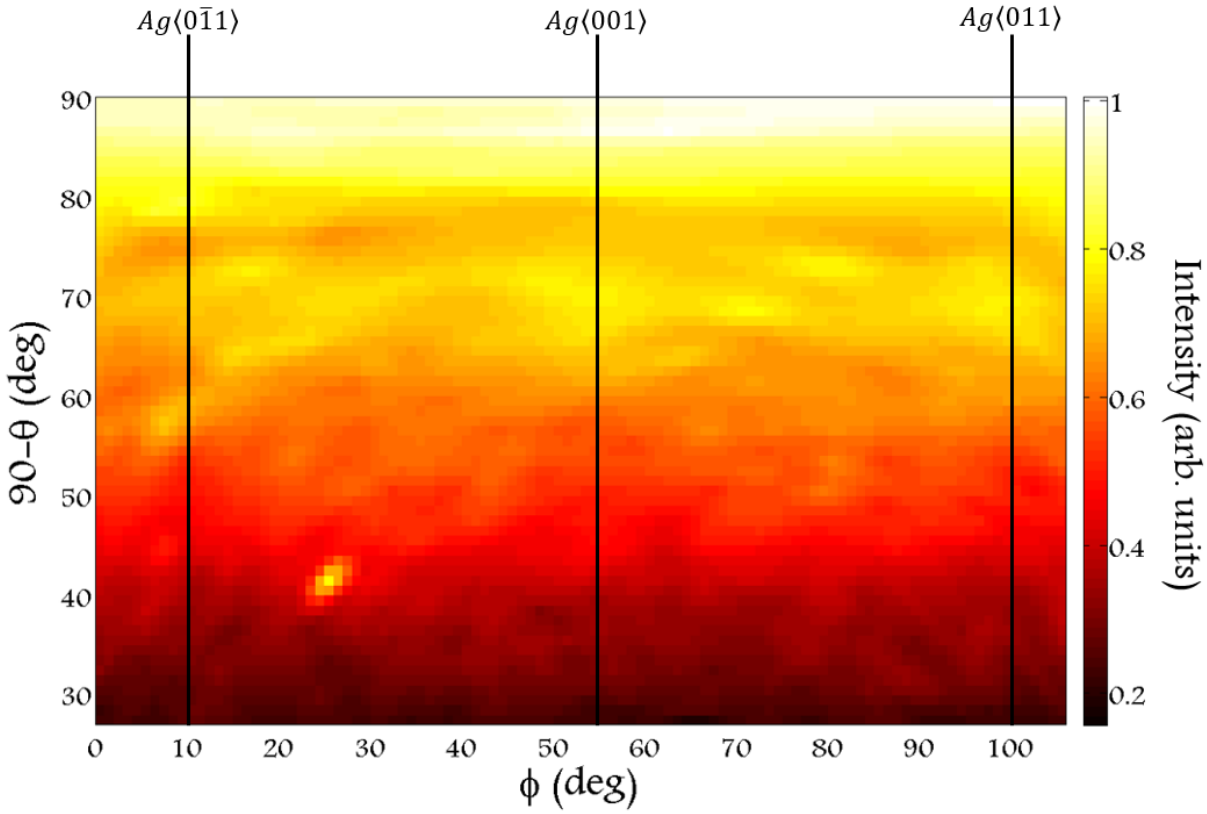

Figure 10: Heat map of the integrated area below the main Co $2p_{3/2}$ peak as a function of the latitude (90-θ) and the azimuthal angle. High symmetry directions of the system have been included for the sake of clarity.

Secondly, there's a ubiquitous steady increase in the signal as the detector approaches the zenith. Axisymmetric trends are reminiscent firstly of the angular dependence of the photoemission matrix element (the probability of emission is proportional to the projection of the direction of emission onto the polarization of the beam), and secondly of the variable probing depth as a function of the angle of emission. That is, if two electrons with the same kinetic energy and hence with the same inelastic mean free path are set to emerge from a material with different polar angles, the one with the most perpendicular speed to the surface can start its path from a deeper point as shown in figure 11. This implies that a greater portion of material contributes with photoelectrons for smaller polar angles of emission.

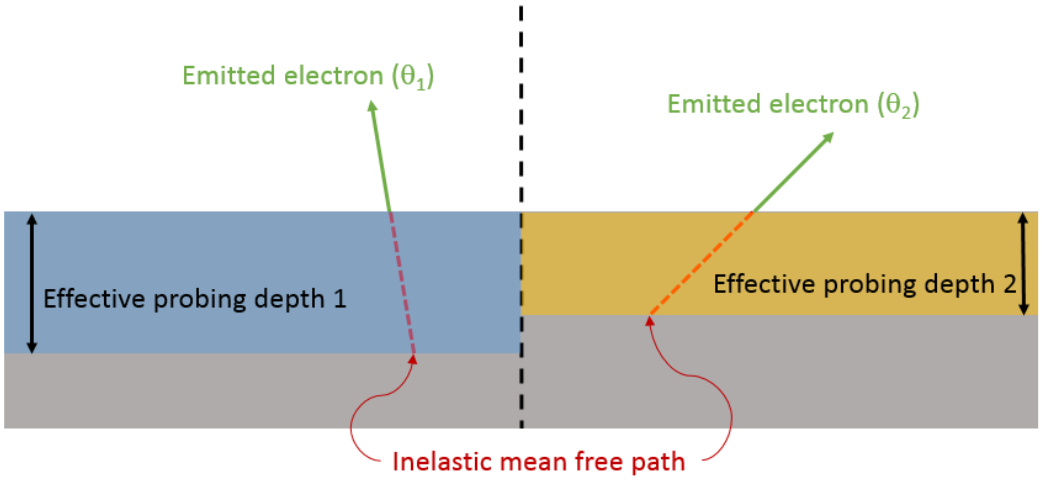

Figure 11: Example of dependence of the probing depth depending on the angle of emission provided that both electrons travel through the same material and have the same kinetic energy.

A sensible objection would be that since the photoelectrons are emitted from the cobalt atoms and those lie at the topmost layer, this argument is faulty. However, the captured electrons either haven't undergone any scattering in the material or have been subjected to a last scattering process before flying towards the detector. The former would create an axisymmetric background around the polarization vector of the x-rays, hence introducing an angle-dependent component, while the latter could emerge after their last scattering from greater depths if they propagated closer to the normal direction of the surface. Because of that, the reasoning holds in this case.

The third unfortunate feature is the apparent absence of diffraction structure in the raw data. There are some reinforcements of the signal in some places but the visual information is barely visible engulfed by the more intense axisymmetric background.

As for the bright spot there's little to be done, but it doesn't have a strong impact on the rest of the image so it can be neglected. The other two difficulties are actually one and the same. There's a false feeling of anisotropy arising from the axisymmetric background and at the same time it conceals the weaker diffraction pattern. The solution is then eliminating the background from the raw data.

The analyser recorded photoemission spectra, but the discussion can be moved forward to the raw data matrix. The raw intensity is then a function of the diffractive signal $D(\phi, \theta)$, the background signal, mainly the aforementioned axisymmetric component $B(\theta)$ and the response function of the instrument $H(\phi, \theta, energy, flux, \dots)$, that is to say, how it translates the flux of electrons into counts.

It can be assumed that the measured raw intensities obey the expression:

$$I(\phi, \theta) = H(\text{parameters}) \cdot [D(\phi, \theta) + B(\theta)]$$

If the assumption of a good behaviour from the response function is made (mainly linearity on the flux and response independent of the position of the detector.) then it becomes a constant that can be incorporated into the two addends:

$$I(\phi, \theta) = \widetilde{D}(\phi, \theta) + \tilde{B}(\theta)$$

In this expression, some counts come from the diffractive component and the rest from the background part.

On figure 10 it can be checked than the intensity is strictly positive as the colour scale on the right side spans the smallest interval that includes all the values in the matrix. Assuming that the diffractive part is positive (diffraction patterns cannot display negative absolute intensities after all) and that there are no diffraction spots covering individually the whole range in azimuth:

$$\forall(\phi, \theta), \widetilde{D}(\phi, \theta) \geq 0$$
$$\forall\theta, \exists\phi : \widetilde{D}(\phi, \theta) = 0$$

The axisymmetric background can then be computed with the expression:

$$\tilde{B}(\theta) = \min_{\theta}\{I(\phi, \theta)\}$$

So for each polar angle θ, the background can be calculated as the minimum intensity over the azimuthal profile corresponding to that value of θ.

The result of that operation, as shown below in figure 12, is a background polar profile that can be subtracted from the raw data to enhance the contrast of the diffractive part. It has been mildly smoothed to prevent abrupt local variations as it can be deduced from the scarce points in which a few profiles have a slightly lower signal than the background.

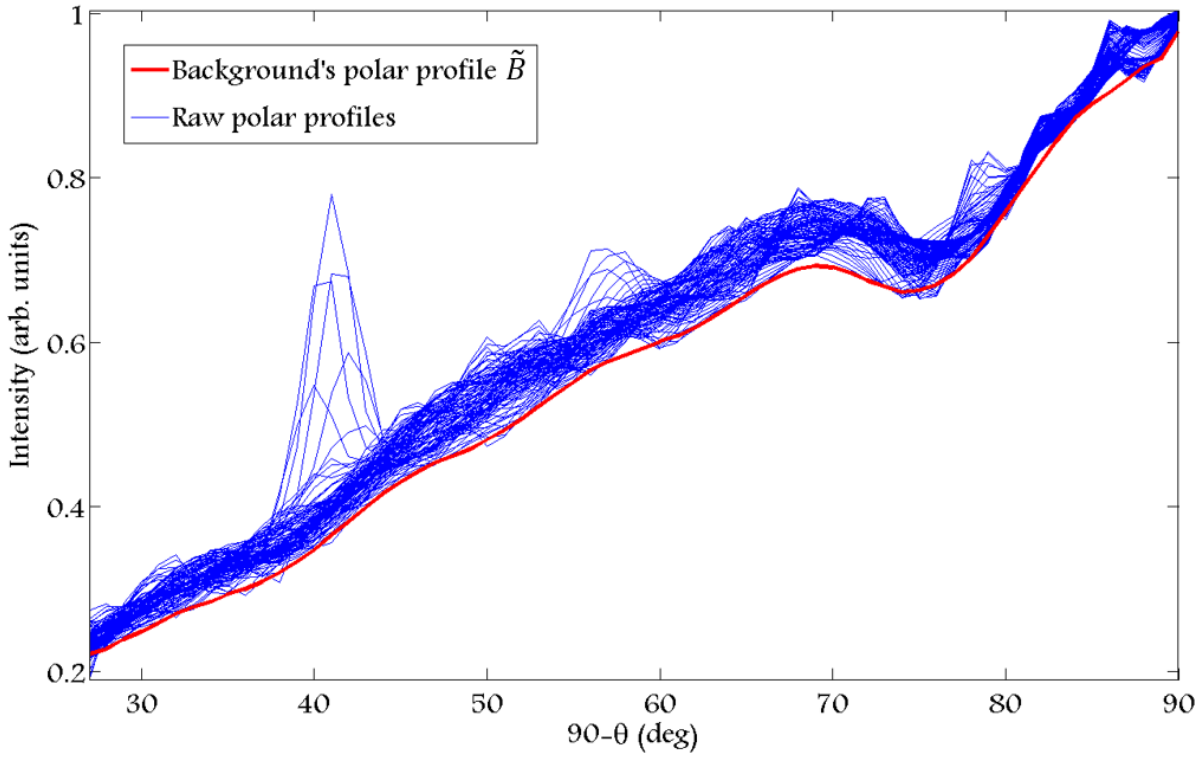

Figure 12: Set of superimposed polar profiles, that is, contour lines of the raw intensity for the each value of the azimuthal angle (blue lines) along with the smoothed background polar profile as calculated from the last expression in the previous page.

After this step, the remaining signal $(I - \tilde{B})$ is highly dependent on the direction and changes throughout the probed region in an unpredictable manner. Nevertheless, as they are in the current state, the background-free data are still hardly comparable to simulations.

The adoption of a dimensionless pattern is imperative because the fluxes of electrons obtained in the simulation code EDAC[26] and through the data analysis of the experimental spectra performed so far are not expressed in equivalent units.

The idea is then to divide (normalise) by something with the same units as the pattern. The resulting magnitude is in that case dimensionless and should be easier to compare.

If the objective is to preserve proportionality between the intensities in any two points, then the normalisation through a constant is imposed. Finally, if the goal is the study of a dimensionless magnitude that changes much with the direction, the word "anisotropy" naturally comes to mind. The reference for the anisotropy could be setting the mean of the normalised intensity over the whole region to 1 (the reasons behind this choice were explained in the introductory XPD section). This approach will be generally adopted from now onwards and so the anisotropy χ shall be defined:

$$\chi(\phi,\theta) = \frac{I(\phi,\theta) - \tilde{B}(\theta)}{\langle I(\phi,\theta) - \tilde{B}(\theta)\rangle}$$

where the angular brackets $\langle\,\rangle$ represent the average over all the pixels.

This normalisation procedure has one additional advantage: it makes all the distributions of anisotropy throughout the probed solid angle equal to first order. Indeed, by adjusting their average value to 1, all the patterns normalised following this method will have the same mean and the comparison will be easier. It would also be possible to make the distributions equal up to second order (through the modification of the variance of the distribution) but it would change the pixel-to-pixel anisotropy ratios, and so this resolution will not be adopted.

The normalised anisotropy pattern is shown below:

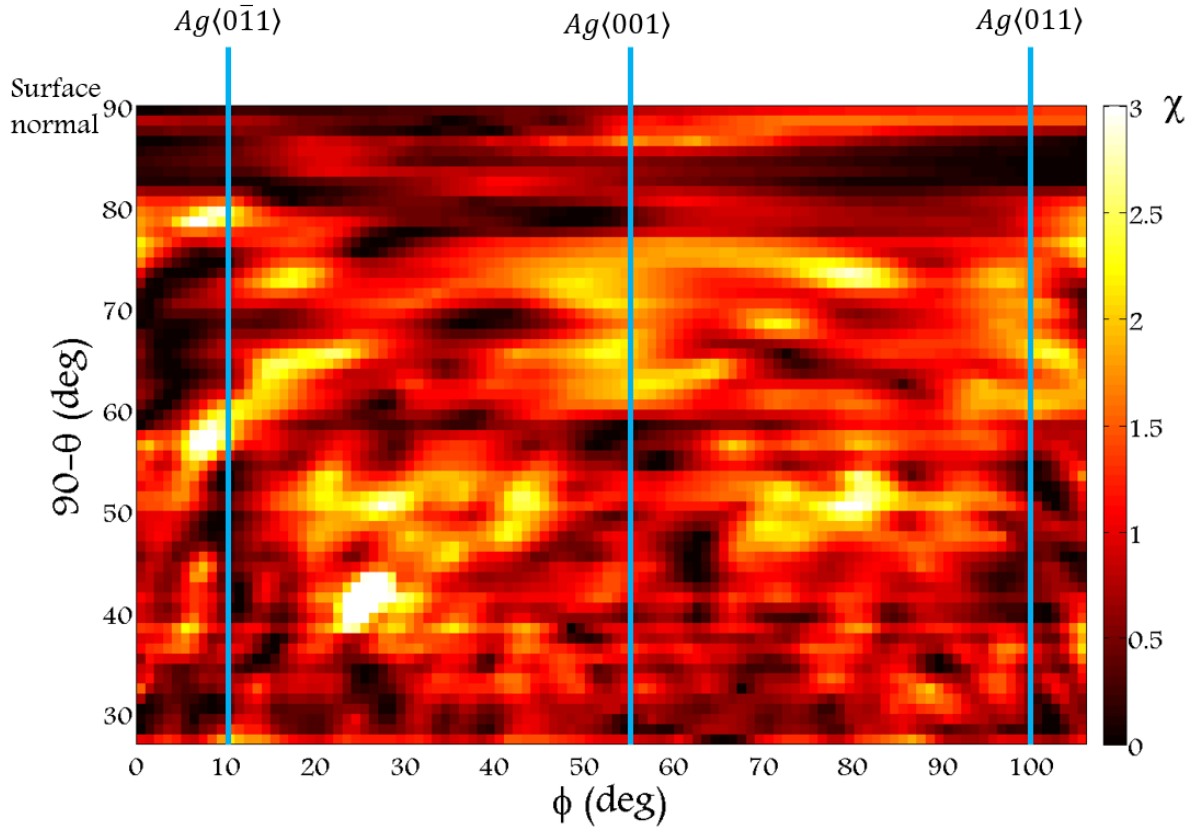

Figure 13: Normalised experimental intensity (anisotropy) of the main Co $2p_{3/2}$ peak as a function of the latitude (90-θ) and the azimuthal angle. High symmetry directions indicated with blue lines.

The normalised diffraction pattern appears to be much richer in spots than the raw one as the contrast of the diffractive component has been significantly improved. As it was expected, the Ag⟨001⟩ direction seems to display bilateral symmetry.

However this representation is not very similar to the physical distribution of anisotropies. In effect, ϕ and θ represent the spherical coordinates of the solid angle, so the data are in reality distributed over a region of a sphere of arbitrary radius. Apart from that, the pixels close to the normal direction (that is those with low values of θ) sample a given area more densely since the distance between neighbouring pixels is smaller, suffice it to say that the differential element of length along lines of fixed polar angle (bear in mind that for the solid angle the radius is set to unity) is $dl_{\phi} = sin\theta d\phi$.

A simple coordinate transformation can offer a visual representation of the data more evocative of the physical distribution of intensities inside the analysis chamber. The idea is plotting the data in spherical coordinates, rather than disposing the azimuth and the polar angle in a Cartesian way.

This is equivalent to making the graphical representation displacing every pixel according to the following equations:

$$\{\phi, \theta, 0\} \rightarrow \{\sin\theta\cos\phi\,, \sin\theta\sin\phi\,, \cos\theta\}$$

The result is:

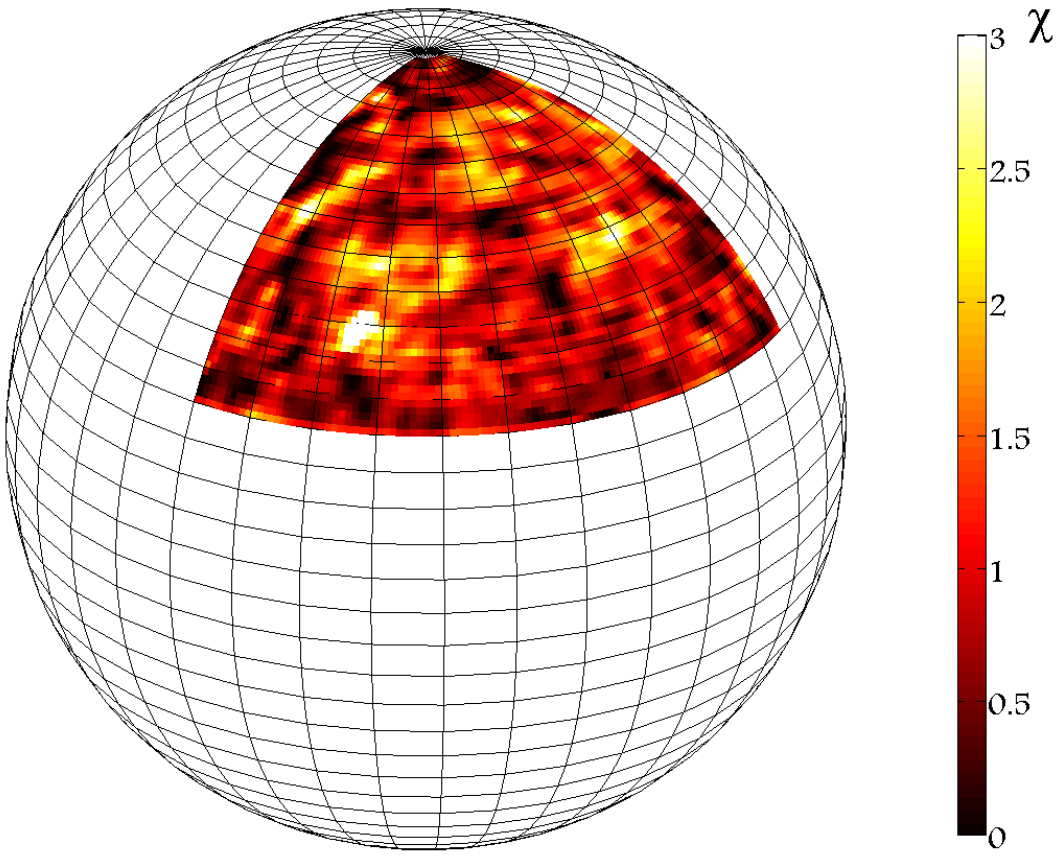

Figure 14: Isometric projection of the spherical representation of the normalised anisotropy.

This figure should be interpreted as if the sample were placed at the centre of the sphere. If the anisotropy is registered by a detector with the shape of the probed solid angle, the pixel at each direction would record (after normalisation) the anisotropy indicated according to the colour scale.

Nevertheless, the three-dimensional distribution doesn't really add much to the discussion and can be problematic when projecting onto the surface of the paper (especially in the case of large regions). For this reason, from now on the patterns will be projected from the sphere onto the equatorial plane as shown in figure 15. This corresponds to what would be seen from a sufficiently long distance if the pattern were observed from the polar axis (or equivalently from the direction normal to the surface).

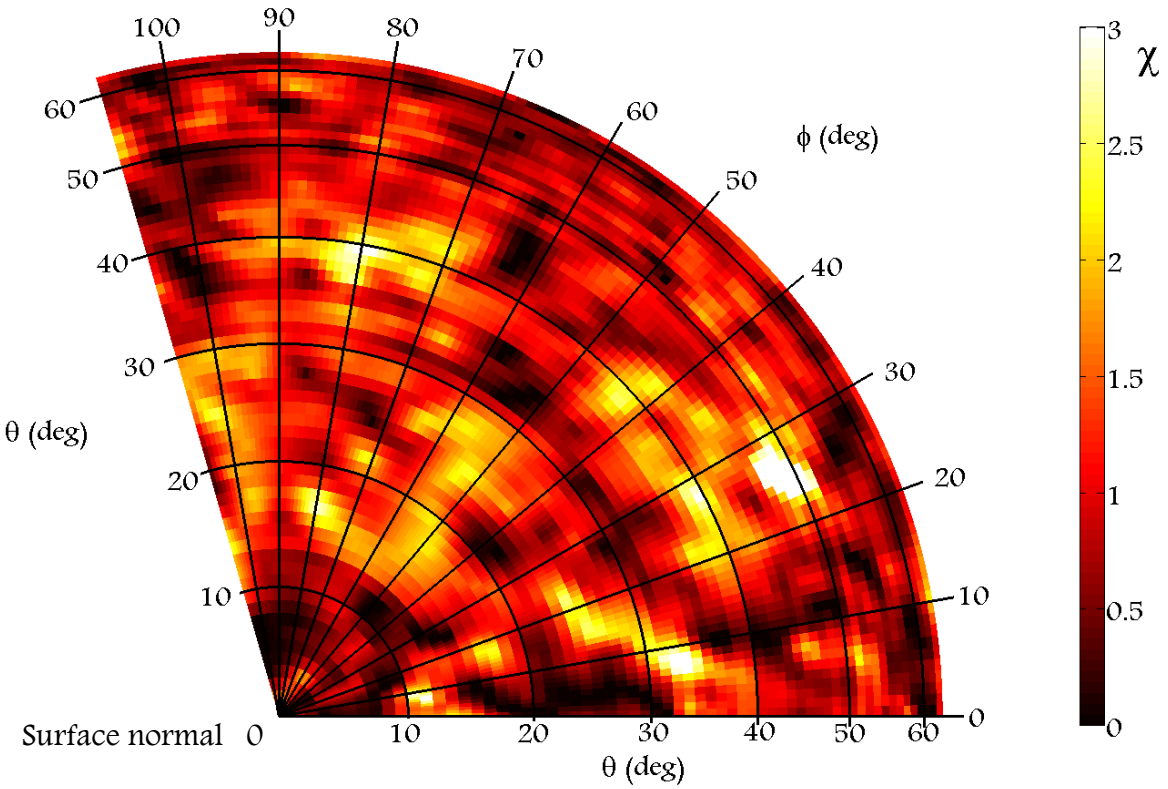

Figure 15: Normalised experimental intensity (anisotropy) at a kinetic energy of 160 eV of the main Co $2p_{3/2}$ peak as a function of the polar angle and the azimuthal angle as it would be seen from the direction perpendicular to the surface of the sample.

6. The XPD simulations

As it has been stated, the experimental diffraction pattern at the used range of energies (the kinetic energy of the electrons was around 160 eV) is difficult to interpret. Because of this obstacle, the approach is rather the simulation of the anisotropy patterns of possible structural models of the system in the framework of multiple scattering in atomic clusters. Those models in general depend on the height of the molecules over the substrate, the relative abundances of the possible adsorption sites and the azimuthal orientation of the molecules.

The output of the *EDAC* code receives the same normalisation treatment as the previous data and in the end both the theoretical and the experimental patterns will be compared in search of the maximum similarity.

The comparison of images is by no means a trivial task. From more rudimentary to more advanced strategies, the comparison could be made via global histograms, brute key-point matching, key-points with integrated decision trees[27] and perceptual hashing[28]. Unfortunately, the small size of the features in the pattern and the randomness of their distribution greatly hinder the application of any of these methods. Instead, a numerical reliability factor[29,30] based on a sum over the pixels will be used.

The underlying model that will produce the most similar simulation will then be the most probable structure of the system.

The first step for running the simulations consists in conceiving the systems. The simulation of the whole silver substrate completely covered with molecules is simply impossible for all practical purposes. With this in mind, the smallest representative section of the system should be chosen, that is, a subsystem small enough to be run on a computer while big enough to display within reasonable limits the same global properties.

As it has been said before, the computational time scales with the second power of the number of scatterer atoms so it would be convenient to disregard as many unimportant atoms as possible.

For this very reason, the molecules were modelled simply as their central cobalt atom. Being the emitter certainly imposes the presence of cobalt but the rest of the molecule can be neglected since the scattering cross-section of carbon, nitrogen and hydrogen is too low[31] to produce significant effects compared to those of silver and cobalt as it can be seen in the figure below. Moreover, the relative abundance of silver in the system is overwhelmingly high so most of the effects come from it.

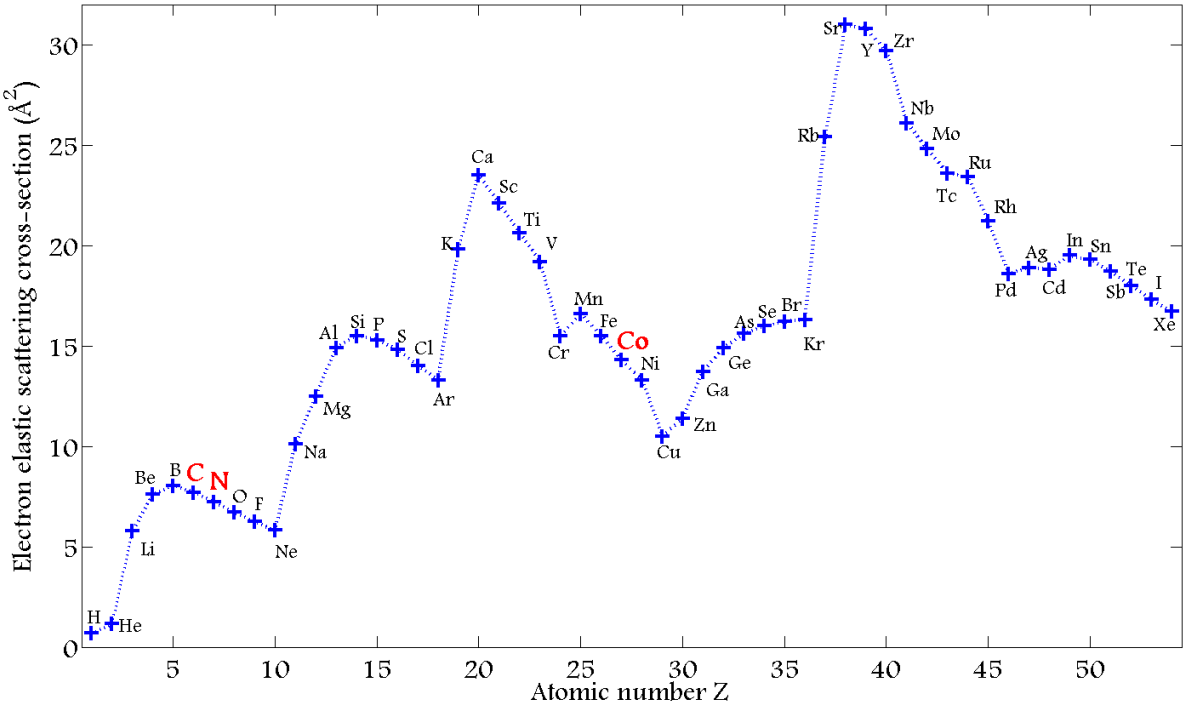

Figure 16: Total electron elastic scattering cross-section for a fixed energy of 160 eV as a function of the atomic number[31].

In most of the simulations only one “molecule” (only its corresponding atom of cobalt) was included in the structural model. This decision was adopted because adjacent molecules are already too far away to have a strong impact on the diffraction pattern. Anyway in order to refine the results the possibility of including several molecules was also tested and had very little effect on the diffraction patterns.

Once these reasonable constraints for practical purposes have been imposed, it's time to model the part of the atomic cluster that will be simulated. There are at least two factors that should be taken into account: the conservation of the underlying symmetry of the global system and the exclusive consideration of high symmetry adsorption sites.

Regarding the adsorption sites, the molecules are going to adsorb on sites where the energy of the system will be minimal. A minimum of energy in a periodic system implies that those points must display the symmetry of the group. In a face-centered system (the case of the silver substrate) there are only three inequivalent points that fulfil the requirements: the top, the hollow and the bridge sites. The following figure depicts the three of them.

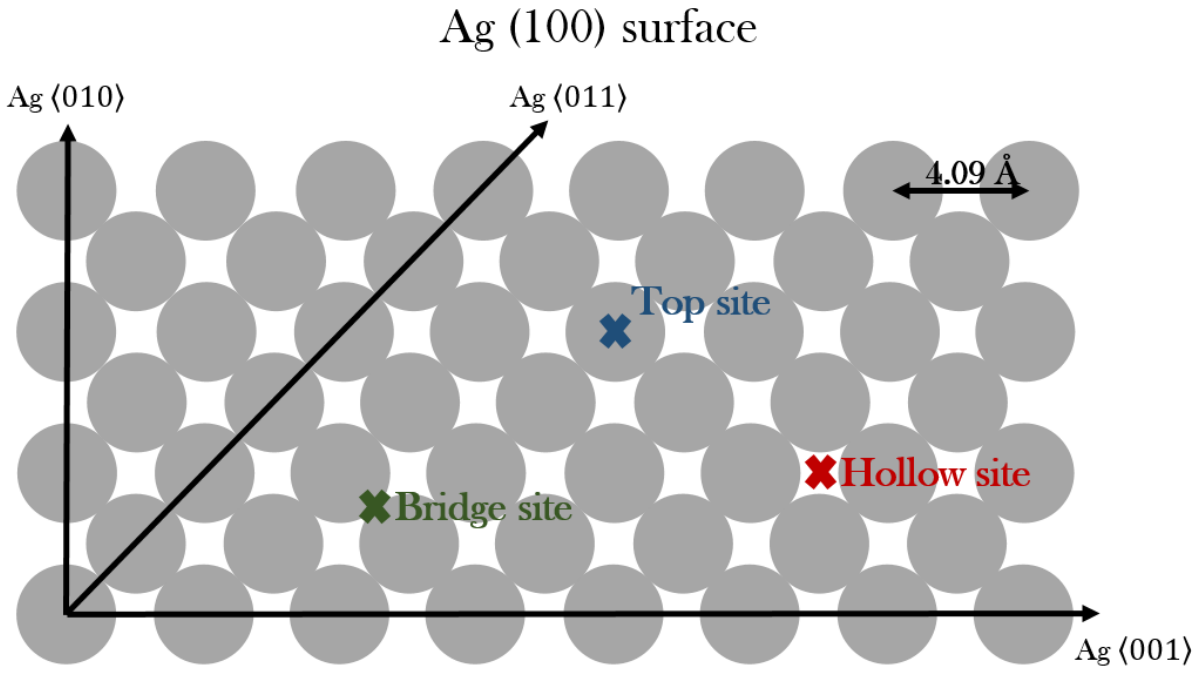

Figure 17: Illustration of the three possible high symmetry sites of adsorption on a portion of a Ag(100) surface.

It must be noted that the top and hollow sites represent local extrema, whereas the bridge site is a saddle point. This fact already points at a greater likelihood of the former sites over the latter, nonetheless the three possibilities were addressed in the simulations.

The centre of the molecule, that is the cobalt atom, is supposed to lie on any of these three sites for the numerical calculations. Since all the molecule is being left behind except for the central atom, and only one molecule is considered in each simulation, this means that the atomic clusters will consist of a fragment of silver terminated with a surface (100) and one additional cobalt atom on any of these three sites.

Apart from that, the diffraction patterns arise from interference between wavefronts cast from nodes (atoms) of a periodic lattice. Because of this, generally the larger the periodic area is, the finer and stronger the diffraction spots become. Consequently, if it's necessary to reduce the system, this operation must absolutely be made in such a way that the symmetry of the system is preserved, otherwise the diffraction features could become weaker or even worse, change altogether.

At this point, great care should be taken of edge effects. The emitter cobalt should then be well surrounded by the system. Given that the mean free path of the electrons is around 5 Å in the conditions of the experiments[32], it is enough to consider the topmost 4-6 layers within a circle of radius ~20 Å.

The following graph portrays one the clusters that were finally simulated, where it's evident that the cobalt is quite far from the edges and within reasonable limits symmetrically surrounded by the substrate.

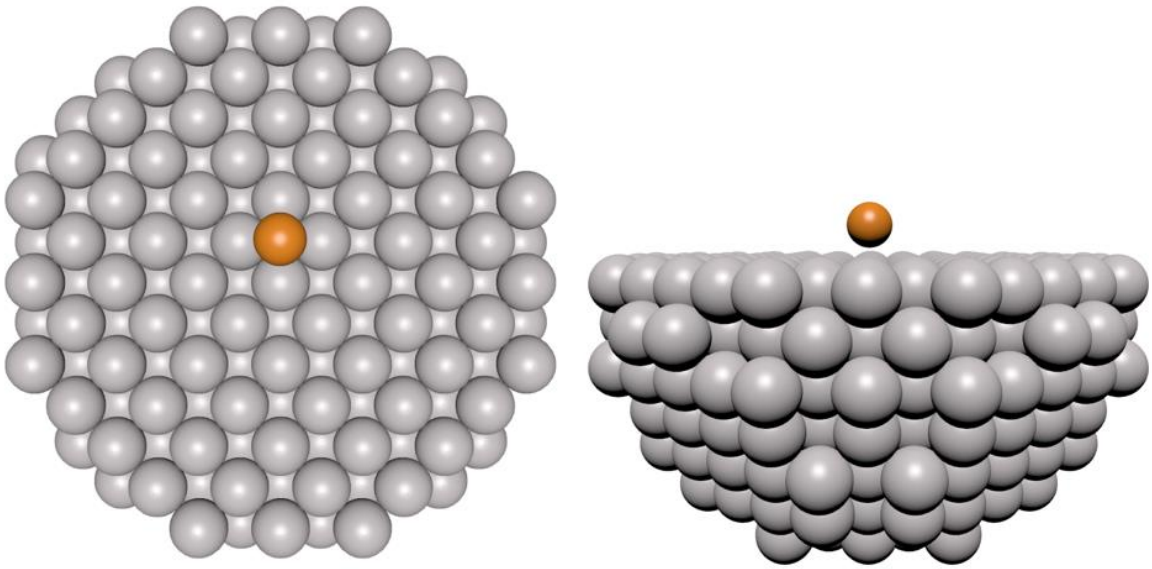

Figure 18: Top (left) and front view (right) of one of the simulated clusters. In particular, this one corresponds to a model with the cobalt atom on a hollow position at a distance of 3 Å over the geometrical plane that contains the centres of the silver atoms of the surface.

Throughout the following pages the effects of modifying the parameters of the model will be shown.

6.a) The effect of the adsorption site

An appropriate starting point would be the study of the influence of the adsorption site on the diffraction patterns.

Even if the two closest sites (bridge and either top or bottom) are separated only by the radius of the silver atom (1.44 Å), such a small displacement changes significantly the vicinity of the emitter and modifies completely the appearance of the anisotropy pattern.

The horizontal shift alters only the orientation of the structure relative to the cobalt atom and the distances between it and the silver atoms.

In effect, by shifting for instance from the hollow site to the top site, there's a rotation of 45º degrees between the horizontal projections of the directions of the closest scatterers to the emitter. Furthermore, this operation modifies the polar angles and the distances with respect to the cobalt atom.

The following figure illustrates the changes in the diffraction patterns as a result of the displacement of the cobalt emitter among the three possible adsorption sites.

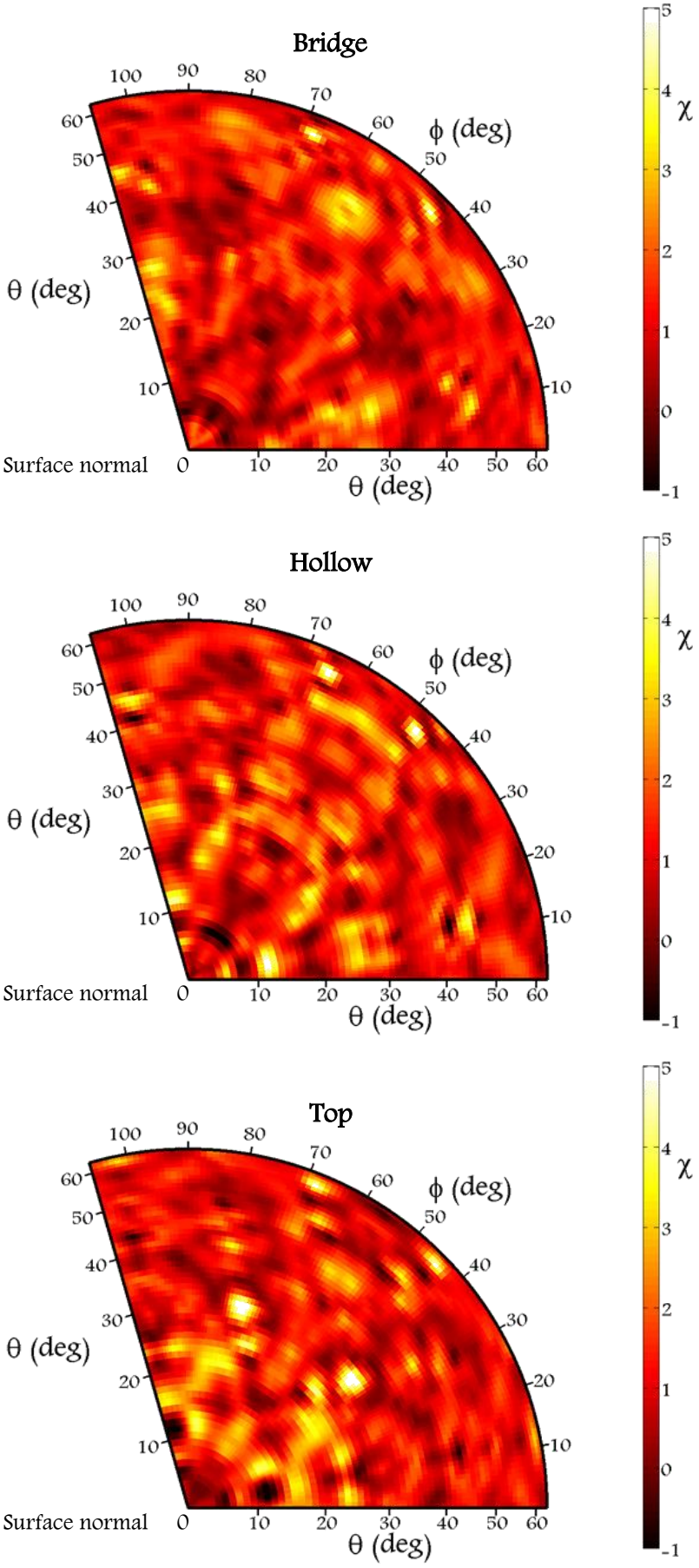

Figure 19: Examples of normalized anisotropy patterns simulated for clusters with the cobalt emitter at 2.8 Å over the substrate at the following adsorption sites from top to bottom charts: bridge, hollow and top. The depicted region matches the one covered by the experimental data shown in figure 15.

As it can be seen, the sites are easily distinguishable with the help of their respective "diffractive signatures".

Keeping in mind the difficulty in the direct interpretation of the patterns, it's possible to expound the most evident features of each configuration. For the sake of discussion, it's convenient to remember that the $\langle 001 \rangle$ direction is at the middle of the pattern at $\phi \approx 55°$ and that there are two equivalent $\langle 011 \rangle$ directions at $\phi \approx 10°$ and $\phi \approx 100°$.

For example, the bridge pattern can be seen as the most isotropic one. Indeed, the contrast in the central part is the dullest among the three. Apart from the spot at $\phi \approx 55°$ and $\theta \approx 50°$, which appears with slight differences in the three sets of data, the only striking structure are both bands along the $\langle 011 \rangle$ directions.

As for the hollow pattern, it displays the two bands referred before, and an additional wide "band" around the $\langle 001 \rangle$ direction made of multiple spots of small size. It also includes two large holes with no structure around $\phi \approx 80°; \theta \approx 50°$ and $\phi \approx 30°; \theta \approx 50°$.

Regarding the top anisotropy, the previously reported bands at azimuths of 10º and 100º are now missing. The most intense excess in signal comes from a region close to the normal direction ($\theta < 25°$) and displays a more pronounced symmetry around the polar axis. This difference with respect to the previous two patterns makes sense because the cobalt atom is on a top site and so the closest scatterer is directly under it, hence enhancing a symmetrical emission along a narrow cone generated from the polar axis. Another interesting feature is the formation of 2 intense spots in the blank zones of the two previous possibilities. It easily allows to tell apart one situation from the others.

In any case, even if the most similar pattern is supposed to be supported by visual perception, the numerical reliability factor will make the task of choosing the optimal simulation much easier.

6.b) The effect of the adsorption height

Within the approximation chosen for the simulations, the other parameter that plays a substantial role in the diffraction pattern is the distance of adsorption, that is, the geometrical distance to the plane defined by the centres of the silver atoms lying at the local surface where the CoPc molecule gets stuck.

In the context of previous research[24,33], numerical simulations performed in the framework of the Density Functional Theory (DFT) have offered values for this parameter that range from 2.7 to 3.1 Å. Those results were obtained for an isolated CoPc molecule on Ag(100) and Ag(111), but it's reasonable to suppose that the effect of completing the CoPc monolayer does not push the height, if at all, beyond those limits.

For the simulations reported in this thesis, the possible interval for the adsorption distance considered was larger. In particular, it spanned the 2.0-3.2 Å range with steps of 0.1 Å because the local density approximation yielded a value of 2.4 Å for this parameter[24]. Likewise, a similar molecule (Co-tetraphenyl-porphyrin) has been shown to get adsorbed at 2.45 Å from a Ag(111) surface[34].

The evolution of the hollow pattern as a function of the distance of adsorption is shown in the figure below.

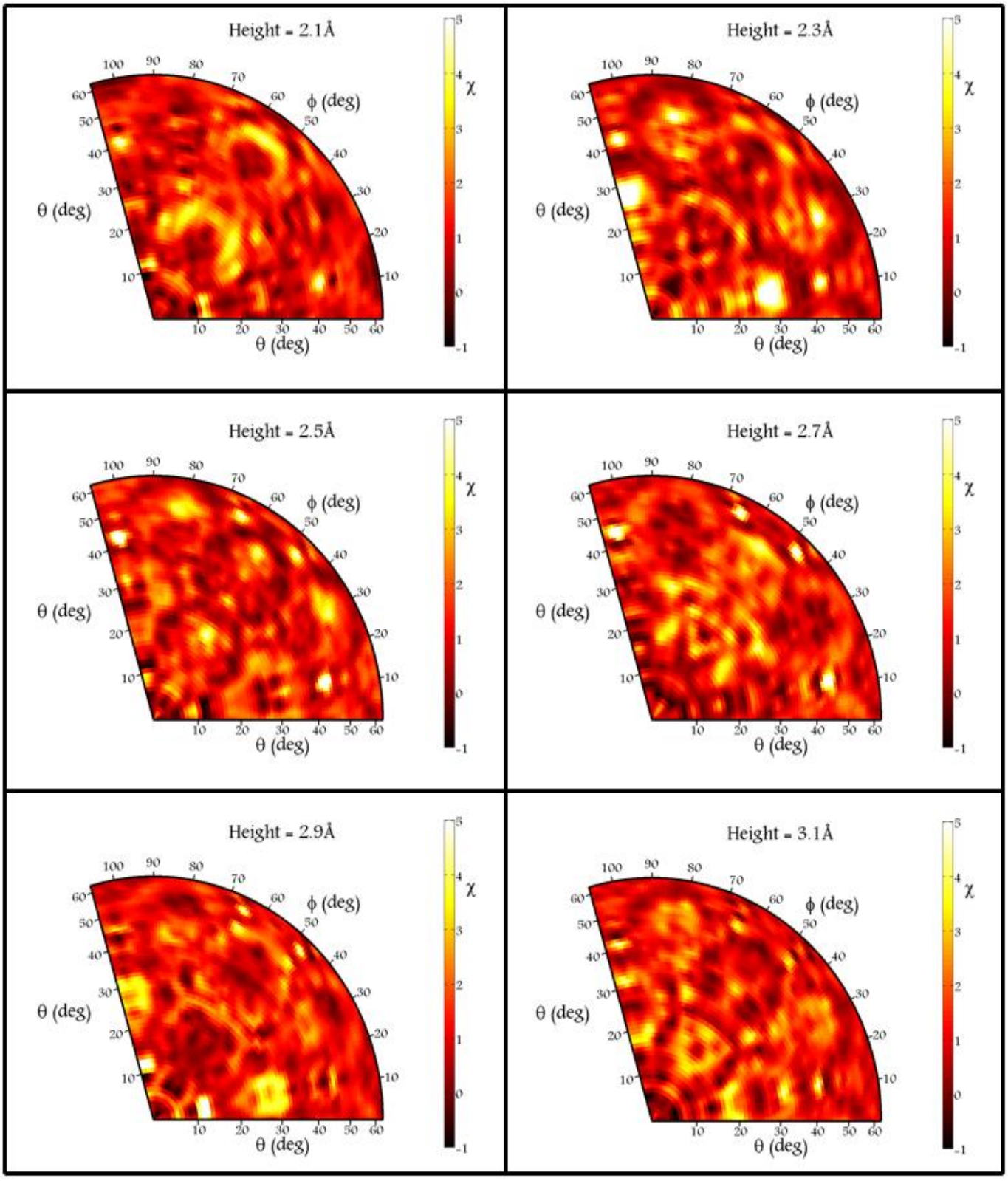

Figure 20: Normalised simulated diffraction patterns of one cobalt atom on a hollow site of a Ag(100) surface as a function of the height of adsorption. The depicted region matches the one covered by the experimental data shown in figure 15.

This shows that even very small variations in the geometrical parameters, such steps of 0.1 Å in the distance of adsorption can induce remarkable changes in the diffraction patterns. This demonstrates that the XPD technique excels at probing the smallest possible scales down to the atomic level.

It's not really worth analysing individually the anisotropies, but at least the previous patterns allow some comments. Several bright structures evolve with the increasing height in a similar way to wave interferences, for instance, the two equivalent zones or "lobes" centred at $\phi \approx 80°;\theta \approx 45°$ and $\phi \approx 30°;\theta \approx 45°$. For 2.3 Å they are one of the most intense features. Then at 2.7 Å they become very dark, nearly blank, they look almost like the negative of their appearance at 2.3 Å. If the cobalt atom is then displaced again 0.4 Å up to 3.1 Å, the structure is bright again.

The described phenomenon is reminiscent of the shift of interference stripes on a device such as the Michelson interferometer when the length of the arms is modified.

As it has been shown, the diffraction patterns change rapidly in a non-evident way when the parameters are adjusted even slightly. Apart from that, the existence of at least two inequivalent sets of molecules seems reasonable, so the experimental pattern may arise from a model more complex than the simple cases that have been examined so far. That makes necessary the introduction of another source of variability: the presence of inequivalent sets of molecules.

7. The search of the appropriate model

In principle, the XPD experiments involve the use of an intense flux of electrons to obtain a good signal to noise ratio. Yet it is small enough to keep at bay charge space effects such as spectroscopic shifts (around 10 meV for a current spectrometer[35]). With this in mind, the electrons are expected to interact weakly among them and the final intensity output can be interpreted as the linear combination of the excited electrons as if they had been extracted independently and far away from the rest of the photoemissions.

For this very reason, the existence of inequivalent sets of molecules is trivial to introduce. If there are 3 different sets (one for each site of adsorption) with population weights w_i and their photoionization cross sections are comparable, which is a sensible assumption as it is an atomic intrinsic property, the "composite" pattern can be generated by adding the intensities pondered with the corresponding population weight:

$$I_{\text{composite}}(\phi,\theta) = \frac{\sum_{i=1}^{3} I_i(\phi,\theta)\cdot w_i}{\sum_{i=1}^{3} w_i}$$

According to this, it suffices to simulate the patterns for each adsorption site (bridge, hollow and top) and for each considered value of the height of the molecules over the surface. Then, those patterns are combined with the desired proportions and the final intensity map accounting for the possibility of multiple adsorption sites is obtained.

The populations studied were all the possible combinations among the three adsorption sites by steps of 10%. So the weights could take the values given by:

$$w_{Top} = \{0,0.1,0.2, \dots ,0.9,1\}$$
$$w_{Hollow} = \{0,0.1,0.2, \dots ,0.9,1\}$$
$$w_{Bridge} = \{0,0.1,0.2, \dots ,0.9,1\}$$

But their sum must be equal to 1.0, otherwise the three populations together would be below or over 100%:

$$w_T + w_H + w_B = 1$$

This restricts enormously the available space of populations when compared to what it would be if the three variables were independent (11^3=1331 possibilities).

So w_T can be chosen to adopt any of its eleven possible values:

$$w_T = 0.1(i-1)\ \forall i \in [1,11] \in \mathbb{N}$$

Then, the sum of w_H and w_B is bound to be equal to:

$$w_H + w_B = 1 - w_T$$

w_H can take any value from 0 to $1 - w_T$, and w_B is then automatically fixed. Under these constraints the number *N* of available options is:

$$N = \sum_{i=1}^{11} \sum_{j=1}^{12-i} 1 = \sum_{i=1}^{11} 12 - i = 66$$

Hence, for every distance of adsorption 66 cases were considered. Taking into account the considered heights of the cobalt atom on the surface:

$$d(\text{Å}) = 2.0 + 0.1 \cdot i, \forall i \in [0,12] \in \mathbb{Z}$$

The space of parameters has 858 points or cases in total. The exclusive ocular inspection of them to choose the best model is absolutely impractical, not only because of the sheer amount of possibilities but more importantly because it's extremely difficult to ascertain the most similar pattern as there are a few of them whose resemblance depends purely on tiny nuances and the criterion used to evaluate the similarity.

The following figure illustrates this diversity. It shows the diffraction patterns that result from the linear combination of the top, hollow and bridge simulations as a function of the relative weight of each component for a fixed distance of adsorption of 2.8 Å.

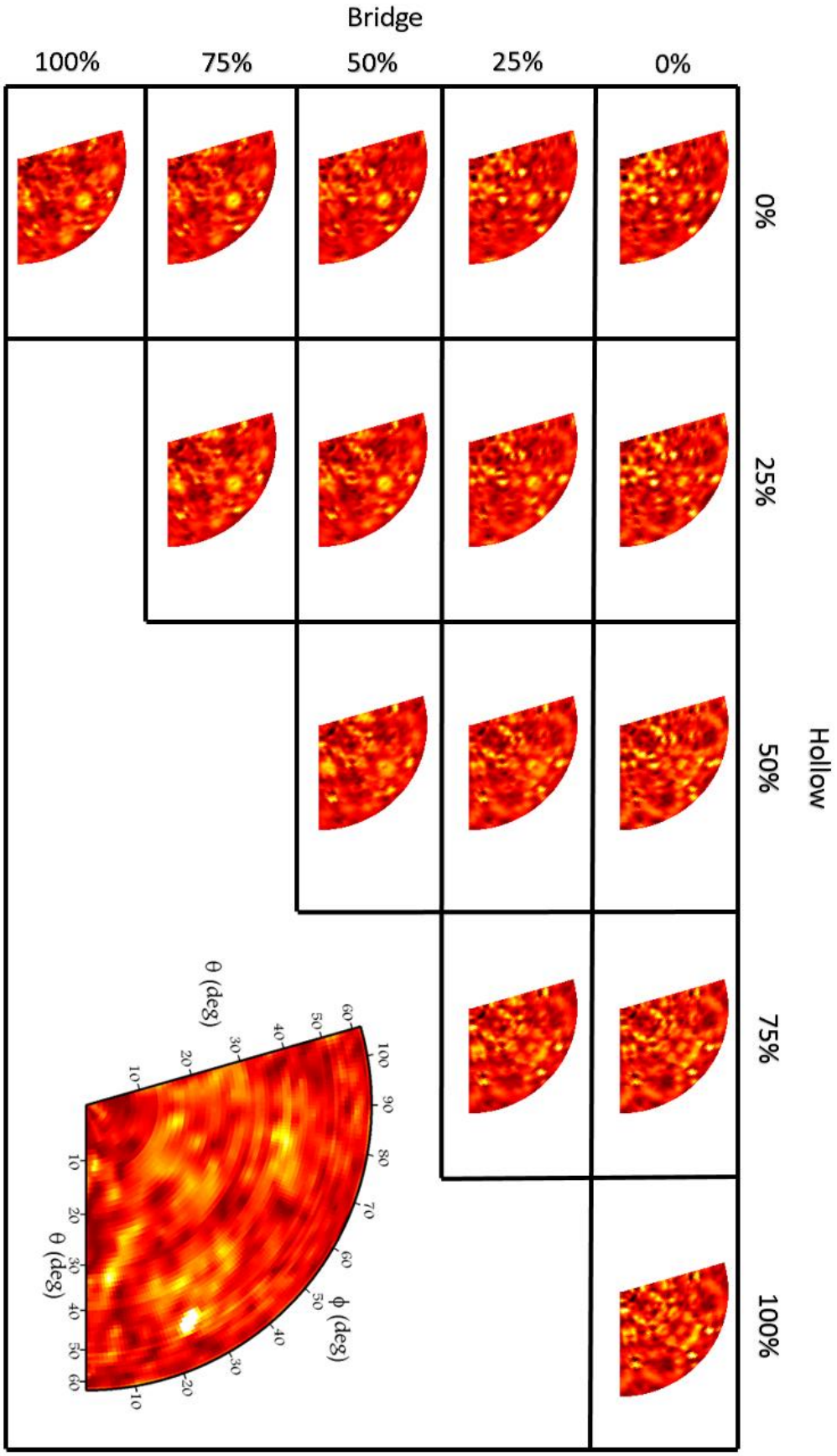

Figure 21: Diffraction patterns for an adsorption distance equal to 2.8 Å that result from combining the top, hollow and bridge contributions as specified by the axes. The top one can be deduced by subtracting the other two from 100%. For the sake of comparison the experimental data have been displayed in the bigger anisotropy map.

At this point the reliability factor *R* comes in handy as it assigns a numerical value to every simulation that tries to quantify how well the simulated patterns match the experimental one. It's mathematically defined as a sum over the pixels of the normalised variance between the mentioned patterns:

$$R = \frac{\sum_{pixels}\left(\chi_{exp} - \chi_{sim}\right)^2}{\sum_{pixels}\left(\chi_{exp}^2 + \chi_{sim}^2\right)}$$

In this expression χ_{exp} stands for the experimental anisotropy and χ_{sim} for the simulated one.

The reliability factor has a minimum value of 0 when both anisotropy patterns are identical. Regarding the upper bound it's simpler to transform the expression:

$$R = \frac{\sum_{pixels}\left(\chi_{exp} - \chi_{sim}\right)^2}{\sum_{pixels}\left(\chi_{exp}^2 + \chi_{sim}^2\right)} = 1 - \frac{2\sum_{pixels}\chi_{exp}\chi_{sim}}{\sum_{pixels}\left(\chi_{exp}^2 + \chi_{sim}^2\right)}$$

Since the anisotropies are non-negative by definition:

$$\chi_{exp}\chi_{sim} \geq 0 \rightarrow \frac{2\sum_{pixels}\chi_{exp}\chi_{sim}}{\sum_{pixels}\left(\chi_{exp}^2 + \chi_{sim}^2\right)} \geq 0$$

The upper bound for *R* will happen if

$$\sum_{pixels}\chi_{exp}\chi_{sim} = 0$$

And this is only possible if either χ_{exp} or χ_{sim} are alternatively equal to zero in every single pixel. In that situation the reliability factor would have a value of 1.

In short, the reliability factor *R* is a coefficient that evaluates the similarity between the experimental and simulated patterns whose value is 0 for a perfect match and 1 in the most dissimilar of the cases.

After determining the method to evaluate the extent to which two patterns are similar, all the anisotropies for every point of the space of parameters were calculated, and the corresponding R factors were computed. The subsequent identification of the most suitable model is done by searching the lowest reliability factor.

The distribution of the R factor for every value of the distance of adsorption is displayed in figure 22.

The first striking result is the relatively small dispersion of the R factor. In effect, the minimum value is around 0.22 and the maximum, which is by far the most significant outlier even within the distribution of 2.5 Å, is found at around 0.42. In fact, more than 90% of the reliability coefficients are included in the interval $[0.25,0.35]$.

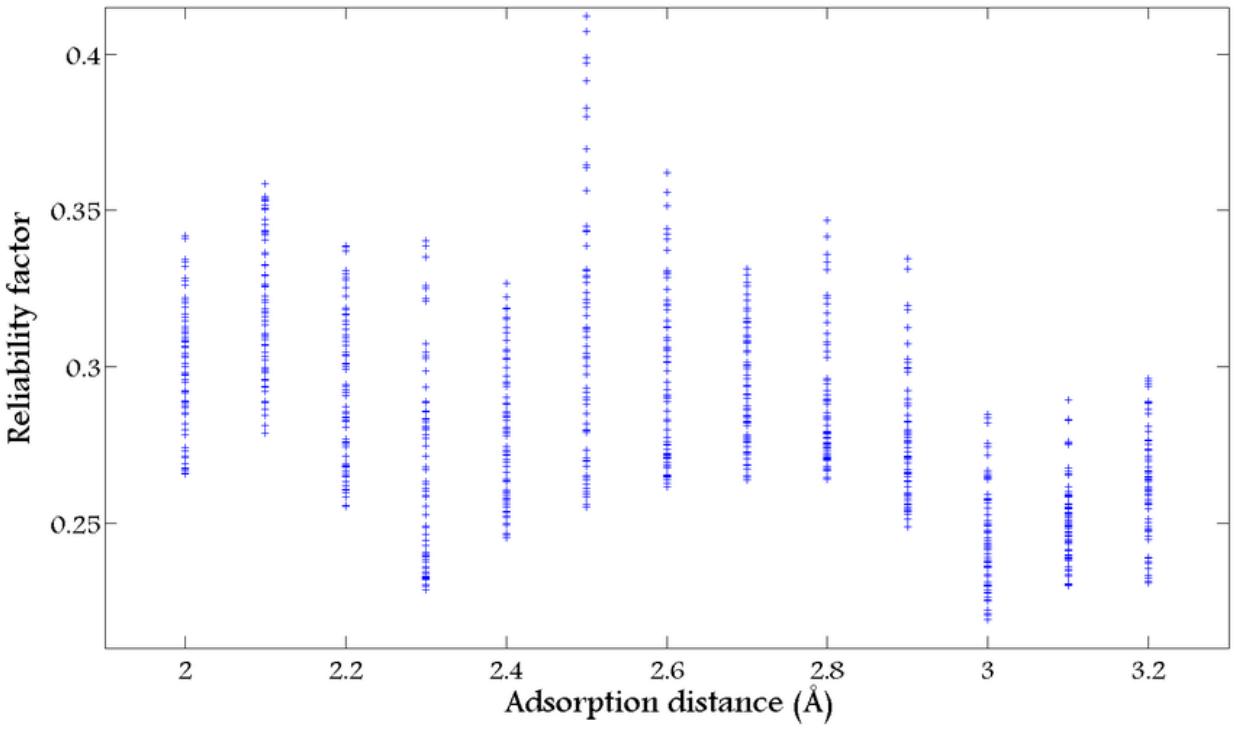

Figure 22: Distribution of calculated reliability factors as a function of the distance of adsorption.

There are two minima of the R factor. The one at 2.3 Å is a relative minimum with a value of 0.229 whose underlying composition is 80% bridge and 20% hollow. The absolute one, with a value of 0.219, is found for a distance of adsorption equal to 3.0 Å and is built from 20% bridge, 40% hollow and 40% top.

The latter option prevails for several reasons. First of all, it is the absolute minimum, so it is already the most probable configuration. Secondly, as it has been stated, within the local density approximation, which is well-known for predicting too short distances, the numerical value was 2.4 Å. This height is already greater than 2.3 Å, so the immediate conclusion would be that the relative minimum is at the very least far-fetched. Finally, as it will be deduced soon from geometrical constraints imposed by the (7×7) reconstruction, the first configuration will be translated into 100% bridge while the second one will turn into 50% hollow + 50% top. In the first case there is only one population, so at least two sets of inequivalent molecules are not expected. However, the second case predicts two identical in size populations that could show different properties.

The preliminary conclusion of this section is that CoPc molecules in the (7×7) phase seem to get adsorbed on the Ag(100) substrate at a distance of approximately 3.0 Å and are distributed on the adsorption sites according to the following proportions: 20% bridge, 40% hollow and 40% top. This result is in agreement with previous evidence[24,36] on isolated MPc molecules on silver substrates which shows that the adsorption height is approximately equal to 3.0 Å.

The next section's objective will be trying to perform a refinement of the model, both by introducing additional constraints on the populations and by adding and determining an additional parameter, the azimuth of the molecules with respect to the surface in order to explain the STM image shown in figure 4.

8. Refining the model

So far, the simulations have provided the most likely configuration of the system but some details and coherent corrections have yet to be introduced. The starting point will be the study of the geometrically possible configurations.

8.a) Constraints imposed by the (7×7) periodicity

The probed system as determined by electron diffraction and STM is a (7×7) reconstruction with the same orientation as the silver substrate. This imposes strict constraints on the sites of adsorptions because once one molecule is fixed on a high symmetry site, the rest of them are automatically fixed and hence the populations cannot vary arbitrarily.

This implies that there are two possibilities. The starting point could be either a top site or a bridge site. The hollow site has been neglected because as it will be shown the produced structure is equivalent to the one generated from the top site.

These two options are reflected in the figures below. If the reconstruction is generated starting from a top site, the obtained unit cell contains one atom on a top site at the centre, and another one (distributed among four neighbouring cells according to the representation below) on a hollow site.

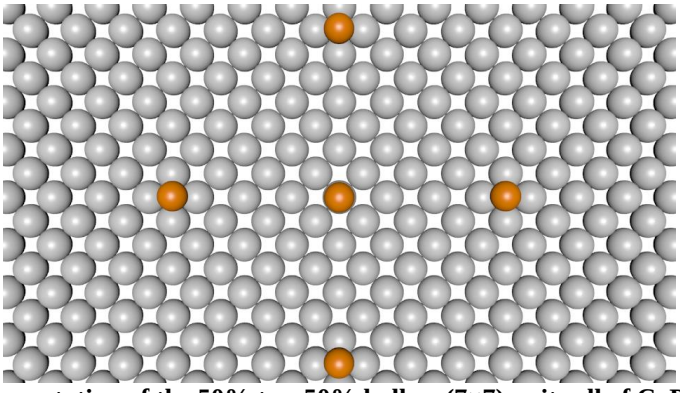

Figure 23a: Representation of the 50% top-50% hollow (7×7) unit cell of CoPc on a Ag(100) surface. Only the cobalt atoms of the molecules have been depicted

If a bridge site is chosen as the starting point instead, each unit cell contains two atoms on bridge sites, as shown below.

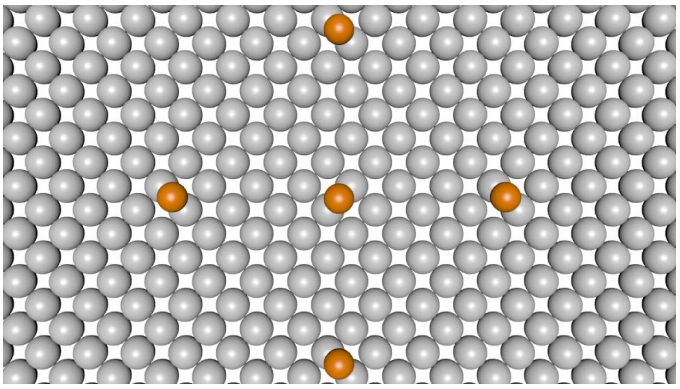

Figure 23b: Representation of the 100% bridge (7×7) unit cell of CoPc on a Ag(100) surface. Again, only the cobalt atoms of the molecules are portrayed.

It is now clear that a molecule on a hollow site or on a top site is immediately translated into 50%-top and 50%-hollow populations whereas a bridge site would impose a 100% bridge population.

In the light of this, the previous configurations could be reinterpreted as specified in the following table:

Distance of adsorption (Å)	Best match populations			Best match reliability factor	Reinterpreted populations			New configurations' R-factor
	%B	%H	%T		%B	%H	%T	
2.3	80	20	0	0.229	100	0	0	0.251
3.0	20	40	40	0.219	0	50	50	0.236

Table 4: Reinterpretation of the results obtained from the comparison between the simulations and the experimental data after imposing the restrictions from the geometry of the phase.

As it can be checked, even after adapting the most probable configurations to stricter geometrical constraints, the one found for a distance of adsorption equal to 3.0 Å remains as the most likely.

8.b) Configurations with populations at different heights

In the preceding discussion, when the bridge, hollow and top patterns were combined to introduce the possibility of several coexisting adsorption sites, the considered addends were always simulations whose cobalt atoms lied at the same height over the last layer of silver. In other words, in every "column" of points in figure 22, the three populations share the same distance of adsorption specified on the abscissa axis.

However, if there are indications that hint at the coexistence of at least two inequivalent sets of molecules, it's reasonable to think that if there are two different orientations of the molecules, there could be two slightly different heights over the surface. This was the idea behind the endeavour to study combinations of molecules at different levels.

Of course, no big changes on the distance of adsorption are expected, but an inspection on the 50% top and 50% hollow configuration may lead to the preliminary conclusion that the cobalt atoms on hollow sites could be at a lower level given that they don't have any silver atom immediately beneath.

This reasoning is overly naïve because even if the rest of the molecule has not been modelled for purposes related to the simulations, the cobalt atom is still the centre of a molecule that covers roughly a square of 1nm of side. This size is more than three times the diameter of silver atoms so the molecule is actually "supported" by approximately 9 atoms. Since the molecule is usually flat[37] when it gets adsorbed and the rest on the atoms cannot penetrate into the substrate either, there could only be a small shift between the molecules on top and hollow sites, if at all.

A test was performed by combining evenly (50%-50%) the top and hollow contributions for all possible pairs of distances of adsorption with the simulated patterns. Such a test was excessive and then not done for a 100% bridge configuration, as all the CoPc molecules would be supposed to adsorb at the same distance.

This verification allows to check if the assumption of all the molecules at the same height is simplistic. The R factors associated to the combinations are represented in the following heat map:

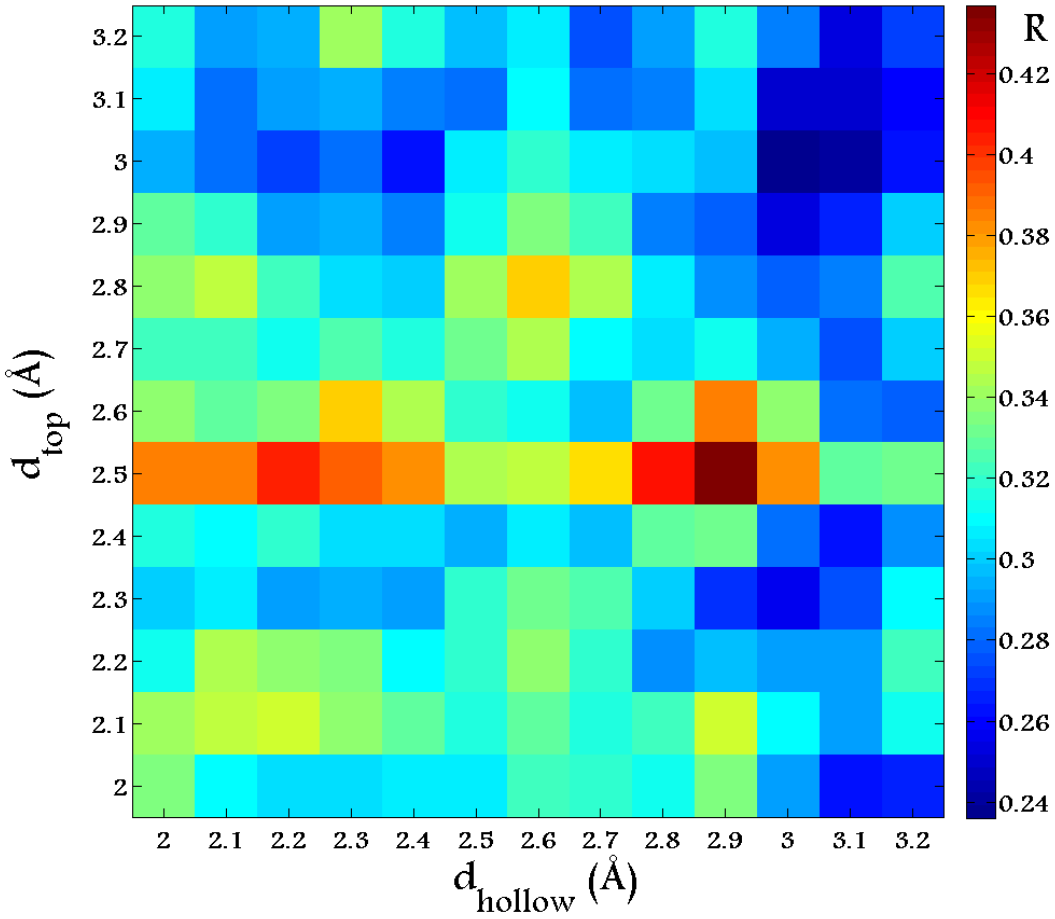

Figure 24: Distribution of the reliability factors corresponding to configurations 50% top + 50% hollow as a function of the distance of adsorption of each population when they are allowed to vary independently.

Once again the system that best matches the experimental data is the configuration that produces the lowest R factor. That corresponds to the darkest shade of blue featured on the image, which is found for a 50% top + 50% hollow phase whose molecules both stick at 3.0 Å over the Ag(100) surface.

Although there are some other blue zones, they're all produced by unreasonable combinations of parameters. In effect, as it was explained before, the difference in height between both populations of molecules should be small. This restricts the search of the minimum R factor to the region close to the main diagonal ($d_{top} = d_{hollow}$) of the map, not beyond a shift of about 0.2 or 0.3 Å at most. Actually, it has been established that a "cross-talk" between adjacent molecules probably mediated by the substrate may take them to a common and intermediate height[38]. In any case, it should be mentioned that within the reached sensitivity a small difference in height between the inequivalent molecules cannot be discarded.

Interestingly the assumption introduced at the beginning, that is, all the molecules adsorbing at the same distance, holds in the light of these results. Now that the adsorption sites and distances have been well determined, some further effort can be devoted to the study of the azimuthal orientation of the CoPc molecules on the surface.

8.c) The azimuthal orientation of the molecules

So far, all the reported simulations have been simplified through the replacement of the molecules with one single molecule reduced to its central cobalt atom. Within this level of approximation, the study of the azimuthal orientation of the CoPc molecules is impossible. Since the cobalt atoms are spherically symmetric, any rotation around any axis has no effect and so the system needs the introduction of more atoms.

The rest of the molecule has been neglected mainly because of the distance to the cobalt atom and the scattering cross-section. These assertions are still valid, so it's only necessary to add the minimum amount of atoms that allow to deduce the azimuthal orientation while respecting the symmetry of the molecule.

The most advantageous compromise is the introduction of the four nitrogen atoms that are the closest to the cobalt atom. The molecule is no longer a single atom, but a cross of four nitrogen atoms with a cobalt in the centre.

The figure below shows the first simplification and the subsequent refinement of the model used to study the orientation of the molecules.

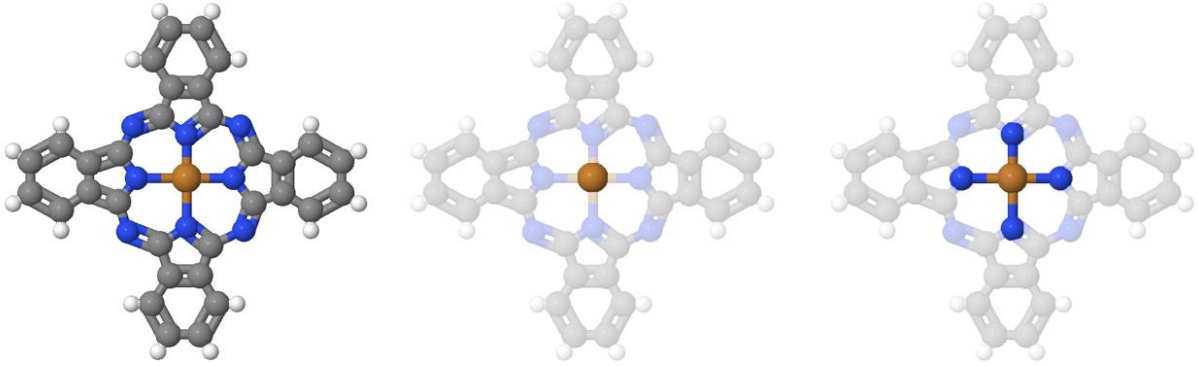

Figure 25: Models of CoPc used in the simulations compared to the real molecule. The semi-transparent parts were neglected in the simulations. The middle model (the cobalt atom) has been used for the simulations reported so far. The right model, including 4 additional nitrogen atoms, was introduced to probe the orientations of the molecules on the surface.

As it can be seen in figure 25, the segments that connect the cobalt atom with each nitrogen are parallel to the directions of the "arms" of the molecule. This is an improvement of the model that has very little impact on the necessary time to perform the calculations of the EDAC code.

Another interesting point of this approach is that it makes possible to test to what extent it is a good idea to replace the molecules only with the cobalt atom. It will be immediate to compare nearly identical simulations whose only difference is the presence of the four nitrogen atoms and check if it's a reasonable to leave most of the molecule behind.

This test was more restricted than the previous analysis as the sites and distances of adsorption are already well established. It was performed on 50% hollow + 50% top configurations at distances ranging from 2.9 to 3.1 Å over the silver surface.

Since the STM measurements revealed two orientations (around 5º and 30º with respect to the compact directions of the substrate), those were the values of the azimuth introduced in the refined clusters for the simulations.

There are two molecules per unit cell and the simulations point at an evenly distribution of top and hollow sites. If the molecules have to fit comfortably in the unit cell, there are two options:

1) 50% top at 5º from the ⟨011⟩ direction + 50% hollow with 30º of azimuth
2) 50% top molecules at 30º + 50% hollow at 5º

The following figure shows one example of the effect on the anisotropy patterns caused by adding the four nitrogen atoms.

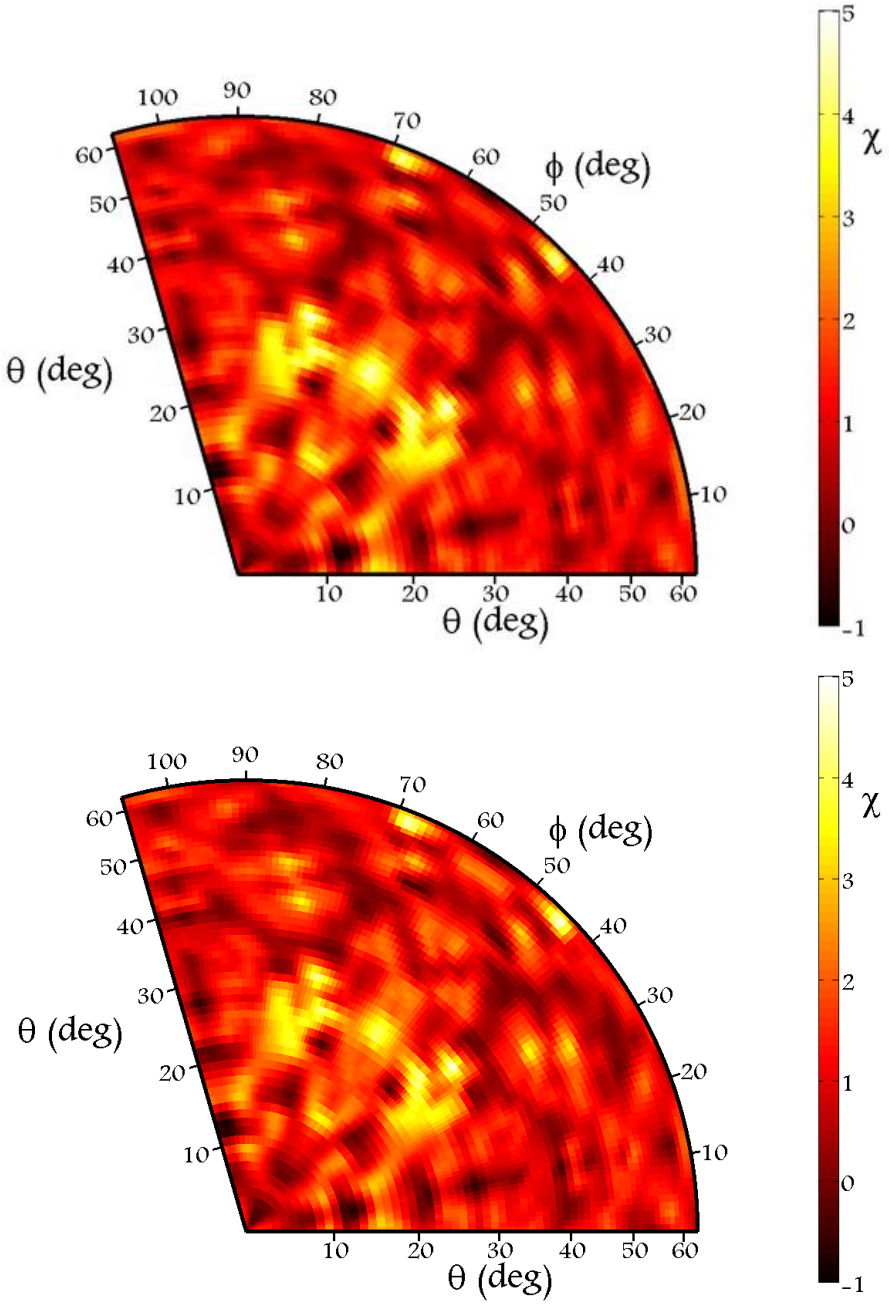

Figure 26: Normalised diffraction patterns of a cobalt atom on a top site at 2.9 Å over the surface (top graph) and the same atom surrounded by four nitrogen atoms at 5º from the compact directions of silver under the same parameters of adsorption (bottom).

The differences are barely noticeable. In order the make them more evident, the absolute subtraction of the first pattern from the second is represented in figure 27. Given the small relative amplitude of the disparities, the colour scale has been modified in the lower graph so as to enhance the contrast.

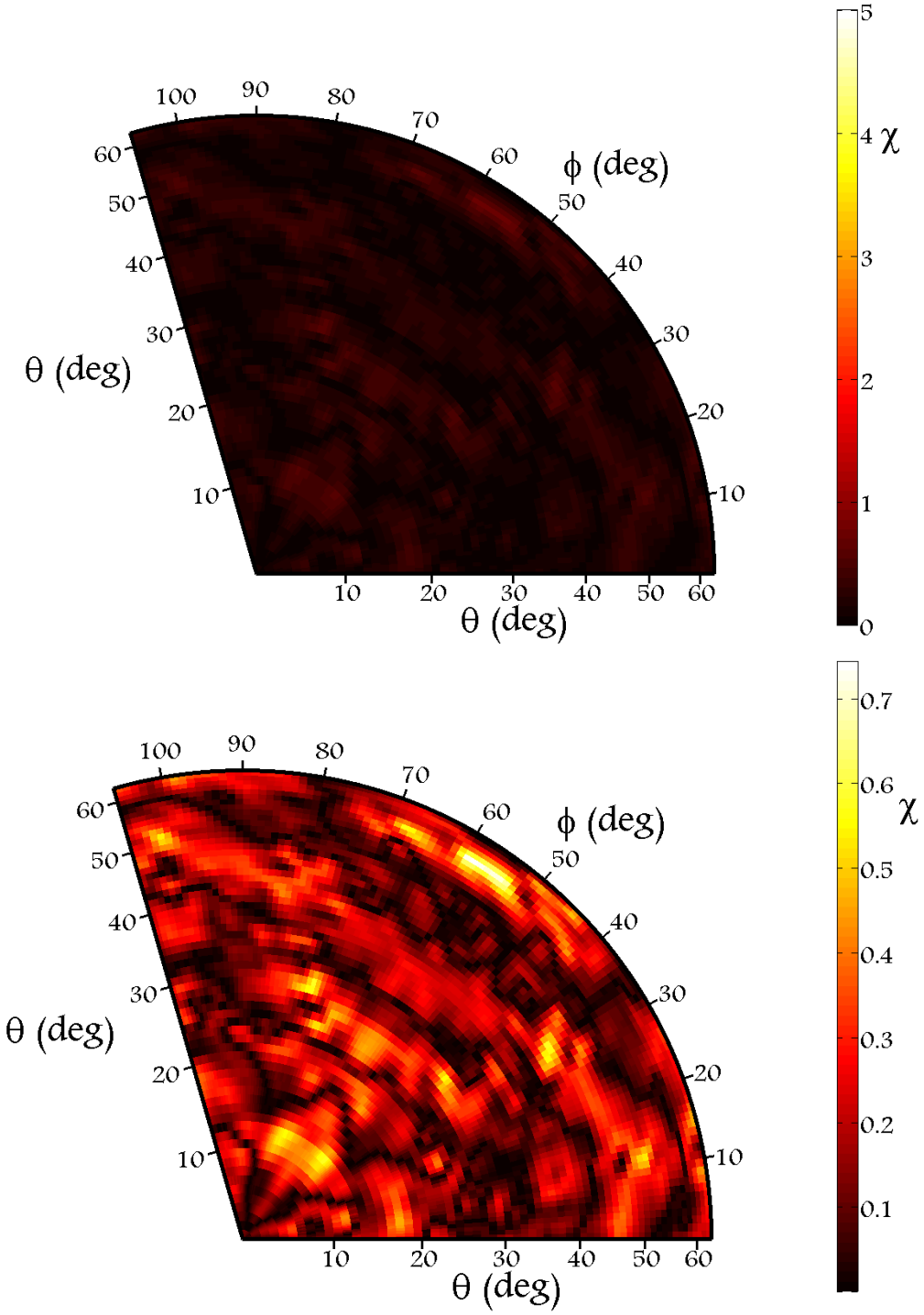

Figure 27: Diffraction pattern that results from the subtraction of the ones shown in figure 26. The same colour scale has been preserved on the upper anisotropy map to better grasp the small contribution of the four nitrogen atoms. The lower figure corresponds to the same data with an adjusted colour scale that enhances the expression of the features.

As the data reveal, both patterns are nearly identical and thus the effect of placing a greater part of the molecule is practically irrelevant. Moreover, the rest of the atoms are located even further away from the centre and should manifest an even smaller impact. This allows to ensure that all the preceding discussion was sensible.

The following step is calculating the reliability factors of the improved clusters and evaluating whether or not the incorporation of the four atoms increases the similarity between the experimental and the simulated patterns.

The table below contains the coefficients R of the new simulations:

Simulations with the distribution of sites: 50% top + 50% hollow			
Distance of adsorption (Å)	**R factor Cobalt atom alone**	**R factor top 5º, hollow 30º**	**R factor top 30º, hollow 5º**
2.9	0.283	0.278	0.289
3.0	0.236	0.228	0.238
3.1	0.254	0.236	0.264

Table 5: Reliability factors for clusters 50% top + 50% hollow with the specifications written in the second row as a function of the distance of adsorption.

As shown in the previous table, the introduction of the 4 closest nitrogen atoms improves the match between the simulated and the experimental data, but only when the azimuth of the molecules adsorbed on top sites is 5º with respect to the ⟨011⟩ direction of silver and the one of those absorbed on hollow sites is 30º. The other possible configuration (30º top + 5º hollow) appears as less probable.

The changes in the R factor are very small but this what was expected after seeing the magnitude of the variations included in figure 27.

After the inclusion of the 4 nitrogen atoms the configuration that yields the lowest reliability factor is in fact 20% bridge, 40% hollow and 40% top again. Coincidence or not, this fact is noteworthy and some arguments could shed light on why such an improbable configuration has turned out to be the most likely from the numerical point of view.

First of all, the studied system is expected to present a significant number of defects or aspects that haven't been modelled in the simulations. Some examples would be vacancies or dislocations in the substrate, terraces on the surface of silver, eventual stacking defects of the molecules, contaminant species etc. Although their effect is probably weak, they could leave an imprint on the diffractive signature (like the effect of the four nitrogen atoms explained before) and be responsible of that small contribution from the bridge site. Some conditions could even force some molecules to lie on bridge sites.

Secondly, the experimental data have undergone and intensive treatment which has cancelled more than 50% of the signal, the part that was identified as the polar profile of background. Even before that process the experimental data are susceptible to modifications such as the ones induced by electronic noise.

And finally, the simulations are by no means perfect. Some systems are more easily simulated while some others are more problematic, but even in the most favourable of cases, the EDAC code uses an approximation of the solution. More iterations could have produced the exact solutions, but the improvement after 20 of them was negligible while requiring increasingly longer times.

The experimental pattern and the best simulation (50% hollow at 30º + 50% top at 5º) are shown for comparison in the figure below:

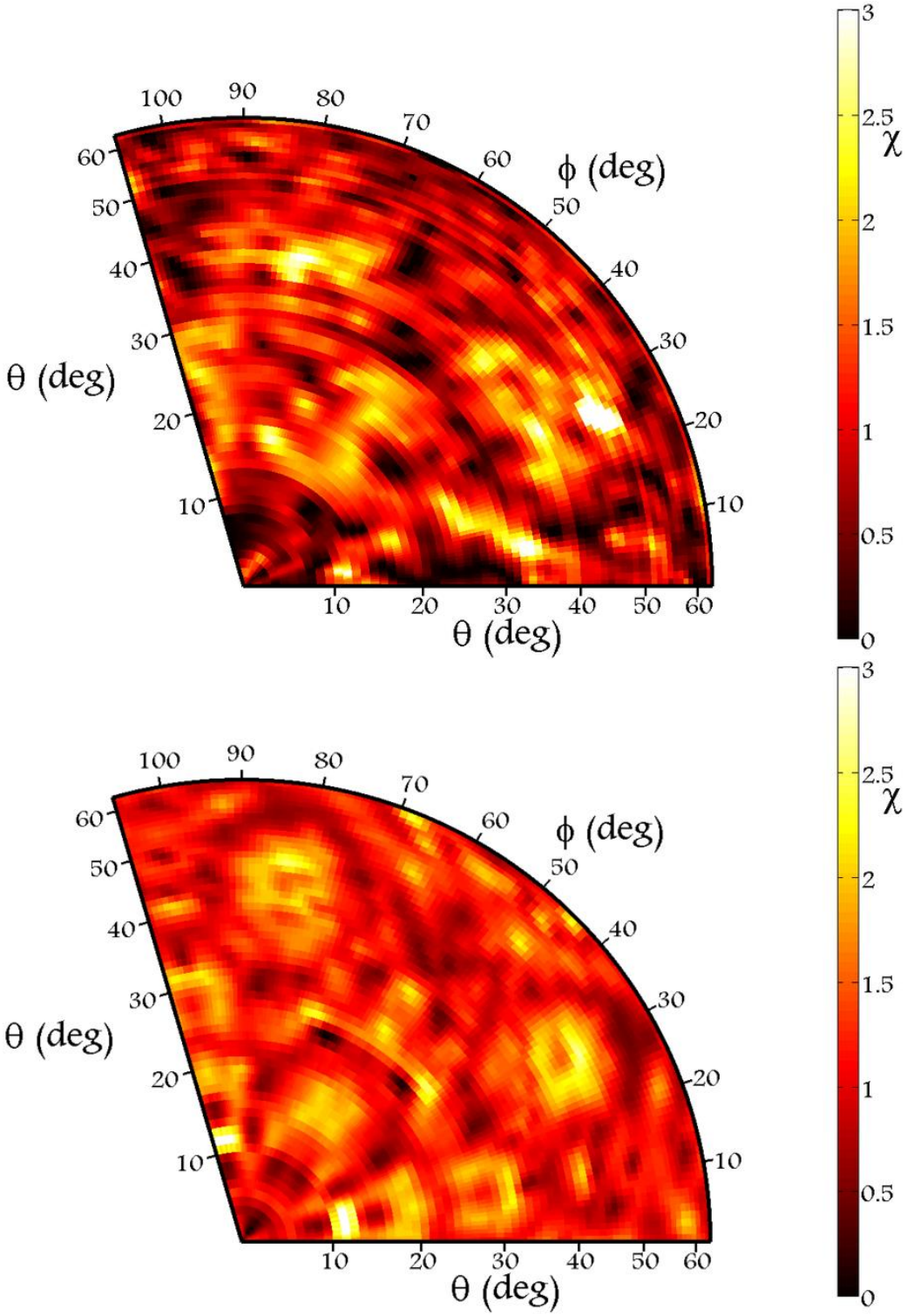

Figure 28: Experimental anisotropy pattern and best match among the reasonable points in the probed space of parameters (50% hollow at 30º + 50% top at 5º).

As the direct visual inspection reveals, both diffraction patterns display the main features at the same positions. The "polar bands" at $\phi \approx 10°$ and $\phi \approx 100°$ occupy the same range of polar angles, particularly in the case of the latter. The spot at $\phi \approx 55°$ and θ between 10 and 30º also appears (although significantly blurrier) in the experimental data. The most prominent characteristic, that is, the two lobes at $\phi \approx 30°$ and $\phi \approx 80°$, is also present as the most intense feature in the experimental pattern. Only the structure at $\theta > 55°$ is missing and that's understandable as it's on the borders of the probed region and no defined spots appear in that azimuthal band in the case of the synchrotron data.

This confirms that the reliability factor has been able to find a good match among the all the of possibilities. Through the treatment of the XPD experimental pattern and the extensive simulations, it has been possible to determine the most likely geometry of the CoPc (7×7) phase on Ag(100). The molecules adsorb evenly on top and hollow sites and while the former present a rotation of 5º with respect to the compact directions of the silver surface, the latter are oriented along a direction shifted 30º from the same compact directions.

The final appearance of the deduced structure is portrayed below:

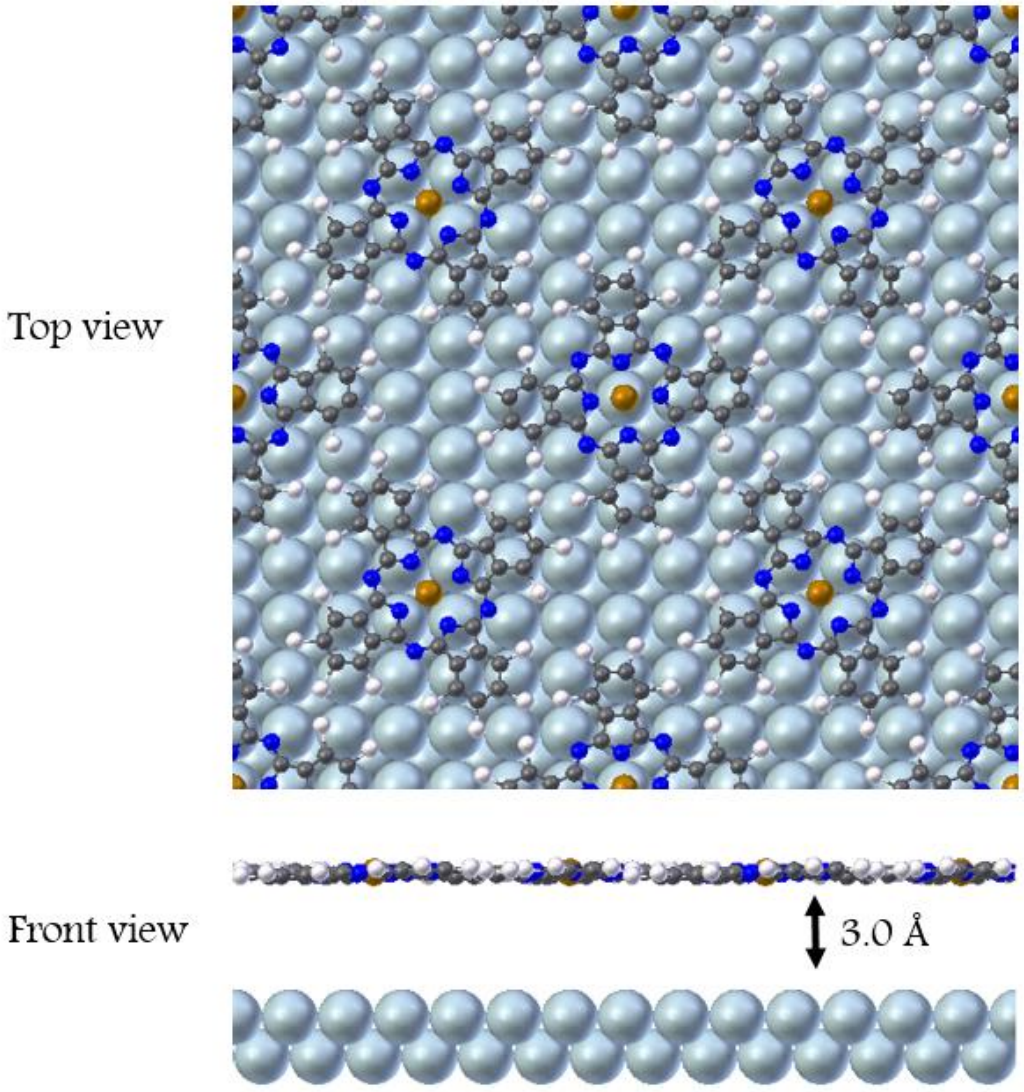

Figure 29: Ball and stick model of the local environment of the CoPc molecules adsorbed on Ag(100) and adopting a (7 × 7) reconstruction. Brown, grey, indigo, pale blue, and white balls correspond to cobalt, carbon, nitrogen, silver, and hydrogen atoms, respectively.

9. Conclusions

The evaporation of approximately one monolayer of molecules of cobalt phthalocyanine on a Ag(100) surface caused the apparition of a (7×7) reconstruction as seen with the help of low energy electron diffraction.

The scanning tunnelling microscopy performed on the system revealed the structure to be slightly more compact than the more frequent (5×5) counterpart. This fact along with the existence of two different orientations of the CoPc manifest a unit cell composed of two inequivalent molecules.

With regard to the vibrational properties, the HREELS spectrum of the (7×7) phase includes some Raman features that are missing in the case of the (5×5). Moreover, some of those exclusive peaks display a strong asymmetry, the so-called "Fano profile". The presence of these structures is linked to a partial filling of the lowest unoccupied molecular orbital, that is, there is a charge transfer between the substrate and the LUMO of the molecule. However, in the case of the (5×5), the charge transfer has been shown to occur between the substrate and an orbital highly localised on the cobalt atom.

The X-ray photoelectron diffraction measurements and simulations have provided the necessary evidence to claim that the (7×7) is formed with half of the molecules adsorbed on hollow sites and the other half on top sites at a distance of 3.0 Å over the surface. As for the (5×5) it had been shown there is only one adsorption site, the hollow one, at a comparable distance.

Interestingly, the hollow molecules have the same orientation on both phases (30º from the compact directions of silver) and are consequently supposed to manifest similar properties. The top molecules display another azimuth, namely 5º with respect to the same reference, and leave room for additional properties, like possibly a new charge transfer mechanism.

This allows to conclude that the different spectroscopic signature and the underlying charge transfer of the (7×7) are most probably due to the molecules adsorbed on the top sites, since they don't exist in the case of the (5×5).

Finally, this system demonstrates that the adsorption site can be a crucial factor when studying the electronic properties of interfaces of organic molecules on metallic substrates.

References:

1. Pochettino A., Acad. Lincei Rend. 15, 355 (1906)
2. Kearns D., Calvin M., J. Chem. Phys. 29 (4), 950–951 (1958)
3. Barbe, D. F. and Westgate, C. R., J Chem Phys, 52, 4046-4049, (1970)
4. Tang, C. W.; Vanslyke, S. A., App. Phys. Let., 51 (12), 913 (1987)
5. Koezuka, H.; Tsumura, A.; Ando, T., Synthetic Metals 18, 699–704 (1987)
6. Nelson, J., Materials Today, 14 (10), 462–470 (2011)
7. Chaidogiannos, G et al., Appl. Phys. A: Mater. Sci. Process., 96, 763−767 (2009)
8. Hohnholz, D. et al., J. Mol. Struct., 521, 231−237 (2000)
9. Stadtmüller, B. et al., Phys. Rev. B: Condens. Matter Mater. Phys., 83, 085416-1−085416-10 (2011)
10. Giovanelli, L. et al., Phys. Rev. B: Condens. Matter Mater. Phys., 82, 125431-1−125431-8 (2010)
11. Peisert, H. et al., Chem. Phys. Lett., 493, 126−129 (2010)

12. Mugarza, A. et al., Phys. Rev. B: Condens. Matter Mater. Phys., 85, 155437-1−155437-13 (2012)
13. Salomon E. et al., Phys. Rev. B 87, 075407 (2013)
14. Mugarza, A. et al., Phys. Rev. Lett. 105, 115702-1−115702-4 (2010)
15. Krull, C. *Electronic Structure of Metal Phthalocyanines on Ag(100)*; Springer International Publishing: New York (2014).
16. Salomon, E. et al., J. Phys. Chem. C, 119, 23422−23429 (2015)
17. Palys, B. J. et al., Journal of Raman spectroscopy, Vol. 26, 63-76 (1995)
18. Ibach, H.; Mills, D. L. *Electron Energy Loss Spectroscopy and Surface Vibrations*, Academic Press: New York, (1982)
19. Bernath, Peter F., *Spectra of Atoms and Molecules* (2nd ed.). Oxford University Press. (2005)
20. Fano, U., Phys. Rev. 124, pp. 1866–1878 (1961)
21. Amsalem, P. et al., Phys. Rev. B: Condens. Matter Mater. Phys., 79, 235426-1−235426-10 (2009)
22. Peremans, A. et al., Phys. Rev. Lett. 78, 2999 (1997)
23. Salomon, E. et al., Phys. Rev. B: Condens. Matter Mater. Phys. 2013, 87, 075407-1−075407-9.
24. Mugarza, A. at al., Phys. Rev. B: Condens. Matter Mater. Phys., 85, 155437-1−155437-13 (2012)
25. Shirley, D.A., Phys. Rev. B 5 , 4709-4714 (1972)
26. García de Abajo F. J. et al., Physical Review B, 63, 075404 (2001)
27. Vincent Lepetit and Pascal Fua, *Keypoint Recognition using Randomized Trees* http://cvlab.epfl.ch/files/content/sites/cvlab2/files/publications/publications/2006/LepetitF06.pdf
28. Buldas, Ahto, Andres Kroonmaa, and Risto Laanoja. *Keyless Signatures' Infrastructure: How to Build Global Distributed Hash-Trees* –Springer Link (2013)
29. Van Hove, M. A. et al. Surf. Sci., 64, 85−95 (1977)
30. Chen. Y, et al., Phys. Rev. B: Condens. Matter Mater. Phys., 58, 13121−13131 (1998)
31. Jablonski A., Salvat F. and Powell C. J. , *NIST Electron Elastic-Scattering Cross-Section Database* - Version 3.2, National Institute of Standards and Technology, Gaithersburg, MD (2010).
32. Tanuma S., et al., Surf. Interface Anal., 43, 689 (2011)
33. Baran J. D. et al., Phys. Rev. B 81, 075413 (2010)
34. Auwärter W. et al., Phys. Rev. B 81, 245403 (2010)
35. Zhou X.J. et al, Electron Spectrosc. Relat. Phenom., 142, 27 (2005)
36. Kröger I. et al., Phys. Rev. B 83, 195414 (2011)
37. Glaser, M. et al., J.Phys.Chem.C, 119, 27569−27579 (2015)
38. Stadtmüller B., et al. Phys. Rev. B 89, 161407 (2014)

Chapter IV:
X-ray photoemission study of silicene on Ag(111) surfaces

X-ray photoemission study of silicene on Ag(111) surfaces

1. Introduction

In principle, it would be most appropriate to study freestanding silicene. Unfortunately, its synthesis has proved to be more difficult than graphene's (actually impossible so far) as it cannot be produced by exfoliation but through epitaxial growth. This fact doesn't render the analysis of supported silicene a futile endeavour. On the contrary, it will be the central element of this chapter.

If the next chapter will be devoted to functionalised silicene, the present one will tackle silicene on its own, that is, the surface will be clean, allegedly free of chemical species other than silicon. Following a scheme that will be repeated later, the properties of the "two-dimensional" allotrope will be examined as a function of its thickness.

The techniques of choice were photoelectron spectroscopy and diffraction. The former makes it possible to probe the electronic bands. As the following paragraphs will show, this is useful to ascertain charge transfers which could eventually improve the performance of a hypothetical device. Furthermore, the spectrum of the core levels of the elements on the sample can offer valuable information. Multiple components may arise from an individual core level[1] indicating different chemical environments. That would be the scenario of a surface component, an oxidised one, etc.

Regarding the photoelectron diffraction, it can be a really powerful tool to distinguish among structural models, even when the only difference lies at small variations of the geometrical parameters as shown in the chapter about cobalt phthalocyanine on Ag (100).

Although the structure of monolayer silicene has been elucidated[2], the geometry of multilayer silicene is still unknown. Its surface reconstruction has been identified[3] as a $(\sqrt{3} \times \sqrt{3})R30°$, but the elaboration of a well-determined model has been more slippery. It is not even only a question of the positions of the atoms, but it also concerns their very nature.

In effect, there are claims about thick silicene with the topmost layer composed by both silicon[4], and silver[5]. The former proposition corresponds to the most straightforward possibility: if silicon atoms are evaporated on a silver substrate, increasingly higher doses increment the thickness of silicene on top. The latter requires additional processes, such as an eventual migration upwards from the silver substrate akin to the effect produced by surfactant substances.

Angle-resolved photoemission spectroscopy is a useful technique to resolve such a conundrum too because the limited mean free path of the emitted electrons allows to increase the sensitivity to the surface. In this respect, the tendency of growth or decrease of the silicon to silver signal ratio as a function of the angle of emission can clarify which chemical species settles at the last layer of the sample.

The present chapter will start with a comprehensive study of the dependency of the photoemission from the core levels of silicon and silver with the thickness of silicene and the angle of emission. This will lead to the test of hypothesis related to the nature of the surface. As for the last part, the X-ray photoelectron diffraction patterns will be presented and compared to simulations of some structural models proposed for multilayer silicene.

2. Experimental procedure

The experiments were performed at room-temperature and under ultrahigh vacuum conditions.

The Ag(111) single-crystal surface was cleaned by repeated cycles of Ar+ sputtering, followed by annealing up to 730 K. Subsequently, the silicon was deposited onto the clean Ag(111) surface held at 500 K by thermal evaporation from a piece of silicon wafer. Typical deposition rates were 0.02 ML/min. Under these conditions monolayer silicene was obtained after approximately one hour, and four different samples were prepared depending on the time of evaporation: 25, 75, 180 and 300 minutes. This interval allows to study the system from sub-monolayer coverage up to an estimated thickness of 5-6 layers.

Regarding the F_4TCNQ molecules, they were transported under the form of powder and were thermally evaporated at room temperature and 10^{-10} mbar from a quartz crucible with rates of about 0.08 monolayers per minute. In this case several coverages were tested, ranging from 4 to 62 minutes.

The photoelectron spectroscopy experiments were performed at the *ANTARES* beamline of the Soleil Synchrotron Light Source in Saint-Aubin, France[6]. The PES scans were measured by collecting the photoemission signal within an interval of polar angle given by the characteristics of the electron analyser for a fixed azimuth. For the acquisition of the diffraction patterns, the plane of the detection was gradually rotated around the direction normal to the surface, thus varying the azimuthal angle. Mainly the Ag $3d_{5/2}$ and Si 2p spin-orbit doublet were selected for the measurements with an energy of the photons between 230 and 800 eV depending on the purpose of the data. Most of the time this parameter was set fixed to 500 eV in order to have a good compromise between photon flux, energy resolution (between 137 and 6 meV depending on the type of measurement), and signal-to-noise ratio. The probed interval of polar angles was between 0º and approximately 55º, and each individual measurement spans approximately 25º because the detector has 546 channels spaced by 0.046º.

3. Study of photoemission from silicene on Ag(111)

The amount of spectroscopic data registered during the stay at the *ANTARES* beamline makes it necessary to write down a concise summary in order to better distinguish whether or not the spectra can be compared directly. The table below specifies the fundamental parameters of the main measurements.

Si evaporation time (min)	**25**	**75**	**180**	**300**
Core level	**Si 2p**	**Si 2p**	**Si 2p**	**Si 2p**
Specifications	Slit: 200 Time step: 500 ms Sweeps: 2 Photon Energy: 500 eV Pass Energy: 100 eV Energy step: 10 meV Angles: 0, 10, 20, 30, 40, 45	Slit: 200 Time step: 500 ms Sweeps: 2 Photon Energy: 230 eV Pass Energy: 20 eV Energy step: 10 meV Angles: 0, 10, 20, 30, 40, 45	Slit: 500 Time step: 500 ms Sweeps: 2 Photon Energy: 500 eV Pass Energy: 20 eV Energy step: 10 meV Angles: 0, 10, 20, 30, 40, 45	Slit: 500 Time step: 500 ms Sweeps: 1 Photon Energy: 800 eV Pass Energy: 50 eV Energy step: 10 meV Angles: 0
Core level	**Ag $3d_{5/2}$**	**Ag $3d_{5/2}$**	**Ag $3d_{5/2}$**	**Ag $3d_{5/2}$**
Specifications	Slit: 200 Time step: 500 ms Sweeps: 2 Photon Energy: 500 eV Pass Energy: 20 eV Energy step: 10 meV Angles: 0, 10, 20, 30, 40, 45	Slit: 200 Time step: 500 ms Sweeps: 2 Photon Energy: 500 eV Pass Energy: 20 eV Energy step: 20 meV Angles: 0, 10, 20, 30, 40, 45	Slit: 500 Time step: 500 ms Sweeps: 2 Photon Energy: 500 eV Pass Energy: 20 eV Energy step: 10 meV Angles: 0, 10, 20, 30, 40, 45	Slit: 500 Time step: 500 ms Sweeps: 1 Photon Energy: 800 eV Pass Energy: 50 eV Energy step: 10 meV Angles: 0

Table 1: Summary of the parameters involved in the acquisition of the sets of spectra analysed in this section.

With the sets of data well identified, it is appropriate to show its appearance and the general treatment they received to extract the desired information.

3.a) Data treatment

As described in the experimental procedure, the photoemission spectra were registered obviously as a function of the kinetic energy of the emitted electrons, but also as a function of the polar angle of emission. This last parameter is useful to vary the bulk to surface relative weight on the total signal, which allows to garner additional information.

The figure below includes the representation of one example of the raw data issued by the spectrometer. The angle zero corresponds to the reference value given in the previous table, that is, for a spectrum indicated as at 30º of polar angle, the values at 0º (on the figure) would correspond to θ = 30º, those at -7.5º would imply θ = 22.5º etc.

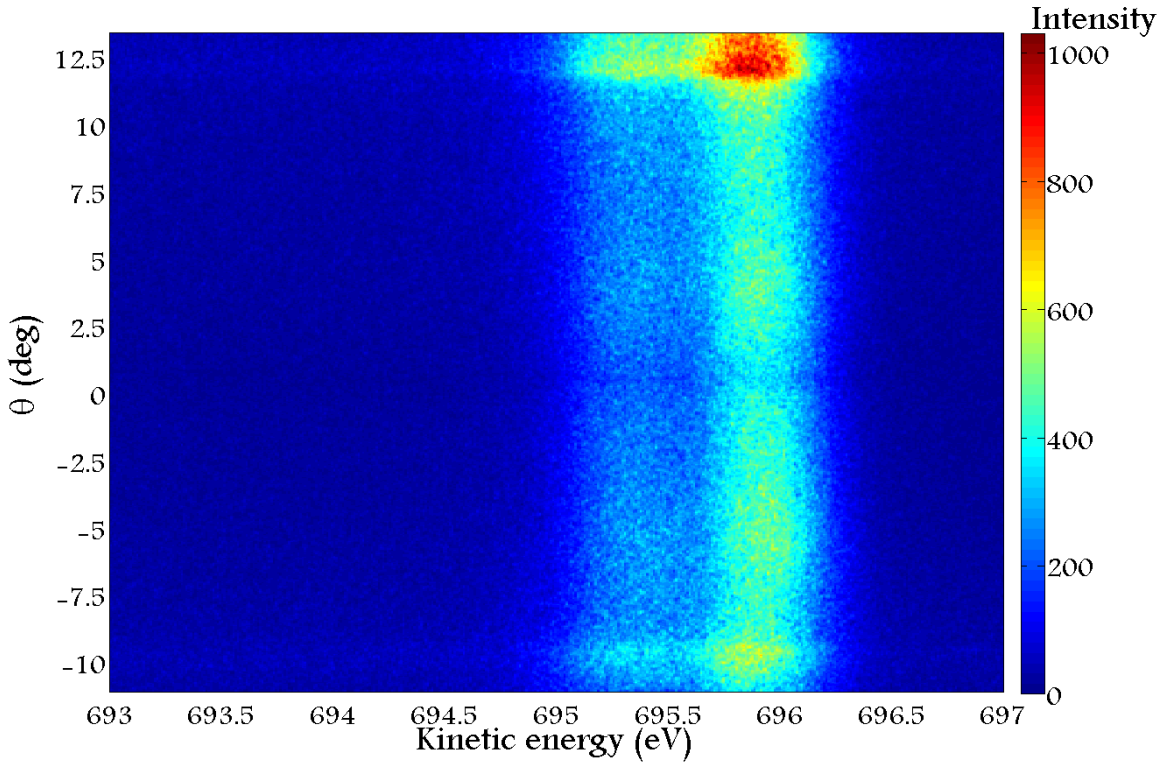

Figure 1: Heat map of the Si 2p core level (E_{photon} = 800 eV) registered on the silicene evaporated for 300 as a function of the kinetic energy of the emitted electrons and the polar angle of emission. The angle 0 in this case corresponds to the direction normal to the surface. Negative angles imply normal positive angles but an azimuth increased by 180º.

These data are affected by unwanted effects such as the instrument function and the background signal. Their repercussions can be mitigated with appropriate treatment, but in order to perform that task, a better comprehension of the spectra is mandatory.

On figure 1, the values along horizontal lines (in other words with the restriction of a constant polar angle) produce an individual photoemission spectrum. Conversely, if the data are read along a vertical line (equivalent to setting a fixed kinetic energy of the electrons), a polar profile of the emission is obtained.

The following figure includes one of the mentioned spectra obtained from figure 1 with a polar angle θ = 0º.

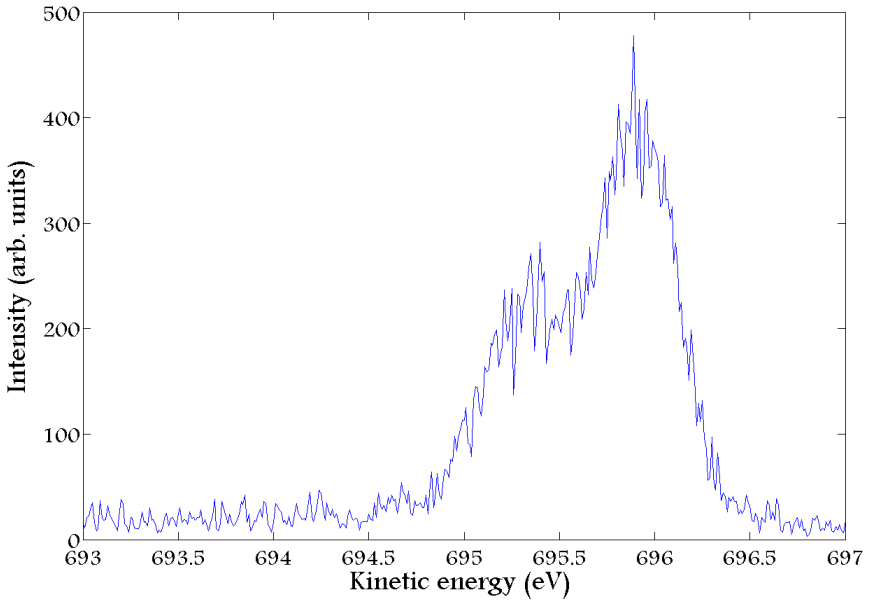

Figure 2: Photoemission spectrum of the Si 2p spin-orbit doublet extracted from figure 1 by imposing a fixed polar angle equal to zero degrees, coincident with the direction perpendicular to the surface.

With the objective of estimating the instrument function, the operation is repeated along a line of constant kinetic energy, yielding the polar profile of intensity shown in figure 3. In this case, caution has been taken to choose an energy outside of the interval of influence of the Si 2p doublet, in particular equal to 693.5 eV. The reason behind this decision is that, if an energy were selected inside the Si 2p peaks, i.e. between 694.5 and 697 eV, it would be possible to observe diffractive effects among other plausible factors that could be mistaken for the instrumental function. A point at a higher kinetic energy would be more appropriate, but as figure 1 shows, the highest probed energy is very close to the doublet, so a point at a lower energy was chosen.

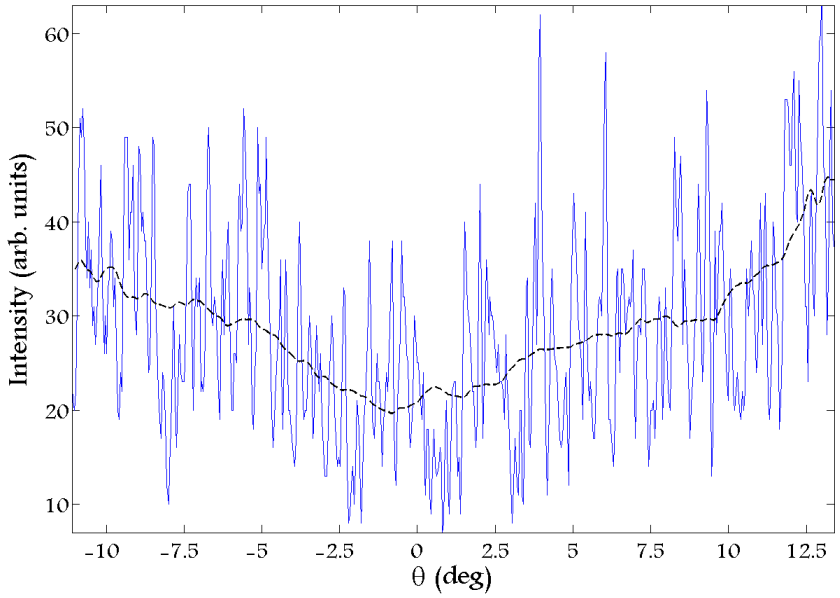

Figure 3: Polar profile of intensity extracted from figure 1 for a kinetic energy equal to 693.5 eV (in the region dominated by the background). A black dashed trend line has been added so as to show that, despite the noticeable statistical noise, the background level varies strongly with the polar angle.

The polar profile, in principle affected by at least the background and the instrumental function, supposes a significant problem. Firstly, it is extremely noisy in the background zone, with signal-to-noise ratios lower than 0.5. Given that the interval of energy has been finely sampled (10 meV), there are hundreds of polar profiles in the background region, so averaging appears as a cheap solution. The features have to be ignored again to avoid biases on the polar profile. Below, the mean polar profiles of the background are shown for the set of data Si 2p and 25 minutes.

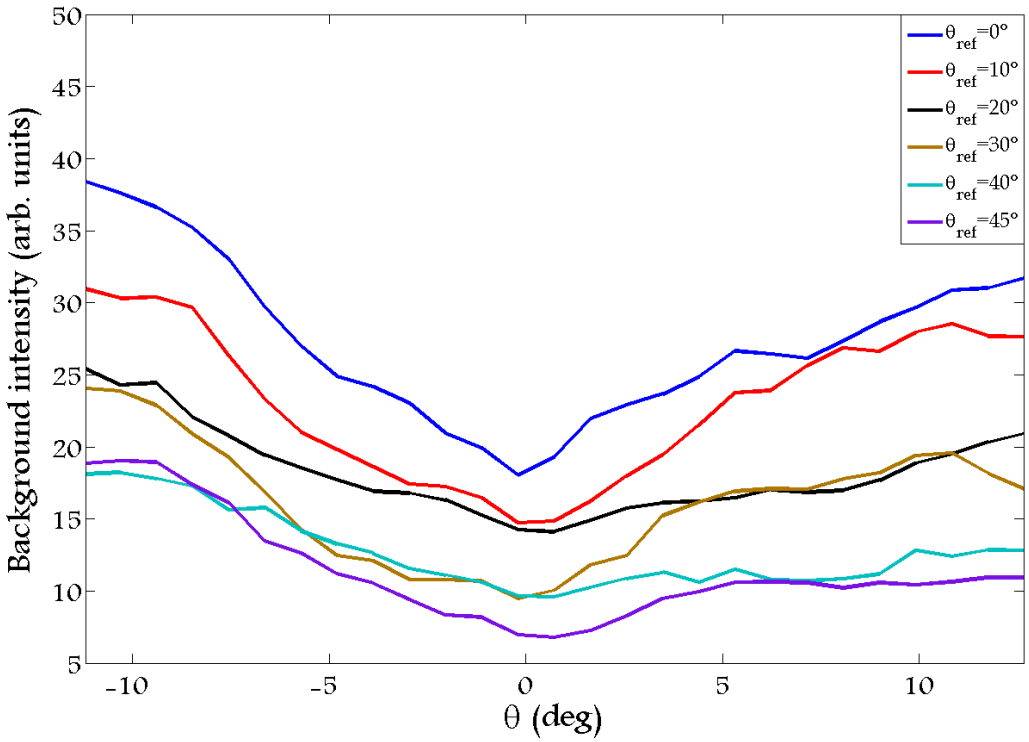

Figure 4: Average polar profiles of intensity computed from the Si 2p (25 minutes) spectra. The legend specifies the reference for the polar angle of each curve, which corresponds to the zero value on the abscissas axis.

As the figure 4 reveals, the background polar profiles change depending on the position of the detector (θ_{ref}). The background signal can be accountable for the evolution of the intensity with the polar angle since the magnitude is expected to decrease as the observations move away from the normal direction.

On the other hand, the modifications are not restricted to the intensity, but they affect the shape of the profiles as well. Indeed, the blue curve in figure 4 displays a "V" shape, rather symmetric if $\theta = 0^o$ is considered as the bilateral axis. However, the turquoise profile manifests a decreasing slope on the negative angle side and stays fairly constant on the positive half, displaying a quite asymmetric character. This constitutes a robust hint of the existence of a non-trivial instrument function, given that its shape can be altered at least through the manipulation of the polar angle.

Further tests also showed that the instrumental profile may not be constant in time or may depend on the amplitude of the signal, because the spectra of Si 2p and Ag 3d taken on the same preparation under the same angle of reference produced very different background polar profiles.

At this point, the instrument function supposed a serious issue that stood in the way of the exploitation of the data. For this reason, a pragmatic approach was chosen although it led to losses on both angular resolution and quantity of the usable measurements.

Despite being severely irregular, the background polar profiles exhibited a less problematic behaviour in the central part of the detector, namely the [-5º, 5º] interval. The data were reasonably symmetric around 0º and the same "V" shape was observed on all the sets of data with small deviations.

With this in mind, for each angle of reference all the set of data comprised in the aforementioned interval was condensed into one unique spectrum by averaging. This decision had the collateral effect of increasing the signal-to-noise ratio.

The figure below portrays the transition from the highly noisy individual spectra towards their average counterpart in the [-5º, 5º] interval.

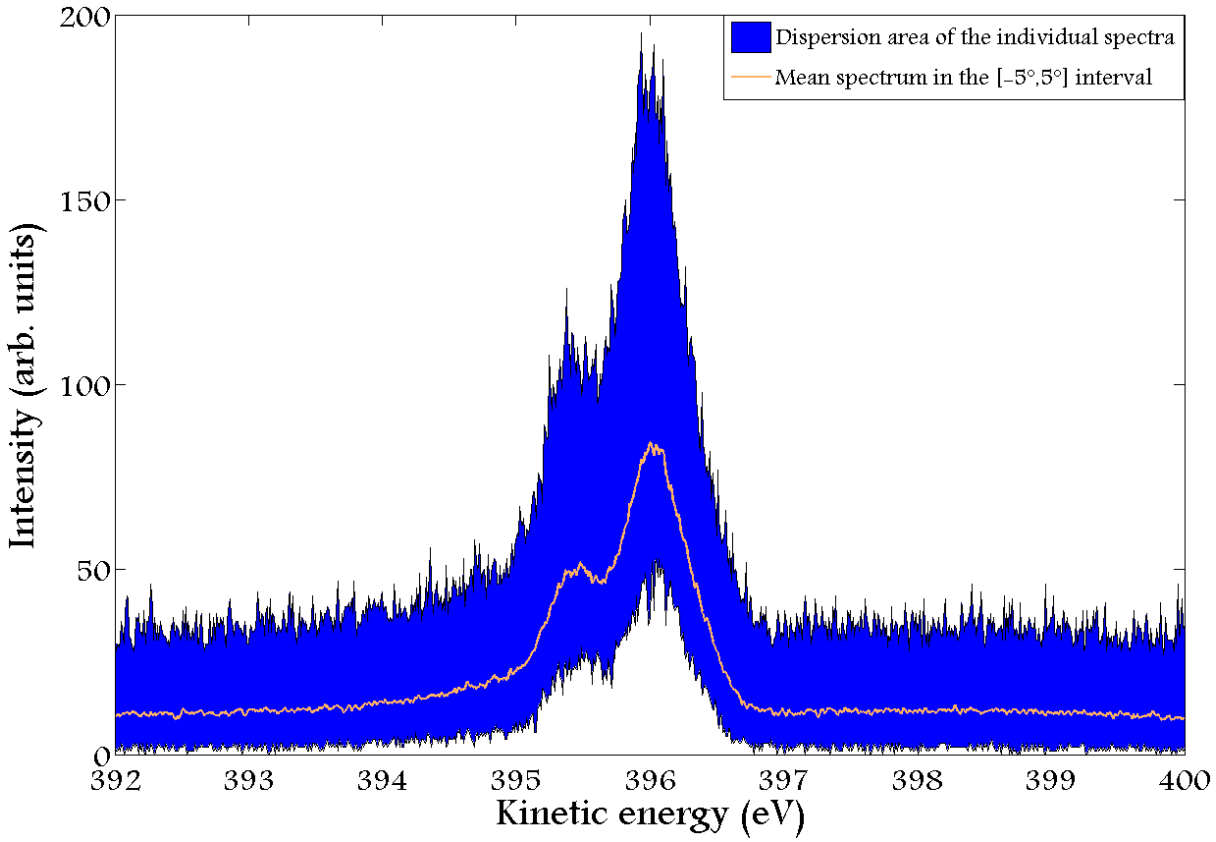

Figure 5: Spectrum obtained from averaging within the [-5º, 5º] interval the set of data corresponding to the Si 2p level (E_{photon} = 500 eV) of the 25 minutes preparation at normal emission. The blue shaded region represents the dispersion area of the data.

As the chart above shows, the signal-to-noise ratio has increased very significantly even in the background regions. The spectrum looks smoother and the analysis becomes simpler at the expense of replacing hundreds of measurements at different angles (which could eventually allow to study the evolution with the polar angle) with their mean value. Anyhow there wasn't any other option as the background polar profiles were so distinct that they made a finer analysis and comparison channel by channel impossible.

The resulting spectrum exhibits a rather intense background. In effect, far from the Si 2p doublet the flux of electrons should in principle decay gradually to zero, but the decrease stalls around an intensity equal to 10 (according to the scale in figure 5). Since one of the ultimate objectives is the integration of the signal so as to calculate the area under the peaks, it's necessary to extract all the signal that would be there even if no feature were present, that is to say, the background.

The usual method for removing the background from an X-ray photoemission spectrum is the iterative calculation of the so-called Shirley background[7,8]. Prior to the computation, two points free of photoemission signal have to be chosen on both sides of the peak. The analytical procedure can be deduced by assuming a special form of the inelastic energy loss cross-section[9]. In fact, the background is generated only from electrons coming out from a photoemission peak. As a result, its numerical value at a given energy is linked to the integral of the part of the feature that lies at higher energies as the expression below establishes:

$$B_1(E) = k_1 \int_E^{E_{right}} dE'[I(E') - I_{right}]$$

In this expression, the variables correspond to the following magnitudes:

-$B_1(E)$: first iteration of the background
-k_1: first value of the scattering factor
-E, E': kinetic energy
- E_{right}: kinetic energy of the point of reference chosen at higher energy
-$I(E)$: photoemission signal at the specified energy
-I_{right}: photoemission signal of the point of reference chosen at higher energy

The n-th iteration is calculated through the expression:

$$B_n(E) = k_n \int_E^{E_{right}} dE'[I(E') - I_{right} - B_{n-1}(E')]$$

The only restriction is imposed on the scattering factors, since at each iteration their values must ensure that the total background, that is, the background once the whole peak has been left behind, has to pass through the other reference point (E_{left}, I_{left}). This requirement is fulfilled by adding the next expression:

$$k_n = \frac{I_{left} - I_{right}}{\int_E^{E_{right}} dE'[I(E') - I_{right} - B_{n-1}(E')]}$$

After reaching convergence, the background is simply obtained as the sum of the intensity at the high energy reference and the integral from the last iteration.

This method in its simplest form requires well isolated peaks because the references have to be chosen far from the influence of any feature. It is nonetheless possible to refine the procedure with the aim of processing blended peaks or even with the objective of measuring the amplitude of the features at the same time that the background is computed[10].

The subtraction of the Shirley background brings the spectrum down in intensity so that both sides of the selected peak lie approximately at an intensity level equal to zero. From that point, any remaining value obtained by integrating the chosen interval of kinetic (or binding) energy is attributed to the real physical signal produced by the photoemission from the core level.

In the most complex cases, such as those involving several blended peaks, the background was approximated by cubic splines whose characteristics were restricted in order to match the requirements of the Shirley background while not creating or supressing small components. In particular, a monotonically decreasing odd function was imposed.

The following figure shows the effect of the removal of the background on one of the spectra.

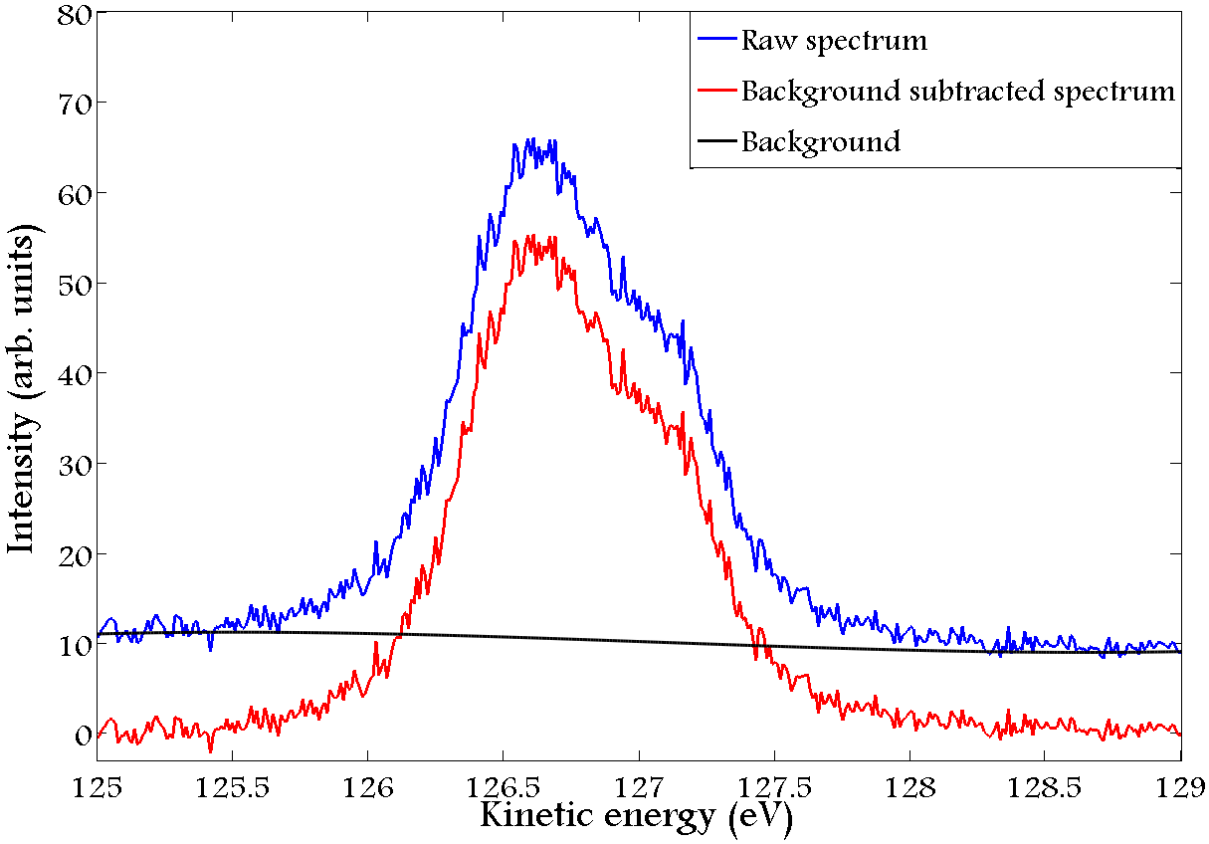

Figure 6: Background subtraction from the Ag 3d spectrum registered on the 3 hours preparation at a polar angle equal to 40º.

Once the background has been suppressed from every spectrum, it is possible to begin measuring the peaks in a quantitative manner.

In order to complete this task, the features were fitted using asymmetric pseudo-Voigt profiles as models as they produced the best fits among the tested options (see figure 7). The details of such models have already been explained in the introductory HREELS section. The fitting procedure relied on a non-linear square least method based on the Levenberg–Marquardt algorithm[11].

As explained before, the pseudo-Voigt profiles consist in the linear superposition of one gaussian and one lorentzian curves which are perfectly aligned. Apart from the amplitudes, the mean and the widths of the distributions, two asymmetry parameters (one relative to the gaussian, and the other linked to the lorentzian) were added to reproduce the asymmetry of the photoemission lines.

The space of parameters was severely restricted to ensure convergence towards reasonable values. In effect, the width of the peaks is related to factors such as the lifetime of the excited state or the collisional broadening due to the temperature of the system. Given that the experiments were performed in almost identical conditions as the only variation was the thickness of the silicon deposit, the spectral shape should remain fairly constant. This was enforced via restrictions on the parameters of the model.

Other well-known requirements that were imposed were the 2:1 spin-orbit flux ratio on the Si 2p doublet, the separation between the same doublet[12], and the binding energy of the core levels when references were available, e.g. for bulk silver[13].

The more canonical Doniach-Sunjic profile[14] was also tested but the goodness of this fit was definitely worse in every case. As an example, the figure below shows the best fit with the Doniach-Sunjic and the pseudo-Voigt profiles of the bulk Ag $3d_{5/2}$ core level.

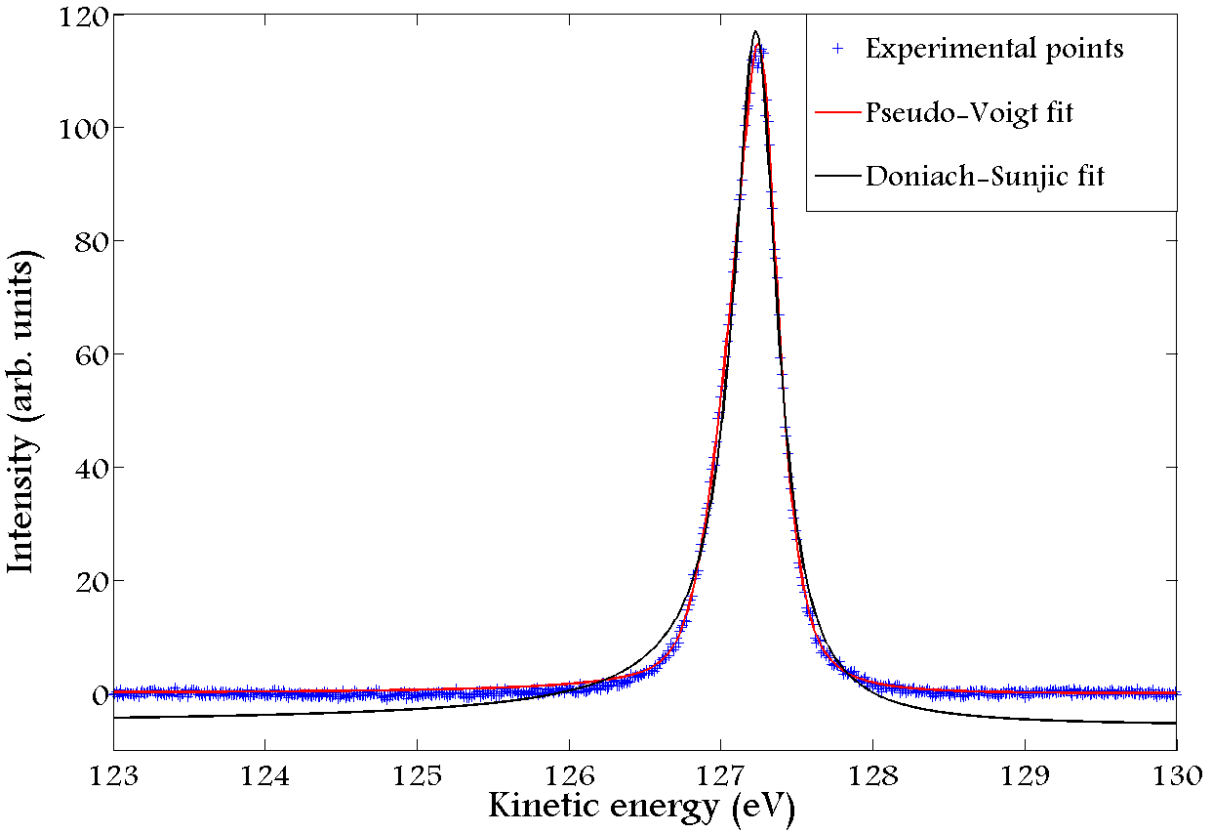

Figure 7: Best fits obtained for the bulk Ag $3d_{5/2}$ peak on the 25 minutes preparation by using the pseudo-Voigt and the Doniach-Sunjic profiles.

As the example in figure 7 reveals, the match of the pseudo-Voigt distribution matches more precisely the experimental points. This happened to be the case in all the sets of data, and so this line profile was chosen for the subsequent analysis.

The least squares method yielded values of the fundamental parameters of the model. Among them, the ones that will play a preponderant role in the discussion will be the position of the peaks, that is to say the binding energy of the line whose broadening gives rise to the profile, and the intensity ratios between different features.

It's true that the fitting performed on the experimental data doesn't provide the binding energy, but the kinetic one, which presents an undeniable inconvenience: it depends on the energy of the X-ray photons that caused the emission of the photoelectron. For this reason, this value is not directly comparable with any magnitude intrinsic to the material. Instead, it has to lead to the calculation of the binding energy of the core level, a magnitude that is reasonably constant although varies slightly (usually less than 1 eV) depending on the chemical environment of the emitter.

A photoelectron that arrives to the detector has to be ejected from its atom first, and then needs to reach a free state in the vacuum from the Fermi level with a given kinetic energy. Writing down the balance of energy and keeping in mind that the X-ray photon is the source of energy in this process, it's simple to obtain the following equation:

$$E_{ph} = E_b + \phi + E_{kin}$$

In this expression, the variables stand for the magnitudes detailed below:

E_{ph}- Energy of the X-ray photon
E_b- Binding energy of the core level
ϕ- Work function
E_{kin}- Kinetic energy of the outgoing photoelectron

Both the kinetic energy of the electron and the energy of the photon are specified or determined by the devices of the beamline. The binding energy is the parameter that the equation should provide, so the only remaining prerequisite is the calculation of the energy of the Fermi level.

With this task in mind, the electronic bands near the Fermi level were systematically registered for each of the four preparations. In the context of electronics, the mentioned level can be understood as a hypothetical energy level, such that at thermodynamic equilibrium it would be occupied with a probability equal to one half. This, at the temperatures of the experiments and particularly on the samples with low coverages (25 and 75 minutes) manifests as a sudden drop of the density of states down to zero.

The following figure shows the valence band of the sample (mostly silver) close to the Fermi level. The data were registered on the 25 minutes preparation along a $\langle\bar{2}11\rangle$ direction.

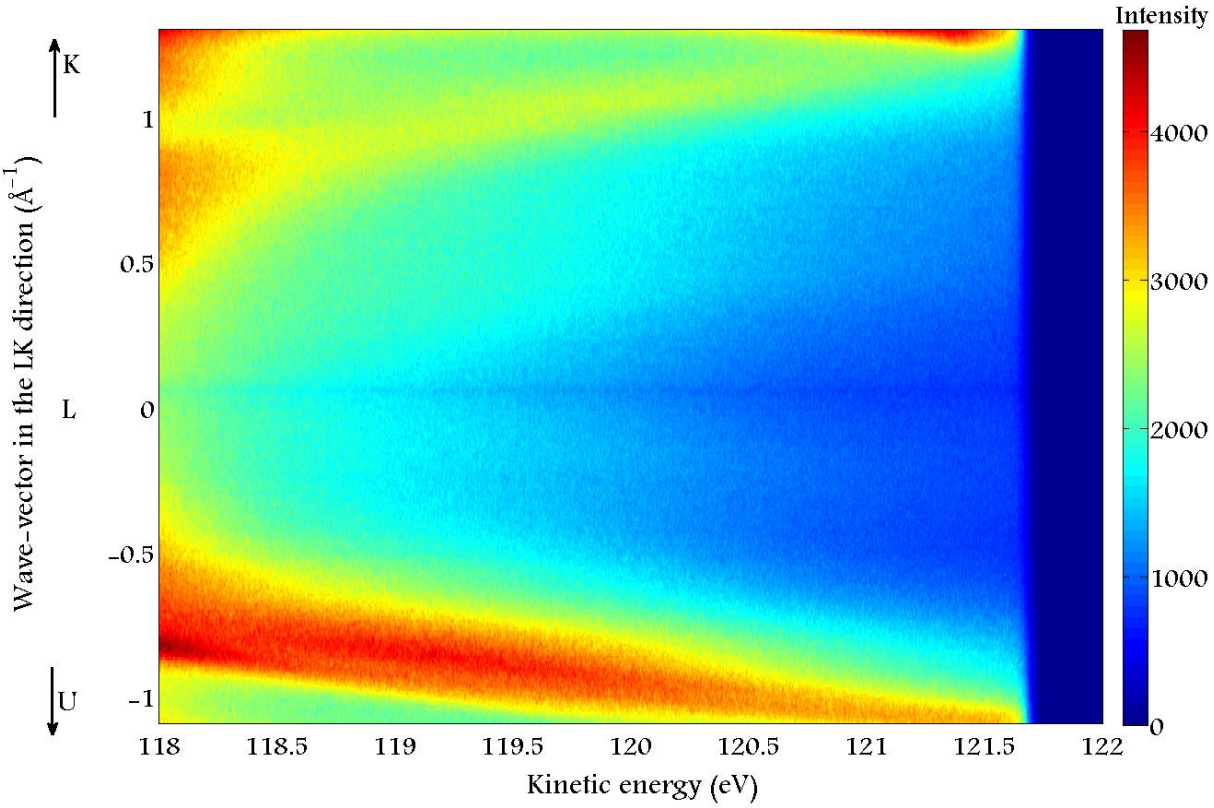

Figure 8: Ag valence band close to the Fermi level obtained from the 25 minutes preparation. The angular scan was performed along a $\langle\bar{2}11\rangle$ direction, equivalent to the ULK direction in the reciprocal space. The energy of the photons was kept fixed at 126 eV.

The graph displays an almost instantaneous decrease of the signal to zero between 121.5 and 122 eV of kinetic energy. In order to determine with higher precision the Fermi level, these sets of data were condensed by adding all the values with the same kinetic energy. This procedure generated vector of data related to the density of states.

The chart below includes the intensities from figure 8 collapsed in the wave-vector space by means of averaging.

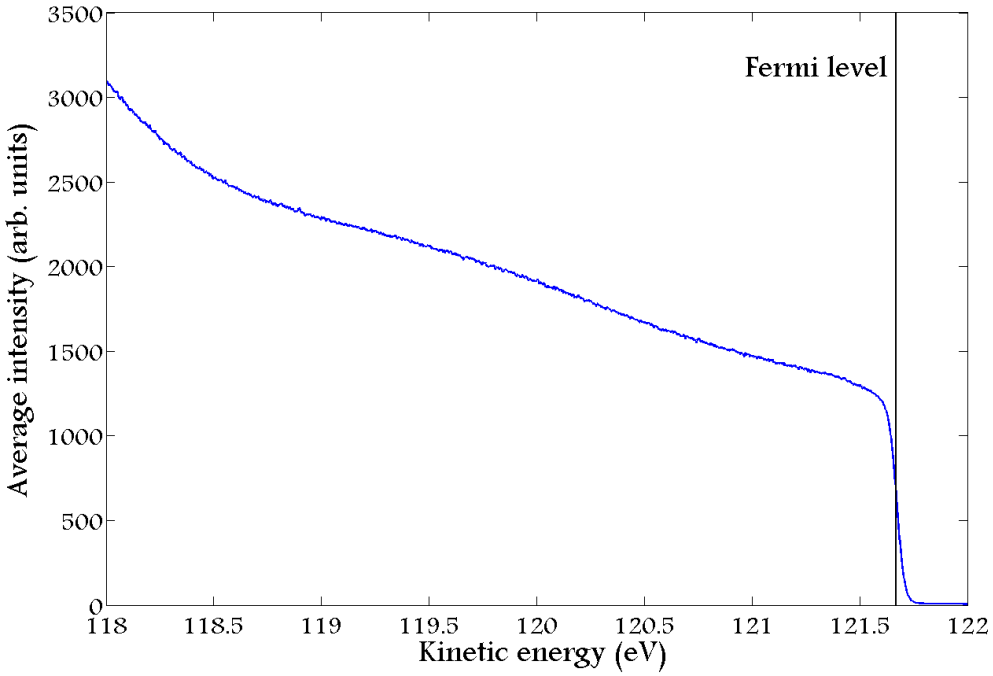

Figure 9: Intensity from figure 8 averaged across the parallel momentum distribution. The Fermi level, found at a kinetic energy equal to 121.7 eV, has been highlighted with the black vertical line.

This rearranged data allow the identification of the Fermi level which will subsequently lead to the determination of the binding energies from the photoemission spectra. It appears as a convolution of the Fermi distribution with a gaussian related to the detector. Keeping in mind that the convolution of an odd and an even function is an odd function, the position of the Fermi level was determined as the mean value of the energies at which the intensity drops by 20% and 80% on the quasi-Heaviside step. The following table includes the results on the difference of energy between the Fermi level and the vacuum obtained on each sample.

Preparation	25 min	75 min	180 min	300 min
E_{photon} (eV)	126	126	126	126
$E_{kin\text{-}Fermi\text{-}level}$ (eV)	121.7	121.7	121.7	121.2
ϕ (eV)	4.3	4.3	4.3	4.8

Table 2: Deduction of the energies of the Fermi level for each preparation obtained from curves equivalent to figure 9.

The method was more complicated in the case of the last two preparations because the Fermi step was more concealed due to the thickness of the silicene layers on top. These layers greatly perturbed the metallic character previously displayed by the silver substrate. In any case, knowing that some photoemission peaks shouldn't shift at all such as the silver bulk component it was possible to double-check that the values inferred from the valence bands were indeed correct.

From this point, all the elements needed to process the XPD spectra have been determined and so the next section will be devoted to the systematic analysis of the peaks featured in each set of data. This will lead to suggestive pieces of information related to the formation and nature of silicene itself as a function of its thickness.

3.b) Calibration of the silicon source

In the "experimental procedure" section the deposition rate has been stated as around 0.02 monolayers per minute. This assertion is supported on the appearance of the LEED patterns registered after the preparation of each sample. The figure below corresponds to a summary of the diffractive signatures of each preparation. It must be noted that the repeated preparation of silicene in PIIM's laboratory along with the extensive use of the LEED technique has made it possible to identify the deposited amount of silicon in the interval from 0 to 3-5 monolayers.

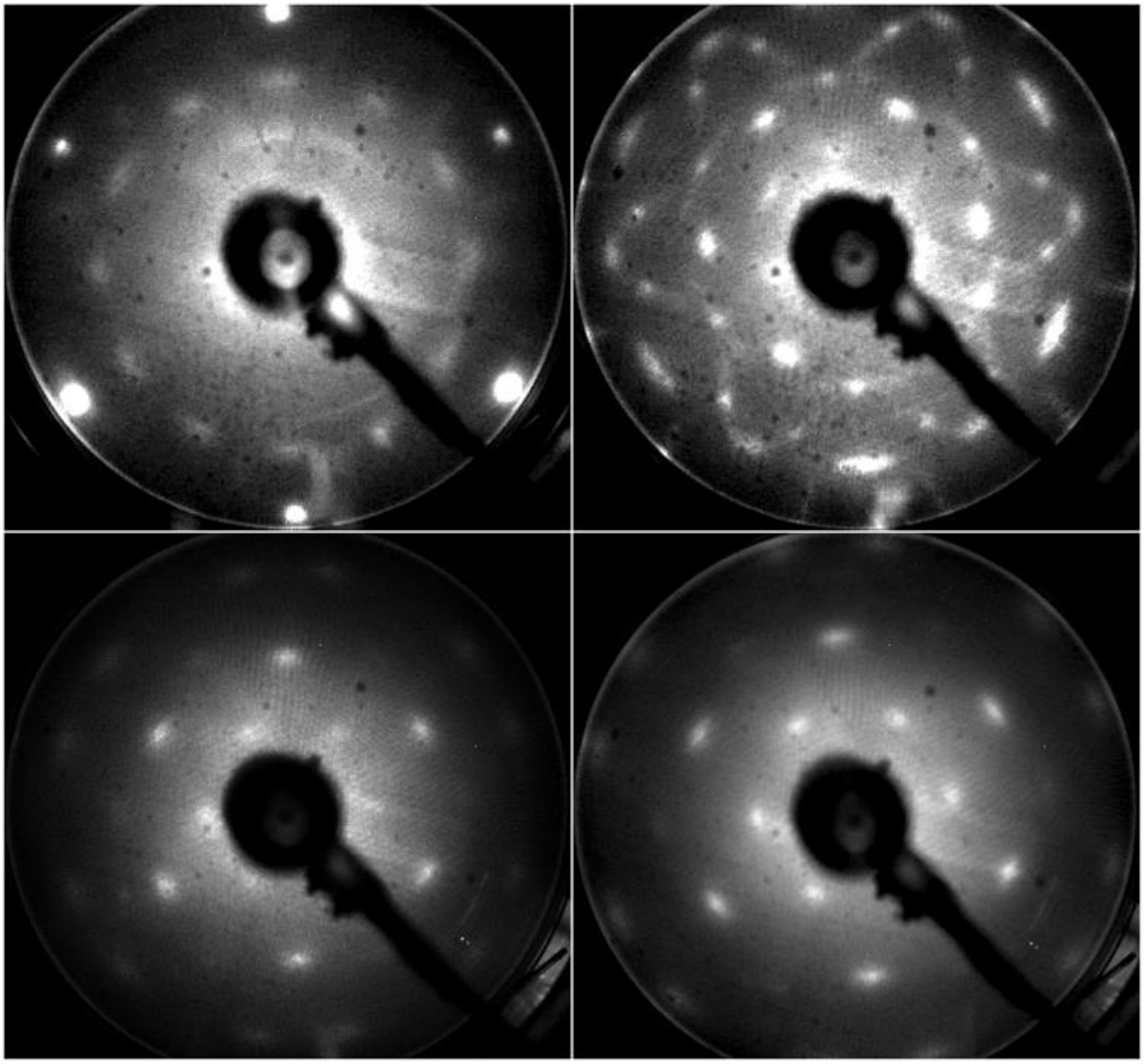

Figure 10: LEED patterns of the four samples detailed in table 1. The upper left image corresponds to the 25 minutes preparation with a kinetic energy of 41.6 eV. The upper right one was registered on the 75 minutes one with an energy equal to 27.9 eV. In the lower part, from left to right, the 3h and 5h preparations, observed respectively with a primary energy of 62.3 eV and 51.2 eV.

The kinetic energy of the electrons for the four LEED patterns is not the same, but they have been chosen so as to show the most characteristic features of each coverage.

Regarding the 25 minutes image, the silver spots are very intense and only the (1×1) of silicene is slightly visible.

The next one doesn't include the spots from silver because the energy is too low, but the pattern reveals a (4×4) + ($\sqrt{13}\times\sqrt{13}$) superstructure, typical of the monolayer range. The presence of the ($\sqrt{3}\times\sqrt{3}$)R30º reconstruction (the innermost ring of 6 large spots) proves that the sample is at the initial stages of the formation of multilayer silicene.

The two last patterns are very similar, because they display mainly the ($\sqrt{3}\times\sqrt{3}$)R30º arrangement, pointing towards multilayer silicene. Another feature further reinforces this argument: the complete disappearance of the Ag spots. This indicates that the substrate is so well covered that the electrons from the cannon cannot reach it and hence its diffracted pattern is not cast onto the screen.

All these evidences support the identification of the different studied thicknesses of silicene during the stay at the synchrotron. According to them, the 25 minutes corresponds to a sub-monolayer range, 75 minutes result in a preparation slightly beyond the monolayer coverage, and 3 and 5 hours should produce around 4 and 6 layers of silicene.

This information will play a prominent role in the discussion of the spectra that will take place near the end of this section and agrees with the expectations for the unusual environment (the beamline), since the growth rate was approximately twice slower than in PIIM's laboratory, but the silicon source was also twice as far from the sample.

3.c) Overview of the spectra

Based on the energy of the photons stated in table 1 and the position of the Fermi level included in table 2, it's possible to display the experimental spectra as a function of the binding energy. In this manner, all of the related sets of data can be displayed on the same chart and some preliminary trends become visible already. The figure below shows the evolution of the Si 2p doublet as a function of the thickness of silicene on Ag(111).

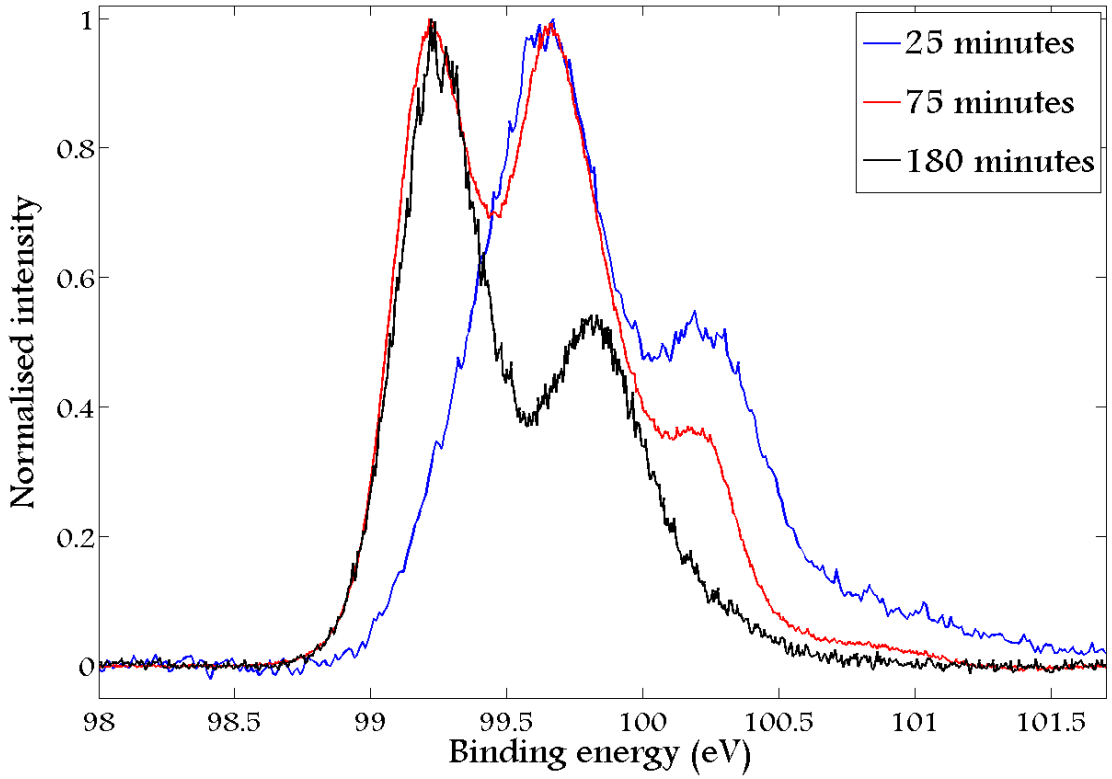

Figure 11: Superimposed photoemission spectra of the Si 2p doublets from the preparations of 25, 75 and 180 minutes taken along the normal direction. The intensities have been normalised with respect to their respective maximum amplitudes.

By repeating the procedure with the spectra of the Ag $3d_{5/2}$ core level the following figure is produced.

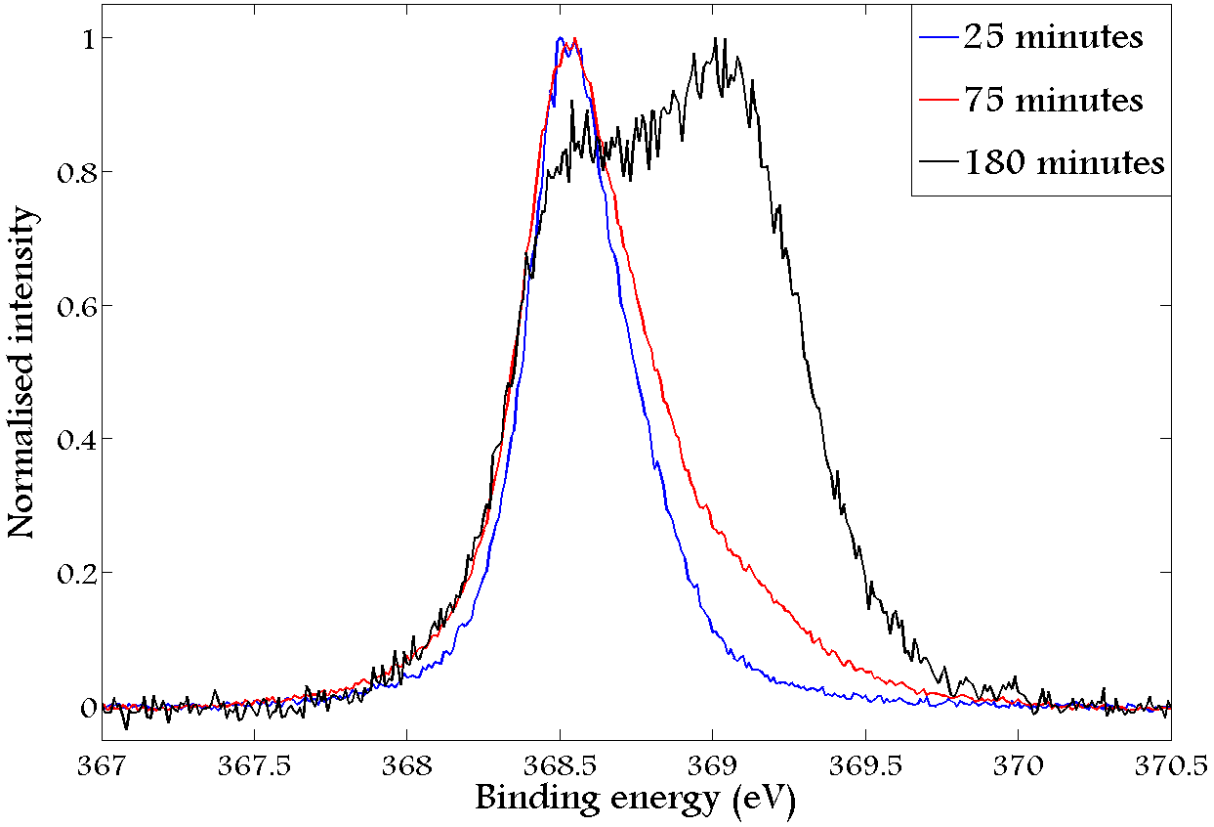

Figure 12: Superimposed photoemission spectra of the Ag $3d_{5/2}$ level from the preparations of 25, 75 and 180 minutes taken along the normal direction. The intensities have been normalised with respect to their respective maximum amplitudes.

As the previous two figures show, the spectra evolve noticeably when the thickness of silicene is increased.

The changes of the Si 2p levels are complex. As a whole the feature seems to shift towards lower binding energy when silicene thickens, but interestingly, after 75 minutes of evaporation, the shape reveals the presence of at least two components (each comprised of a spin-orbit doublet). The angular evolution of the spectra will shed more light onto this question in subsequent pages.

Regarding the Ag $3d_{5/2}$ level, the 25 minutes data resemble a single, well-isolated peak. Around monolayer coverage, a small bump seems to have risen on the high energy side. When the exposure time is increased up to 180 minutes, the previously small bump grows and becomes the predominant component. It is quite straightforward to assume (at least with the current information) that increasing the silicon dose results in the growth of this component in principle absent on the pure silver surface.

The spectra registered after 300 minutes of exposure have been intentionally left apart because the energy of the photons involved in their acquisition was 800 eV instead of 500 eV. This increases their penetration depth which in turn biases the visual appearance of the spectra, and also certainly modifies the diffractive effects. Indeed, these consequences conceal the preliminary conclusions that could be drawn from the overviews included in figures 11 and 12. They are nonetheless included below and can be explained following the same reasoning.

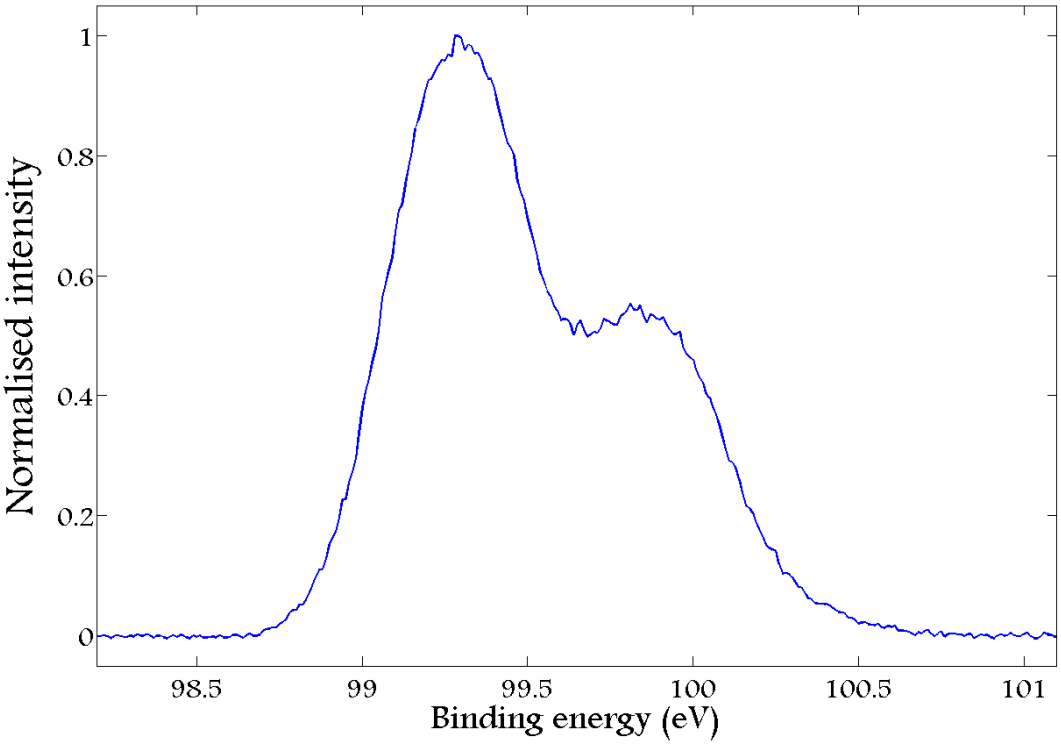

Figure 13: Photoemission spectrum of the Si 2p doublet from the 5 hours sample registered along the normal direction. The intensities have been normalised considering the maximum equal to 1.

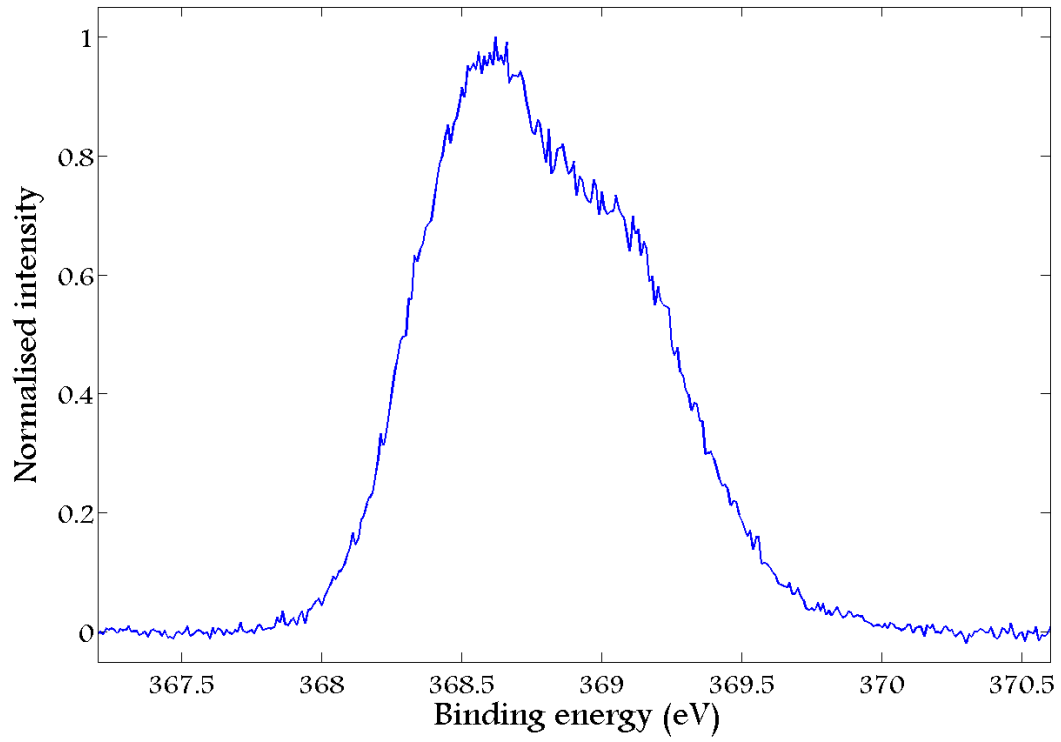

Figure 14: Photoemission spectrum of the Ag $3d_{5/2}$ level from the 5 hours sample registered along the normal direction. The intensities have been normalised so as to make the maximum equal to 1.

Figure 13 is nearly identical to the black curve in figure 11, confirming the overall shift towards lower binding energies. With regard to figure 14, two components are visible as in the black spectrum in figure 12, but they have roughly switched their places amplitude-wise. This fact will be explained later in the light of the data related to the evolution of the spectra with the polar angle.

3.d) Isolation of the peaks

After general inspection of the spectra, and given that on some of them several components display non-negligible overlaps, the next step is the separation of the features that appear in every set of data. The figure below includes the breakdown of the Si 2p spectra.

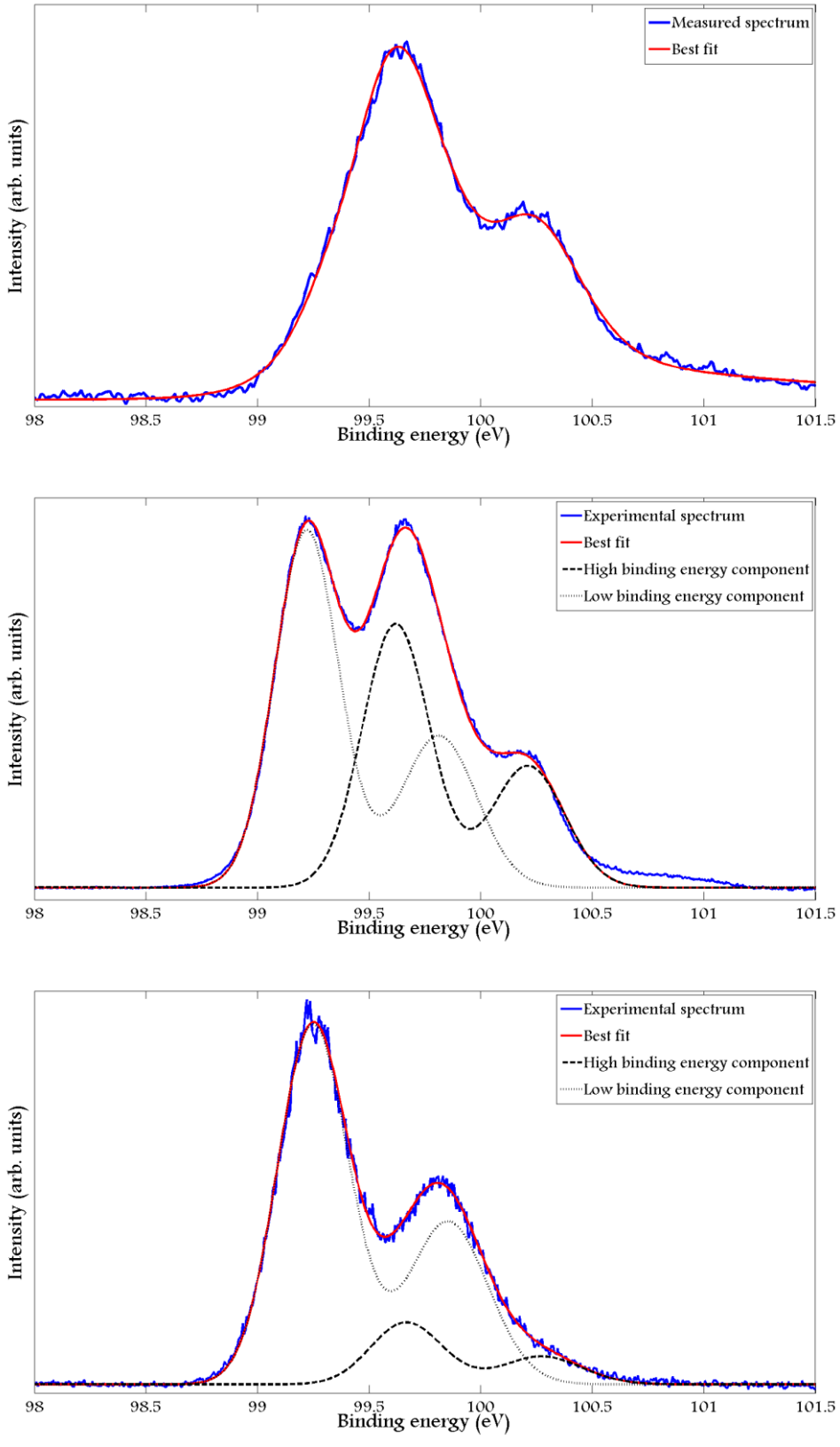

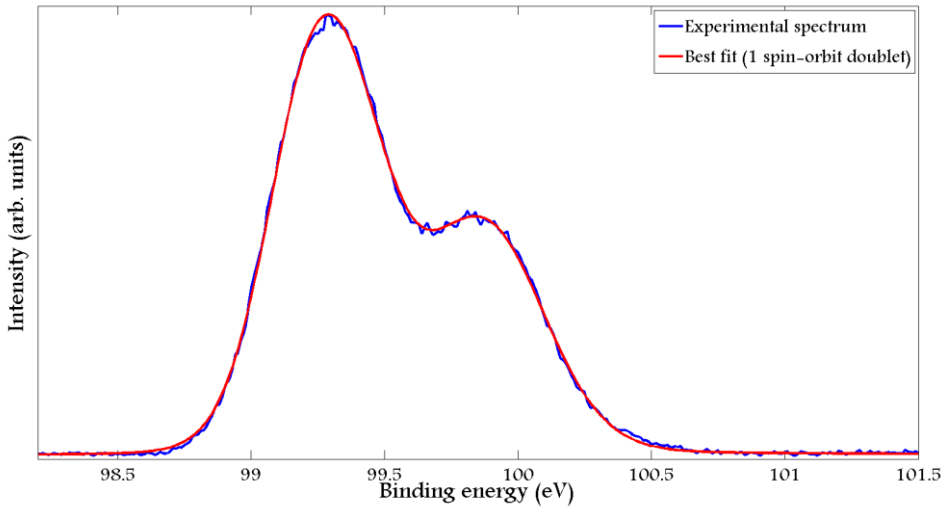

Figure 15: Breakdown of the photoemission spectra from the Si 2p spin-orbit doublet observed along the normal direction. Starting from the top of the previous page downwards, the charts correspond to the preparations in the order: 25, 75, 180 and 300 minutes. The first and the last sets of data include the only component they feature (beyond a reasonable signal-to-noise ratio).

The following table contains a list of the parameters of every fit. Those values will be useful to characterise the evolution of the spectrum when the dose of silicon is increased. The correspondence of the variables and the expressions can be found in the HREELS section.

Sample (min)	**25**	**75**	**180**	**300**
Common parameters				
σ_G (eV)	0.25	0.23	0.20	0.25
γ_L (eV)	0.52	0.32	0.23	0.20
Asymmetry G	-1.0	-0.1	-0.5	-0.7
Asymmetry L	3.8	2.5	0.3	2.0
Amplitude ratio #1/#2	2.0	0.72	0.17	2.0
Component #1 (Low binding energy)				
Binding E (eV)	-	99.8	99.8	99.8
Component #2 (High binding energy)				
Binding E (eV)	100.2	100.2	100.2	-

Table 3: Parameters of the fits shown in figure 15. The width of the gaussian and the lorentzian, their asymmetries and the ratio of amplitudes are listed under "common parameters". The binding energy corresponds to the Si $2p_{1/2}$ peak. The Si $2p_{3/2}$ level is less bound by 0.6 eV.

As the analysis reveals, in the sub-monolayer range the spectrum only manifests a Si 2p doublet at high binding energy (99.6 and 100.2 eV). Around monolayer coverage (it's important to bear in mind that the corresponding LEED pattern has revealed an incipient multilayer) a formerly absent less bound component (99.2 and 99.8 eV) rises and surpasses the previous one, although both have similar amplitudes. From that point, further evaporation of silicon atoms leads to the disappearance of the most bound doublet, and in the last spectrum only the one with the lowest binding energy persists. In short, from the first to the last stage the process resembles a solid shift towards lower binding energies, though the intermediate steps are more complex.

A similar processing can be done on the Ag $3d_{5/2}$ peak. The results are displayed in the following collection of spectra.

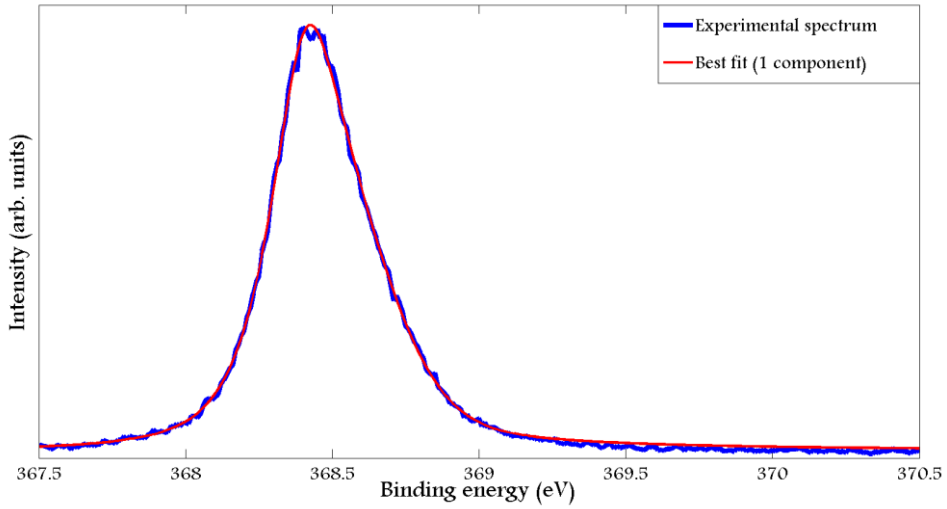

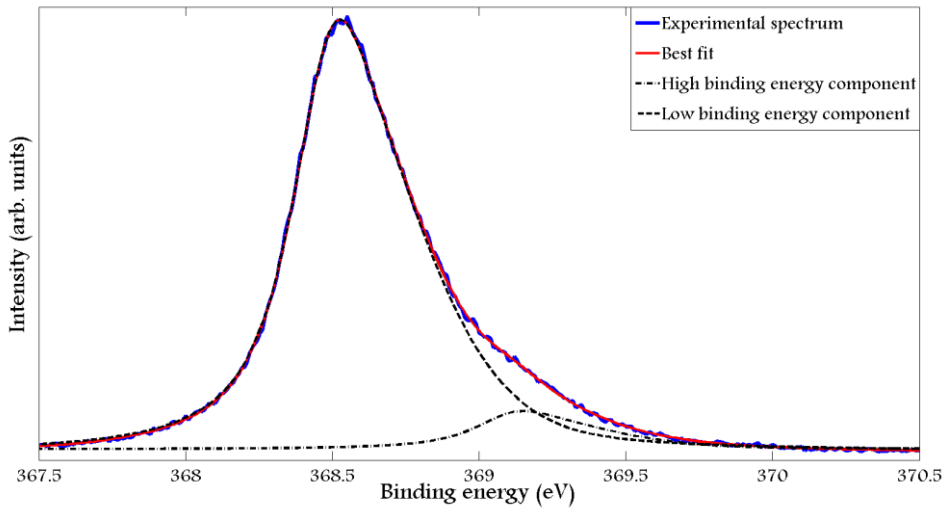

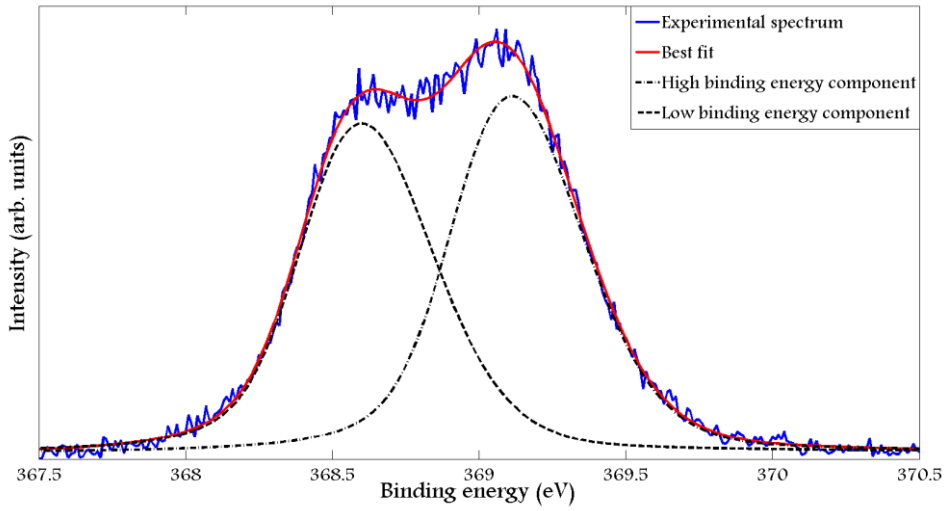

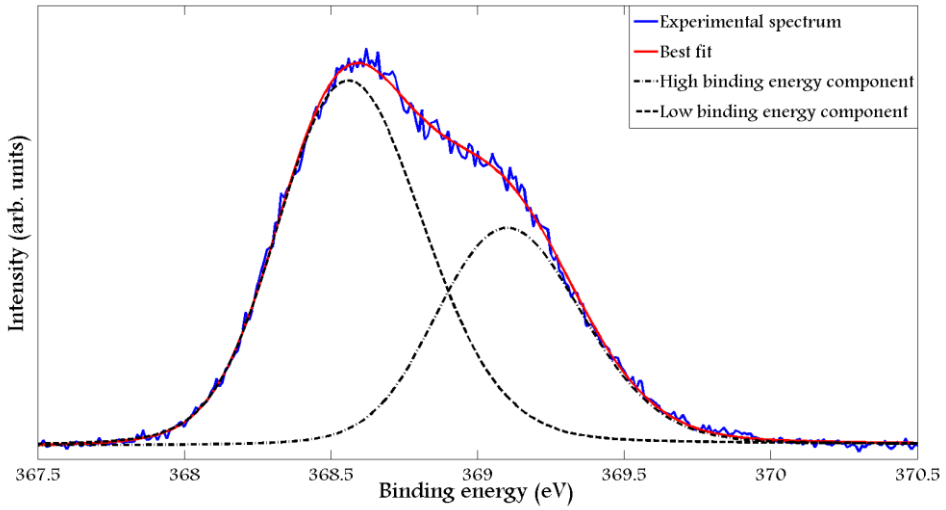

Figure 16: Breakdown of the photoemission spectra from the Ag $3d_{5/2}$ level observed along the normal direction. Starting from the top of the previous page downwards, the charts correspond to the preparations specified by the order: 25, 75, 180 and 300 minutes. In the first spectrum only one component is necessary to reproduce the measured values.

Once again, the values of the parameters involved in the models are key elements to discuss the change of the spectrum as a function of the silicon dose. The table below contains them.

Sample (min)	25	75	180	300
Common parameters				
σ_G (eV)	0.21	0.30	0.29	0.30
γ_L (eV)	0.15	0.19	0.27	0.30
Asymmetry G	-0.6	-1.3	-1.0	-0.8
Asymmetry L	1.0	0.4	0.7	1.9
Amplitude ratio #1/#2		11.36	0.93	1.66
Component #1 (Low binding energy)				
Binding E (eV)	368.5	368.6	368.6	368.6
Component #2 (High binding energy)				
Binding E (eV)		369.1	369.1	369.1

Table 4: Parameters of the fits shown in figure 16. The width of the gaussian and the lorentzian, their asymmetries and the ratio of amplitudes are listed under "common parameters". The first spectrum displays only one peak, that's the reason why two cells related to the eventual second one are blank.

Generally speaking, the spectra show two features at low and high binding energy (368.5 and 369.1 eV respectively). However, the latter is not detected in the first set of data and grows gradually as the dose of silicon is increased. On the preparation of 3 hours, the most bound peak has reached an amplitude greater than the other one. This situation is reverted in the last spectrum, but the reason for this "anomalous behaviour" lies in the fact that the energy of the photons is 800 eV in the last case. This changes the diffractive effects and increases the kinetic energy of the electrons consequently enhancing the signal from deeper layers.

The next section will show that the high binding energy components are related to silicon or silver atoms located at the surface or an interface, and the less bound one comes from the bulk silver or bulk silicon. In the end, that will be enough to elaborate a scenario of the growth of silicene on Ag(111) substrates in the conditions of the experiment.

3.e) Angular dependence of the spectra

As table 1 shows, for the first 3 preparations the spectra were registered along several directions separated by different angles (from 0º to 45º) from the direction perpendicular to the surface. By choosing higher angles of emission, the mean free path of the free electrons stays constant, but the probing depth is determined by the projection of the free path onto the direction normal to the surface. As a result, an increase in the angle of emission reduces the signal from deep layers compared to the most superficial ones. Consequently, the integrated flux from all the sample displays eminently the characteristics related to the surface.

The following figure contains the spectra of the Si 2p doublet emitted from the 75 minutes preparation as a function of the angle of emission.

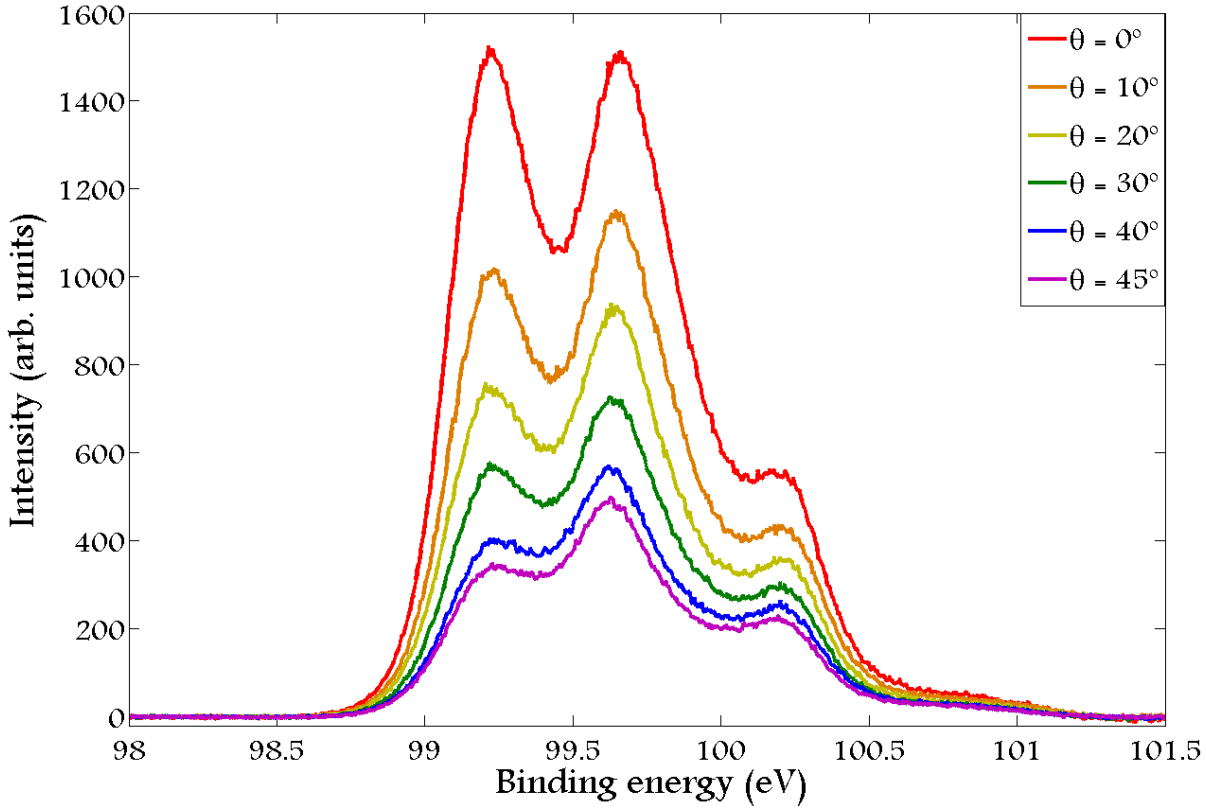

Figure 17: Collection of spectra of the Si 2p level registered from the silicene grown for 75 minutes as a function of the angle of emission.

Figure 17 hints a gradual decrease of the least bound component (see figure 15 and table 3 for the identification) compared to the other one. The integration of such components offers a quantitative manner of keeping track of the ratio of fluxes between both features.

The chart below represents precisely the area of the most bound component divided by the area of the least bound one.

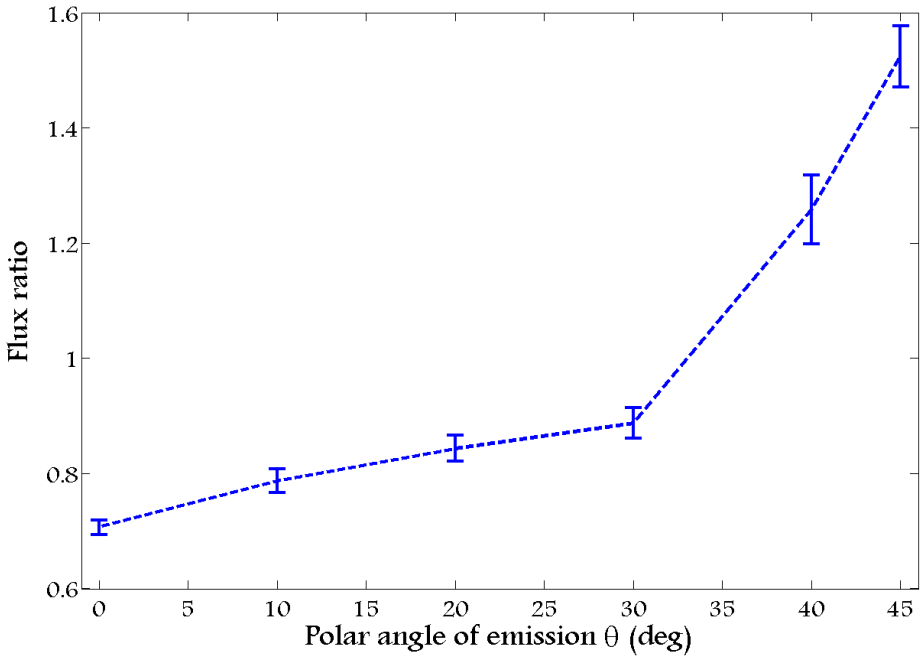

Figure 18: Ratio of flux (intensity integrated under one component) of the most bound component of the Si 2p level ($E_{2p1/2}$=100.2 eV and $E_{2p3/2}$=99.6 eV) over the least bound doublet ($E_{2p1/2}$=99.8 eV and $E_{2p1/2}$=99.2 eV) as a function of the angle of emission.

Figure 18 shows that the most bound component grows undeniably compared to the other one when the angle of emission is increased. This implies that the mechanism at the origin of the former lies closer to the surface than that of the latter.

The first spectrum of figure 15 only shows the surface component. At the beginning, not even a monolayer has been formed, so all the silicon atoms should be on top of the sample and it's logical to assume that they should all display the "surface" behaviour. After 75 minutes of evaporation, the bulk component has risen significantly due to the emergence of the multilayer counterpart. As a result, atoms in the bilayer or multilayer silicene leave the "exotic" chemical environment induced by the immediate neighbouring silver atoms. However the monolayer is probably the most abundant configuration, whence its strong flux. Later, after 3 hours of evaporation most of the sample would be covered by multilayer silicene. This produces an important decrease of the surface/interface component as the bulk one becomes more important. Finally, after 5 hours of preparation the silver substrate is completely covered with a thick multiple layer of silicon atoms. This scenario leaves no room for significant zones of monolayer silicene while the interface emission would be diluted in the bulk, consequently the only component observed in the spectrum is the bulk one.

According to this, the most bound component will be considered hereinafter a surface/interface variant and the least bound one will be identified with a bulk feature. Upon thoughtful examination this statement is in agreement with all the information provided so far.

Globally the process can be perceived as a shift towards lower binding energies, but the intermediate stages includes the rise and fall of two components that are intimately related to the thickness of silicene and the chemical environment.

This deductive reasoning has been based on the data provided by the 75 minutes preparation, but all of the Si 2p sets of spectra agree entirely with the trends explained in the preceding paragraphs.

The Ag 3d level is susceptible to receive the same analysis to deepen the understanding of the growth of silicene. The following figure includes the spectra of the Ag 3d peak emitted from the 180 minutes preparation as a function of the angle of emission.

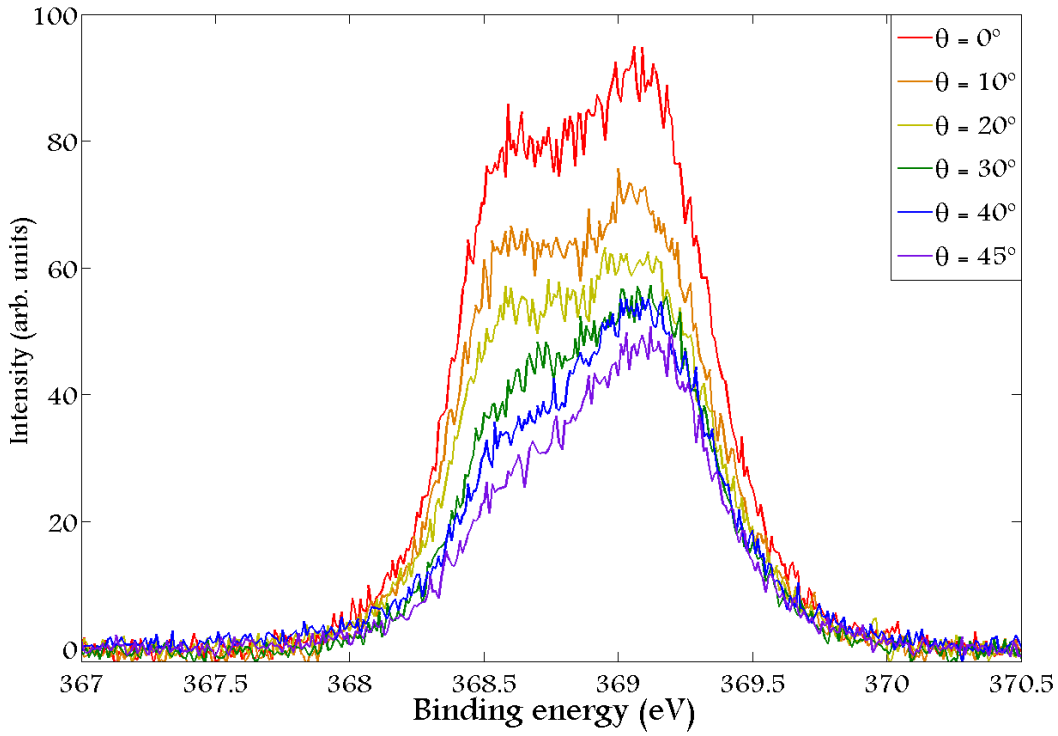

Figure 19: Collection of spectra of the Ag 3d level registered from the silicene grown for 180 minutes as a function of the angle of emission.

Figure 19 also shows the gradual decrease of the least bound component compared to the most bound one. The graph below quantifies the evolution of the ratio of areas enclosed by each component.

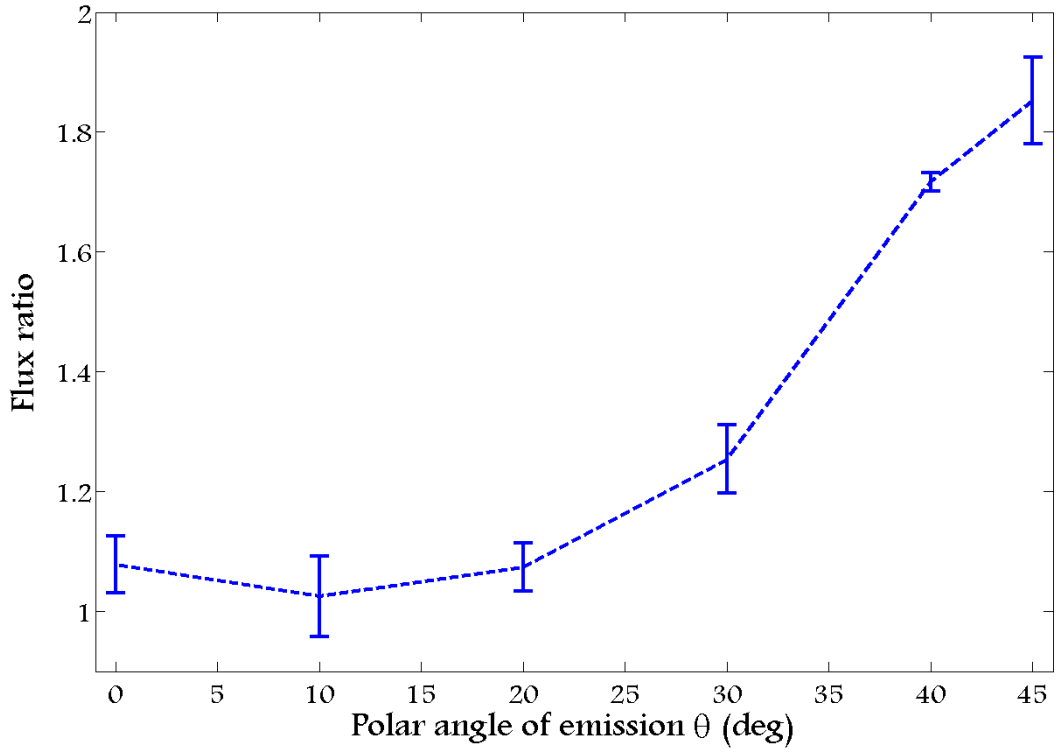

Figure 20: Ratio of flux of the most bound component of the Ag 3d level (E=369.1 eV) over the least bound one (E=368.6 eV) as a function of the angle of emission.

The interpretation of these data is very similar to the one derived from figures 17 and 18: There are two components at high and low binding energies (369.1 and 368.6 eV respectively). The ratio of the former divided by the latter increases significantly as the line of observation gets further away from the normal direction. The most straightforward conclusion would be that the most bound peak comes from atoms that are closer to the surface, thus explaining its relative enhancement. Given that there's a shift in the binding energy, it seems that the chemical environment of both components is rather different.

In the spectra taken after 25 minutes of evaporation, only the least bound component is manifest beyond an acceptable signal-to-noise ratio, so it's safe to assume that that feature is produced by the bulk silver of the substrate. The other peak rises as the dose of silicon is increased and is located closer to the surface as well as shifted from the bulk. The simplest hypothesis would be that such a component is created by silver atoms at the surface or at an interface with silicene.

Nevertheless, even if the interpretation is the same, in the case of the Ag 3d spectra the consequences are much more interesting. As the deposit of silicon grows, silver should be covered by increasingly greater thickness of silicene, so the discovery of Ag atoms on the very surface is undeniably striking. At this point it's convenient to remember the polemic among the silicon-terminated[6] and silver-terminated[7] proposals of thick silicene on Ag(111). The data shown here so far, which were registered on a beamline where it's more difficult to control the growth parameters, appear to support the silver variant, suggesting that a migration of about a layer of Ag atoms from the substrate towards the surface is highly probable. However, by no means these data prove that the most conventional scenario is impossible under some other conditions.

The next section will be devoted to the conception of a global vision of the growth of silicene on Ag(111) substrates and will try to harmonise all the information exposed in the previous pages.

4. The growth of silicene on Ag(111) substrates

The data acquired at the synchrotron facilities shed light on four possibly different stages of the formation of silicene on Ag(111) substrates. Those stages are ordered by the dose of silicon on the substrate and consequently expose four lapses of the evolution. This section will be organised by chronological order and will be divided in four subsections that will integrate the details provided by each set of data.

4.a) The sub-monolayer range

After 25 minutes of growth of silicene on the substrate, the LEED pattern implies that the patches of monolayer (4×4) silicene are in any case so scarce that they cannot cast their corresponding diffractive pattern onto the fluorescent screen. Equivalently, a significant part of the surface is still *bare* silver while the rest would display small zones of covered by a layer of silicon with the thickness of one atom.

The corresponding Si 2p spectrum only features the surface/interface component because there is not enough silicon to form thick clusters that could produce the bulk signal. Regarding the Ag 3d spectrum, only the bulk peak is detectable. Immediately under the patches of silicon, the silver atoms probably display their interface character, but the underlying bulk silver emits such an intense flux that the interface component cannot be captured reliably under the restrictions imposed by the noise level.

The following figure portrays the scheme of the situation described in the last two paragraphs.

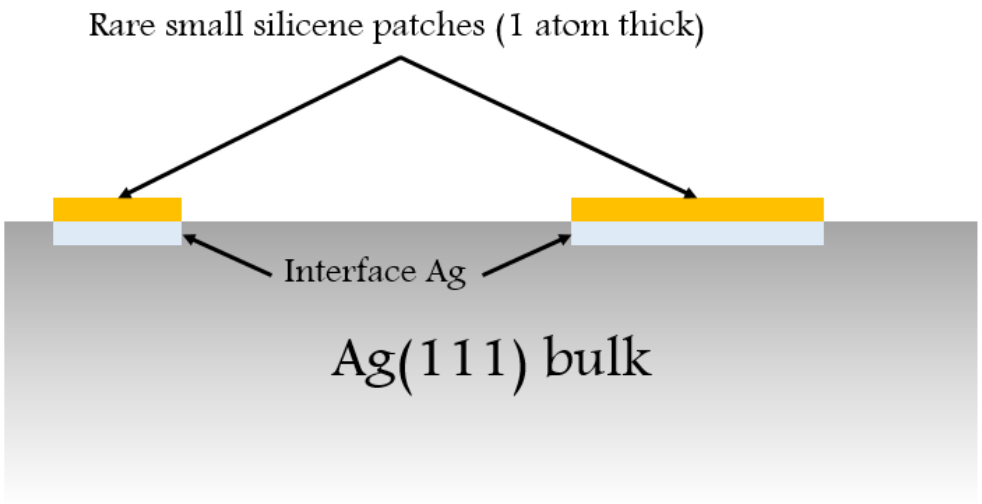

Figure 21: Schematic side-view (along a direction parallel to the surface) of the scenario proposed to account for the spectra registered on the 25 minutes preparation. The silver substrate can be assumed semi-infinite for all practical purposes.

Although no reasonable doubt exists on the silicon nature of monolayer silicene, no proof about the presence of the silicon atoms on top of the substrate has been given yet. This can be checked easily by studying the Si/Ag ratio as a function of the angle of emission. The chart below include such values.

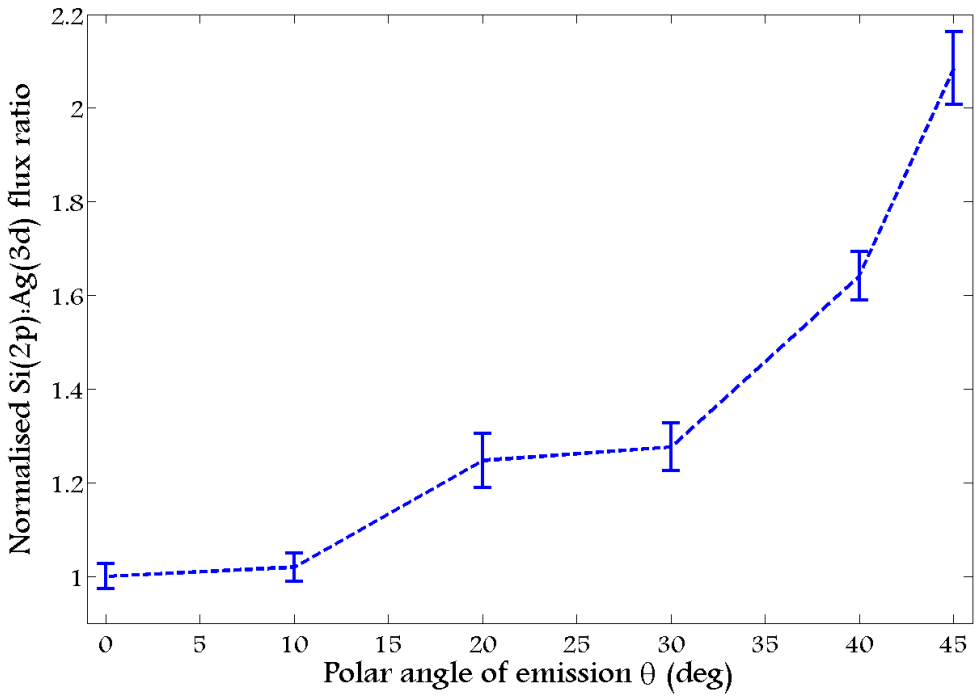

Figure 22: Si(2p)/Ag($3d_{5/2}$) flux ratio normalised to its value at normal emission (θ=0º) for the preparation of 25 minutes.

As figure 22 reveals, the Si(2p) to Ag($3d_{5/2}$) flux ratio steadily increases as the sensitivity to the surface is enhanced. Consequently, the silicon atoms lie at the surface as expected.

4.b) Around monolayer coverage

The situation after 75 minutes of depositing silicon has changed much. The most obvious modifications is the appearance of the Si 2p bulk component and the Ag 3d surface component. The mechanism of growth has to be able to accommodate these two new peaks.

The main idea would be that, as the amount of silicon adsorbed on the substrate grows, multilayer silicene starts to form. As soon as the silicon atoms are not in direct contact with silver atoms, the chemical environment responsible for the surface/interface behaviour of the Si 2p level is lost, that is, some silicon atoms are surrounded exclusively by more silicon atoms and as a result they display their bulk character.

As for the Ag surface/interface component, it is weak compared to the bulk one, but its presence is confirmed beyond any doubt. This along with the trend exposed in figure 22 strongly suggest the migration of silver atoms (silver atoms that probably form the incipient $(\sqrt{3} \times \sqrt{3})R30°$ reconstruction visible on LEED) towards the surface. The proposed scenario can be seen in the following figure:

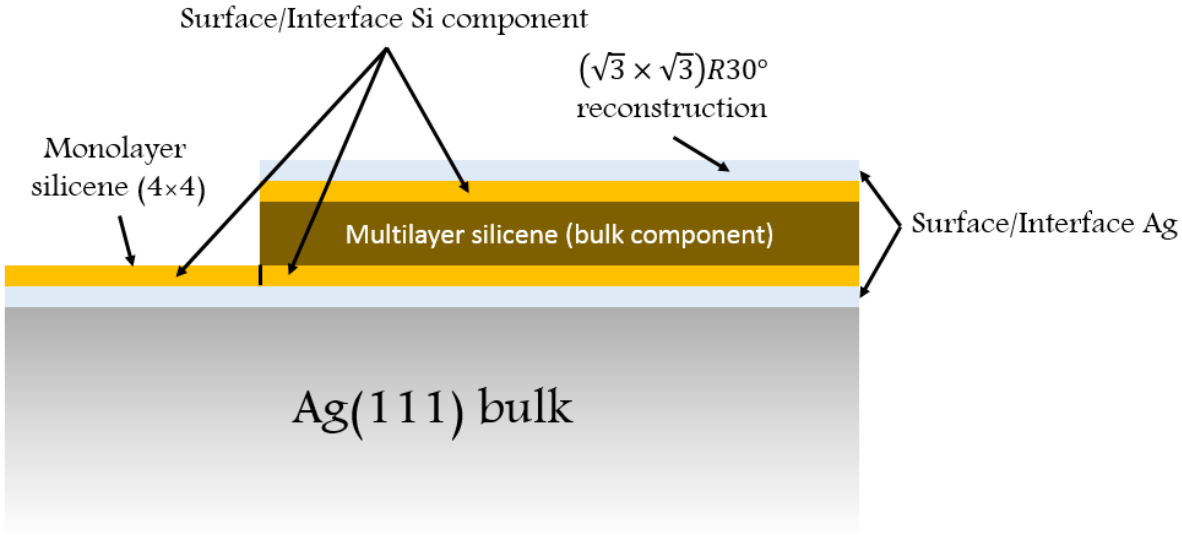

Figure 23: Schematic side-view of the scenario proposed to explain the spectra registered on the 75 minutes preparation.

Some precisions must be added to figure 23. Firstly, the LEED pattern seems to discard the possibility of significant uncovered zones of the substrate because samples with similar diffractive signatures have been almost free of bare Ag areas as seen on STM images.

Secondly, silicene is known to display a growth similar to the Stranski-Krastanov mechanism[15,16]. This implies that multilayer silicene doesn't grow uniformly and consequently a more rigorous treatment would require many bulk components with different thicknesses.

However figure 23 captures well the fact that some areas of the sample are supposed to be covered by monolayer silicene while the rest should be occupied by the multilayer counterpart. Furthermore it explains the sudden appearance of the two new components at least qualitatively.

This proposal is supported by the stratification that can be inferred from the ratios of intensity of the different features.

Probably, the most controverted aspect of the model sketched in figure 23 is the layer of silver on top of multilayer silicene. The chart below shows the ratio of the surface/interface Ag component and the silicon bulk one.

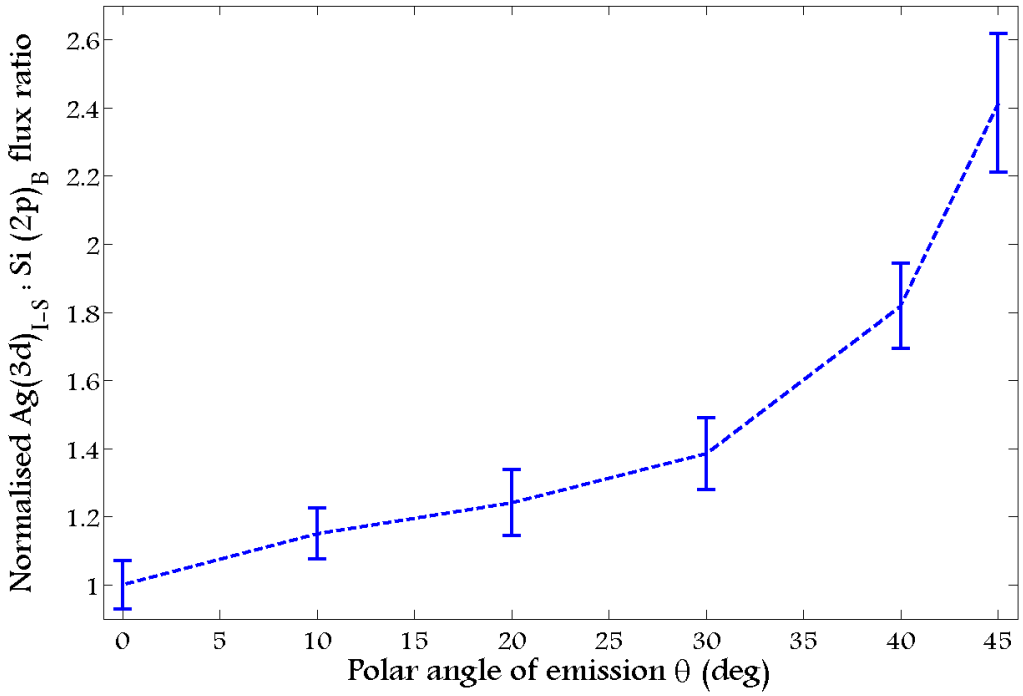

Figure 24: $Ag(3d)_{interface-surface}/Si(2p)_{bulk}$ flux ratio normalised to its value at normal emission (θ=0º) registered on the preparation of 75 minutes.

The figure above reveals an incessant growth of the surface/interface Ag component compared to the bulk of silicon. This strongly suggests that there are silver atoms located at a higher level than most of the silicene.

If both interface/surface components are compared, it should be possible to determine which one is farther away from the surface. The result is shown in the following figure:

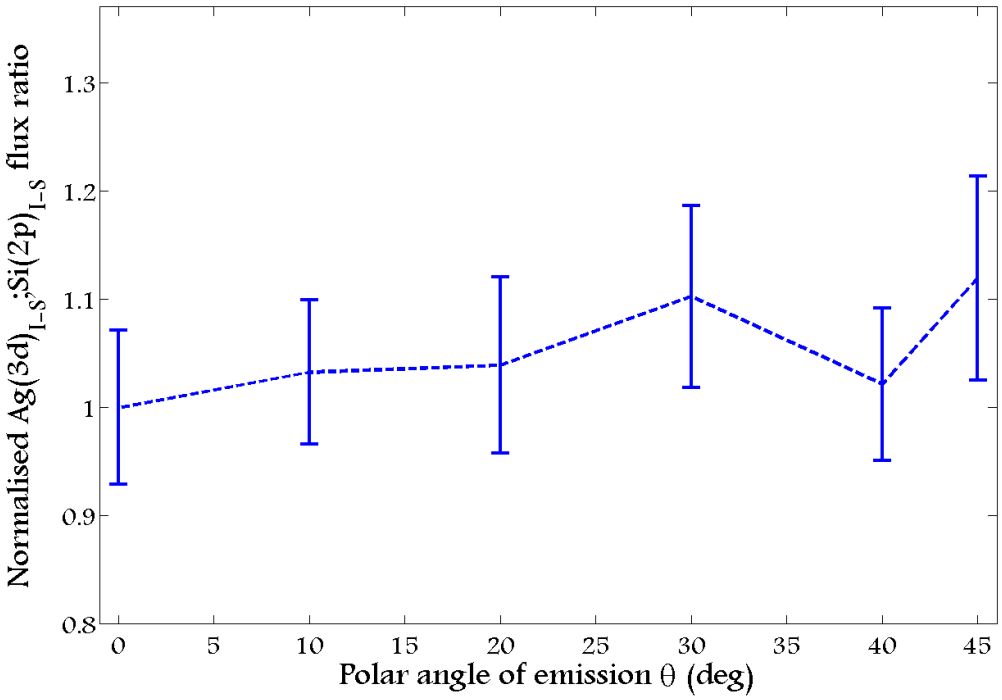

Figure 25: $Ag(3d)_{interface-surface}/Si(2p)_{interface-surface}$ flux ratio normalised to its value at normal emission (θ=0º) registered on the preparation of 75 minutes.

The previous graph is absolutely compatible with the constancy of the ratio between the interface-surface features within the margins of error. This fact is easily explained by the model depicted in figure 23: if there is one portion of the surface covered by atoms of silicon, and the rest covered by silver, as the line of sight drifts away from the direction perpendicular to the surface the flux ratio shouldn't change significantly because the topmost layer is practically free of attenuation. Bearing in mind that at 130 eV of kinetic energy the electron mean free path is around 4.6 Å in silver[17] and 5.9 Å in silicon[18], only 2-3 layers are effectively probed even under in the most favourable case (normal emission), so fixed heterogeneous distributions of atoms on the surface should be reflected in a constant ratio of fluxes.

It is necessary to remind that the $(\sqrt{3} \times \sqrt{3})R30°$ reconstruction is not supposed to form with segregated Ag atoms, but rather with Si ones. According to this, the top silver layer could be an undesired effect of preparing thick silicene in an environment (the beamline) where the conditions (the temperature appears to be of critical importance) couldn't be controlled like in the everyday laboratory.

4.c) The multilayer range

3 hours of deposit leave very little room for the persistence of monolayer silicene. Consequently, the expected evolution from the previous stage would be the consolidation of multilayer silicene. As a result, the bulk Si 2p feature should become more intense compared to the surface/interface variant, which is indeed observed in figure 15. Regarding the signal from the Ag 3d level, the addition of silicene layers should increase the screening of the flux produced by the bulk silver substrate. According to the model proposed in figure 23, the surface silver would be free of any screening, so the net effect would be the reinforcement of the Ag surface/interface to bulk ratio. Once again, this is the factual evolution derived from the spectra included in figure 16.

The proposed situation after 180 minutes of Si deposit is presented below.

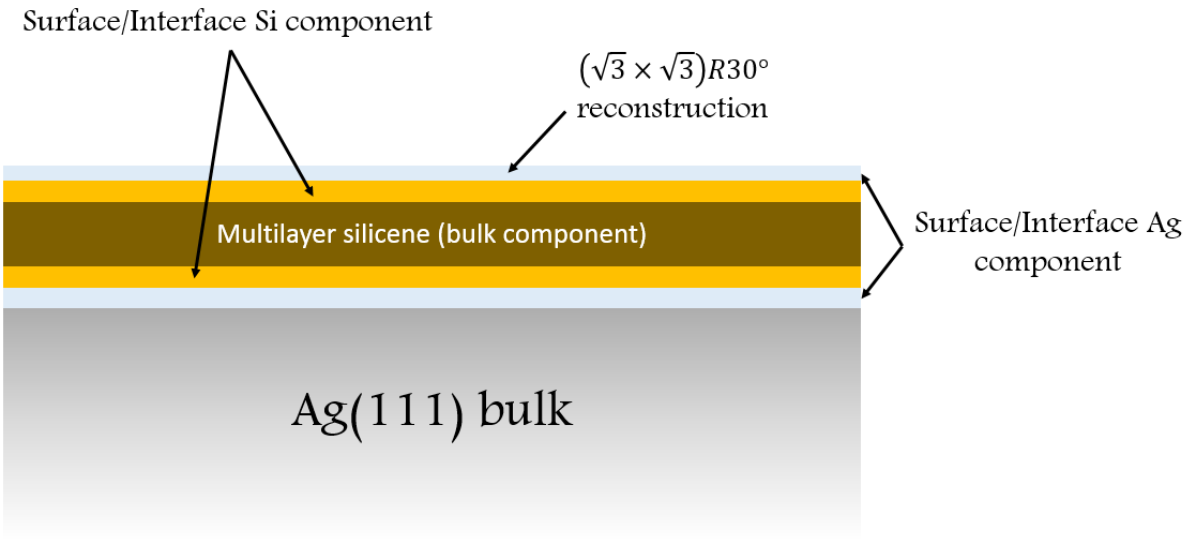

Figure 26: Side-view of the scenario proposed to explain the spectra registered on the 180 minutes preparation.

It's again necessary to keep in mind that the mechanism of growth of silicene doesn't follow the Frank–van der Merwe mode[19], but rather the Stranski-Krastanov one. This implies that even if the terraces of silver are overlooked, silicene doesn't form uniformly flat layers and displays both 2D layer and 3D island growth. Anyway a distribution of clusters with different thickness doesn't affect in the slightest from the qualitative point of view at what has been depicted in figure 26.

With regard the two spectra acquired from the 5 hours preparation, they don't introduce any novelty apart from the disappearance of the surface-interface contribution from the Si 2p doublet. It was already remarkably weak in figure 15 and the situation shouldn't change much. However, these data were registered with more energetic photons, in particular the kinetic energy of the photoelectrons went up from around 400 eV to 700 eV. This causes an increase of the mean free path[18] from 13.8 Å to 21.1 Å. Therefore, the bulk signal is enhanced significantly. A longer probing depth along with a greater thickness of silicene produces the disappearance of the surface/interface doublet behind the intensity of the bulk counterpart and the inherent noise level.

5. The photoelectron diffraction signature of multilayer silicene

Finally, with the intention of verifying the silver nature of the topmost layer of the preparation of thick silicene, some hours were devoted to the acquisition of the X-ray photoelectron diffraction pattern of multilayer silicene. The purpose of this set of measurements was the determination of the nature and the local structure of multilayer silicene.

The core levels chosen for the experiment were the same analysed in the previous section about the study of photoemission from silicene on Ag(111) surfaces, that is, the Si 2p doublet and the Ag $3d_{5/2}$ peak. The energy of photons was kept fixed at 800 eV, which in turn causes the emission of electrons from the Si 2p level with a kinetic energy of 696 eV. The same parameter had a value of 427 eV when the electrons were extracted from the Ag $3d_{5/2}$ level. The registered maps span the interval [0,55]º of polar angle θ, and 183º in the azimuthal direction. Supposing at the very least a three-fold rotational symmetry (a more reasonable assumption would be a six-fold one), the probed region is more than enough to include once or twice all the features in the scanned interval of polar angles.

The treatment performed on the data is the same as the one explained both in the introductory section about photoelectron diffraction and in the CoPc/Ag(100) chapter. Here the procedure won't be explained in detail again. The only variation was the fact that the diffraction pattern was registered within 3 overlapping independent regions. The first one covered the interval [0,21]º in polar angle, the second spanned [15,39º] and the last one was acquired between 31º and 55º. The first region is smaller because the detector included 4º beyond the direction perpendicular to the surface, in other words, it also scanned the angles $\phi + 180º$. Since two-fold rotations are included in six-fold groups but are not included in three-fold ones, these data were intentionally left apart. In any case they covered a very small solid angle, not only due to the interval of 4º, but also because the size of the solid angle is proportional to the sine of the polar angle.

In the overlapping regions the repeated values were combined through averaging after subjecting the data to the rescaling that produced the best agreement between the overlapping intervals. This ensures that the intensity ratios are conserved at least within each one of the three acquisitions and minimises sensibly the mismatch between the final combined pattern covering 55º of polar angle and the individual sets of 24º.

The figures below represent an example of the effect of the normalisation procedure on the Si 2p raw diffraction patterns.

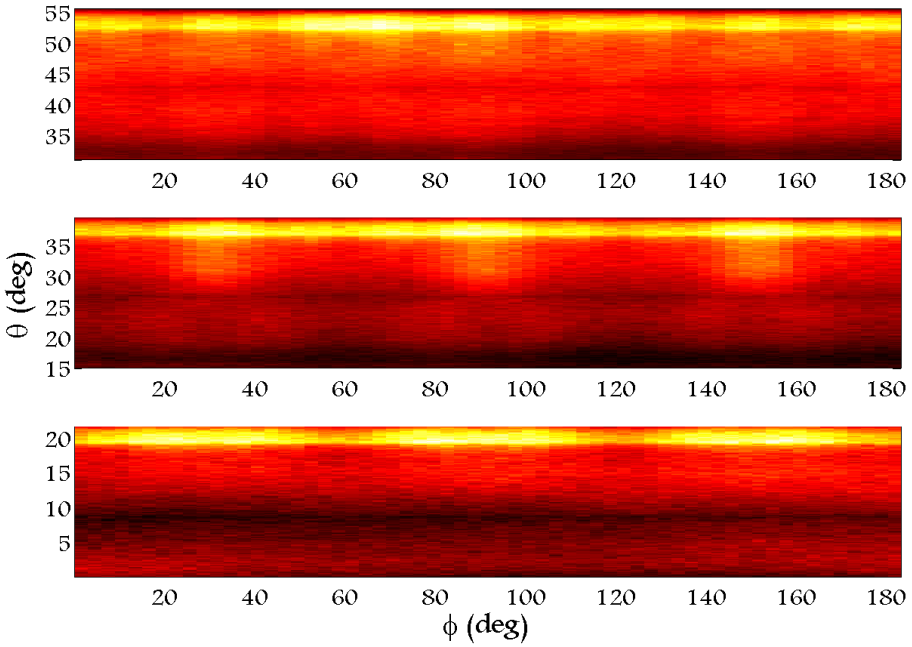

Figure 27: Raw XPD patterns of thick silicene obtained by photoemission from the Si 2p spin-orbit doublet with a kinetic energy of 696 eV. Each chart includes one individual measurement.

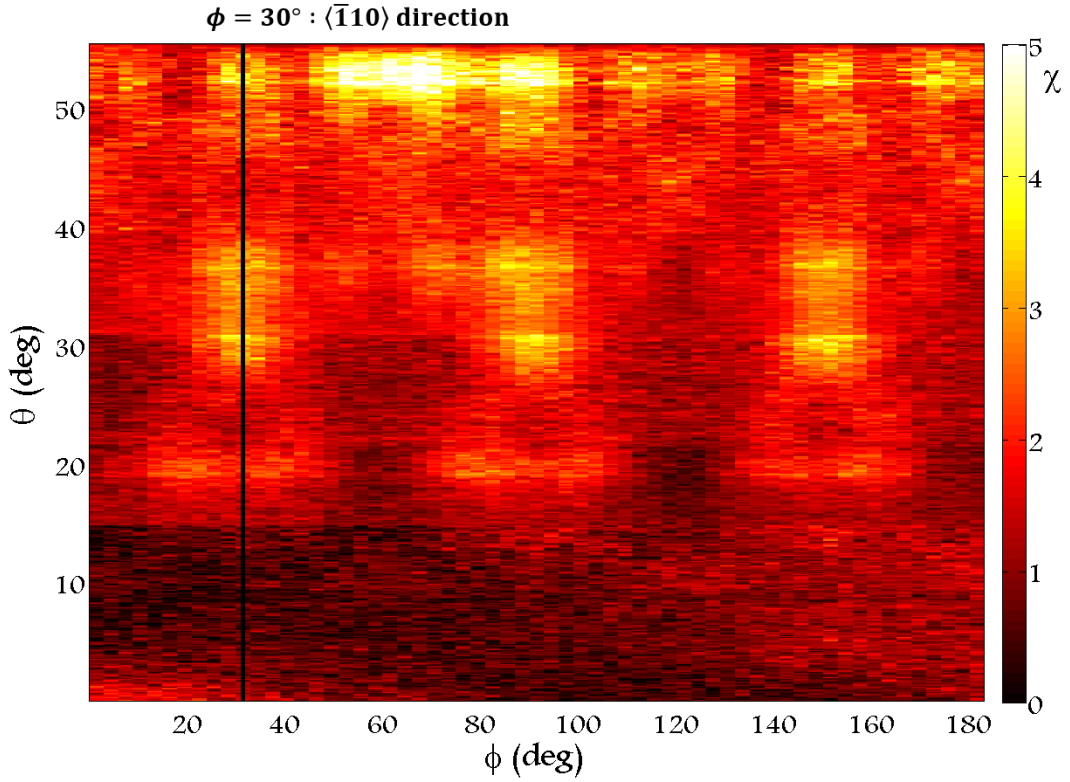

Figure 28: Normalised anisotropy (χ) pattern of thick silicene produced by combination of the individual sets of data portrayed in figure 27. The compact directions of silver have been indicated with a vertical black line.

As for the Ag $3d_{5/2}$ diffractive signature, it's shown after normalisation in the following anisotropy map.

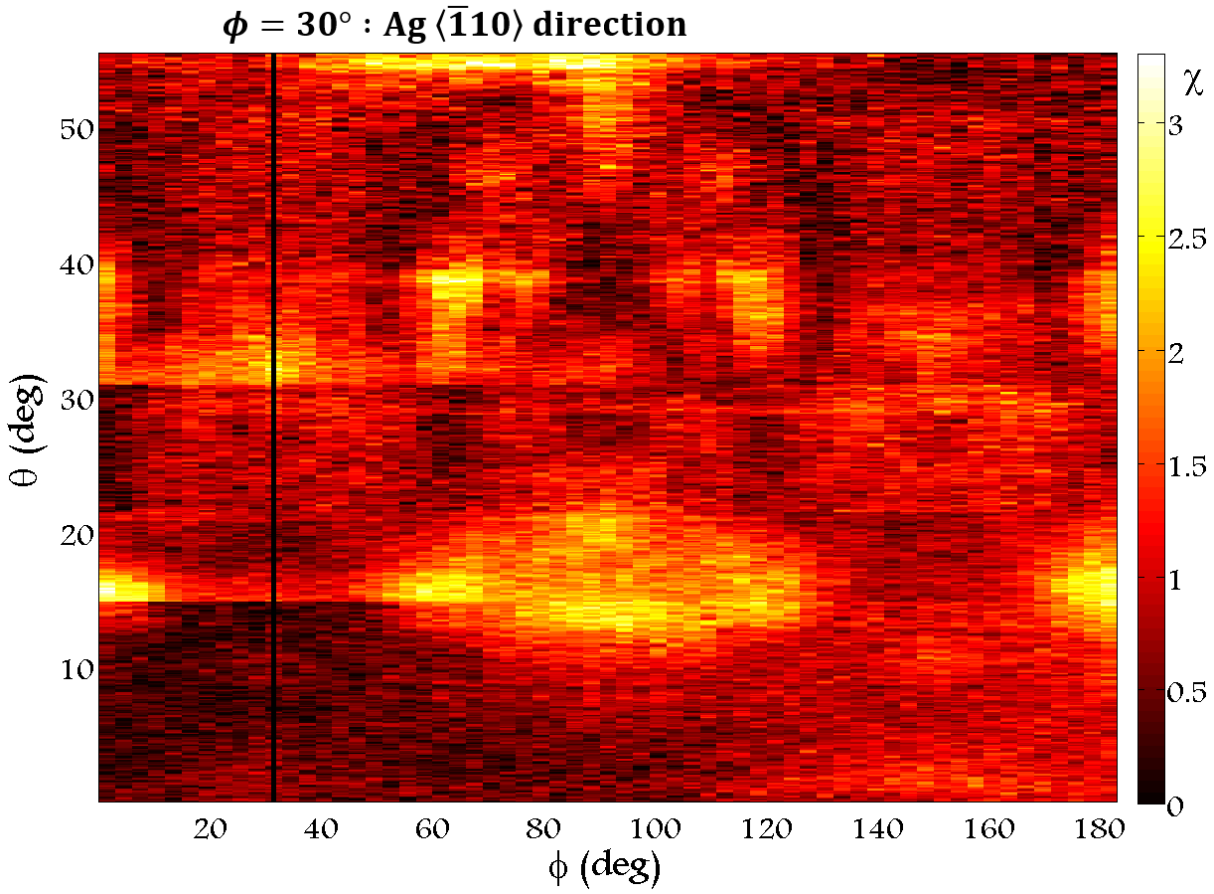

Figure 29: Normalised anisotropy (χ) pattern of thick silicene obtained by photoemission from the Ag $3d_{5/2}$ level with a kinetic energy of 427 eV. The compact directions of the silver substrate have also been marked.

A naïve preliminary analysis on the normalised patterns appears to imply that the anisotropy shown in figure 28 displays a six-fold symmetry (the structures are repeated every 60º) whereas the Ag pattern exhibits three-fold symmetry and reflection symmetry with respect to all the compact directions of the silver substrate (30º, 90º, 150º and so on).

After normalising the experimental data, the models proposed for the structure of multilayer silicene can be tested by simulating their diffractive pattern with the help of the EDAC code[20].

One of these models is the honeycomb dumbbell silicene[21]. According to DFT calculations, some silicon atoms could form five chemical bonds in the special conditions of silicene. Evidently, the situation is not predicted to be very stable, which could explain why multilayer silicene is destroyed upon hydrogenation whereas the monolayer variant is passivated. In effect, an excess on the usual maximum number of chemical bonds for silicon (4) would make the material very reactive, and the transition into silane would be fast and irreversible.

Unfortunately, the precise coordinates of the atoms for the model weren't available and so the model couldn't be tested. It's important to notice that the simulations require not only the positions of silicene, but it's also crucial to know where exactly the silicon atoms lie with regard to the underlying substrate. The latter information is frequently missing in articles related to the structure of multilayer silicene. As it happens with the electric properties of silicene, the presence of the substrate can have a critical impact on the diffraction pattern.

Back in the nineties of the 20th century, several articles were written about the system produced by deposit of silver atoms on Si(111) substrates. It is well-known that with the appropriate preparation the silver top layer adopts a $(\sqrt{3} \times \sqrt{3})R30^{o}$ surface reconstruction, similar to the one displayed by multilayer silicene[22]. This, paired with the apparent presence of silver atoms on top derived from the photoemission data, seemed a good reason for trying the Honeycomb Chained Triangle (HCT) of silver on silicon[23].

The figure below includes a schematic vision of the HCT model.

Label		Interatomic distances (Å)
a	Ag–Ag	4.938 ± 0.021
b	Ag–Ag	3.426 ± 0.005
c	Ag–Si(1)	2.593 ± 0.029
d	Ag–Si(1)	2.596 ± 0.013
e	Si(1)–Si(1)	2.308 ± 0.047
f	Si(1)–Si(2)	2.396 ± 0.028
g	Si(2)–Si(3a)	2.365 ± 0.023
h	Si(2)–Si(3b)	2.374 ± 0.045
i	Si(3a)–Si(4a)	2.383 ± 0.027
j	Si(3b)–Si(4b)	2.265 ± 0.059
k	Si(4a)–Si(5)	2.363 ± 0.019
l	Si(4b)–Si(5)	2.315 ± 0.036
m	Si(5)–Si(6)	2.363 ± 0.018
n	Si(6)–Si(7)	2.311 ± 0.025 *
o	Si(7)–Si(8)	2.367 ± 0.013

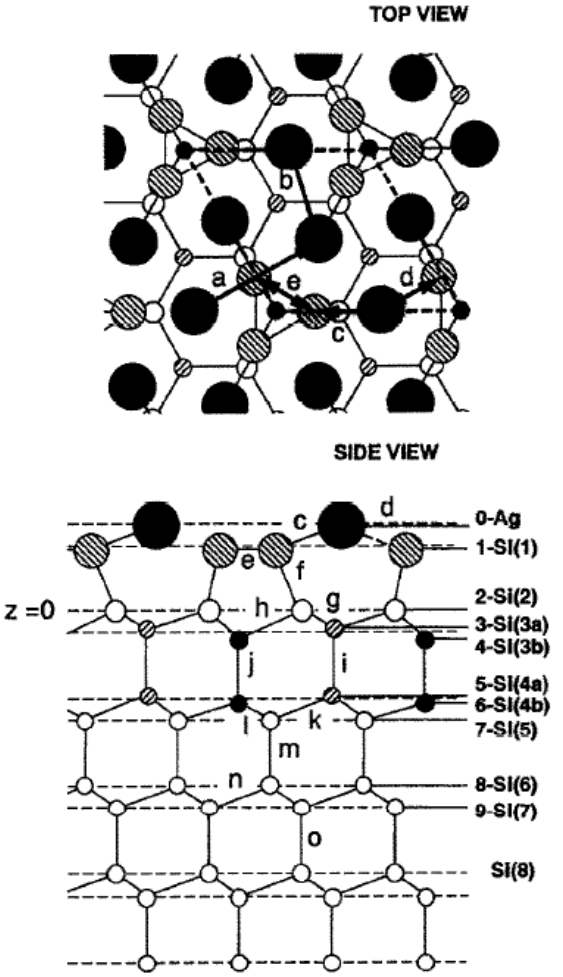

Figure 30: Details of the HCT model. On the right side the top and side views of the model are shown. The table on the left side includes all the distances indicated in the scheme.

This model possesses the advantage of being completely specified. This simplifies the labour of running the simulations because no parameters have been left to be guessed. Obviously, this model can never be an accurate description of thick silicene as at least it lacks the silver substrate. In any case, if the last layers of the cluster (those effectively probed by the electrons) are correct, the agreement between simulations and experiments should be patent.

The following figure shows the experimental data along with the simulated pattern for the HCT model.

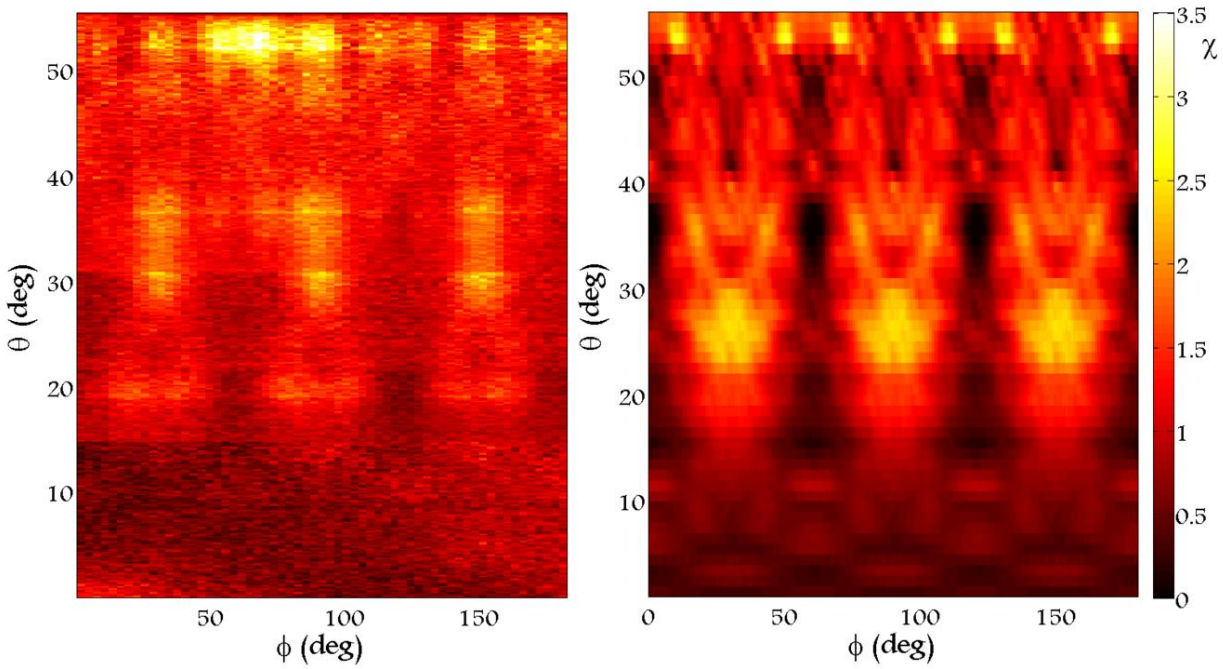

Figure 31: Normalised anisotropy (χ) pattern of thick silicene obtained from the intensity maps in figure 27 (left) and from simulations by means of the EDAC code with parameters equivalent to those involved in the experiments (right).

The comparison between the anisotropy maps of figure 37 is intriguing. There are many similarities. Firstly, below 18º of polar angle there isn't any appreciable signal in the experimental pattern. The simulation reveals a very weak anisotropy that would probably be lost in the noise conditions of the data on the left. Between 20º and 55º degrees of polar angle, there's a significant reinforcement of the emission that is organised around three azimuthal angles: roughly speaking 30º, 90º, and 180º. The anisotropy reaches one of its maxima between 20º and 40º of polar angle. It's true that according to the simulation the brightest spot around 25º appears to be missing in the experimental counterpart, but it's also true that this region displays three visible haloes that enclose the missing spots, so the presence of that feature cannot be ruled out completely. The resemblance in the 30º to 40º interval is more obvious, as even the lateral "wings" manifested in the simulation appear to be present in the "column" located at 90º of azimuth in the experimental pattern. The region between 40º and 50º has a strong but rather isotropic signal on the left side. Such character could arise from the limited azimuthal resolution of the closely packed features revealed by the simulation. Finally, a second narrow maximum appears at approximately 53º of colatitude which is also expressed with strength in the data provided by the calculations.

To conclude, the calculation of the reliability factor between the two patterns shown in figure 37 yields a value of 0.17, lower than the values found in the CoPc/Ag(100) chapter. This further reinforces the statements about the good match of the previous paragraph that were solely based on visual appearance.

Ideally it would be interesting to compare the diffractive pattern casted by the photoelectrons emitted from the Ag $3d_{5/2}$ level, unfortunately this is not possible. With X-rays of 800 eV, the kinetic energy of the photoelectrons is 427 eV, which implies that the experiment occurs in the forward scattering regime. As it has been mentioned, the HCT model was conceived for silver on Si(111) substrates. Thick silicene would be in any case silver on silicene on a Ag(111) substrate.

Consequently, the silver substrate is missing in the HCT model. Keeping in mind that there are many unsolved questions around multilayer silicene, currently there is no way to incorporate a silver substrate to the HCT model. The orientations, locations and distances of the interface between the bulk silver and thick silicene are unknown, therefore the cluster needed for the simulation is beyond the current understanding of this material. Since the main mechanism is forward scattering, the alleged silver atoms from the surface would emit photoelectrons in an isotropic way. Hence, the anisotropy of figure 29 originates in the bulk substrate which, as of now, cannot be introduced in the simulations.

6. Conclusions

The present chapter has exposed a study about the structure of silicene on Ag(111) substrates as a function of its thickness analysed by means of photoemission spectroscopy.

Firstly, the photoemission spectra of the Si 2p spin-orbit doublet and the Ag $3d_{5/2}$ core level have revealed that before the completion of monolayer silicene, there are only a bulk component of silver and a surface/interface component of silicon. As the amount of silicon deposited is increased, a surface feature of silver and a bulk doublet of silicon appear and become gradually more important. The stratification of the sample has been deduced from the evolution of the ratio of the peaks as a function of the angle of emission. Eventually, the new components eclipse the original ones, implying that the topmost layers are occupied mostly by bulk silicon and a surface of silver possibly responsible for the $(\sqrt{3} \times \sqrt{3})$R30º reconstruction.

Currently, there is an ongoing discussion on the very nature of silicene[6,7], but the most fervent defenders of the "silicon on surface" theory argue that even if there is a non-negligible amount of data supporting the "silver on surface" variant, a silicon surface reconstruction is indeed possible, although it may be restricted to a very narrow interval of temperatures or some other very tight conditions. In fact, a recent work of De Padova demonstrates that both systems exist for different growth temperatures (around 200ºC for the silicon composition and higher for the Ag one). This possibility cannot be discarded, however the data shown here strongly point at the most complex stratification.

The X-ray photoemission diffraction from both of the aforementioned core levels has been reported in this chapter, and a silver on Si(111) model has been tested. The match between the simulations and the experimental pattern (for silicon) is promising, but more robust claims could be made if a simulation of the Ag $3d_{5/2}$ pattern were available. Unfortunately the situation of the sample would include an additional Ag substrate which is missing in the tested model and is not trivial to introduce at all.

As the previous paragraphs explain, the analysed data are all compatible with the "silver on surface" hypothesis and a great part of them are highly suggestive of this possibility. It is in any case interesting as it's possibly the first time that a double Ag component is observed on thick silicene and could be helpful for future studies about the conditions that trigger the formation of either option.

References:

1. De Padova, P. et al., J. Phys. D: Appl. Phys, 44, 312001 (2011)
2. Vogt P. et al., Phys. Rev. Lett., 108, 155501 (2012)
3. Feng B, et al., Nano Lett., 12 (7), 3507–3511 (2012)
4. De Padova, P. et al., 2D Mater., 1, 021003 (2014)

5. Chun-Liang, L. et al., J. Phys. Chem. C, 120 (12), 6689–6693 (2016)
6. http://www.synchrotron-soleil.fr/Recherche/LignesLumiere/ANTARES
7. Shirley D.A., Phys. Rev., 55, 4709 (1972)
8. Proctor A. et al., Anal. Chem., 54 (1982)
9. Vegh, J, Journal of Electron Spectroscopy and Related Phenomena, 151, 159–164 (2006)
10. A. Herrera-Gomez. *The active background method in XPS data peak-fitting.* Internal Report. Cinvestav-Querétaro.(2011).
11. Marquardt D., SIAM Journal on Applied Mathematics, 11 (2), 431–441, (1963)
12. Alfonsetti R., et al., Appl. Surf. Sci., 70, 222 (1993)
13. Romand R., et al., J. Solid State Chem., 25, 59 (1978)
14. Doniach S. and Sunjic M., J. Phys. 4C31, 285 (1970)
15. Venables J, *Introduction to Surface and Thin Film Processes*. Cambridge: Cambridge University Press (2000)
16. Vogt, P. et al., App. Phys. Let., 104, 021602 (2014)
17. Powell C. J. and Jablonski A., *NIST Electron Effective-Attenuation-Length Database* – Version 1.3, National Institute of Standards and Technology, Gaithersburg, MD (2011).
18. Lesiak et al., Proc. ECASIA 95, Wiley, Chichester p. 619 (1996)
19. Pimpinelli, A. and Jacques V., *Physics of Crystal Growth. Cambridge: Cambridge University Press* (1998)
20. García de Abajo F. J. et al., Phys. Rev. B, Volume 63, 075404 (2001)
21. Cahangirov, S. et al., Phys. Rev. B 90, 035448 (2014)
22. Takahashi, T. and Nakatani, S. Surface Science, 282, 17-32 (1993)
23. Aizawa, H. et al., Surface Science 429, (1999)

Chapter V: Functionalization of silicene films grown on Ag(111) substrates

Functionalization of silicene films grown on Ag(111) substrates

1. Introduction

As it has already been mentioned, one of the main reasons behind the thriving interest in silicene is its similarity with graphene as both are 2D materials from the same group. The properties of the latter have astounded the scientific community and the industry, and silicene is expected to share a great part of its characteristics while incorporating some new ones, such as an easier integration on current electronics technology. However, silicene is a novel material whose properties have yet to be examined. One of them is its functionalization with chemical species, in line with what has been done with graphene. This topic entails the verification of theoretical predictions and the comparison with the behaviour of pristine silicon.

Intrinsic graphene is a semiconductor with zero band gap which can be modified in multiple manners[1]. Hydrogenation is one of those methods as it allows to vary under control its electronic properties. In effect, a complete hydrogenation of graphene turns the material into a wide gap (3.5eV) semiconductor[2] known as graphane. It has been shown to be stable at room temperature. In addition to that, hydrogen can also induce a change in graphene from nonmagnetic to magnetic[3]. This research is in the forefront of novel technologies and devices, such as the flexible screens.

Although the hydrogenation will span most of the chapter, the possible functionalization of this material by means of organic molecules will also find its place here as it supposes another manner to modify the properties of silicene by physisorption of a different chemical species. The experimental data were registered during a one-week visit at the *ANTARES* beamline (the details of the experimental device have been included in the section that explains the theoretical aspects of photoelectron diffraction) of the *Soleil* synchrotron facilities.

Nowadays, silicon is a keystone of technology. Although it is one of the best electronic materials, its optoelectronic properties are less spectacular. Indeed, its fundamental band gap has a value of 1.12 eV but with the inconvenience of being indirect[4]. The direct gap on the contrary is as large as 3 eV[5]. One example of the consequences is the low efficiency regarding the light absorption in solar cells because the process requires the cooperation of phonons. This low performance imposes thick cells, thus increasing the production costs.

This chapter will be devoted to a comprehensive description of the process that might make it possible to overcome such weak aspects: the functionalization of silicene. In any case, it's convenient to introduce briefly all the possibilities allegedly associated to functionalised silicene to evaluate later what truth lies beneath.

Hydrogenated silicene is predicted to greatly surpass silicon's optoelectronic performance[6]. Free bilayer silicene is expected to be a strongly indirect semiconductor. Upon reaction with hydrogen, it becomes a semiconductor with a direct gap than can be accurately tuned through modification of the hydrogen dose. At low concentrations, the configurations of the system that appear display quasi-direct gaps ranging from 1 to 1.5eV, which would be very convenient for solar applications. If the dose is increased, the gap is also enlarged attaining the values of red, green and blue photons. This implies that the material would be suitable for the design of light emitting diodes.

The following figure summarises the variation of the band gap as a function of the hydrogen dose for a silicene bilayer with bound hydrogen on one and both sides.

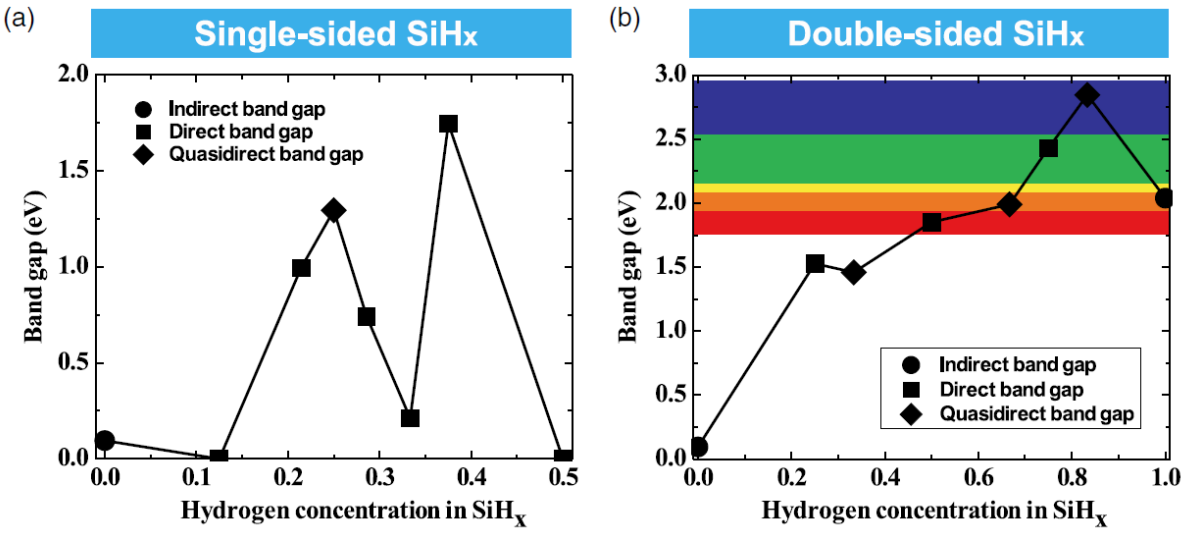

Figure 1: Calculated band gaps of a) single-sided and b) double sided SiH_X. In panel b), a sketch of light spectrum is overlaid to aid visualization of the size of band gap[6]. The abscissas axis is specified in units of atoms of hydrogen per atom of silicon[6].

Regarding freestanding monolayer silicene, its band structure has been determined to be the one of a metal or zero gap semiconductor[7]. However, hydrogenation can widen the gap too and its value depends on the amount of hydrogen chemisorbed. Numerical calculations have shown that a controlled dose of gas on a masked or patterned silicene substrate can produce a system with insulator, semiconductor and metallic zones at the same time.

On another matter, even if the storage of hydrogen in graphane is more performing in terms of weight ratio, it's important to remember that silicene's one is similar in area density of hydrogen atoms and more importantly, the chemical reaction that precedes the hydrogen storage is significantly more favourable and easier in the case of silicane[8] (the silicon analogue of graphane).

As for the magnetic properties, it has been shown that half-hydrogenated silicene possesses localised and unpaired 3p electrons that introduce a ferromagnetic character[9]. According to the same article, silicene that reacts first to semi- and then to fully hydrogenated, undergoes a change in its character as well, evolving from metallic to magnetic semiconducting and to nonmagnetic semiconducting in the end.

The separation of silicene from its substrate is not a trifling question. The epitaxy on silver is on itself a milestone, but for most practical purposes, it would be necessary to detach silicene and make it free-standing. Given the chemical character of the bonds between the substrate and the overlayer, a chemical treatment cannot be circumvented. Interestingly, hydrogenation has been proposed as a way to detach silicene from its substrate so as to obtain freestanding silicane. Tsetseris[10] states two possible ways to break bonds between the silicene and its silver substrate: intercalation of calcium atoms, which would lift the Si atoms without destroying the interlayer silicene bonds; and hydrogenation, which would produce a silicane monolayer that could be subsequently etched away.

In addition to that, Qiu[11] has reported that hydrogenation can be a useful tool to reveal the silicon lattice when dealing with defective or incomplete phases. In particular, he has analysed the $\left(2\sqrt{3} \times 2\sqrt{3}\right)R30°$ superstructure and has found that, although the original phase displays poor periodicity manifested in the abundance of apparent defects, its hydrogenation produces the same structure (as seen with STM techniques) as the paradigmatic (4×4).

Regarding the organic molecules, the first driving force behind the visit to the synchrotron during this thesis was probably the reports of tuning epitaxial graphene on SiC by molecular doping[12]. In particular, a scientific team managed to cancel the strong n-type doping intrinsic to graphene on SiC(0001) with the electron acceptor tetrafluorotetracyanoquinodimethane (F_4TCNQ). These organic molecules can be deposited on the sample not only by means of evaporation but also by wet chemistry.

In effect, while graphene on SiC presents several advantages related to its enhanced stability and the possibility of producing large sheets of graphene compared to the limited size of those obtained by cleavage, it's not exempt of some downsides, such as the shift of the Fermi level away from the Dirac point. This hinders the exploitation of the properties of graphene.

The figure below shows the dispersion relation of the electrons near the Dirac point as a function of the amount of F_4TCNQ deposited on the surface.

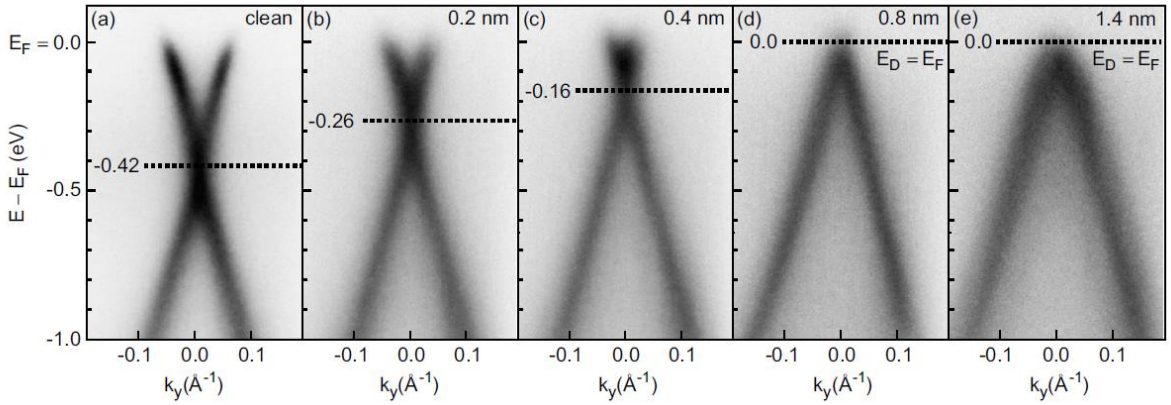

Figure 2: Dispersion of the π-bands measured with UV-excited ARPES around the K point of the graphene Brillouin zone for (a) an as-grown graphene monolayer on SiC(0001) and (b-e) the same sample covered with a F_4TCNQ layer whose thickness is indicated on the upper right corner of each cell[12].

From left to right, the Dirac point (indicated with the dotted line) approaches the Fermi level as the coverage with F_4TCNQ is increased. When the sample is clean, there is an energetic separation equal to 0.42 eV between the aforementioned two references. When the adsorbed layer reaches a thickness of 0.8nm, the Dirac point lies exactly at the Fermi level, and further evaporation has no effect on the dispersion bands, implying that it has reached saturation.

At a microscopic level, the high electron affinity of F_4TCNQ, equal to 5.24 eV, injects holes on the sample, or equivalently, the electrons in excess are captured by the molecules. As a result, the states they were occupying become free and so the Fermi level shifts down toward the Dirac point. After attaining 0.8 nm of thickness, the system is saturated and the molecules cannot capture more electrons.

In pristine silicene the starting situation is similar as the figure 3 reveals. It displays the dispersion bands of thick silicene on Ag(111) as a function of the energy (with the reference of the Fermi level) and the angle of emission. The point of convergence of both bands is 0.3 eV below the Fermi level, and one of the objectives of the visit was to reproduce the p-doping induced by the evaporation of F_4TCNQ seen on graphene.

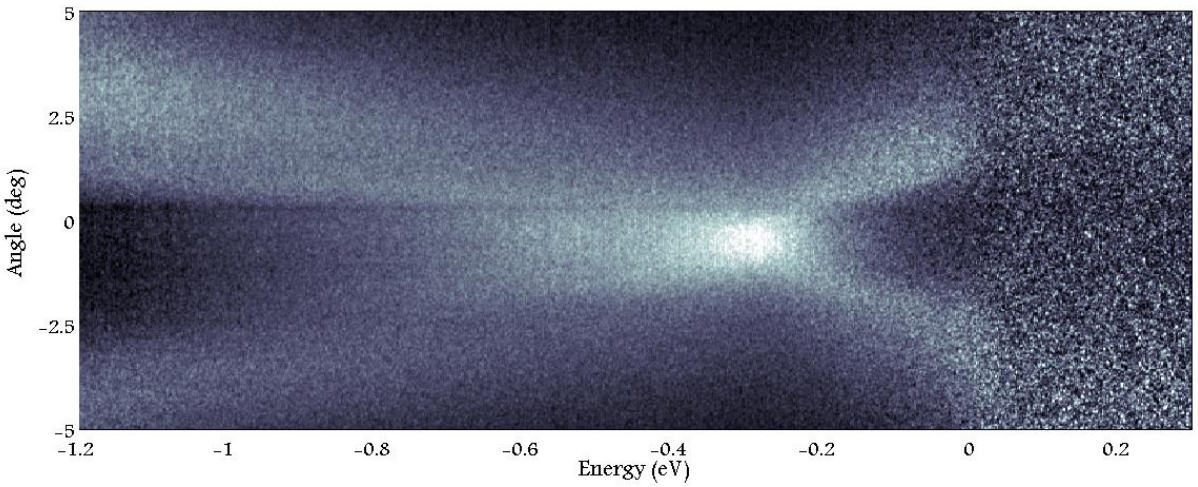

Figure 3: ARPES intensity map of a thick silicene (approximately 4 layers) on a Ag(111) substrate along the Γ-K direction (E_{photon} = 126 eV).

Apart from the precedents of graphene, a preliminary HREELS study of F_4TNCQ (see figure 4) on silicene had revealed that upon adsorption, the C≡N vibrational modes of the molecule are shifted towards lower energies (from around 2200 cm^{-1} to 2075 cm^{-1}).

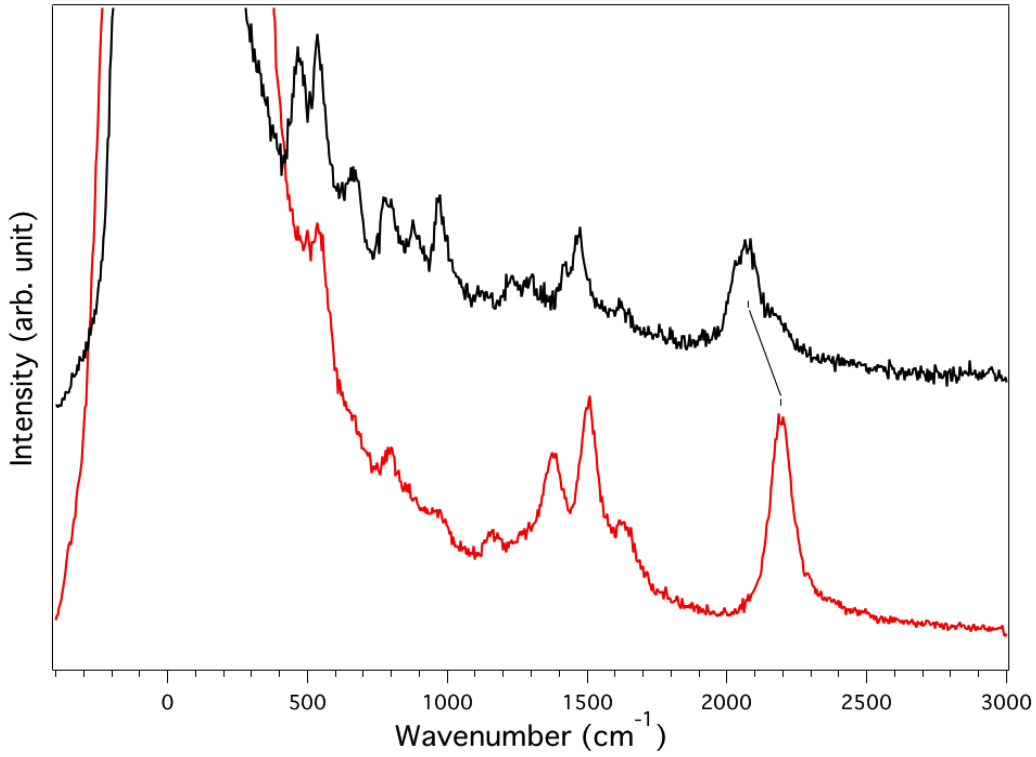

Figure 4: HREELS data of a thick film of F_4TCNQ (red curve) and a monolayer of F_4TCNQ adsorbed on silicene-(√3×√3)R30° (black curve)

Since the lowest unoccupied molecular orbital (LUMO) of F_4TCNQ is an anti-bonding orbital, this weakening of the C≡N bonds can be attributed to a partial or complete filling of the LUMO that results from adsorption[13,14]. This actually indicates that there is a substantial charge transfer from the silicene to the F_4TCNQ and thus that the silicene is molecularly doped.

2. Hydrogenation of monolayer silicene

Hydrogenated monolayer silicene will be analysed from several perspectives, mainly STM images and HREEL spectra.

2.a) Vibrational spectrum

Before engaging in discussing the vibrational spectrum of hydrogenated monolayer silicene, it's convenient to reproduce first analogue information relative to hydrogenated silicon. After all, both systems consist of silicon and hydrogen, and the only difference lies on the former, as it is present in the form of two distinct allotropes in each system.

Given that the Si-H vibrational modes depend strongly on the atoms on both extremes of the chemical bonds and are nearly insensitive to the rest of the silicon cluster, it's reasonable to expect very similar vibrational signatures.

Lucovsky[15] conducted a thorough research on the vibrational spectrum of hydrogenated silicon, and was able to identify the normal modes along with their associated wavenumbers. The figure below constitutes a helpful sketch for visualising the motion of the atoms linked to every vibrational mode.

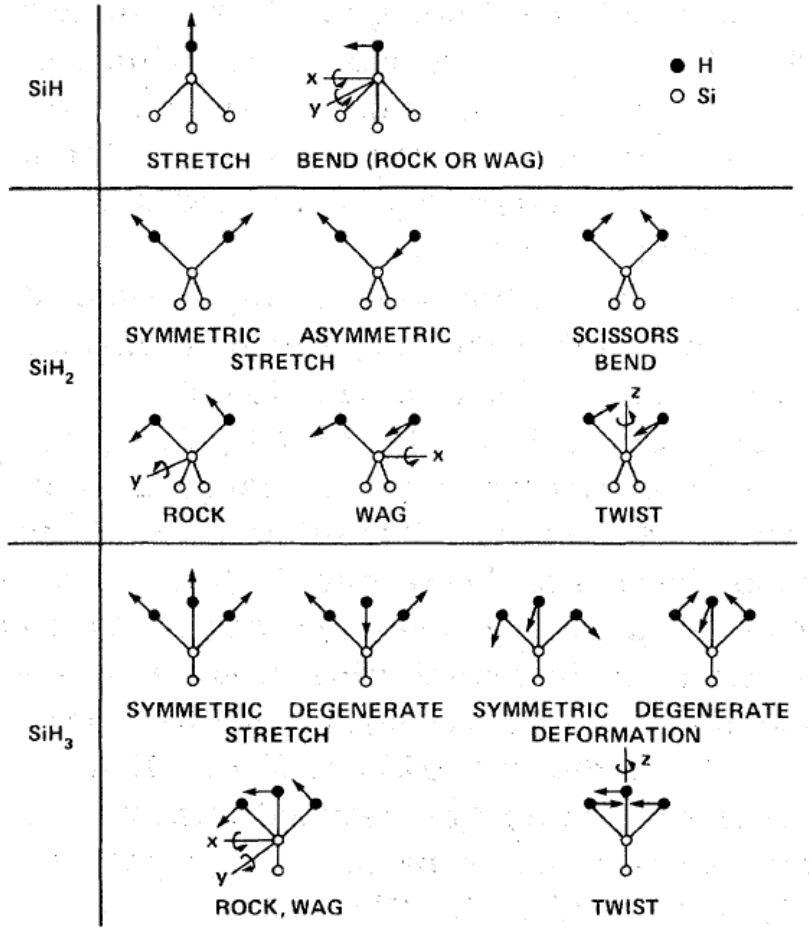

Figure 5: Local Si-H vibrations for simple, double and triple hydrides[15]. (Silane SiH_4 would escape the system as a gas)

There are reported electron-loss characterizations of hydrogenated silicon[16] that should be very similar to the spectra included in this work. Those reference data are reproduced in the following figure:

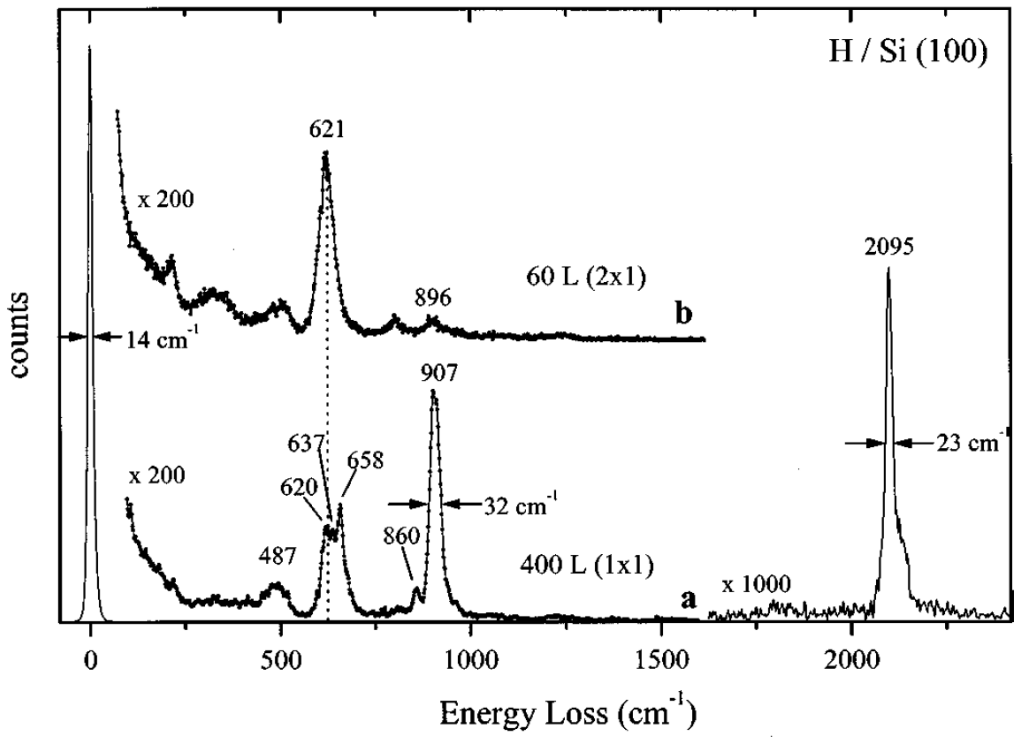

Figure 6: HREEL spectra of hydrogenated Si(100) taken with a primary energy of 2.3 eV and under specular conditions with an angle of incidence of 55 degrees[16].

The identification of the vibrational modes is not always unanimous, but a good starting point is included in the table below.

Mode	Phase/ species	H/Si(100) vibration frequency (cm^{-1}) HREELS[a]	H/Si(100) vibration frequency (cm^{-1}) HREELS[b]	H/Si(100) vibration frequency (cm^{-1}) IRAS[c]
Rocking	1×1	485		
Bending, wagging, twisting	2×1	621	(625)	
	3×1		622, 657	
	1×1	620, 630–640, 658		
Scissor	3×1		905	
	1×1	907		
	T'	858		
Stretching	2×1	2090 peak position (2100, 2085)	(2105)	2091 (M_s=2099, M_a=2088)
	3×1		2104, 2108	2097 (D_s=2091, D_a=2104)
	1×1	2095 peak position		
	M' (1×1)	(2083, 2070)		2077 (M_s=2083, M_a=2072)
	D' (1×1)	(..., 2118)		2111 (D_s=2107, D_a=2117)
	T' (1×1)	(2131, 2142) (1×1)		2137 (T_s=2129, T_a=2139)

Table 1: Vibration frequencies of the H/Si(100) system as measured by infrared and HREEL spectroscopies[16]. M, D and T stand for monohydride, dihydride and trihydride respectively on atomically rough surfaces. The values in parentheses correspond to less certain fitted components within blended features.

On another matter, some of the experiments have involved the use of deuterium (^{2}H or D) rather than ^{1}H (the so-called protium). The isotopic substitution implies a double mass on one of the sides of the Si-H bonds. This entails a decrease in the energy of the associated vibrations that becomes more significant as the vibrating system becomes smaller in terms of number of atoms[17].

Consequently, the greatest effect is observed for diatomic molecules. However, singly hydrogenated silicon atoms can be considered as isolated from the rest of the cluster, and equivalent to diatomic SiH molecules because the Si-H modes are barely influenced by the rest of the atoms.

The SiH system can then be studied as a harmonic oscillator whose vibration is determined to first order by the frequency:

$$\omega = 2\pi\sqrt{\frac{k}{m}}$$

For a classical harmonic oscillator, *k* represents a parameter that measures the tendency of the system to restore the equilibrium configuration such as the elastic constant of a spring. Continuing with the same example, *m* would be the mass of the object fixed to the end of the spring, the oscillating particle.

The spring model is very similar to the Si-H isolated system with the exception of having two masses instead of only one. It is easy to circumvent this difference by replacing the mass with the reduced mass μ. In the case of free singly hydrogenated/deuterated silicon, this parameter would be:

$$\mu_{Si-H} = \frac{m_{Si} \cdot m_H}{m_{Si} + m_H}; \mu_{Si-D} = \frac{m_{si} \cdot m_D}{m_{Si} + m_D}$$

Where m_X stands for the atomic mass of the species X.

Since the deuterium mass is roughly twice the one of hydrogen, it's immediate to calculate:

$$1.93\mu_{Si-H} \approx \mu_{Si-D}$$

This produces an isotopic shift of the frequency of vibration whose quantitative expression is:

$$\omega_{Si-H} \approx \sqrt{1.93}\omega_{Si-D}$$

This is a reasonable approximation for the only possible mode of an isolated Si-H molecule, the Si-H stretching. As for the other vibrations, the isotopic shift still exists, but it's more difficult to calculate as the systems incorporate more than one H atom (for example the scissor mode) or require the cluster to enable the vibration (like in the case of the Si-H bending mode).

In any case, the square root of 1.93 is still a sensible factor when trying to guess the magnitude of the isotopic shift of the modes featured in the HREELS spectra included in this thesis.

The following figure displays two spectra of hydrogenated and deuterated monolayer silicene to illustrate the isotopic shift.

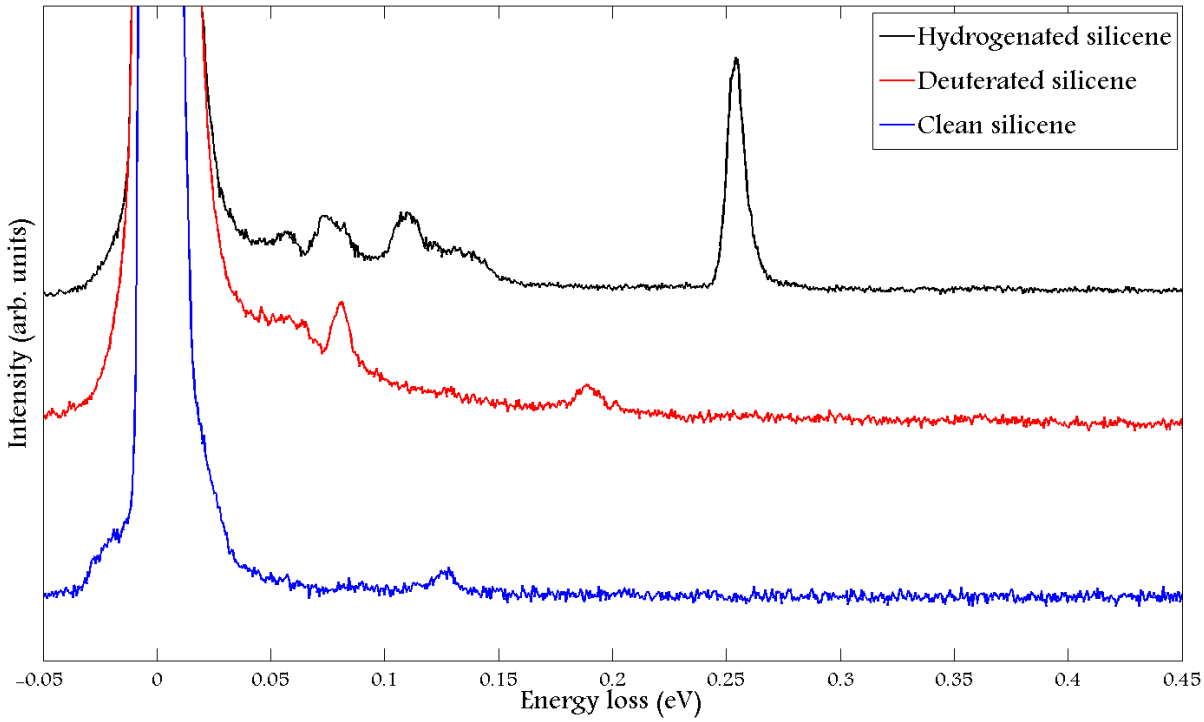

Figure 7: HREEL spectra of clean, hydrogenated and deuterated monolayer silicene. The primary energy of the electrons was 5 eV and they were recorded under specular conditions.

Although at first sight they seem to be completely unrelated, the spectrum of deuterated silicene is simply the one of hydrogenated silicene shifted towards lower energies. For the sake of clarity the origin of the manifested features is written in the table below:

Vibrational mode	Hydrogenated silicon energy (meV)	Hydrogenated silicene energy (meV)	Deuterated silicene energy (meV)	Isotopic factor
Stretching	261	255	188	1.36
Scissor	112	111	81	1.37
Wagging, twisting, bending	79	77	57	1.35
Rocking	60	57	-	-

Table 2: Vibration frequencies of hydrogenated silicon, hydrogenated silicene and deuterated silicene. The isotopic shift has been included in the last column. The rocking mode couldn't be reliably detected in the spectrum taken after the exposure to deuterium.

The isotopic shift is quite constant on all the modes and very similar to the theoretical value deduced in the previous page ($\sqrt{1.93} = 1.39$). This shows that even if the system is not diatomic at all, the approximation still yields rather good results. It's especially true if the uncertainty on the energy of the modes is taken into account, which is about 2 meV. This uncertainty is due to three main reasons: the full width half maximum (easily estimated from the elastic peak), the blended peaks and the noise.

Another interesting result is related to the position of the peaks. Indeed, if columns 2 and 3 of the previous table are compared, it seems that the vibrations of silicene are slightly shifted towards lower energies with respect to the analogue modes of hydrogenated silicon.

Salomon[18] observed a similar behaviour after studying the vibrational modes of silicon nanowires. It must be noted that silicon nanowires are the emerging structure when evaporating moderate doses of silicon on Ag(110) substrates. The chemical species are the same, coverages are similar and the only difference resides in the geometric distribution of silver atoms on the surface.

Angot[19] also reported a parallel trend in the case of erbium silicides. Erbium silicides display a structural arrangement formed through the alternative intercalation of silicon and erbium layers with the former element on top. The surface layer has also been shown to display some buckling, which further reinforces the parallelism with silicene.

The HREELS spectra of ErSi surfaces reveal that the Si-H modes move to lower frequencies when going successively from hydrogenated Si(111) to $ErSi_2$ and $ErSi_{1.7}$ surfaces (increasing coverage). Hydrogen coverage dependency via lateral H-H interaction was ruled out as a possible cause, and so the phenomenon was attributed to a true change of the Si-H interatomic potential function. Given that erbium is a strongly electropositive metal, it is prone to transfer electrons. Those electrons are paired with silicon electrons that occupy the dangling bond orbitals increasing the stability and reducing the reactivity of the surface. As a result, hydrogen bonds less tightly to silicon and the force constant is consequently reduced. A reduction of the force constant is immediately translated into a decrease of the vibrational frequency, enabling the shifts towards lower energies manifested in the reported spectra. The figure below illustrates the shift of the Si-H modes on ErSi surfaces.

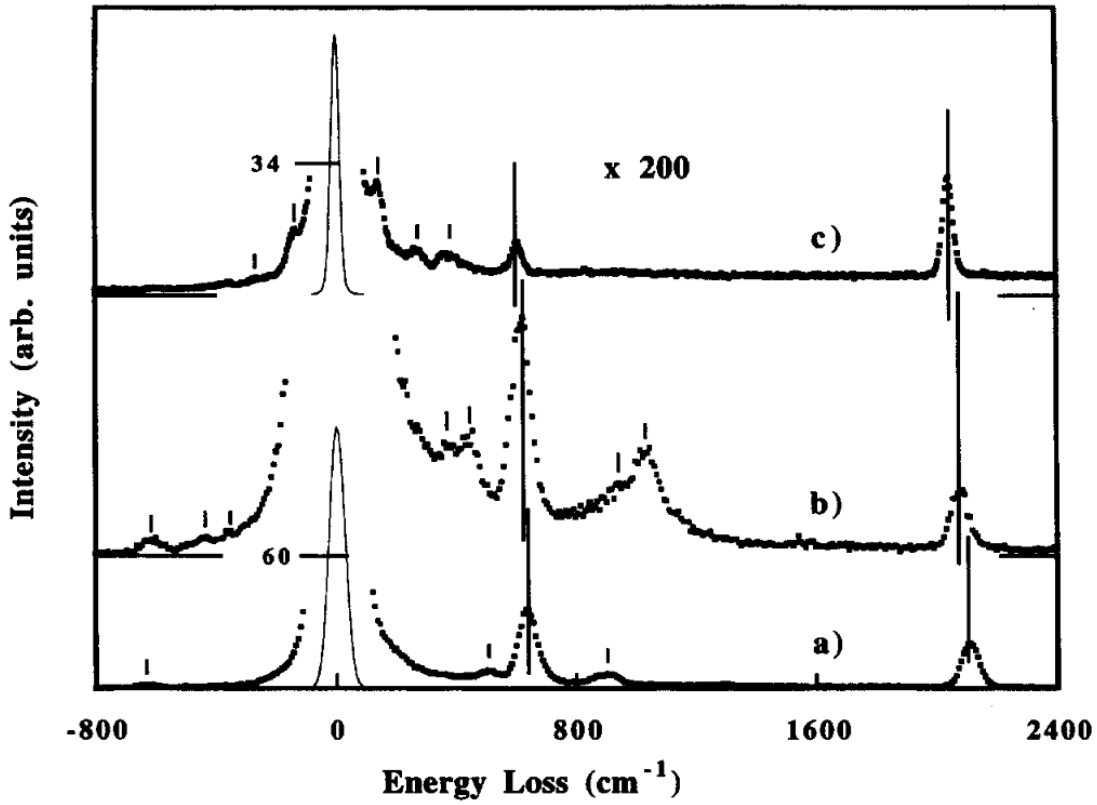

Figure 8: HREELS spectra in specular conditions obtained with a primary energy of 6.5 eV after room temperature hydrogenation of a) Si(111) (7×7), b) Monolayer erbium silicide on Si(111) and c) 300 Å thick $ErSi_{1.7}$. The stretching (~2100cm^{-1}) and bending (~635cm^{-1}) modes have been emphasised with the vertical lines to clearly appreciate the shift[19].

In the case of monolayer silicene or silicon nanowires, they are produced by epitaxial growth of silicon on a silver substrate. The enormous amount of silver atoms beneath could provide the surface layers with many electrons that would end up again in the dangling bonds. This should weaken partially the Si-H bonds reducing the force constant of the oscillators and would explain the observed shifts towards lower energies.

On another matter, the list of the table 2 is not exhaustive since there is one peak around 132 meV that hasn't been identified. Given that the feature appears even for silicene not contaminated and not exposed to hydrogen, the most direct conclusion would be that it is in fact one intrinsic vibration of monolayer silicene. This structure is absent in the spectrum of deuterated silicene because in that case the system had 3-5 layers of silicon, and the spectroscopic data seem to imply that this mode is exclusive of monolayer silicene.

In order to support this affirmation the following figure displays the HREELS spectra of two samples of clean silicene, one close to monolayer coverage and the other one at around 6 or 8 layers of thickness.

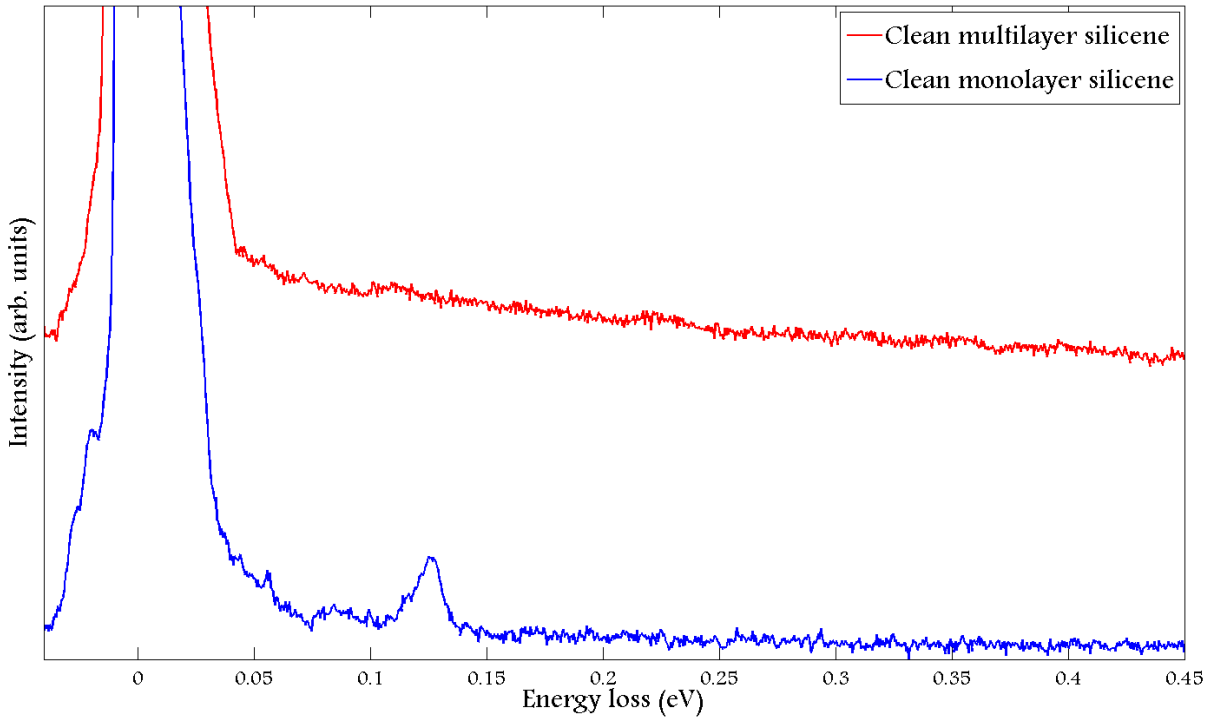

Figure 9: HREEL spectra of clean silicene for monolayer and multilayer coverages. The kinetic energy of the electrons was set to 5 eV and they were recaptured along the specular direction.

Despite being very simple (2 visible losses at most), the spectra are very different. No peaks are apparent on thick silicene whereas the monolayer spectrum includes two features at 132 and 88 meV. This could be interpreted as the characteristic vibrational signature of monolayer silicene because it disappears almost completely as soon as the second and third layers are formed.

Regarding the interpretation of those two peaks, there have been several theoretical studies dedicated to the calculation of the phonon dispersion in silicene. The HREELS spectrum of clean monolayer silicene represent a convenient way to check if any of those features have been predicted by the numerical methods.

Scalise[20] has reported a pseudo-degeneracy of the in-plane longitudinal and transversal optical modes of silicene. He has argued that both dispersive branches give rise to a G-like peak at around 71 meV. His group also obtained two additional D-peaks associated to breathing motions of the hexagons at 64 meV. However the calculations were performed for a free-standing silicene and he admits that the investigation of the electronic and vibrational properties of silicene on silver is not trivial, since the metallic substrate dominates the overall behaviour of the structure.

Yan[21] also predicts a degenerated branch that spans the interval of energies between 62 and 70 meV but their work doesn't take into account the silver substrate either, which could have a significant impact on the vibrational modes.

Aizawa[22] conducted a HREELS study of silicene grown on a ZrC substrate and found several vibrational modes. The most energetic one (a Si-Si vibration) was predicted slightly below 60 meV. Interestingly enough, his group reported that the presence of defects of substitution such as replacing a silicon atom with a carbon one could increase the energy of the vibration up to 90 meV. This value is closer to the two allegedly intrinsic peaks shown in the previous page and might hint at the existence of significant defects in the supposedly pristine silicene. Significant substitution with carbon atoms is nonetheless discarded since the Si-C peak is missing.

Looking again at the data reported in this thesis, the feature at 88 meV is not extremely different from the optical modes predicted for free-standing silicene so the origin of the discrepancy could be in the influence of the silver substrate.

However, the peak at about 132 meV has an energy equal to the double of the most energetic predicted phonon. It could be due both to the substrate and to the existence of defects, but its source could be a completely unrelated one as well. Another possibility would be the Si-Ag vibrations, although the latter atom seems to be too heavy to produce such an energetic vibration.

That assumption would make the disappearance of the mode upon increase of the coverage easily justified. The penetration of the probing beam is very superficial so by adding silicon layers the Si-Ag units couldn't vibrate anymore as they wouldn't receive energy from the electrons. Regarding the disappearance of the mode at 88 meV, the manifestation under the dipole regime of a Si-Si stretching require both some buckling and some chemical inequality between the silicon atoms. In this case, the addition of silicon layers would drastically reduce the chemical disparity between the Si atoms as the lower ones would lose their contact with the silver substrate. As for the buckling, the structural model of multilayer silicene hasn't been elucidated yet but it's not absurd to expect a modification of the buckling from monolayer to multilayer silicene.

Summarising, both hypotheses appear to be coherent with the expression of these vibrational modes only in the case of monolayer or quasi-monolayer silicene and don't contradict the theoretical research done on phonon bands of silicene.

So far the discussion has been restricted to the description of the vibrational spectrum of hydrogenated silicene. It has allowed to find subtle yet physically meaningful differences between silicon and silicene and it can also shed some light on the reactivity and preservation of the latter as the ensuing paragraphs will show.

The currently known preparations of silicene involve the use of ultra-high vacuum environments. In such conditions, the effects of the atmospheric gasses, contaminant species etc. are generally negligible if they exist at all. However, normal operating devices are not usually enclosed in ultra-high vacuum chambers, so it's important to evaluate the impact of a normal atmosphere on the characteristics of silicene. During the realisation of this thesis, silicene was not subjected to the atmospheric pressure, but that wasn't any impediment to study its interaction with oxygen and carbon.

In effect, the passage of the samples through the different chambers in order to perform experimental measurements (STM, HREELS, LEED…) subjected monolayer silicene to pressures ranging from 10^{-8} to 10^{-10} Torr. Even if those values are many orders of magnitude smaller than sea-level pressure, the sensitivity of the HREELS technique made it possible to detect the gradual chemisorption with time of contaminant species, mainly oxygen and carbon, on the silicene samples.

The figure below displays HREELS data of hydrogenated silicene as a function of the hydrogen dose.

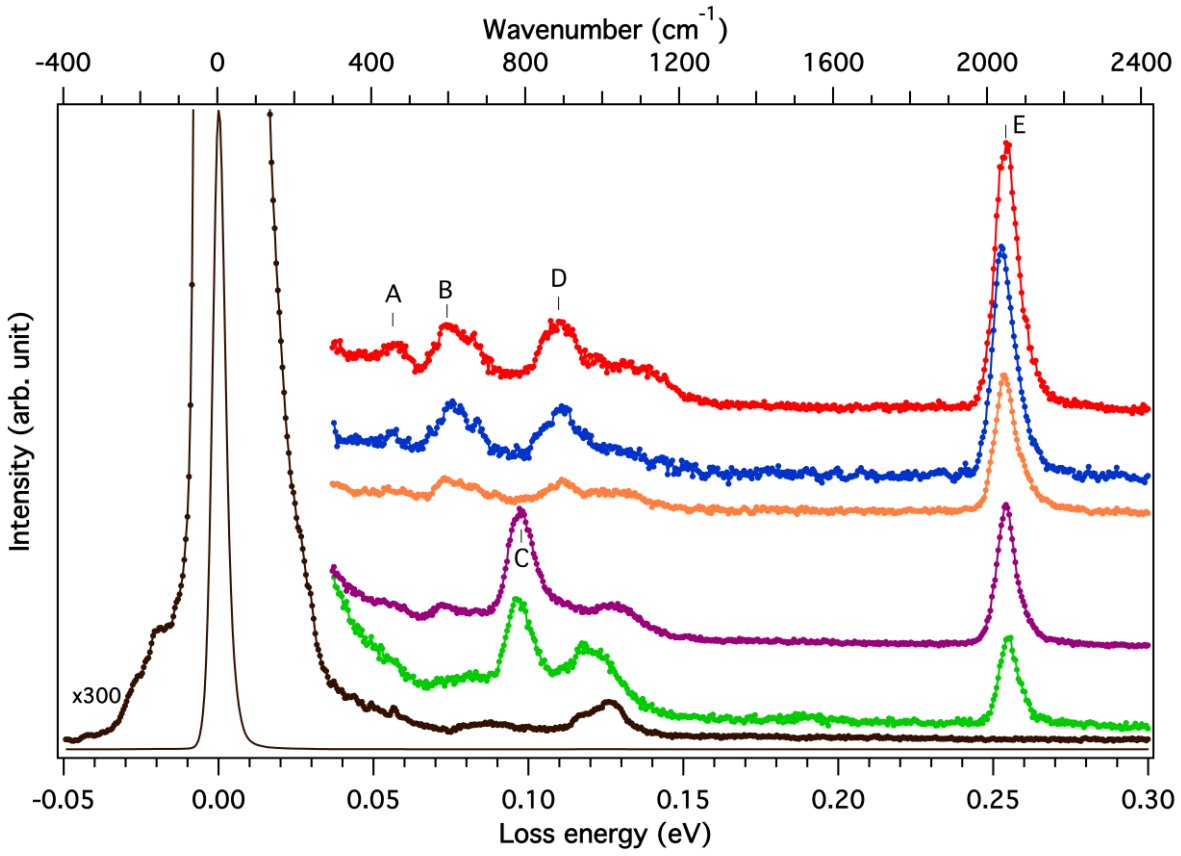

Figure 10: HREELS spectra of hydrogenated monolayer silicene as a function of its exposure to atomic hydrogen. The pressure was kept constant at 10^{-6} Torr during the processes. The respective times of exposure from the black curve to the red one in order are: 0, 30, 150, 360, 420 and 480 seconds. For information, the sample is shaped in the form of a circle of radius 4mm and the flux on it at the specified pressure was around 10^{12} hydrogen atoms per second.

Depending on the exposure, different loss structures are observable as summarized in Table 1. For the sake of clarity the HREELS spectrum of the bare silicene-(4×4) is also reported.

		Observed peak					
Label		A	B	C	D		E
Loss energy (meV)		56	74	98	110	118 - 150	254
Wavenumber (cm^{-1})		452	597	790	887	952 - 1210	2049
Exposure time (s)	60	✓	✓	✓	-	✓	✓
	150	✓	✓	✓	-	✓	✓
	360	✓	✓	-	✓	✓	✓
	420	✓	✓	-	✓	✓	✓
	480	✓	✓	-	✓	✓	✓
Assignment		Rocking Si-H	Bending, Twisting, Wagging Si-H	Stretching Si-O	Scissor $Si-H_2$		Stretching Si-H

Table 3: Vibrational modes observed in the spectra of hydrogenated silicene-(3×3).

For the two smallest doses the HREELS spectra are dominated by two main features at 98 meV (790 cm^{-1}) and 254 meV (2049 cm^{-1}). While the latter corresponds to the Si-H stretching mode and demonstrates hydrogen adsorption, the first one corresponds to the Si-O stretching mode. This shows that the silicene-(4×4) surface is reactive and could easily be contaminated during the experiment. It also implies that the surface is not fully saturated. For exposure doses over 5 minutes the overall trend of the HREELS spectra differs. They are dominated by loss-peaks attributed to Si-H vibrational modes and the peak corresponding to the Si-O mode is no longer observed, as described in Table 1.

Those spectra were not recorded immediately after the hydrogenation of the sample but after several hours under pressures between of 10^{-8} and 10^{-9} Torr. The acquisition of one HREELS spectrum takes around 20 minutes and the final set of data is obtained by averaging all the individual spectra recorded during the acquisition. Additionally, the highly noisy individual spectra were stored. This allowed to observe the build-up of the Si-O stretching peak over time. The implication is that, even under the very low pressure of the HREELS chamber (at most $5 \cdot 10^{-9}$ Torr), silicene gets progressively contaminated with oxygen, so silicene samples have to be handled and preserved with great care. The Si-O mode appears then as a good indicator of the contamination of silicene.

Previous studies[23] have stated that thick silicene is stable in air claiming that the only visible effect is the formation of an oxide layer at the surface that protects the material from further chemical damage. The data shown here prove that a similar oxidation occurs in the case of monolayer silicene, and since there is only one layer, its impact is hardly conceivable as minimal.

In principle it could be possible to calculate the magnitude of the Si-O feature with respect to the elastic peak, but given that the silicene was being hydrogenated it was simpler to compare to any of the hydrogen-related features. Since the Si-H stretching mode seems to be every time the most intense of the Si-H peaks, the comparison of Si-H and Si-O stretching peaks seems to be the wisest approach.

Figure 11 represents a magnitude proportional (through the oscillators' forces) to the ratio of Si-O and Si-H bonds as a function of the exposure to hydrogen. The intensity of the signal has been calculated by following the fitting procedure described in the HREELS section.

As it can be seen on figures 10 and 11, as the exposure to hydrogen increases, so does the Si-H stretching peak before saturation, which is completely logical as the number of those oscillators goes up too. As for the Si-O peak, the effect is inverse: More significant pre-emptive doses of hydrogen cause the decrease and eventually the absence of the Si-O feature.

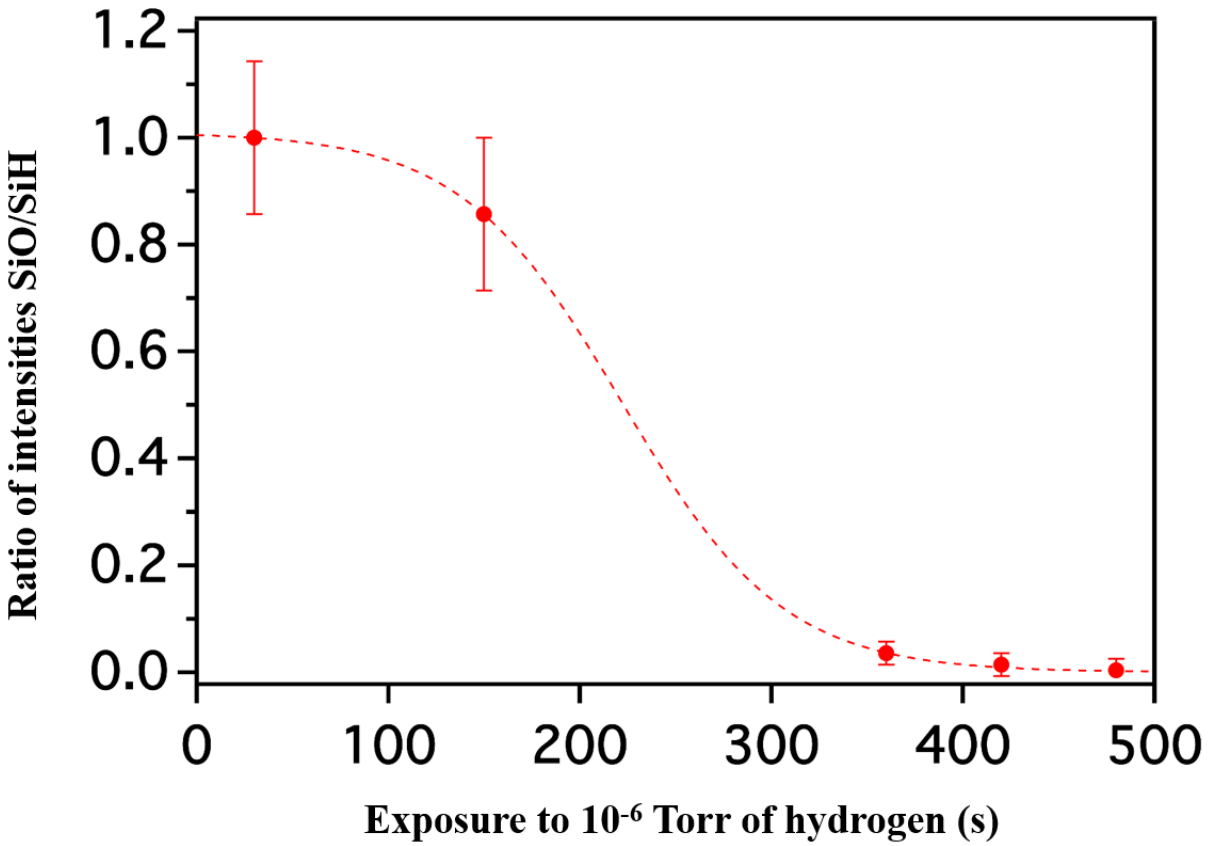

Figure 11: Ratio of intensities of the Si-O and Si-H stretching modes as a function of the dose of hydrogen.

If the hydrogenation is a reversible process that can be undone through annealing at moderate temperatures (in any case below the temperature of formation of silicene to avoid undesired structural changes) as claimed in a recent article[24], the conclusion is immediate. In order to protect silicene from common and reactive contaminant species such as oxygen, the samples could be saturated with hydrogen, manipulated in less demanding environments and eventually dehydrogenated in the end if it were necessary. This last step could even be avoidable because for several practical applications there has to be a gap, and that is exactly the role of hydrogen: opening the gap at the Dirac point. However, as the ensuing structural study will reveal, the reversibility of the hydrogenation might as well be only partially reversible, thus reducing its potential as a protective mechanism.

Regarding the storage of hydrogen, it appears as a more tricky matter. In effect, it's easy to stock hydrogen on silicene surfaces and all that it takes to recover it is a moderate heating of the material. However, in most of practical situations the liberation of hydrogen will expose silicene to a harsh environment that will contaminate it in a way that so far cannot be reverted without causing its destruction. In short, the results reported here suggest that for most of practical purposes, silicene may be used to stock hydrogen, but only once.

2.b) Structural study

In the previous section, the HREELS technique has provided insightful information about how hydrogen reacts with silicene. The shifts of the peaks have also revealed that from the chemical point of view, silicon and monolayer silicene are not identical. This will become even more evident when addressing the hydrogenation of multilayer silicene.

Very little has been said about the changes that the chemisorption of hydrogen induces on monolayer silicene. The study of the evolution of the gap with the dose is beyond the scope of this thesis because it would require to have freestanding silicene, which hasn't been synthesised yet, as well as access to the necessary experimental techniques.

It is nevertheless possible to take a look at the modifications undergone by silicene when it is exposed to hydrogen. It is with that aim that such a system has been analysed by means of Scanning Tunnelling Microscopy.

The following pages will show how the structure changes under the effect of the reaction with hydrogen and will serve to test some of the statements included in the few recent articles about this topic.

Before starting the discussion about the subject itself, it is convenient to set a reference so as to compare the images obtained after hydrogenation with the appearance of silicene before the chemical reaction.

Vogt[25] proposed a correct model for the most common phase of monolayer silicene on silver. They describe (3×3) silicene unit cells that perfectly match the (4×4) Ag(111)-(1×1) area. Some of the Si atoms lie on top of Ag atoms, while some others are located more between Ag atoms (at a higher level). The DFT calculations conceived to support their experimental observations yielded the distances and angles between atoms, and showed that the hybridisation of the Si atoms ranged from sp^2 to sp^3 and some "mixed" configurations depending on their positions within the lattice.

This structure, which will serve as reference for comparison is depicted in the following figure.

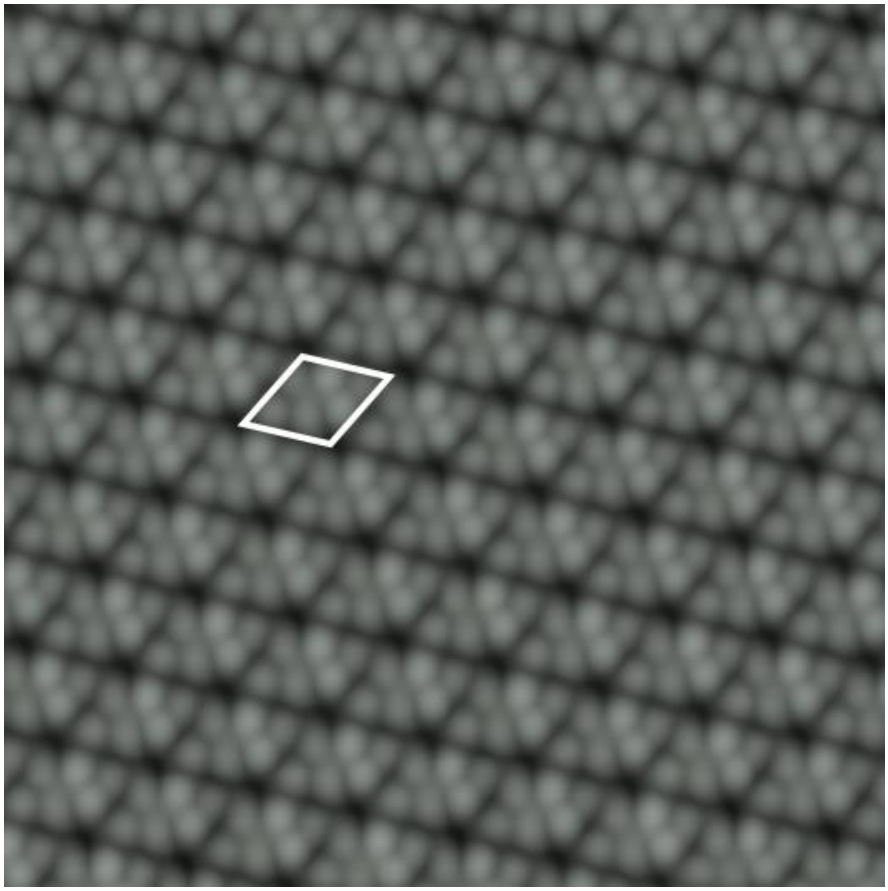

Figure 12a: 10 nm × 10 nm STM image of (4×4) silicene taken with the tunnelling parameters specified by I=0.14 nA , V=-49mV (filled states).

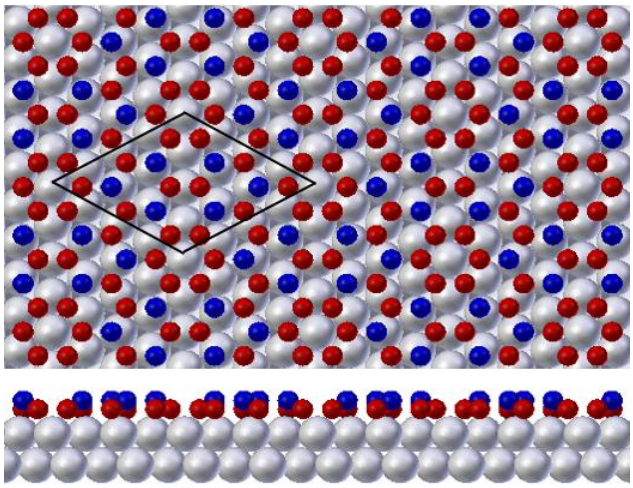

Figure 12b: Structural model that gives rise to the geometry observed in figure 12a.

This is the so-called α-silicene[25]. It is by far the most common phase displayed by this kind of system. The blue and red balls correspond respectively to the upper and lower silicon atoms, while the grey ones represent the silver atoms. The unit cell has been highlighted in both illustrations. This allows to check that the STM pattern is produced by the silicon atoms on the upper level.

After having saturated a monolayer silicene sample with hydrogen according to the calibration deduced from the data in figure 11, it was introduced in the STM chamber and the surface was scanned again as finely as possible.

The image below is an example of the state of the surface obtained in the process.

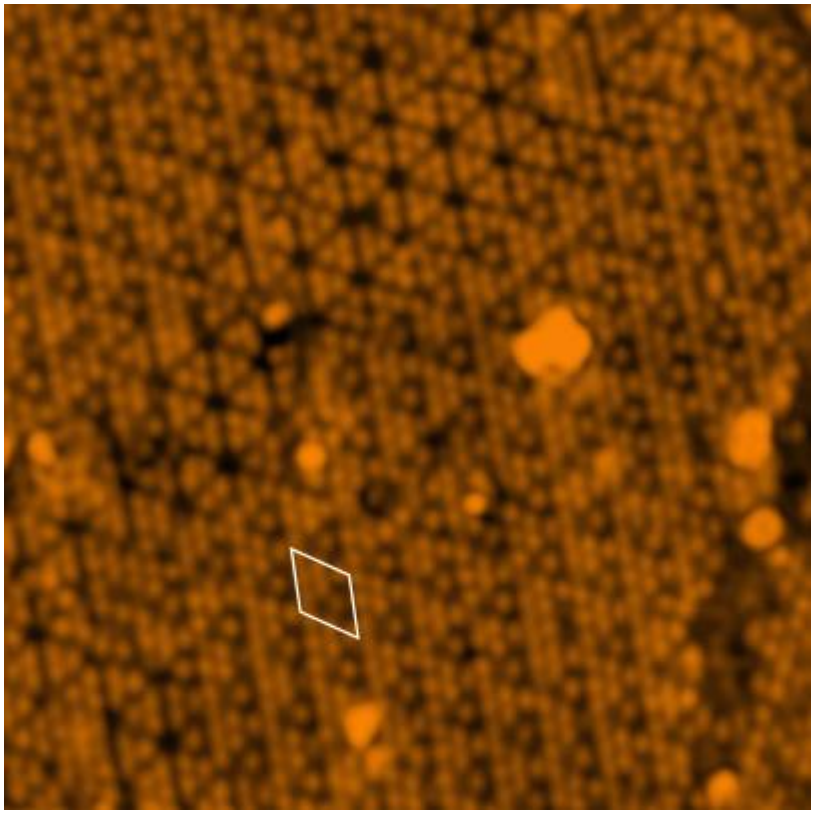

Figure 13: 14.5nm × 14.5nm STM image of silicene-(4×4) saturated with cracked molecular hydrogen. I_{tunnel}=0.55nA, Bias=-515mV (filled states).

Most of the image displays a recurring motif (the white rhombus in figure 13): a regular tiling is formed with the juxtaposition of rhombi divided by their minor diagonal in two distinct equilateral triangles. The first one has six bright spots, whereas the other one is mostly dark, with the exception of one unique bright spot in the centre.

This structure has been recently identified by Qiu et al.[24] as the archetypical surface arrangement of hydrogenated monolayer silicene. The evolution of the appearance from clean to hydrogenated silicene is not attributed to a new reconstruction of the hydrogen atoms. Instead, it's claimed that the reaction only occurs with the silicon atoms of the higher level. Following this reasoning, no horizontal change is expected, and only the corrugation (difference of height between the high and low points) should increase. The structure has nonetheless evidently changed because α-silicene (visible in figure 12a) is very different from the aforementioned tiling. The adduced explanation lies in a different phase believed to become more stable than the α-phase after the reaction with hydrogen, thus enabling the transition. This is the so-called β-silicene.

In effect, it is another (4×4) phase which is significantly less frequent and hence believed to be less energetically favourable. Liu[26] proposed a structural model to explain the STM images corresponding to this metastable configuration. The interatomic distances are very similar and the main difference is found at the height distribution of the Si atoms, responsible of the different appearance in the topography image.

The figure below shows this alternative phase along with the proposed model.

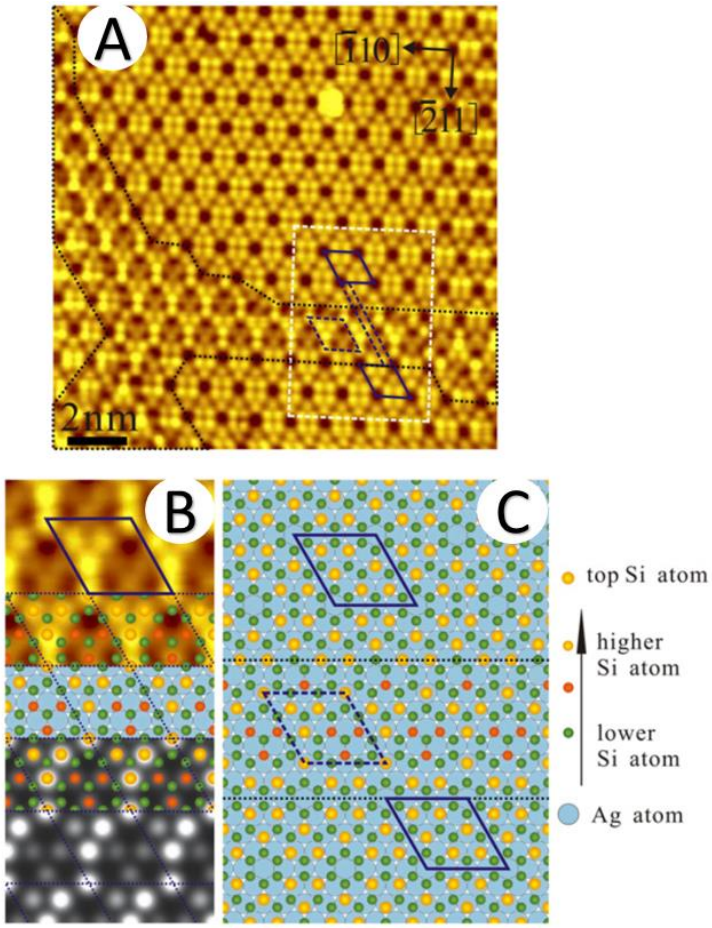

Figure 14: A) STM image taken on (4 × 4) phase domains at V = 115 mV and I = 0.2 nA. Rhombi superimposed on the image indicate the (4 × 4) unit cells. Dotted lines indicate the boundaries between two phase domains. B) 3×2.5 nm^2 STM image of the β phase at V = 5mV and I = 0.2 nA. Below, the proposed model and a simulation of the STM pattern arising from the model have been added. C) Ball structural model of the area enclosed in the white dashed rectangle in A)[26].

Once these two structures have been introduced, the discussion about the effects of the hydrogenation on monolayer silicene is simpler.

First of all, it's necessary to state that during the experiments reported in this thesis, the monolayer silicene has mostly adopted time the α configuration. This is a proof of the exceptionality of the metastable phase. Consequently, all the comparisons will be established with the α phase as reference.

Apart from the most common pattern highly similar to the β-phase[24], at numerous locations the structure adopts a different form. There are punctual or small defects (the very bright clusters that appear scattered throughout the surface), unexpected dark areas attributed to missing spots (if the symmetry were to be conserved), large triangles made of 15 bright spots etc.

Interestingly, the asymmetric rhombi pattern is separated in two regions by a narrow stripe (3-5nm) where the "flower pattern" of the α phase is recognisable. This feature is striking because the sample is supposed to have been saturated with hydrogen, so uncovered zones are not expected and the less energetically stable hydrogenated α-phase should have turned into its β-counterpart.

A zoom of the coexistence of both reconstructions is included below.

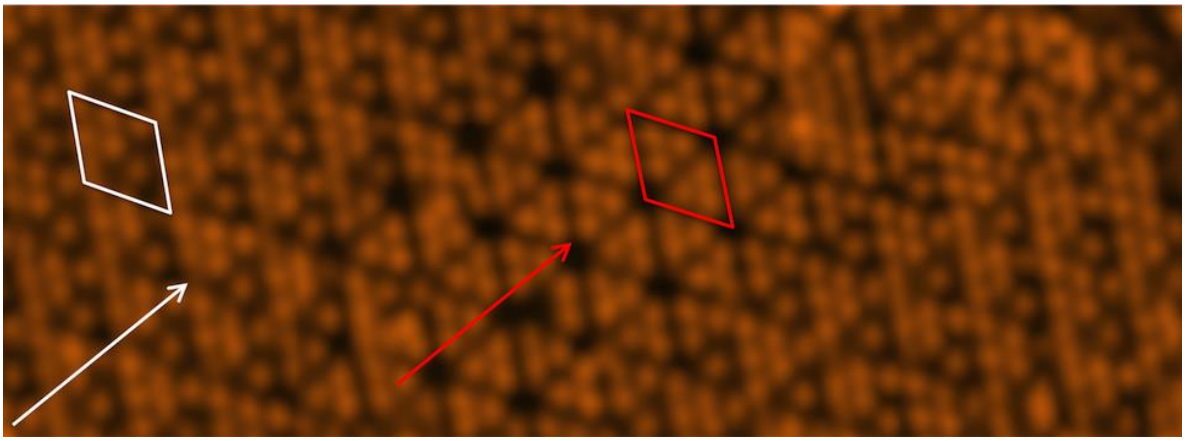

Figure 15: STM image (11nm× 4nm) of hydrogenated silicene-(4 × 4). The unit cells of each phase are enclosed in the rhombi. The arrows indicate chosen directions for the study of the corrugation (see figure 14).

Qiu argued that the presence of patches of α-silicene is due to an incomplete hydrogenation. Consequently, that pattern simply reveals zones where hydrogen hasn't reacted with silicene.

This is at odds both with the time of hydrogenation and HREELS spectrum of the sample. Indeed, the silicene shown in the image was exposed to a dose of hydrogen undoubtedly beyond saturation and the HREELS spectrum taken after STM scanning indicated absence of oxygen. Given that oxygen reacts very easily with silicene and that the pressure in the STM chamber is two orders of magnitude higher than in the HREELS chamber (where oxidation had taken place with ease), the absence of Si-O stretching peak is a strong evidence of saturation.

In order to delve into this apparent contradiction, the image was analysed with respect to the remaining coordinate: the z-direction perpendicular to the surface. In other words, the corrugation profiles along the directions specified by the arrows in figure 15 were statistically studied and compared to the clean surface.

Figure 16 constitutes an example of the many profiles analysed to determine the corrugation of each phase.

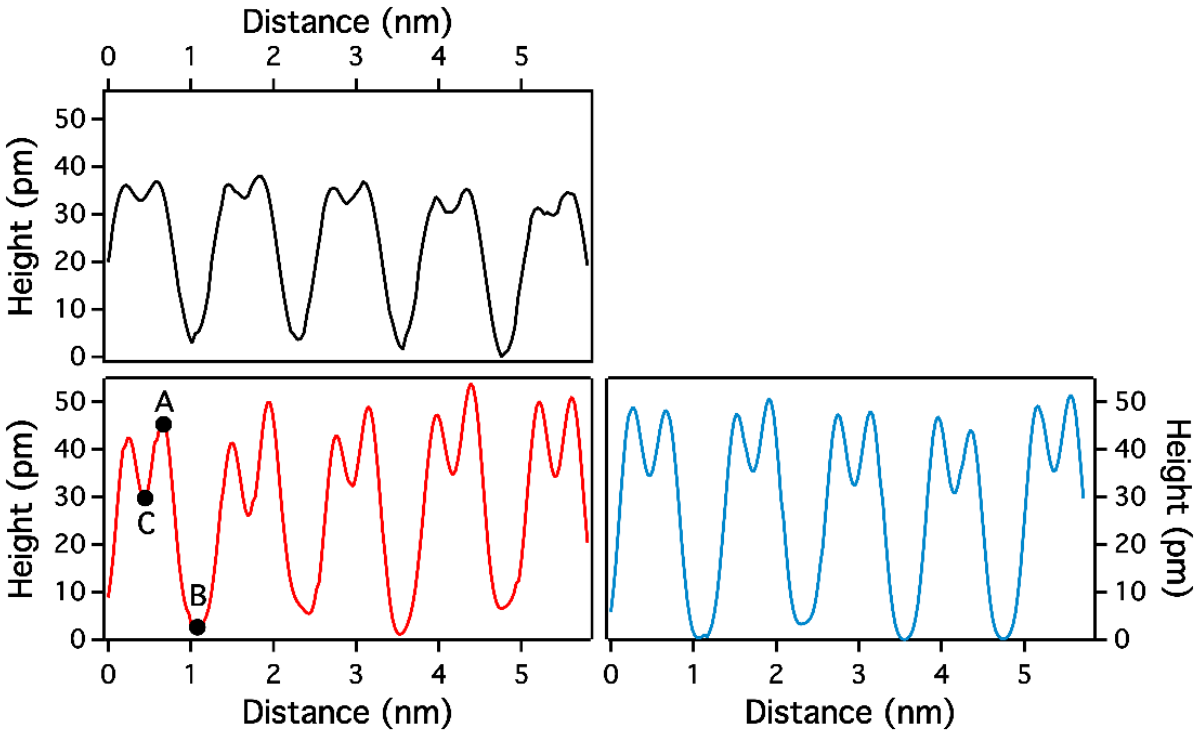

Figure 16: STM height profiles measured on clean α-silicene (top-left, black), on the flower pattern of figure 15 (bottom-left, red) and on the asymmetric rhombi zone (bottom-right, blue). The chosen directions are indicated with arrows in the same figure.

The choice of the direction is convenient because it makes the comparison of the profiles easy. In effect, their periodicities are the same (which is simple to ensure as all of them are (4×4) reconstructions) and they also display a very similar shape: two close maxima are separated by a relatively small trough and consecutive pairs of maxima lie at both sides of a wider and much deeper minimum.

The examples shown here are very regular and the first impression could be that very few of them are necessary to estimate the corrugation. Actually, an analysis along equivalent directions made it clear that a strong variation was present, whence the need for statistical averaging.

In any case, the corrugation was evaluated in terms of the difference in height between points A, B and C as marked in figure 16. The results are summarised in the table below.

	Clean Silicene-(4×4)	H-Silicene-(4 × 4)	
	"Flower patter"	"Flower pattern"	"Triangle pattern"
h_{A-B} (pm)	30 ± 5	41 ± 6	39 ± 5
h_{A-C} (pm)	5 ± 2	14 ± 4	15 ± 4

Table 4: Corrugation values obtained from profiles equivalent the ones shown in figure 16. Flower pattern stands for the phase with the symmetric unit cell and triangle pattern makes reference to the phase with the asymmetric unit cell.

On clean silicene (4×4) two different corrugations are reported. The first corresponds to the height difference between points A and B, of about h_{A-B}=30 ± 5 pm. This value is comparable to the one reported by Vogt[25]. The height difference between points A and C is given by h_{A-C}=5 ± 2 pm.

On the hydrogenated silicene-(4×4), the profile on the pattern generated by the asymmetric unit cell exhibits the following height differences: h_{A-B} = 39 ± 5 pm and h_{A-c} =15 ± 4 pm. This demonstrates that the corrugation of this phase corresponding to hydrogenated silicene is significantly greater than for clean silicene. Interestingly enough, the height profiles measured on the pattern generated by the symmetric unit cell (flower pattern) of the hydrogenated silicene-(4×4) is h_{A-B} = 41 ± 6 pm and h_{A-C} =14 ± 4 pm, which are quite similar to the latter couple of values rather than to the former. This suggests that this part of the surface is also hydrogenated even if there hasn't been any transition towards the other configuration of hydrogenated silicene. It should be noted that the distance A-B increases about 10 pm upon hydrogenation, and so does the distance A-C. This is in agreement with the hypothesis of hydrogen atoms only bonding to the silicon atoms in the upper level, which would increase exclusively the height of the highest points of the structure (the points marked as A). Actually, the increase has been calculated to be equal to 0.1 Å[24], which matches perfectly the results reported here.

Since the formation of the hydrogenated flower pattern appears as not favourable for defect-less silicene according to DFT simulations, its actual occurrence may hint at its stabilisation with the help of the surrounding defects observed on the image. Indeed, visual inspection of both figures 13 and 15 reveals that the region exhibiting the flower pattern is surrounded by several defects. For instance there is a bright protrusion in a flower pattern corner hole. There is also a region where fifteen bright spots form a triangle surrounded by three half flower patterns.

To draw a conclusion it's worth taking into consideration both the HREELS and the STM data. The former have revealed that clean-silicene-(4×4) can be fully saturated with doses over $2 \cdot 10^{15}$ atoms of hydrogen/cm^2. Furthermore, the height profiles have displayed similar corrugations (~15pm) for both of the predominant phases in figure 15, whereas the corrugation of clean silicene-(4 × 4) was found to be around 3 times smaller, as shown in figure 16. These two facts favour the possibility of a phase with the appearance of clean silicene (from the STM point of view) that would actually have been hydrogenated. Hence, there seems to be at least two possible phases (the ones with the symmetrical and asymmetrical unit cells), although the structural arrangement reported by Qiu[24] probably tends to cover a significantly larger area perhaps because of its lower energy in normal conditions. In any case, these two phases may arise from the conformation of α-silicene and β-silicene during the exposure.

3. Hydrogenation of multilayer silicene

The previous section has had the aim of describing the effects of hydrogenation on monolayer silicene. From a naïf perspective, it could seem sensible to believe that the outcome of the chemical process on thick silicene should be similar. After all, hydrogenation only affects the topmost layer, and in both cases it would be one layer of atoms of silicon.

Actually, the reality is more complex, and even before subjecting the sample to a flux of hydrogen, the materials display different properties. As an example, the surface reconstruction is no longer a (4×4) phase, but eminently a $(\sqrt{3}\times\sqrt{3})$R30º one displaying different orientations with respect to the substrate[27].

The characterisation of thick silicene is more elusive than its monolayer counterpart. Several models have been proposed[28,29,30] but so far there is no clear consensus even on the element on top (there are models with the topmost layer constituted by silver instead of silicon), let alone on the precise positions of the atoms within the reconstruction.

In any case, in order to study the evolution of thick silicene under the exposure to hydrogen it's not absolutely necessary to ascertain the structure beyond any doubt. As in the previous section, it's possible to compare the experimental data before and after the chemical reaction.

If there's something incontrovertible about multilayer silicene is that the atoms get rearranged in the aforementioned $(\sqrt{3}\times\sqrt{3})$R30º phase. This is revealed when probing the surface with the STM or LEED techniques. The figure 12 of the introductory silicene section shows a general topography map of thick silicene and a more detailed scan.

Since the hydrogenation of thick silicene will also be analysed from the LEED point of view, it's convenient to take a look at the diffraction pattern shown below and the identification of the spots.

Now that the starting point of the hydrogenation is clear, hydrogenated multilayer silicene will be studied in terms of the changes in the structure (both in the reciprocal and in the real spaces) and in the vibrational spectrum.

3.a) Structural study in the reciprocal space

The LEED patterns reported here are only sensitive to alterations of the periodicity of the lattice. The reason for these alterations could be the formation of a new phase with a different lattice parameter or orientation, or more subtly, a change in the number of irregularities on the structure, e.g. an increase of the number of defects on the surface.

Figure 17 shows the evolution of the diffraction pattern of thick silicene as a function of its exposure to atomic hydrogen. There are several aspects to consider in these four LEED patterns:

Firstly, the first three images were registered sequentially for the same sample after performing consecutive hydrogenations. The last one is part of a later campaign of measurements and was thus obtained from a new preparation on a different sample. This explains the rotation of the silver spots as well as the randomness of the middle ring passing from 12 spots to barely 6 and back to 12 clear spots in the last pattern. The latter condition arises from a less uniform distribution of domains. In other words, some orientations that were faintly manifest on the first three patterns due to their scarcity, become brighter on the last preparation because of their greater abundance. This doesn't mean that both preparations are not comparable, since the focus must be set on the rings rather than on individual spots.

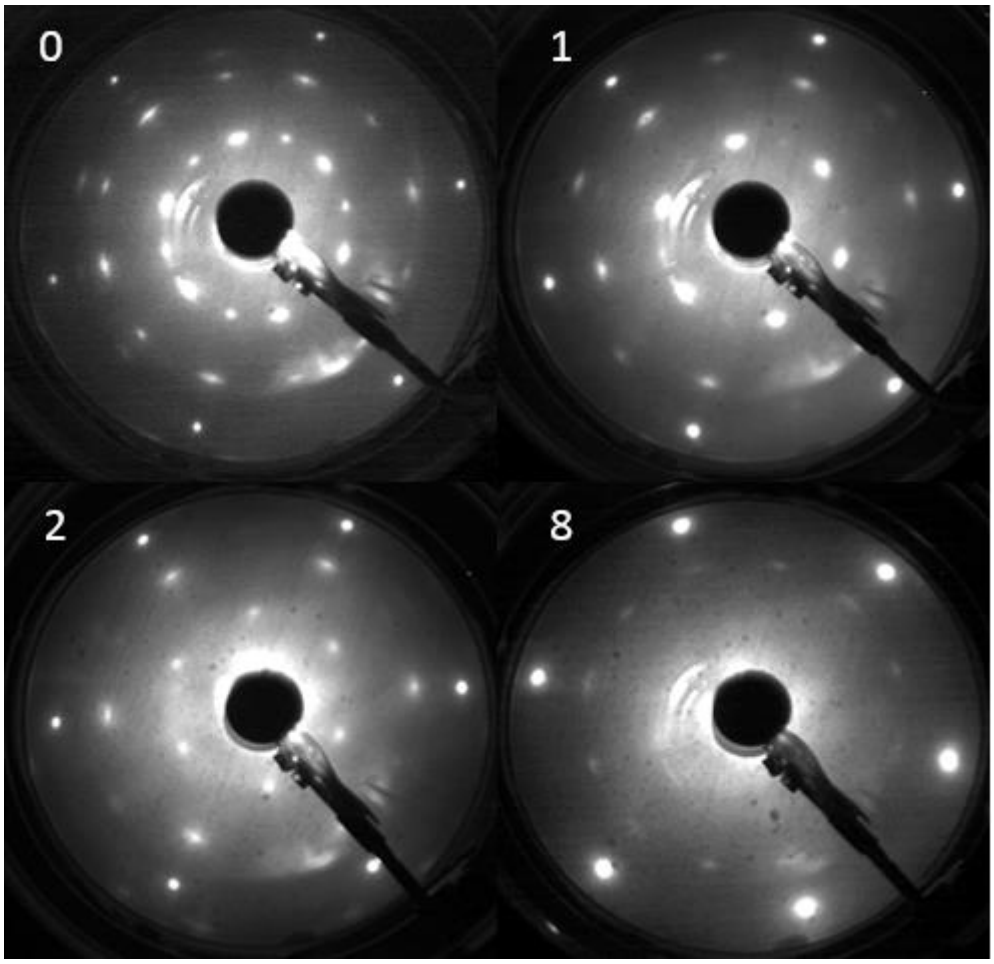

Figure 17: LEED patterns (E = 46.8 eV) of silicene $(\sqrt{3} \times \sqrt{3})$ labelled proportionally to their exposure to hydrogen. The actual doses are equal to 0 (top left), 1 (top right), 2 (bottom left) and 8 (bottom right) · 10^{12} atoms of hydrogen.

On a more general level, the most striking evolution is the disappearance of the central ring. For the clean thick silicene, it is by far the brightest ring, constituted by a double set of 6 spots that alternate in intensity. Since it is the closest structure to the centre, it corresponds to the largest periodicity in the real space, namely the $(\sqrt{3} \times \sqrt{3})$ reconstruction whose origin lies in the buckling. As the hydrogenation progresses, these spots become gradually fainter. Eventually they vanish altogether in the last pattern leaving the middle silicon ring and the outer silver spots. It's relevant to mention that these doses are two orders of magnitude below the saturation threshold found for the monolayer. This implies that the amount of atoms that have had the chance to react so far is not big at all, and consequently the $(\sqrt{3} \times \sqrt{3})$ spots disappear even after very mild exposures.

On another matter, the progressive reaction with hydrogen has an effect on the sharpness of the diffractive features. The easiest manner to notice the trend is paying attention at the evolution of the silver spots, although it's also perceptible on the silicon ones. In effect, as the dose increases, the spots become larger and the pattern blurs gradually. Given that the LEED image is only the Fourier transform of the structure in the real space, larger and more diffuse spots are a manifestation of the increasing number of defects on the surface. Such defects hinder the arrival in phase of the de Broglie waves dispersed from distant nodes of the surface. As a result, the combination of the complex exponentials derived from the individual path lengths produce a less sharp pattern.

Finally, the hydrogenation of silicene induces a more intense and more extended background profile. On the first pattern the background noise is mostly confined within the innermost ring and to a lesser extent inside the middle ring. In the case of the highest exposure, it is significantly less concentrated and becomes more uniform throughout the fluorescent screen. Once again, the background is linked to irregularities on the structure because they tend to randomise the phases of the scattered matter waves. This produces small intensities at random locations. After combining all of those weak signals, the result is a rather uniform background that increases the threshold of detection.

To summarise, all the studied phenomena point in the same direction: the exposure of thick silicene to hydrogen, even to small doses, has an evident negative impact on the periodicity of the system. The $(\sqrt{3} \times \sqrt{3})$ ring completely disappears for doses between one hundredth and one tenth of monolayer and from that point only the silver imprint and the (1×1) from silicene remain. If defects are created, the larger structures need longer distances free of defects to cast their diffractive signal. Since the (1×1) is smaller, shorter pristine distances are required, and hence that ring persists for a longer time. The increase of the background and the progressive blur of the pattern concur with this explanation, as they entail a greater disorder such as the one created by the defects responsible for the disappearance of the innermost ring.

3.b) Structural study in the real space

The changes produced in the structure by hydrogenating thick silicene can be studied more straightforwardly by directly examining the state of surface with the help of the STM technique. Below, there is a series of images of progressive hydrogenations depicting the general modifications induced by the process.

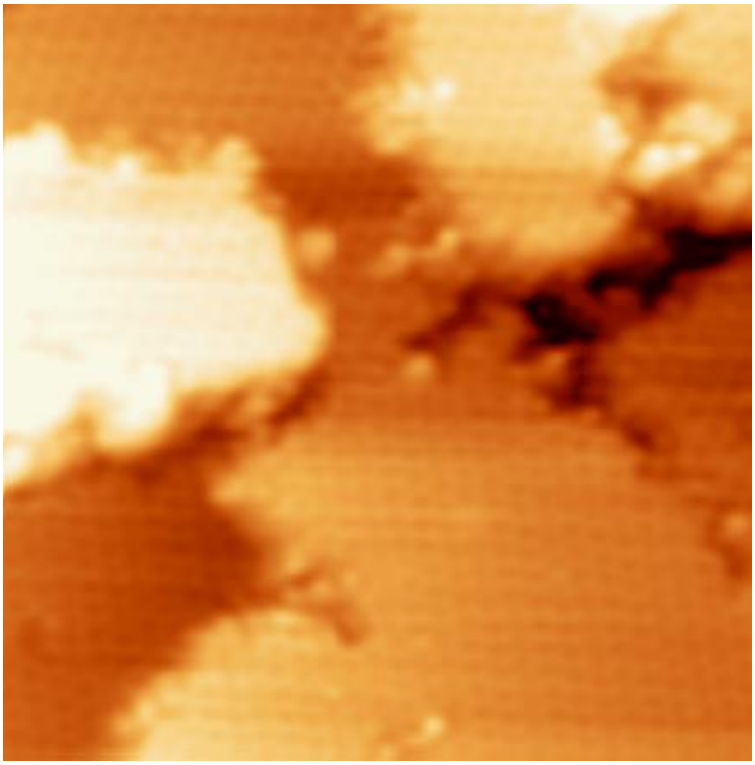

Figure 18: 20 nm × 20nm STM image of pristine multilayer silicene $(\sqrt{3} \times \sqrt{3})$. The tunnelling conditions are specified by V = -2.2 V (occupied states) and I_t = 0.19 nA.

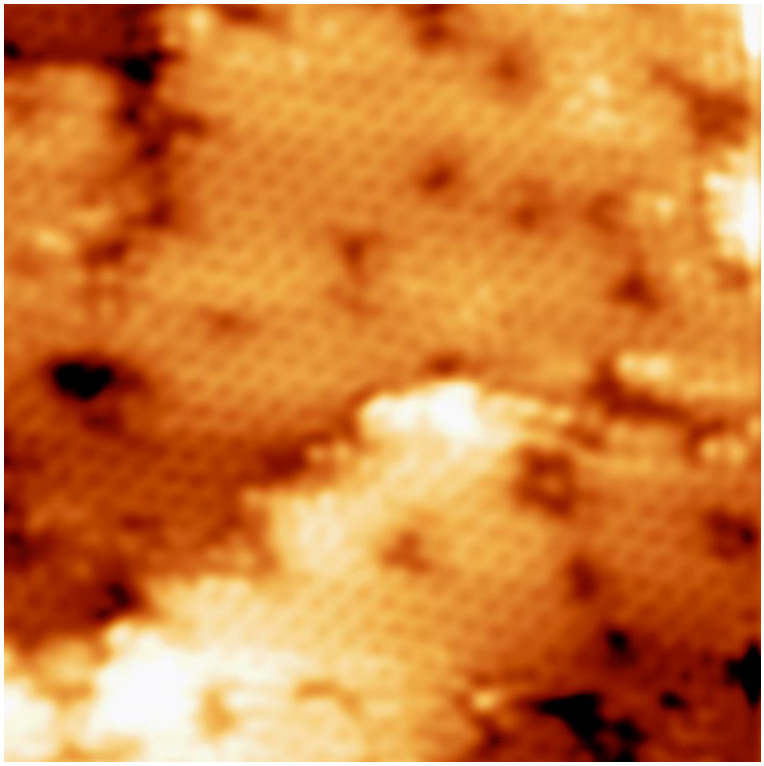

Figure 19: 20nm × 20nm STM image of multilayer silicene subjected to 10^{12} atoms of hydrogen. The tunnelling conditions were V = -1.4 V (occupied states) and I_t = 0.12 nA.

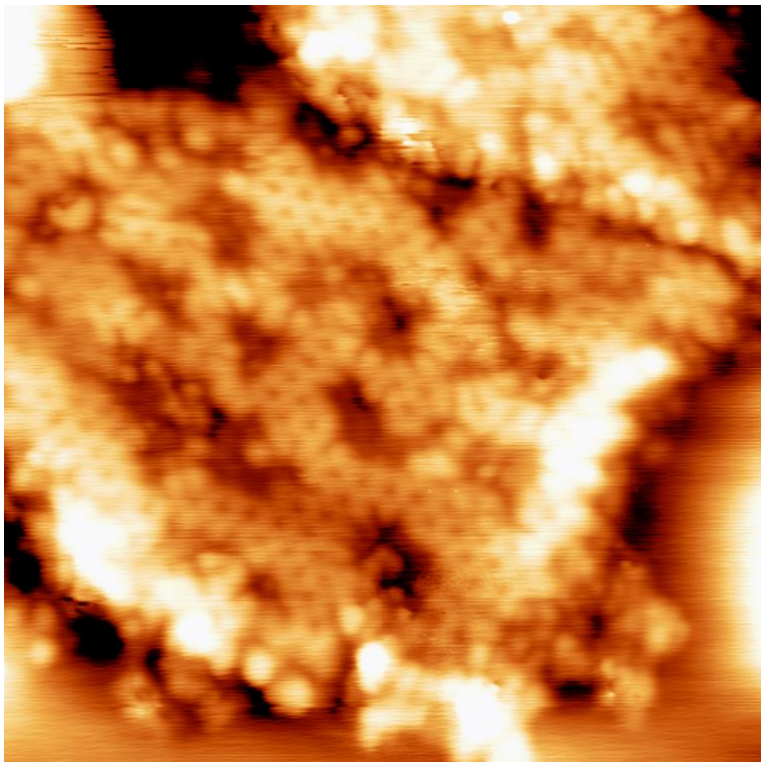

Figure 20: 20nm × 20nm STM image of multilayer silicene subjected to $2 \cdot 10^{12}$ atoms of hydrogen. The tunnelling parameters are given by V = -1.0 V (occupied states) and I_t = 0.11 nA.

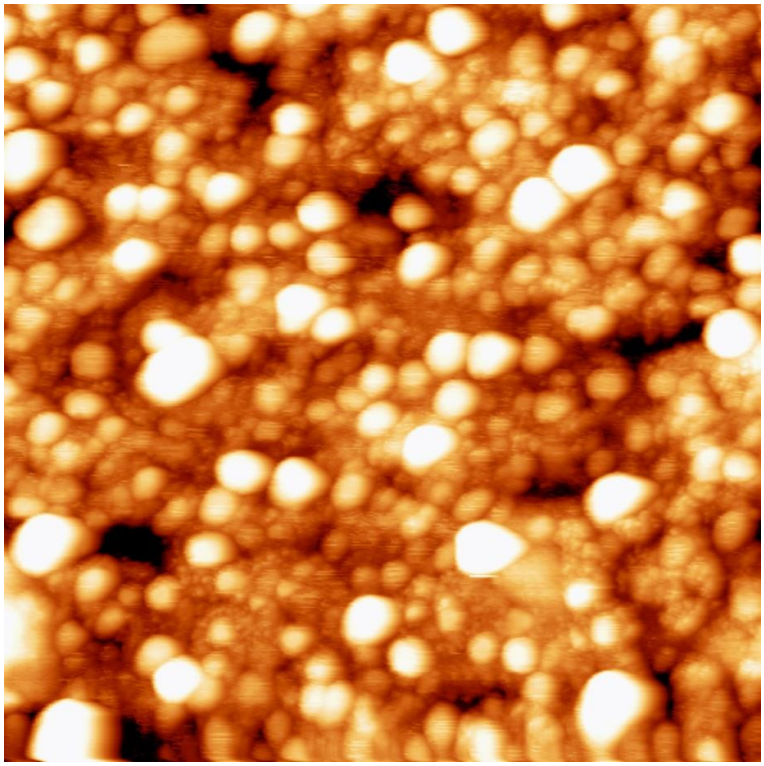

Figure 21: 100nm × 100nm STM image of multilayer silicene exposed to 10^{13} atoms of hydrogen. The tunnelling values were by V = -2.3 V (occupied states) and I_t = 0.29 nA.

In the light of this sequence of STM images the effects of hydrogenating thick silicene become evident. The four of them were obtained respectively on equivalent if not the very same samples as the LEED patterns included in figure 17, so comparisons can be established directly. As expected, they prove a steady and quick increase of the disorder on the surface.

On figure 18, a pristine multilayer silicene can be observed. The surface lies at three different height levels due to uneven coverage with silicon atoms. The cause is the growth mode of silicene, which causes the appearance of successive flat terraces. In any case, the small proportion of defects makes it look very regular.

After the first hydrogenation of 10^{12} atoms, the structure is still easily recognisable but a previously missing feature appears: small holes on the surface. In effect, groups of a few atoms seem to disappear at seemingly random locations. The holes have approximately the same size and apparently don't coalesce despite their proximity.

After doubling the dose the etching of the surface is much more evident. The holes have increased in size to the point of occupying a similar area to the unaffected silicene and still don't appear to group in spite of the short distances among them. Furthermore, amorphous blocks of atoms are now present at the borders of the terraces, probably implying a displacement of some silicon atoms from the holes to those places.

The trend so far has been rather fast so the expectations for the 10^{13} atoms dose aren't very promising for the conservation of the material. Indeed, on figure 21 it has even been impossible to obtain proper images. The amount of defects, especially the amorphous clusters of atoms, is staggering. This complicates the acquisition of images of the surface as the feedback loop tracks with difficulties the surface due to its random and aperiodic nature. The situation cannot be qualified as anything by absolute destruction of the surface, in harmony with the deductions extracted from the LEED patterns.

3.c) Vibrational spectrum

After the analysis of the structure of hydrogenated thick silicene, it's time to study its vibrational spectrum by means of the HREELS technique. For the sake of comparison, the figure below shows the spectra of hydrogenated monolayer and multilayer silicene.

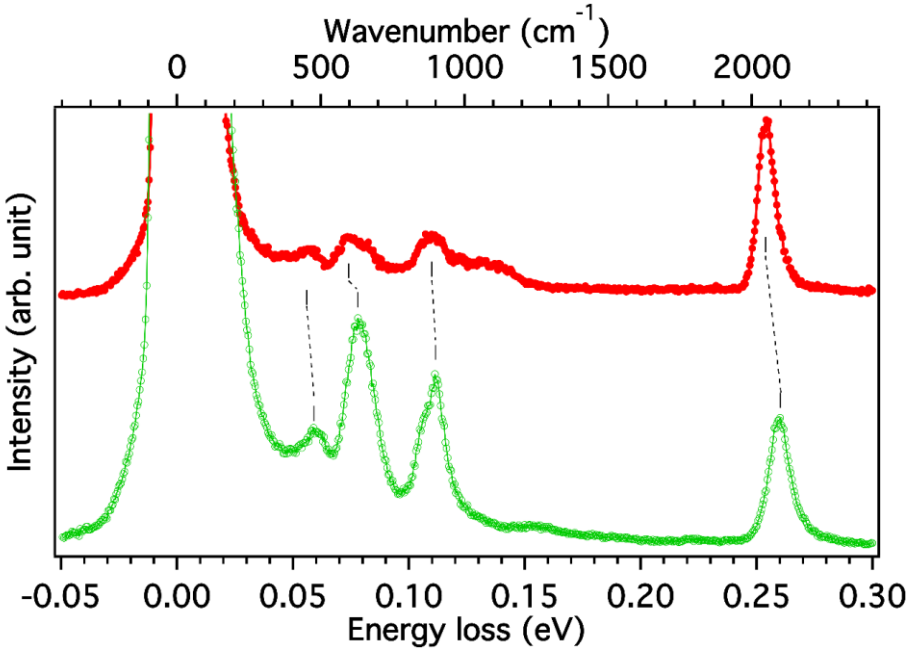

Figure 22: HREELS spectra (E = 5 eV) in specular conditions hydrogenated silicene $(\sqrt{3} \times \sqrt{3})$ (green) and hydrogenated silicene (4×4) (red).

Both spectra display the same features except for the unattributed peak of monolayer silicene at approximately 130 meV. The other two differences between them are small shifts of the Si-H peaks towards higher energies (for multilayer silicene) and the intensity ratios of the features. The following table includes the energies of the vibrational modes for both thicknesses of silicene, along with the same data for hydrogenated silicon.

Vibrational mode	Hydrogenated silicon energy (meV)	Hydrogenated monolayer silicene energy (meV)	Hydrogenated multilayer silicene energy (meV)
Stretching	261	255	260
Scissor	112	111	112
Wagging, twisting, bending	79	77	80
Rocking	60	57	59

Table 5: Vibration energies of hydrogenated silicon and hydrogenated silicene as a function of the thickness.

As the table shows, the softening of the modes previously noticed on monolayer silicene is absent in the case of its multilayer counterpart. This is reasonable because a thick silicene implies several silicon layers made of silicon atoms between the silver substrate and the surface. The greater distance between them associated to this new situation prevents the electrons from travelling from the substrate towards the orbitals of the dangling bonds. As a result, the hydrogen atoms can bind more tightly and easily to the surface, which in turn increases the force of the oscillators and thus the energy of vibration.

Additionally, the intensity ratio among the peaks is significantly different. The dominant mode of the monolayer spectrum is clearly the Si-H stretching since the rest of the features displays fluxes smaller by about one order of magnitude. In contrast, the vibrational modes of hydrogenated multilayer silicene are manifest with similar amplitudes, and the Si-H stretching doesn't appear as the preponderant peak anymore.

The amplitude of the signal is, among other factors, proportional to the number of oscillators. Consequently, and given that the spectra were registered in similar conditions, the relative increase of the multiple hydrides modes (scissor, wagging, twisting, etc.) suggests that the populations of mono-, di- and trihydrides have changed. The latter have become relatively more abundant, which implies that thick silicene reacts more readily with hydrogen, much like ordinary bulk silicon would do. As it was expected, thick silicene's behaviour seems to approach to bulk silicon with increasing coverage.

Last but not least, if dihydrides and trihydrides form more easily than on monolayer silicene, there's no reason to suppose that the process stops there. The formation of gaseous silane SiH_4 should also be possible and would explain the rapid etching of the surface. As the surface is more and more attacked by hydrogen any sort of order is destroyed and arrangements such as the one depicted on figure 21 are to be expected.

As a support for this last statement, the figure below contains HREELS spectra of hydrogenated multilayer silicene. All of them correspond to the same silicene preparation and are associated firstly to one hydrogenation and then to deuterations performed in succession.

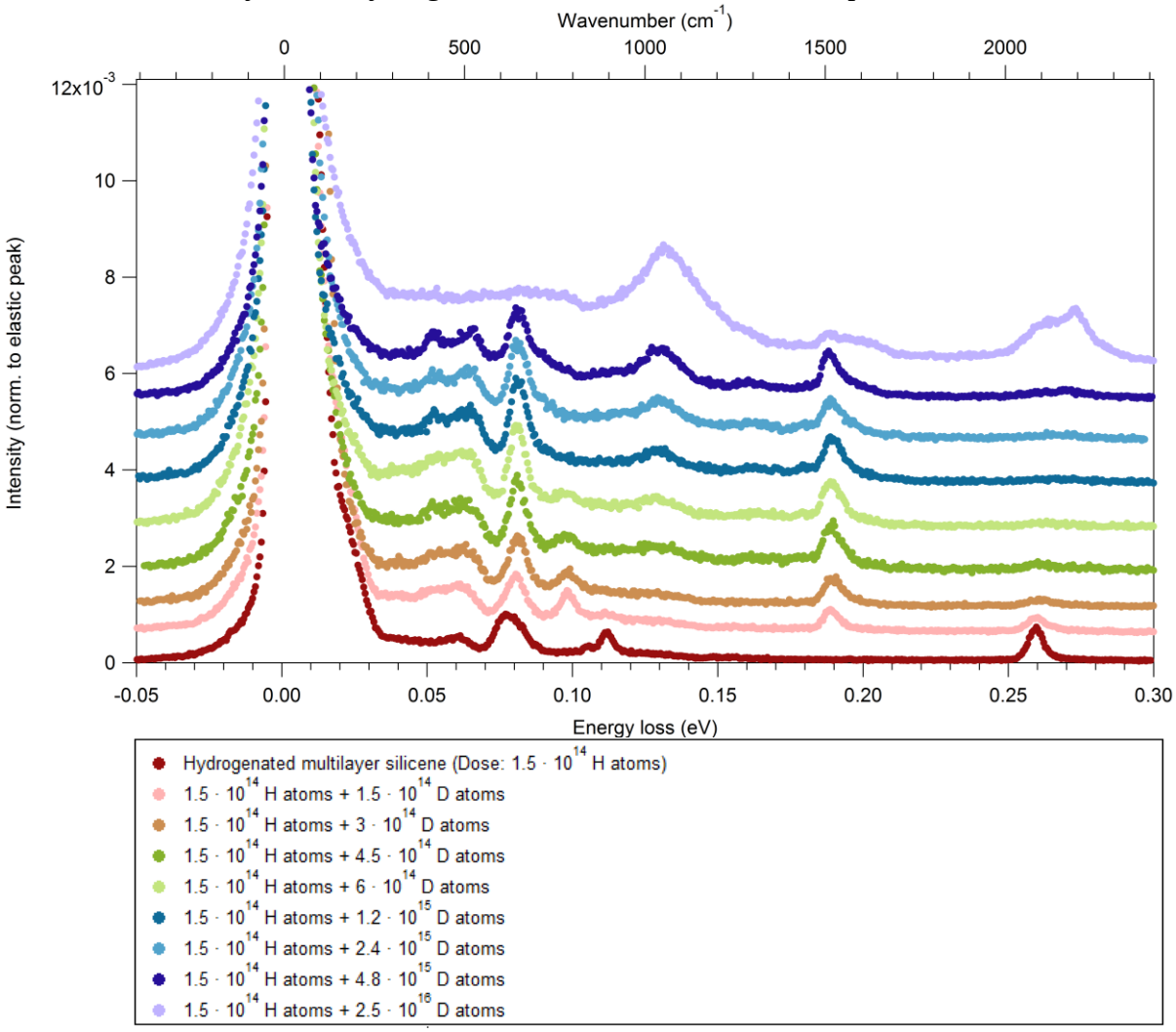

Figure 23: HREELS spectra taken with a primary energy equal to 5.2 eV in specular conditions after successive deuterations of hydrogenated multilayer silicene.

The abstraction of hydrogen with deuterium causes the appearance of several vibrational modes involving both isotopes. Below there's a list of the featured peaks.

Mode	Energy (meV)
Si-D_2 Bending	52
Si-H_2 Rocking	60
Si-H_2 Bending	72
Si-H_2 twisting	76
Si-D_2 scissor	81
Si-H_2 wagging	81
Si-HD scissor	98
Si-H_3 umbrella	105
Si-H_2 scissor	112
Si-D stretching	189
Si-H stretching	260

Table 6: Vibrational modes identified in the spectra of abstraction of hydrogen with deuterium on thick silicene (figure 24).

The lowest spectrum (red) corresponds to a typical hydrogenated thick silicene and can be compared with the green one in figure 22. From that point, the sample was subjected many times to different exposures of deuterium covering a large range of doses: from roughly $2 \cdot 10^{14}$ to $2 \cdot 10^{16}$ atoms of deuterium.

The figure shows the gradual transition from the vibrational signature of hydrogenated multilayer silicene to its deuterated counterpart. At the middle stages some modes produced by units comprised of silicon, hydrogen and deuterium at the same time are visible. Of course, they are missing when the sample has only been exposed to hydrogen and again when all of it has been replaced by deuterium.

The last spectrum demonstrates the destruction of thick silicene under the action of deuterium. All the Si-D peaks are gone except maybe a very weak Si-D stretching. All the new features are due to defects on the surface, clusters of atoms, deuterium atoms trapped beneath etc. The evident conclusion is that silicene seems to have mostly left the surface under the form of silane.

The remnant of the dramatic process is a surface seriously deteriorated. It obviously cannot be restored even partially by moderate annealing as it was possible for monolayer silicene.

4. Doping silicene with F_4TCNQ molecules

As it has been explained in the introduction, one of main goals of the stay at the synchrotron facilities was the repetition on silicene of some experiments performed on graphene in which the Fermi level was shifted down to the Dirac point by evaporating on top of the sample strong electronic acceptors, namely F_4TCNQ molecules[12]. These molecules were able to capture the "excess" of electrons effectively lowering the Fermi level.

One of the reasons why silicene has attracted interest lies in its linear electronic dispersion around the Γ point of the Brillouin zone[22]. Before addressing the doping itself, it is mandatory to examine the electronic bands prior to exposure to F_4TCNQ. The following figure includes an ARPES intensity map registered from the clean preparation of 3 hours along the Γ−K direction.

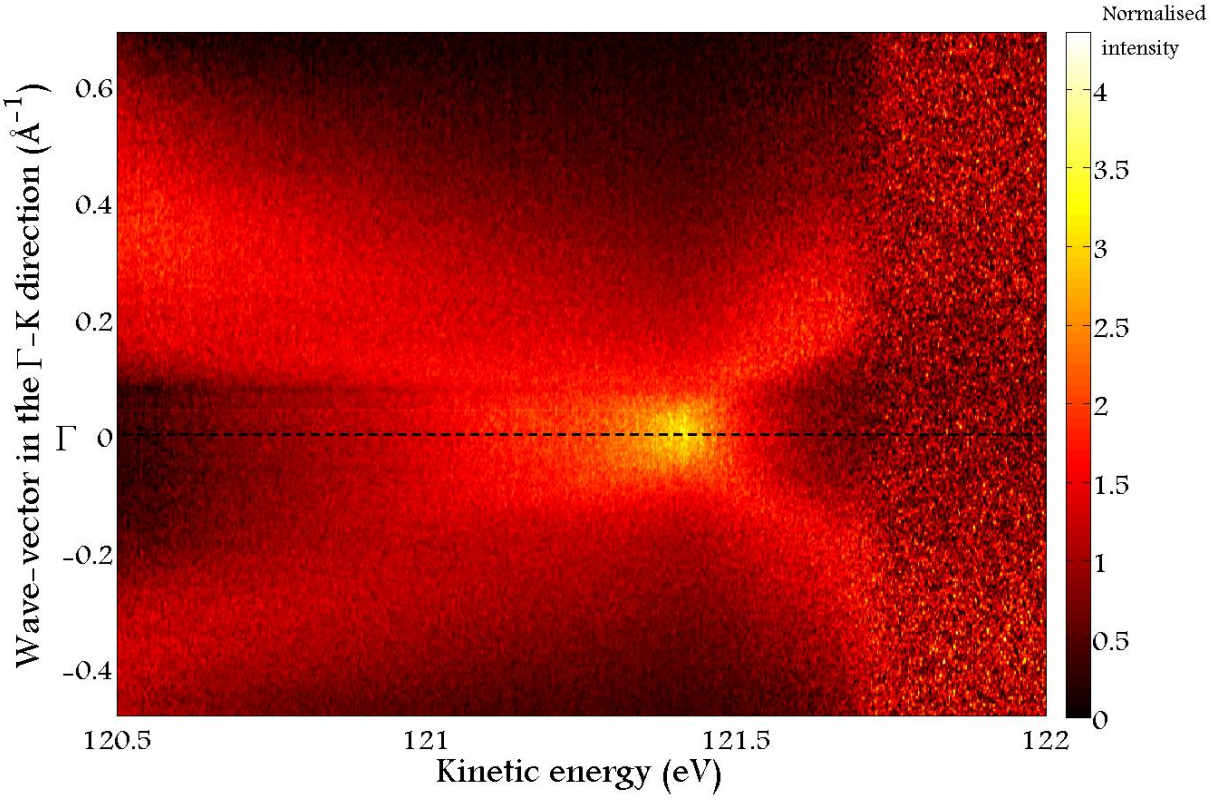

Figure 24: ARPES intensity map registered from a silicene grown for 3 hours along the Γ-K direction. The energy of the photons was fixed at 126 eV. The dashed black line corresponds to the Γ point.

The electronic bands contain useful information such as the effective mass of the electrons or its group velocity. In order to obtain those data it's necessary to identify precisely the bands present in figure 24. The noise level and the width of the branches greatly hinder the endeavour of finding the *backbone* of the bands. Thus, numerical methods are to be used to uncover the generatrix of the bands.

Two different approaches have been applied. In either case the data have been separated in slices of constant kinetic energy. From that point, the two manners diverge:

The first one consisted in performing a fit with two gaussian curves with the aim of accounting for both of the branches expressed in every slice. However, the profiles of the features not only were noisy, but in many cases also quite different from a gaussian shape. Anyway this yielded good estimations of the centre of the branches for every kinetic energy.

The second one separated the data in two parts (negative and positive wave-vectors) and then computed the average wavevector of the points located over the threshold determined by the 60th percentile in intensity. This method was more sensitive to the noise but was best-suited to deal with distributions of signal very distinct from gaussian profiles.

An example of both strategies is displayed in figure 25.

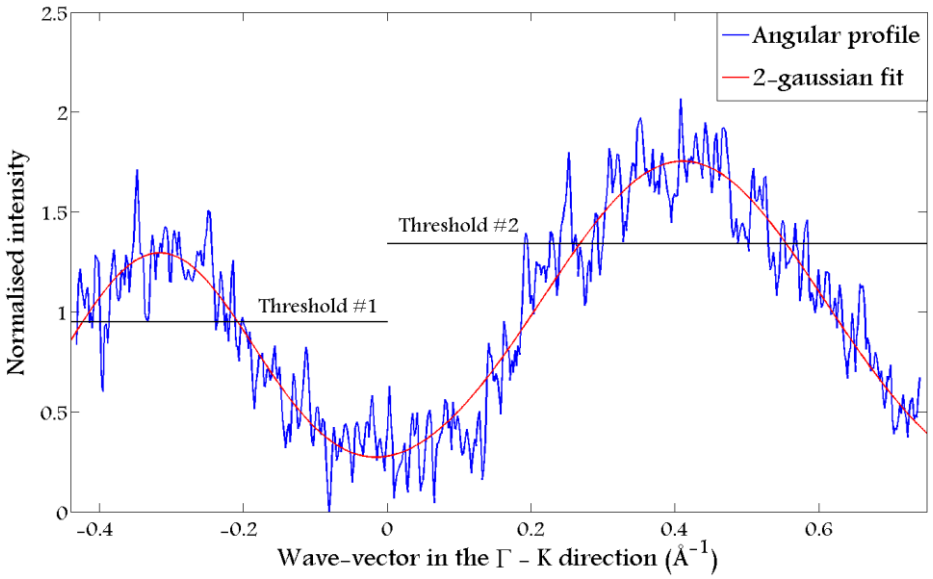

Figure 25: Double gaussian fit and thresholds of the angular profile obtained from figure 24 at 120.6 eV of kinetic energy.

In the end, acknowledging the limitations of each approach, both were combined to find the core loci of the branches. The results are shown in the figure below.

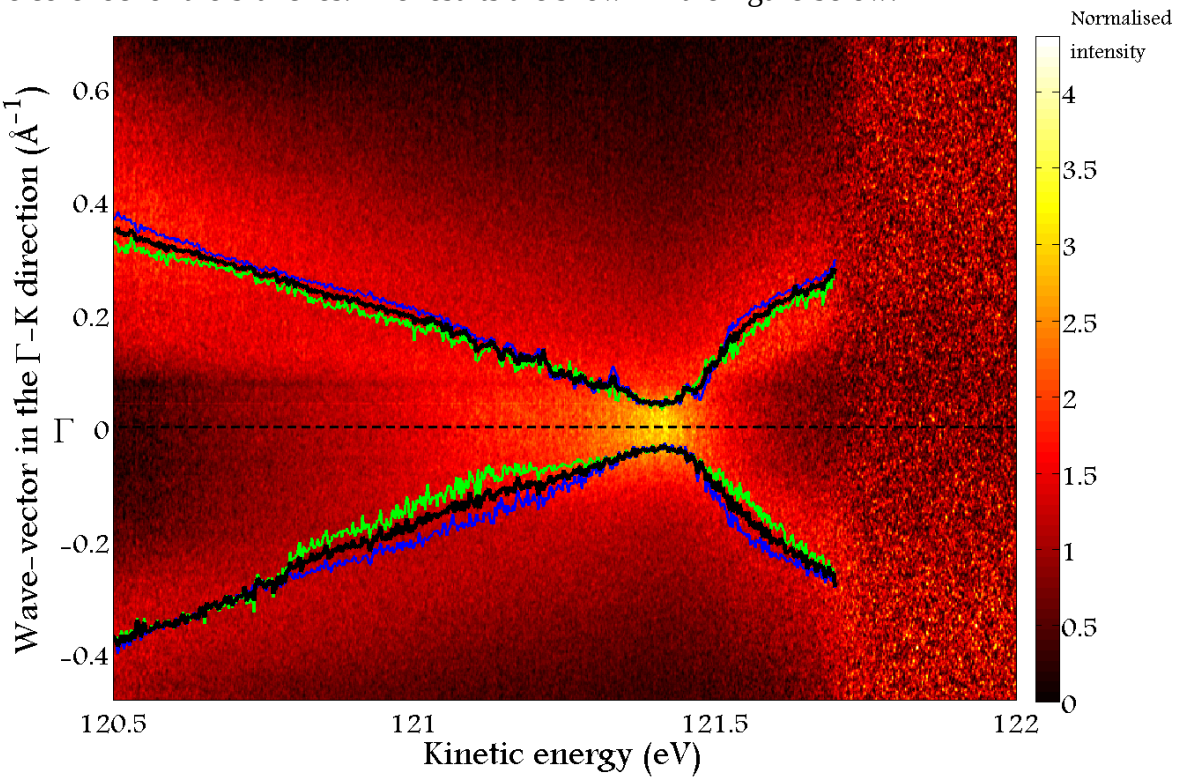

Figure 26: ARPES intensity map registered from a silicene grown for 3 hours along the Γ-K direction. The energy of the photons was fixed at 126 eV. The dashed black line corresponds to the Γ point. The green curves were produced by the method based on the 60th percentile, while the blue ones were the result of the gaussian fits. The black lines represents the average of the previous two curves.

Now, the loci that generates the branches is determined and the analysis can be pursued by means of the black lines. They have been fitted to two cones (one within the region under 121.35 eV and the other one beyond 121.50 eV) specified by the expression:

$$E_k = A \cdot \left|k_{||}\right| + B$$

The parameter A is related to the slope of the branches and B is the position on the energy axis of the vertex of the cone. The results of the fits are included in the following table:

A_1 (eV/Å^{-1})	B_1 (eV)	A_2 (eV/Å^{-1})	B_2 (eV)
-2.68 ± 0.02	121.5 ± 0.1	1.27 ± 0.04	121.3 ± 0.1

Table 7: Parameters of the fits with the Dirac cone's model performed on the black curves displayed in figure 26.

The figure below displays the superposition of the generatrices of the branches and the Dirac cones fitted to them.

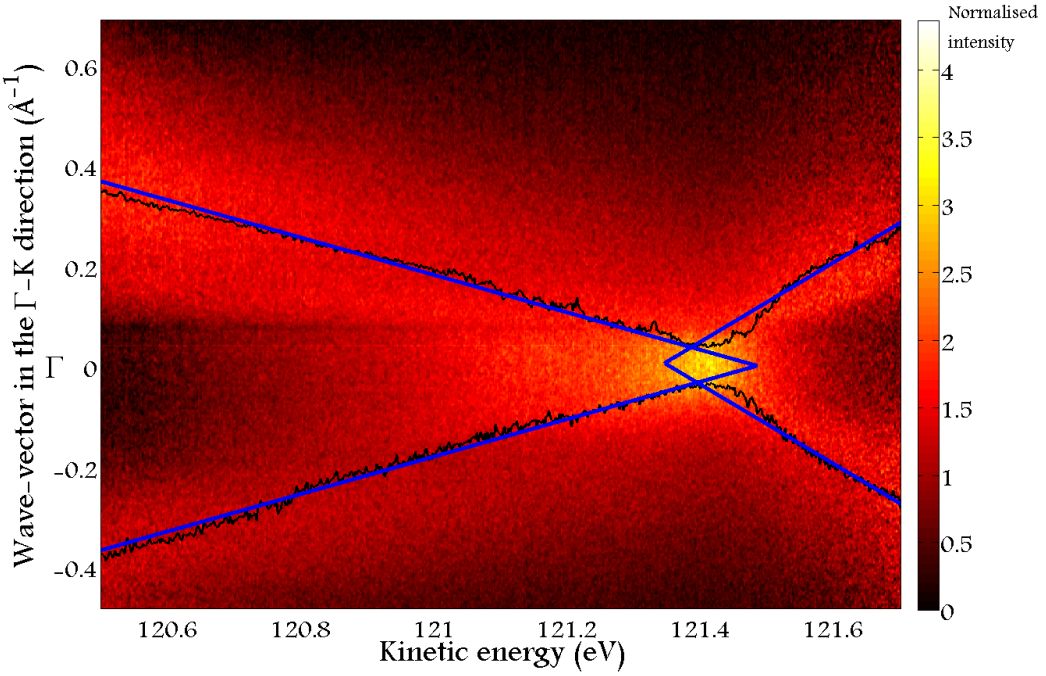

Figure 27: ARPES intensity map registered from a silicene grown for 3 hours along the Γ-K direction with photons of 126 eV. The black lines represent the generatrices of the branches. The straight blue segments are the best fits for the black curves found assuming a Dirac cone model (linear dispersion).

The parameter A is directly related to the group velocity of the electrons, the so-called Fermi velocity. In effect, the group velocity can be deduced from the dispersion relation as derivative of the energy with respect to the wave-vector as the next equation establishes:

$$v_g = \frac{1}{\hbar} \cdot \frac{dE}{dk}$$

By replacing with the parameters of the fits, it's immediate to find:

$$v_g = \frac{1}{\hbar} \cdot A$$

This yields two results for the group velocity, one relative to the less energetic π band ($4 \cdot 10^5$ m/s) and the other related to the higher π^* branches ($2 \cdot 10^5$ m/s). These results can serve as references to ascertain that the Fermi velocity of thick silicene is approximately $3 \cdot 10^5$ m/s. This value is in excellent agreement with the one obtained from a very similar experiment[23]. The conclusions of the previous chapter suggest that the topmost layer of the sample was at least partially composed by silver, so this Fermi velocity may correspond to the silver terminated thick silicene. However, Crain[31] reports a Fermi velocity for the system Si(111) $(\sqrt{3} \times \sqrt{3})$-Ag equal to $1.3 \cdot 10^6$ m/s, more in line with the Fermi velocity of bulk silver. The value found here is 4 times smaller, suggesting that it actually comes from silicene.

Regarding the Dirac point, the fitted cones display a significant non-punctual overlap, but it's obvious that the high noise along with the great width of the branches (around 0.2 $Å^{-1}$) make the task of finding a unique Dirac point quite unfeasible. For this reason the overlap zone can be considered as an uncertainty trapezoid that encloses the real apex of the cones. One convincing argument that supports this statement is the fact the most intense region (indicated by the yellow colour) is located inside the trapezoid. The final position of the Dirac point would be 121.4 ± 0.1 eV, or equivalently, 0.3 ± 0.1 eV below the Fermi level. This is compatible with what was found by De Padova as well[23].

At this point, an individual electron dispersion near the Fermi level of thick silicene has been examined in detail. It is now possible to study the doping of silicene with F_4TCNQ molecules and evaluate whether it causes the same results[3] as in graphene or not.

As made clear in figure 28, the only visible effect of the addition of molecules is the gradual fading and blurring of the electron bands. In other words, the signal-to-noise ratio from the branches becomes weaker with increasing amounts of molecules. The noise beyond the Fermi level has been left constant intentionally to facilitate the verification of this trend.

Concerning the electronic structure, the Fermi level stays fixed at 121.7 eV of kinetic energy, hence the molecules cannot capture enough electrons and the separation between the Fermi level and the Dirac point remains constant.

In the case of monolayer silicene, such a result could be attributed to a transmission of electrons from the silver substrate towards the silicene layer, however after three hours of evaporation the silicene on this sample should be thick enough to prevent this effect. The explanation probably doesn't lie beneath silicene, but on top of it. Indeed, in the previous section the spectra have shown a very powerful surface/interface Ag feature coming from the 3h preparation which seems to point at the existence of a monolayer of silver on top of the sample. If that were the case, the silver atoms could overwhelm the F_4TCNQ molecules with electrons, unfortunately rendering the tentative of doping fruitless.

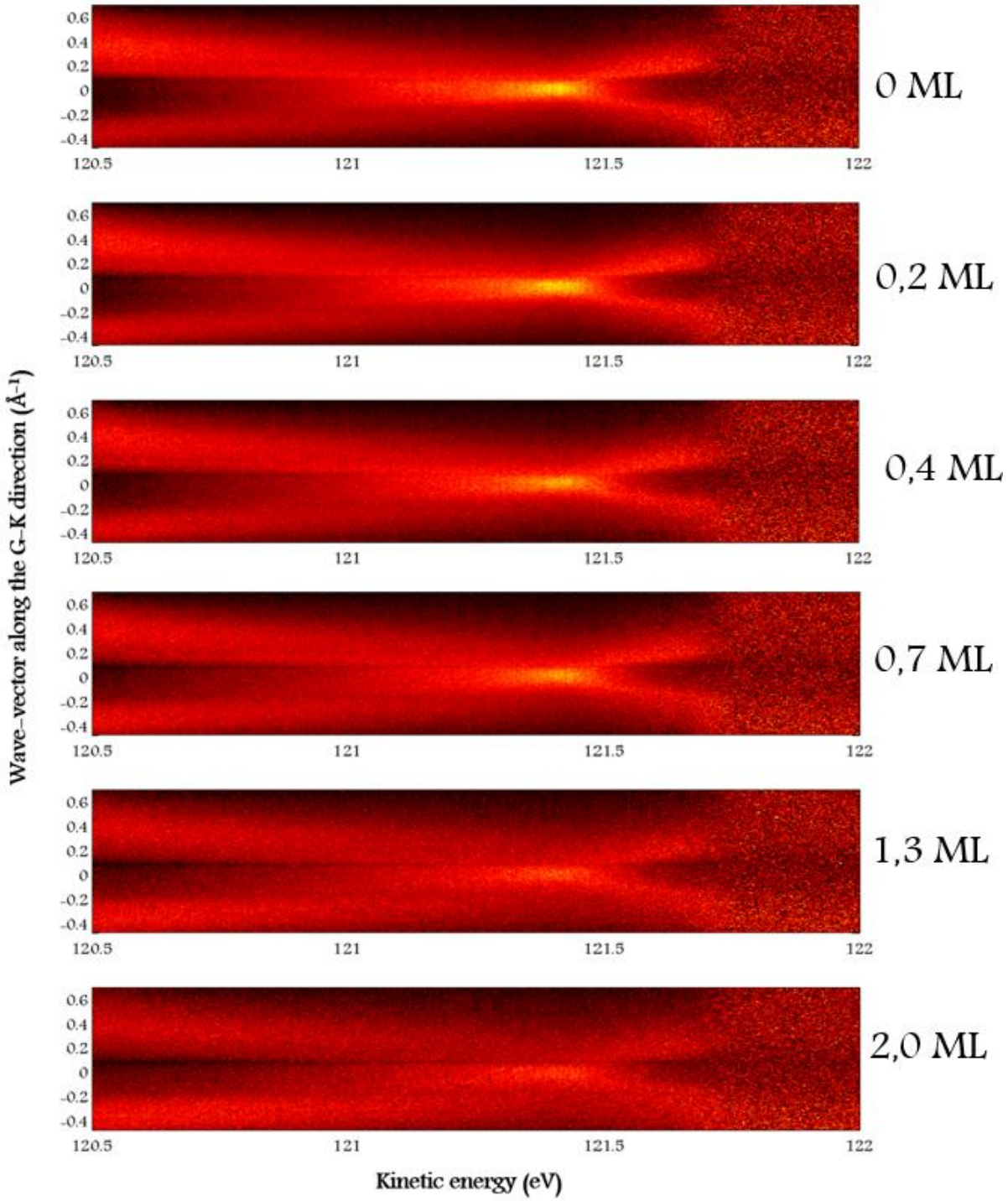

Figure 28: ARPES intensity maps registered from a silicene grown for 3 hours along the Γ-K direction with photons of 126 eV as a function of the amount of F_4TCNQ deposited on the sample. From the top chart in descending order the respective doses are: 0, 0.2, 0.4, 0.7, 1.3 and 2.0 monolayers.

5. Conclusions

Hydrogenation has been proposed as a simple way of varying the physical properties of silicene, notably its electronic gap[6,7]. Interestingly, the behaviour of this material when exposed to hydrogen varies dramatically as a function of its thickness. In particular, the transition between the two studied reactions with the said gas seems to be discrete: while monolayer silicene exhibits a well-ordered change, the multilayer analogue, even when it only consists of two extensive layers, manifests a much more destructive trend.

Monolayer silicene tends to adopt an arrangement similar to β-silicene (4×4) when exposed to hydrogen. The new phase replaces progressively the α configuration as the dose increases, however the latter can persist after the process according to the corrugation measurements. The reason of its persistence is not a defective hydrogenation, since hydrogenated α-silicene has displayed the same enhancement of the corrugation as the predominant phase compared to the pristine surface. It is nonetheless clear that the β configuration covers a significantly vaster area and that the α arrangement may need the presence of some defects to increase its stability and avoid the phase transition. The profiles also support the exclusive chemisorption of hydrogen on the atoms lying at the higher level of the monolayer.

Regarding the HREELS spectra, they reveal the pre-eminence of the stretching mode. This fact is also in agreement with the chemisorption of mainly one hydrogen atom per silicon on the upper level of the monolayer. Furthermore, the peaks appear shifted a few meV towards lower energies, replicating a mechanism already observed on erbium silicide[19] or silicon nanowires[18]. The phenomenon is produced by a charge transfer from the silver substrate towards the silicene on the surface. In effect, delocalised electrons are transferred to the dangling bonds reducing the reactivity of the surface. Hence the Si-H bonds become less tight and the vibrational modes soften.

On the other hand the modifications undergone by multilayer silicene under the effect of hydrogen are less benign. Even doses well below monolayer coverage induce the etching of the material, which is observable through the appearance of holes and amorphous clusters of atoms on the surface. The tendency is steady and the defects increase in size and spatial frequency until silicene loses completely its crystalline lattice during a process that is not reversible and leads to the destruction of the material.

The HREELS spectra concur with this explanation and display no significant Si-H modes for doses sufficiently high. Instead, large bumps appear that are linked to the existence of numerous defects such as the ones visible on the STM images. Additionally, the softening of the modes is no longer appreciated, implying that multilayer silicene reacts to hydrogen in a more similar way to bulk silicon[16]. For this reason, passivation of silicene by means of hydrogen seems only appropriate for the monolayer variant.

Regarding the doping with F_4TCNQ molecules, it has proved to be unsuccessful. Even at high coverage of acceptors the Fermi level seems to stay fixed. This probably indicates that the molecules are unable to cope with the excess of electrons in contrast with what happened with graphene on SiC. In the light of the results of the previous chapter, this is probably due to the fact that the surface is Ag terminated.

References:

1. Giovannetti G., et al., Phys. Rev. B: Condens. Matter Mater. Phys., 76, 073103 (2007)
2. Sofo J. O., et al., Phys. Rev. B: Condens. Matter Mater. Phys., 75, 153401 (2007)

3. Zhou, J., et al., Nano Lett., 9, 3867 (2009)
4. Bludau W., et al., J. Appl. Phys. 45, 1846 (1974).
5. Hybertsen M. S. and Louie S. G., Phys. Rev. Lett. 55, 1418 (1985).
6. Huang B. et al., Physical Review X 4, 021029 (2014)
7. Osborn T. H. et al., Chemical Physics Letters 511 101–105 (2011)
8. Deepthi, J. and Aran D., Phys. Chem. Chem. Phys., 13, 7304–7311 (2011)
9. Wang, X. Q. et al., Phys. Chem. Chem. Phys., 14, 3031–3036 (2012)
10. Tsetseris L. and Kaltsas D., Phys.Chem.Chem.Phys., 16, 5183 (2014)
11. Qiu, J et al., ACS Nano 9, 11192 (2015)
12. Coletti, C. et al., Phys. Rev. B, 81, 235401 (2010)
13. Meneghetti M., and Pecile, C., J. Chem. Phys. 84, 4149 (1986)
14. Bröker, B. *"Electronic and structural properties of interfaces between electron donor and acceptor molecules and conductive electrodes"*, Ph.D. Thesis (2010)
15. Lucovsky G., et al., Phys. Rev. B 19, 2064 (1979)
16. Tautz F. S. and Schaefer J. A., J. Appl. Phys., Vol. 84, No. 12 (1998)
17. Harris, D. C.; Bertolucci, M. D. *Symmetry and Spectroscopy*; Oxford University Press, Inc.: New York, NY (1989)
18. Salomon, E. et al., Science of Advanced Materials Vol. 3, 1–8 (2011)
19. Angot, T. et al. Surface Science 368, 190-195 (1996)
20. Scalise, E. et al., Nano Research, 6(1): 19–28 (2013)
21. Yan, J. et al., Phys. Rev. B 88, 121403 (2013)
22. Aizawa, T. et al., J. Phys. Chem. C, 118, 23049−23057 (2014)
23. De Padova, P. et al., 2D Mater. 1, 021003 (2014)
24. Qiu J. et al., Phys. Rev. Lett. 114, 126101 (2015)
25. Vogt P. et al., Phys. Rev. Lett. 108, 155501 (2012)
26. Liu Z. L., et al., New J. Phys. 16, 075006 (2014)
27. Salomon, E. et al., J. Phys.: Condens. Matter 26, 185003 (2014)
28. Cahangirov, S. et al., Phys. Rev. B 90, 035448 (2014)
29. Shirai, T. et al., Phys. Rev. B 89, 241403(R) (2014)
30. Fu, H. et al., Nanoscale, 7, 15880 (2015)
31. Crain, J. N. et al., Phys. Rev. B 66, 205302 (2002)

General conclusions

Throughout this thesis, several interface architectures on metallic substrates have been thoroughly analysed. Apart from the supporting material, they had in common its low dimensionality as they comprised either one or just a few layers of adsorbates. Regarding these, they were diverse from the chemical point of view since organic molecules, atomic hydrogen and atoms of silicon were all used in the experiments, frequently even combining two of them. The great range of available techniques of surface analysis during the elaboration of this work has been crucial for deepening the knowledge on fundamental aspects of surface physics. This has also had the advantage of providing exhaustive and transversal information of the studied systems.

The analysis of the CoPc/Ag(100) interfaces began with the unexpected observation of a previously unreported surface arrangement of the molecules, the (7×7) phase. Interestingly, in the light of the HREELS spectra, it was possible to verify that the difference wasn't only structural, but also involved the charge transfer mechanisms, manifested through the expression of asymmetric features exclusive to the new phase. At this point, the photoelectron diffraction and the numerical simulations were very appropriate tools for determining up to a very high level of detail and precision the geometrical structure of the interface. The sites and distance of adsorption and the orientation of the molecules were elucidated for the new phase. The most remarkable difference was the existence of a site of adsorption completely absent in the better understood (5×5) reconstruction, which causes small geometrical variations supposed to be at the origin of the differences in the mechanism of charge transfer. Finally, a consistent model of the (7×7) phase was conceived and verified with all the available experimental evidences.

Regarding silicene, it has been examined from the perspective of its reactivity and its intrinsic structure.

The second main topic has been the growth of silicene studied by means of photoemission spectroscopy. The experiments reported in this thesis imply that the evaporation of silicon atoms on Ag(111) surfaces starts with the formation of the silicene (4×4) monolayer on top. As soon as multilayer silicene appears, most of its atoms transit from a surface/interface character to a bulk behaviour. Interestingly enough, multilayer silicene has also been related to the rise of a silver surface/interface peak, probably associated to a silver $(\sqrt{3} \times \sqrt{3})$R30º surface reconstruction on top. This seems to be the situation derived from the data presented here, but it could be different by varying very slightly parameters such as the temperature of formation.

In this respect, the additional photoelectron diffraction pattern is compatible with a "silver on bulk silicon" hypothesis, but the lack of a more complete model makes a more conclusive statement impossible.

On another matter, the ARPES measurements are compatible with the existence of the Dirac cones in the studied system but the uncertainty is too high to choose between a linear or non-linear dispersion. The attempted doping with F_4TCNQ molecules was unsuccessful, which at multilayer coverage seems to imply again a last layer of silver on the surface.

Thirdly, hydrogenation has proved to be a satisfactory and reversible way of protecting monolayer silicene from the chemical attack of species such as oxygen. It has been shown that it produces the appearance of a new STM pattern probably linked to the less stable β configuration of clean silicene. However, the data have also demonstrated that the α phase persists after hydrogenation, though it occupies a significantly smaller portion of the surface and is possibly stabilised by defects in the surface.

On the other hand the perspectives for hydrogenating multilayer silicene are less promising. Hydrogen interacts in a completely different manner with thick silicene and causes a fast transformation into silane. The net effect on the surface is the appearance of irreversible etching even for very small doses of hydrogen. As it stands, the reactivity of this material appears to depend critically and in a discrete way on the number of layers.

All in all, silicene could be a milestone in the next technological paradigm as the recent production of a field-effect transistor has shown. Anyway such two-dimensional materials require deep studies and behind the findings included in this thesis there are probably as many new questions to be solved.

Summary

Nanosciences and surface science are key elements in the conception of a diversity of innovative materials designed to better cope with the needs of current technology. Within this context, we have resolved to characterise the properties of different two-dimensional structures grown on silver substrates with the help of several complementary techniques of surface analysis.

Firstly, we have studied auto-assembled 2D films of cobalt phthalocyanine on Ag(100) substrates. In situations with coverages close to the monolayer, two phases were observed: the (5x5) and the (7x7). The electron energy loss spectroscopy has allowed us to support the existence of two inequivalent charge transfer mechanisms between the substrate and the molecules. On one hand, the (5x5) reconstruction displays a transfer that involves the silver atoms and only the cobalt atoms of the molecules. On the other hand, the phenomenon rather occurs between the substrate and lowest unoccupied molecular orbital in the case of the (7x7) phase. A fine analysis of the adsorption geometry of the molecules on the surface performed by means of photoelectron diffraction along with the comparison to simulations in the framework of multiple scattering approximation have made it possible to identify the presence of sites of adsorption particular to each phase as the underlying cause for the distinct charge transfer mechanisms.

Secondly, we have synthesised both monolayer and multilayer silicene by evaporating silicon atoms on Ag(111) substrates. Silicene is a two-dimensional material akin to graphene but made of one or a few layers of silicon atoms. However, many physical properties of this allotrope are still unexplained. For this reason, we have decided to delve into the characteristics of multilayer silicene as it's less well-known than its monolayer counterpart. With this aim, the system has been subjected to experiments of photoemission spectroscopy and diffraction. In this manner, several hypotheses on the very nature of this material have been tested. In particular, we have observed that both the silver substrate and the silicene on top display at least two different characters (bulk and interface) manifested through the splitting of the analysed core levels. Furthermore, the ratio of intensities as a function of the angle of observation have hinted at a puzzling stratification of the system.

On another matter also related to silicene, we have studied its functionalization by adsorption of F_4TCNQ molecules and atomic hydrogen. We attest that hydrogenation is a convenient way of protecting monolayer silicene from damaging chemical reactions such as oxidation. Unfortunately, the multilayer variant undergoes a more drastic change as a non-reversible etching takes place on its surface instead. Regarding the F_4TCNQ exposure, these molecules were successfully used in the past to dope supported graphene, but an analogue experiment didn't alter significantly the electronic properties of our multilayer silicene near the Fermi level. We suspect that the unexpected stratification deduced from the photoemission spectra, which seems to include a silver layer on top of multilayer silicene, could be at the origin of this divergent behaviour (compared to its carbon cousin). In effect, a silver layer on top could be able to provide enough electrons to saturate the acceptor molecules without modifying the electron bands, thus rendering the doping fruitless.

Résumé

La physique des surfaces et nanosciences est une discipline qui permet la conception d'une diversité de matériaux innovants pour mieux répondre aux besoins de la technologie actuelle. Dans ce contexte, nous nous sommes intéressés à caractériser les propriétés de différentes structures 2D élaborées sur des substrats d'argent en combinant différentes techniques d'analyses de surface.

D'une part nous avons étudié des films 2D auto-assemblés à base de phtalocyanine de cobalt adsorbées sur Ag(100). Au régime de la monocouche, deux phases ont été essentiellement observées : la (5×5) et la (7×7). La spectroscopie de pertes d'énergie nous a permis de mettre en évidence deux mécanismes de transfert de charge métal/molécule différents. Un entre le substrat et les atomes de cobalt de la molécule dans le cas de la (5×5). L'autre, pour la phase (7×7), entre le substrat et l'orbitale moléculaire la plus basse inoccupée de la molécule. Une analyse fine de la géométrie d'adsorption des molécules sur la surface d'Ag(100) par diffraction de photoélectrons, et une comparaison avec des simulations réalisées dans le cadre de diffusion multiple, nous ont permis d'établir l'existence de différents sites d'adsorption, dépendant de la phase, et comme étant à l'origine de ces différences de mécanismes de transfert de charges.

D'autre part, nous avons synthétisé, par évaporation d'atomes de silicium sur de l'Ag(111), du silicene en monocouche et multicouche. Le silicène est un matériau bidimensionnel analogue du graphène constitué d'une ou plusieurs couches d'atomes de silicium. Néanmoins, de nombreuses questions restent ouvertes quant aux propriétés physiques du silicene. Ainsi nous avons entrepris des mesures dans le but de comprendre les propriétés structurales du silicene en multicouche. Pour cela nous avons engagé des mesures par spectroscopie de photoémission et diffraction de photoélectrons, et comparé nos données avec des simulations réalisées dans le cadre la diffusion multiple. Plusieurs hypothèses concernant la nature de ce matériau ont pu être testées. En particulier nous avons observé que l'argent et le silicene présentent au moins deux caractères différents (interface et *bulk*) qui se manifestent par le dédoublement des niveaux de cœur analysés. Néanmoins, les rapports d'intensité des diverses composantes en fonction de l'angle d'observation ont signalé une stratification qui n'est pas évidente à interpréter.

Par ailleurs nous avons étudié la fonctionnalisation du silicene par hydrogénation et adsorption de molécules de F_4TCNQ. Nous avons constaté que l'hydrogénation est une bonne manière de protéger la monocouche, par exemple de l'oxydation, mais beaucoup plus destructive vis à vis du silicène multicouche, qu'elle détériore par attaque chimique. Par ailleurs, nous avons déposé des couches de molécules F_4TCNQ, molécules utilisées avec succès pour le dopage du graphène, sur silicène multicouche dans le but d'en modifier ses propriétés électroniques. Nous n'avons malheureusement pas été en mesure d'observer une modification notable de la structure électronique près du niveau de Fermi. Ceci potentiellement en raison de la couche d'argent formée en surface, lequel disposerait de suffisamment d'électrons pour empêcher l'effet du dopage escompté.